THE TROPICAL CYCLONE DIURNAL CYCLE

by

Jason P. Dunion

A Dissertation

Submitted to the University at Albany, State University of New York

in Partial Fulfillment of

the Requirements for the Degree of

Doctor of Philosophy

College of Arts and Sciences

Department of Atmospheric and Environmental Sciences

2016

ABSTRACT

The research presented in this thesis explores a phenomenon referred to as the tropical cyclone (TC) diurnal cycle (TCDC) and presents satellite, numerical modeling, and observational perspectives pertaining to how it can be monitored, its evolution in time and space, its relevance to TC structure and intensity, and how it manifests in numerical simulations of TCs. Infrared satellite imagery was developed and used to investigate diurnal oscillations in TCs and finds a diurnal pulsing pattern that occurs with notable regularity through a relatively deep layer from the inner core to the surrounding environment. A combination of satellite, numerical model simulations, and aircraft observations found diurnal signals in operationally analyzed radii of 50 kt winds in TCs and in satellite intensity estimates from the Advanced Dvorak Technique and spawned the development of a 24-hr conceptual clock that approximates the temporal and spatial evolution of the TCDC each day. TC diurnal pulses are revealed to significantly impact the thermodynamics and winds in the TC environment and appear as narrow, convectively active rings of high radar reflectivity in NOAA aircraft radar data and are hundreds of kilometers in length. Enhanced nighttime radiational cooling that is particularly favored in the TC outflow layer acts to pre-condition the TC environment in a way that favors triggering of the TCDC and TC diurnal pulses, while in the daytime, the stabilizing effects of shortwave warming begins to suppress TCDC processes in the storm, leading to the culmination of the TCDC each day. Schematics are presented that summarize many of the main findings in this work, including descriptions of the basic state of the TC environment as the TCDC evolves during its early and later stages each day and a TCDC-centric daytime evolution of a TC diurnal pulse, associated squall lines and gust fronts, and radial and vertical winds in the lower and upper levels of the storm. The TCDC represents a largely unexplored, yet possibly fundamental TC process.

ACKNOWLEDGEMENTS

I would like to thanks Chris Thorncroft for his interest in working with me and accommodating my complicated balance of commitments to school, family, and a full-time job. I have valued his insight and open-mindedness throughout this process and am especially appreciative of his support and encouragement to pursue my early-stage TC diurnal cycle work when I first began my PhD work.

Thank you to John Molinari, Ryan Torn, Lance Bosart, Frank Marks, and Chris Velden (aka the "*hive*") for their willingness to serve on my committee. The many hours of brainstorming with Chris and the "*hive*" provided more ideas, hunches, and leads to even count. The inquisitive nature of this group was and continues to be infectious and I am indebted to each of them. Special thanks also to Frank Marks for always supporting my unending battle to balance my PhD work with my job at the University of Miami/CIMAS - NOAA/HRD.

Personal thanks goes out to my family for their support throughout my time at Albany- I could not have completed my first few years of classwork, qualifying exam studying, and commuting thousands of miles without them. Thank you to my Mom, Dad, and Connie for helping us care for our kids, Erika and Corey, during my many days away from home and to Erika and Corey for their patience when their Dad was busy with schoolwork. Finally, I would like to extend a very special thanks to Paige for her support and encouragement from start to finish.

Lastly, I would like to acknowledge that this research would not have been possible without financial support from the NASA Hurricane and Severe Storm Sentinel (HS3) program (NASA grant NNX10AU44G).

CONTENTS

1. Introduction

Although numerous studies have documented the existence of diurnal maxima and minima associated with tropical oceanic convection and the tropical cyclone (TC) upper-level cirrus canopy, relatively less research has been done in the areas related to the nature and causes of these variations and the extent to which these variations are important for TCs. This current work includes the development of new infrared (IR) satellite imagery that is used to investigate diurnal oscillations in TCs and finds an intriguing diurnal pulsing pattern that appears to occur with remarkable regularity through a relatively deep layer of the TC from the inner core (R~ ≤150 km, Rogers et al. 2012) to the surrounding environment (R~ 150-450+ km). These TC diurnal pulses begin forming in the storm's inner core near the time of sunset each day and continue to move away from the storm overnight, reaching areas several hundred kilometers from the circulation center by the following afternoon. A detailed investigation of the TC diurnal cycle (TCDC) and associated TC diurnal pulses will be presented that incorporates analyses from a variety of sources, including geostationary and polar orbiting satellites, numerical simulations from a hurricane nature run, an idealized hurricane vortex, and observations from NOAA hurricane hunter aircraft. Analyses from these various resources are used to investigate the TCDC's formation, evolution, forcing mechanisms, potential implications on TC intensity and structure, and manifestation in numerical models. Findings suggest that the TCDC may be an unrealized, yet fundamental process of TCs and organized tropical convection. The following subsections will review in further detail previous research on the diurnal variability of tropical convection and the TC upper-level cirrus canopy.

1.1 Diurnal Convection in the Tropics

It is well known that the coherent diurnal cycle of deep cumulus convection and associated rainfall is different over the land and ocean (Gray and Jacobson 1977; Randall et al. 1991; Yang and Slingo 2001). While over land, maxima tend to occur in the late afternoon/early evening due to daytime boundary layer heating, over the ocean peaks occur in the early morning hours. Gray and Jacobson (1977) examined hourly March-October precipitation data over a 13-year period from 1961-1973 for 8 Pacific island stations that they classified as "small" versus "large" in size (Fig. 1.1). They noted that large islands (e.g. Koror, Yap, Guam, and Ponape) followed a distinct bi-modal pattern of morning and afternoon peaks in precipitation. Conversely, the small islands (e.g. Truk, Wake, Majuro, and Johnston Island) exhibited a single precipitation maximum in the morning and a single minimum in the evening (Fig. 1.2). They noted that the summer and autumn precipitation distributions for these large and small islands were very similar to the springtime analysis shown in Fig. 1.2 and also hypothesized that the large islands experienced an afternoon heat island effect that was not affecting the smaller atolls in their study. Presumably, these small islands are more representative of the oceanic diurnal precipitation cycle, where in both observations and numerical simulations, a single rainfall peak tends to occur from ~0300-0900 local standard time (LST), followed by a distinct rainfall minimum from ~1700-2300 LST. Yang and Slingo (2001) found similar patterns in oceanic versus overland infrared (IR) brightness temperatures (BTs) using data from the European Union Cloud Archive User Service (CLAUS). CLAUS is a global dataset of 11-12 μm IR satellite imagery from a combination of geostationary and polar orbiting platforms that spanned the years 1984-1992 during the time of their study. They found that oceanic deep convection (inferred by IR BTs) tends to peak in the early morning, while continental convection tends to peak in the

evening. This is similar to findings by Mapes and Houze (1993) who found that deep convection associated with "large and giant" cloud clusters peaks before dawn, decreases through the morning, and is followed by a sudden increase in the moderate cold cloud top area in the afternoon. Finally, Yang and Slingo (2001) noted that the strong overland diurnal signal that they found in the CLAUS data appeared to spread out over adjacent oceanic areas for several hundred kilometers and suggested that gravity waves might provide a mechanism for this signal spread from overland to oceanic regions. Although they did not speculate on this, it is also possible that in areas with propagating weather disturbances, (e.g. westward propagating African easterly waves (AEWs) with embedded mesoscale convective systems (MCSs) over Africa), deep convection originating over inland coastal areas each day may advect the overland diurnal signal out over the ocean.

1.2 Diurnal Fluctuations of the TC Cirrus Canopy

Previous studies have highlighted diurnal changes in the cirrus anvils of tropical deep convection and TCs. Weikmann et al. (1977) noted that anvils emanating from large cumulonimbus clouds tended to grow preferably between 2200 and 0300 LST. They examined geostationary and polar orbiting IR satellite imagery over the GARP Atlantic Tropical Experiment (GATE) A/B Array and the Amazon region of South America and noted the following characteristics of rapidly growing, large cumulonimbus clouds in their study areas:

1. Rapid growth of cloud tops in a region where little or no cold cloud tops previously existed. These convective regions have a typical growth period of 3-5 hours.
2. A bright circular or oval appearance in the growth stage.

3. A mature stage with horizontal dimensions of 50-200 km (they also note a study by Martin (1995) that examined relatively larger cloud clusters with mature-stage average dimensions of 100-500 km).

Browner et al. (1977) examined Synchronous Meteorological Satellite-I and II (SMS-I and II) geostationary IR satellite imagery for 8 TCs that occurred during the 1974-1975 Atlantic hurricane seasons and found that the areal extent of the TC cirrus canopy was a minimum at 0300 LST and a maximum at 1700 LST and suggested that this diurnal oscillation might be important for the TC. Figure 1.3 shows the diurnal oscillation of the cirrus canopy areal extent for 8 North Atlantic TCs from 1974-1975 and indicates maxima from ~1200-1800 LST and minima from ~0000-0700 LST in their 253 K (-20^{o}C) and 239 K (-34^{o}C) isotherm analyses. Browner et al. (1977) also noted a shorter (less than 1 day) oscillation that was robust at their 223 K (-50^{o}C) isotherm analysis threshold and "suggestive" at their 239 K (-34^{o}C) threshold. This sub diurnal signal was mentioned to be beyond the scope of their study. Kossin (2002) expanded on the work by Browner et al. (1977) and used storm-centered IR imagery from the Geostationary Operational Environmental Satellite (GOES) to calculate azimuthally averaged BTs and create Hovmoller-type diagrams of BT diurnal oscillations over time. That study concluded that although a clear diurnal oscillation of the TC cirrus canopy was present at larger radii (e.g. 300 km, Fig. 1.4), few storms exhibited diurnal oscillation signals in their innermost 100 km and sometimes revealed a semidiurnal signal in this region of the storm. It was hypothesized that different processes might be forcing periodic oscillations in TC inner-core deep convection and the region of the TC cirrus canopy. For the latter, Kossin (2002) was proposed that radiatively (diurnal) driven subsidence at the level of the cirrus canopy was

creating a predictable harmonic oscillation of canopy heights with a 24 hr period that was detectable using GOES IR imagery.

1.3 Diurnal Fluctuations of Organized Versus Disorganized Convection

Gray and Jacobson (1977), Mapes and Houze (1993), and Liu and Moncrieff (1998) found that oceanic peaks in rainfall are more prominent when the pre-existing convection is more intense and associated with an organized weather system such as an AEW, MCS, or organized cloud cluster. Gray and Jacobson (1977) specifically noted that with more intense deep tropical convection, particularly convection linked to an organized weather system, the more prominent its diurnal signal of precipitation was. They further hypothesized that organized weather disturbances enhance the diurnal pattern via day versus night variations in tropospheric longwave cooling differences between the weather system and its surrounding cloud-free region. Mapes and Houze (1993) used IR imagery from the Japanese GMS satellite to detect what they called tropical cloud clusters and concluded that the diurnal cycle of cold topped cloudiness (e.g. "very cold" cloud tops $\leq$208 K and "moderately cold" cloud tops $\leq$235 K) exhibits a distinct diurnal cycle that is driven by large mesoscale cloud clusters and not by cumulus or cumulonimbus clouds.

Liu and Moncrieff (1998) used a numerical simulation with full microphysics and fully interactive radiations to examine modeled convection and similar to previous studies, found a significant diurnal cycle characterized by peaks in heavier precipitation in the early morning and relatively lighter precipitation from the afternoon to evening. Interestingly, their more organized case (EX1) had more pronounced convective intensity in the predawn hours than their relatively less organized case (EX2) and is shown in Fig. 1.5. Here, domain averaged precipitation, total

cloud condensate, and maximum vertical velocity (all proxies for convective intensity) exhibited marked diurnal variability, though trends were more robust with the former 2 parameters. These findings correlating convective organization with diurnal convective signals suggest that TCs may possess particularly robust diurnal convective signals.

1.4 Recent Work Investigating Diurnal Signals in Numerical Simulations

Tang and Zhang (2016) used the Advanced Research version of the Weather Research and Forecasting Model (WRF ARW) to examine the impacts of the diurnally varying radiation cycle on the formation, intensity, structure, and track of 2014 Hurricane Edouard. They found that diurnal effects varied depending on the intensity of the tropical disturbance or TC being simulated. During the genesis stage, nighttime destabilization of the atmosphere occurred via radiative cooling, which promoted deep convection neat the disturbance center and eventually led to TC genesis. For TCs, they found that in the absence of nighttime conditions (i.e. in daytime-only simulations), storms fail to develop because of a lack of nighttime cooling and destabilization that typically enhances the primary storm vortex. They also concluded that nighttime destabilization was a key factor in stimulating convection outside the TC inner core and can eventually promote the development of outer rainbands and even increase the size of the storm. Finally, Tang and Zhang (2016) found modest diurnal impacts on TC intensity (as measured by the maximum sustained 10-m wind speed) and also observed that their control simulation of Hurricane Edouard (using a normal solar cycle) exhibited a marked secondary eyewall formation (SEF, Willoughby et al. 1982). However, their other simulations either did not show SEFs (nighttime-only run) or exhibited a more radially compact SEF (daytime-only run) and were hypothesize to be linked to the development (or lack of development) of

convection just outside the TC inner core that were being driven by these differing environments of shortwave and longwave radiation.

Navarro and Hakim (2016) used a numerical simulation to examine the role of the diurnal cycle of radiation on axisymmetric hurricane structure. They found coherent diurnal signals in the temperature, wind, and latent heating tendency fields that account for up to 62% of the variance in the TC outflow layer and 28% of the variance in the TC boundary layer. They hypothesized that the TCDC is a combined response from 2 distinct circulations in the storm: 1) a radiatively driven circulation in the outflow layer due to absorption of solar radiation and 2) a convectively driven circulation in the lower and middle troposphere due to anomalous latent heating that is linked to a diurnal cycle of anomalous convection.

1.5 Scientific Issues to be Addressed

Previous research that has examined diurnal fluctuations of tropical precipitation, the TC cirrus canopy, and organized versus less organized convection using satellites and numerical models have provided an important foundation from which this thesis builds. The research presented in this thesis will focus on the following scientific questions:

1. What are the spatial and temporal characteristics of the TCDC?
2. What remote sensing techniques can be developed/utilized to track the TCDC in time and space?
3. What are the physical mechanisms responsible for the onset and evolution of the TCDC?
4. What is the influence of the diurnal cycle on TC structure (e.g. spiral bands/convective arms outside the inner core), outflow at the level of the cirrus canopy, and upper level divergence)?

5. To what extent are diurnal variations important for TC intensity and structure?
6. What are the implications of the TCDC on the structure and intensity of TCs, African easterly waves, and tropical convection in general?

The data and methodologies used throughout this thesis will be detailed in Chapter 2. Following this section, research related to the TCDC will be presented across four chapters. Each chapter will include a brief introduction and specific details about methodology where necessary. The chapters will also each close with a discussion and concluding remarks of the research presented therein. The chapters are organized as follows: Chapter 3 will present a satellite-based perspective on the TCDC that will include: discussion of a new technique for tracking the TCDC with geostationary IR satellite imagery, highlights of a few case study examples, spatial, temporal, and spectral analyses of the TCDC using a 10-yr database of North Atlantic major hurricanes, and presentation of a TCDC conceptual clock that predicts the timing and propagation of TC diurnal pulses that emanate from mature TCs each day. Chapter 4 will present a modeling-based perspective on the TCDC that will include: examination of an idealized hurricane nature run numerical simulation to look for signals of the TCDC in the model, characterize these signals in time and space, and document how the TCDC forms, evolves, and possibly impacts TC structure and intensity. Chapter 5 expands on the numerical modeling component of the TCDC research by examining an idealized hurricane vortex simulation with different solar cycles to better understand the relationship between the TCDC and TCs. Chapter 6 will present an observationally-based perspective on the TCDC that will include: analyses of aircraft data (e.g. flight-level, lower-fuselage radar, tail Doppler radar, and GPS dropwindsondes (dropsondes) from missions into 2010 Hurricane Earl and 2014 Hurricane

Edouard to better understand and characterize the TCDC and how it affects both the inner core and surrounding environments of TCs. The final chapter of the dissertation will discuss the overall results and final conclusions and present ideas for future work.

1.6 Figures

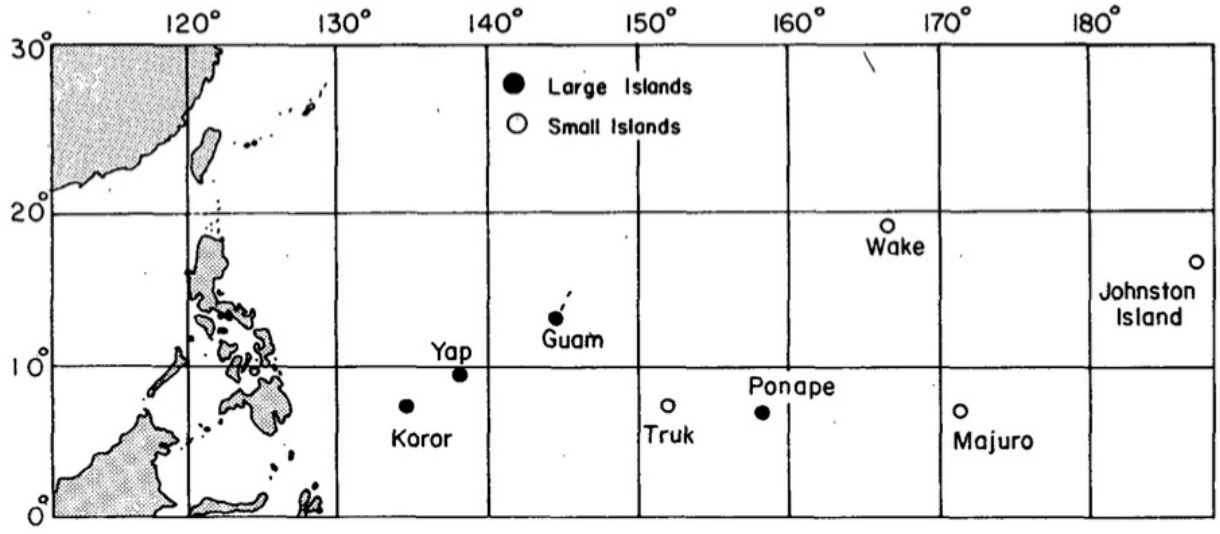

Figure 1.1: Western Pacific upper air stations for which 13-year (1961-1973) hourly rainfall data were examined in Gray and Jacobson's 1977 study. From Gray and Jacobson (1977).

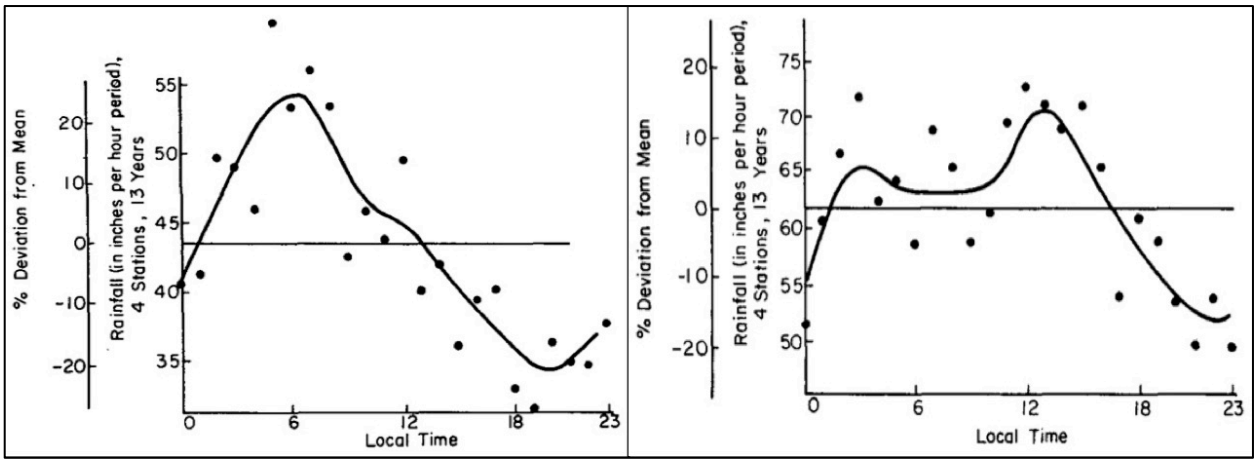

Figure 1.2: Hourly distribution of the 13-year (1961-1973) average precipitation for the spring season (March-May) for the (left) small and (right) large Pacific island stations shown in Fig. 1.1. From Gray and Jacobson 1977.

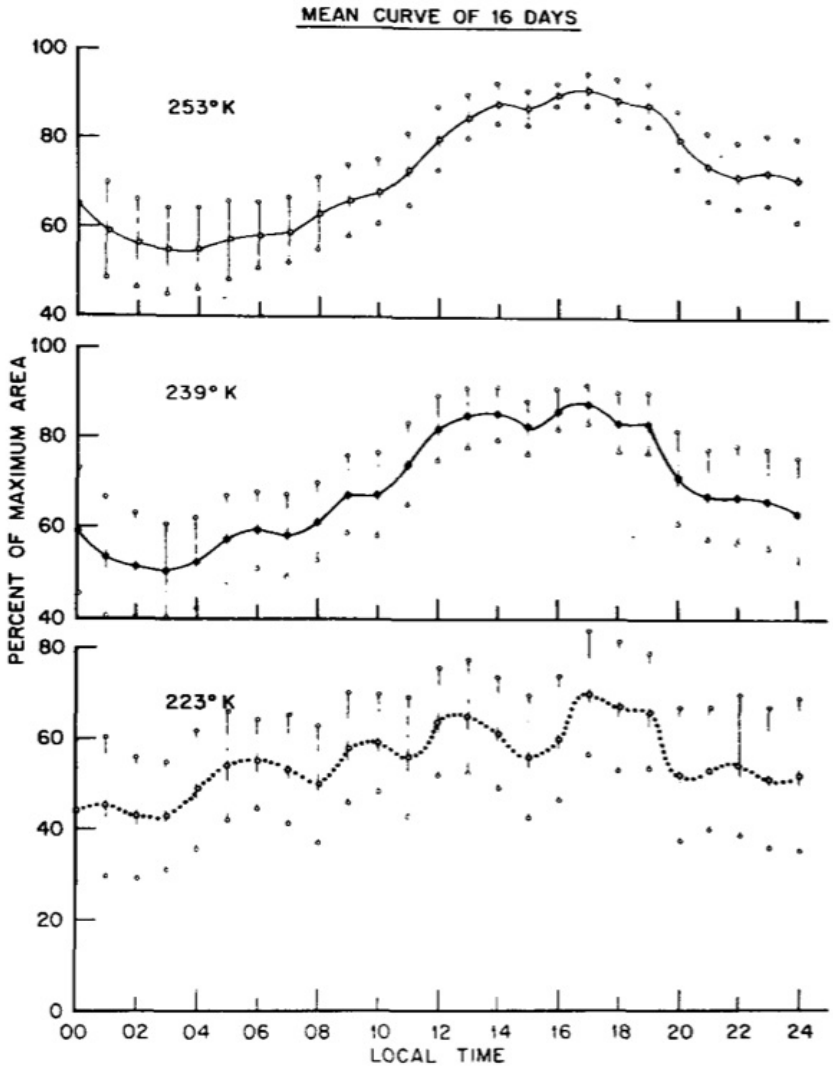

Figure 1.3: Composite diurnal oscillations of 8 TCs from 16 days of the 1974-1975 Atlantic hurricane season. Storm areas at each isotherm were normalized to the corresponding threshold maximum area for the day, composited according to local mean solar time and then averaged. 95% confidence intervals are shown. Due to the variability of the occurrence of the maximum areas from storm to storm, these curves do not pass though 100%. From Browner et al. 1977.

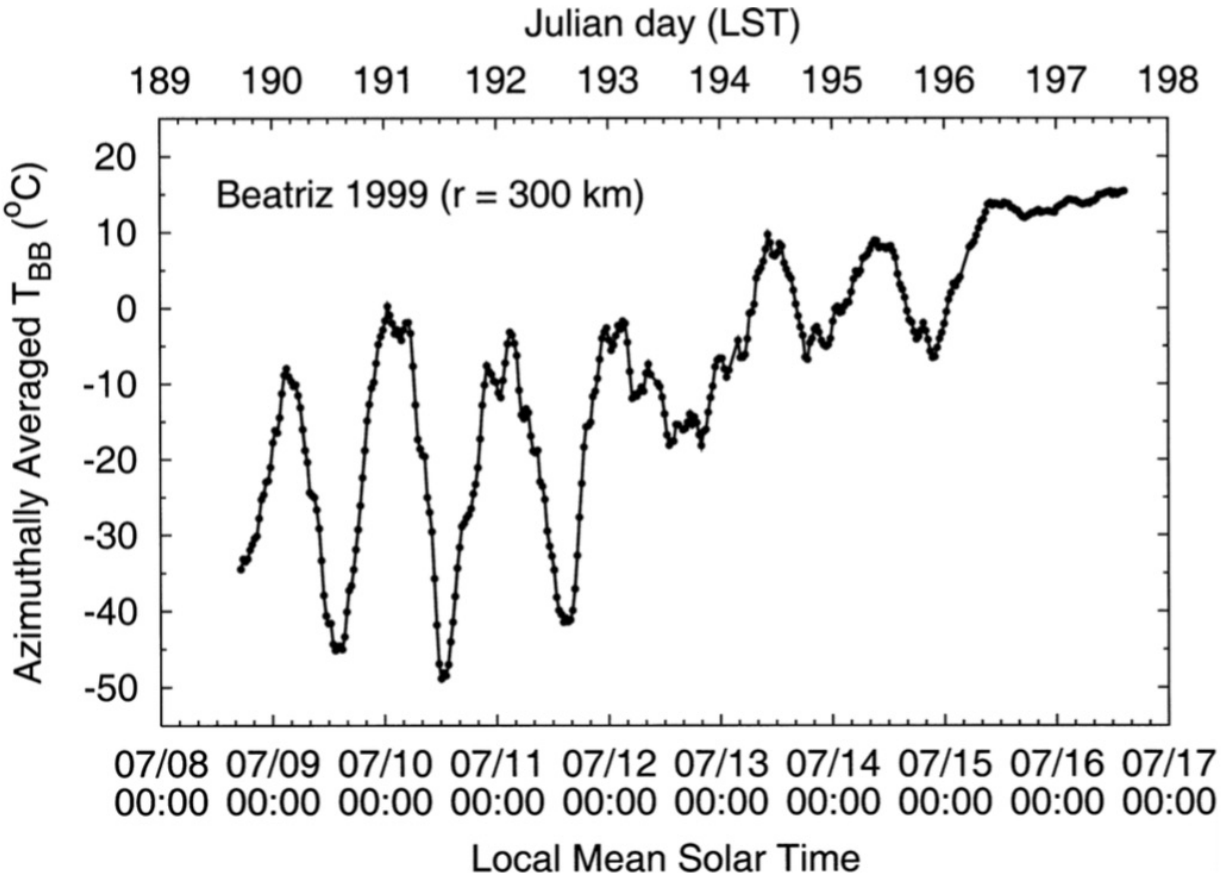

Figure 1.4: Time series of azimuthally averaged GOES BTs in Hurricane Beatriz at r=300 km. Time period is 08-17 July 1999 (Julian days 189–198). From Kossin (2002).

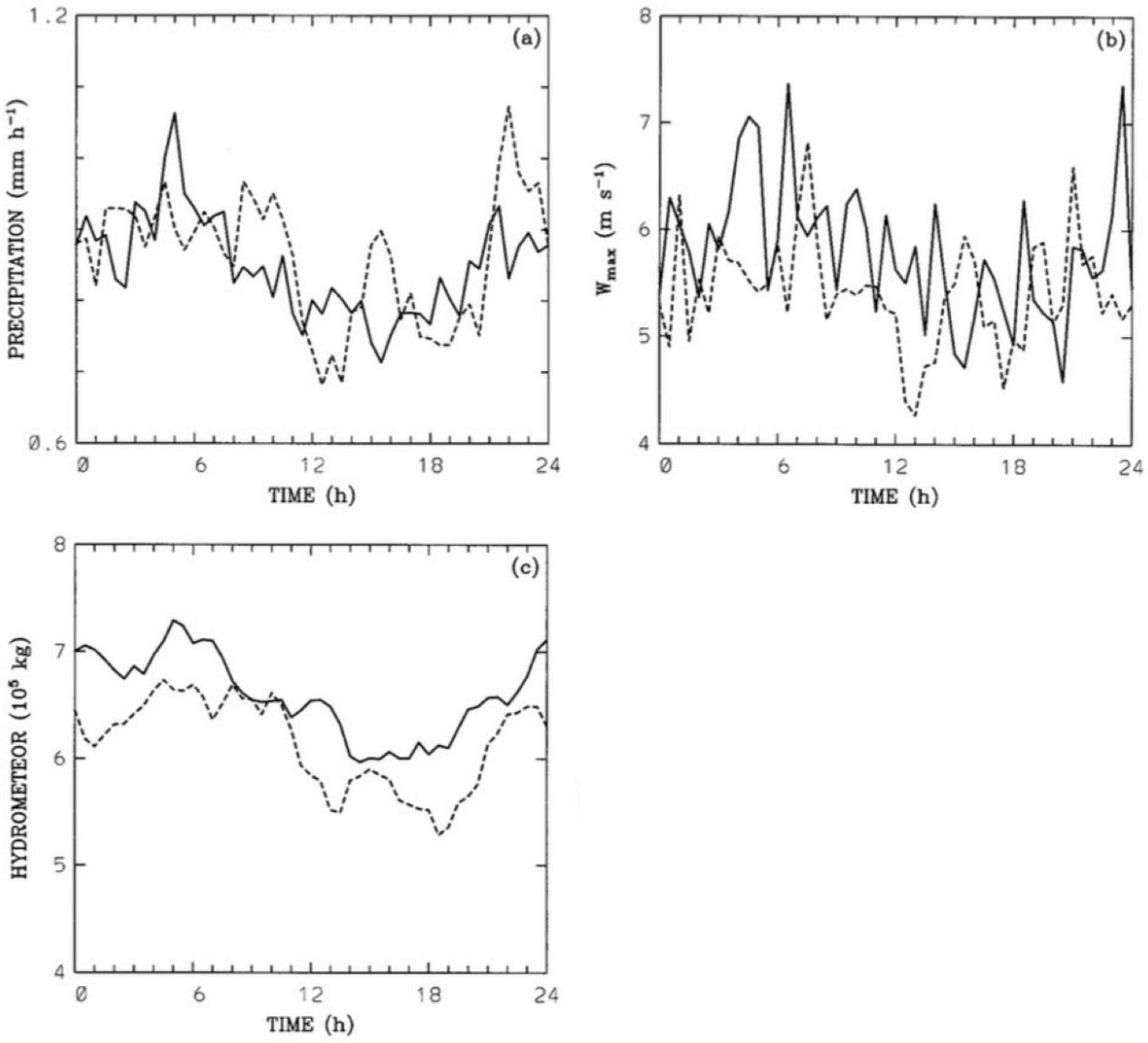

Figure 1.5: Ensemble means over the last 10 days in the more organized EX1 (solid curves) and less organized EX2 (dashed curves) numerical simulations. Plots show (a) domain-averaged precipitation (mm hr^{-1}), (b) maximum vertical velocity (m s^{-1}) and (c) total condensate in the entire domain (10^5 kg). From Liu and Moncrieff (1998).

2. Data and Methodology

2.1 Data

2.1.1 Satellite-Based Observations

Chapter 3 utilizes 3-hourly GOES 4-km IR (10.7 μm) imagery for all Atlantic major hurricanes from 2001 to 2010 and included over 850 satellite images for 36 TCs (Meteosat Second Generation IR imagery (10.8 μm) was used to supplement the GOES IR imagery for storms located east of 37.5°W). The 3-hourly image increment that was selected minimized satellite eclipse period data gaps and when images were missing, temporal discontinuities from substituted images never exceeded 30 min. Each storm-centric image was geolocated using a combination of National Hurricane Center best track data, aircraft center positions, and (when an eye was present) positions determined manually using the Man Computer Interactive Data Access System (McIDAS; Lazzara et al. 1999). Two types of storm-centered IR imagery (re-mapped to Mercator projection) were examined in detail: standard geostationary imagery and 6-h brightness temperature differencing imagery (i.e., IR differencing imagery). The latter was created by differencing the brightness temperature fields of two consecutive storm-centered IR images separated by 6 h and color enhanced to resemble conventional IR brightness temperature scales (i.e., warm colors represent colder cloud tops). The resulting satellite image has utility for quantifying brightness temperature changes in the TC environment and for monitoring structural changes in the TC cirrus canopy, eye, and regions of deep convection (in areas not obscured by the cirrus canopy). Azimuthal means of the IR brightness temperatures and 6-h IR brightness temperature differences (i.e., trends) were calculated every 3 h at 100-km radius intervals (100–600km) for each storm in the 10-yr dataset. This information provided a means to monitor diurnal variations in the brightness temperature fields of the various storm environments. It

should be noted that other IR brightness temperature differencing increments (e.g., 3h) and satellite channels (e.g., the 6.5- and 6.8-mm water vapor channels) were also tested and will be investigated in more detail in the near future.

Microwave satellite imagery (37- and 85/89/91-GHz channels) from the National Aeronautics and Space Administration (NASA) Aqua Advanced Microwave Scanning Radiometer for Earth Observing System (EOS) (AMSR-E) and the Defense Meteorological Satellite Program (DMSP) microwave imagers [Special Sensor Microwave Imager (SSM/I; F-8, -10, -11, -12, -13, -14, and -15) and the Special Sensor Microwave Imager/ Sounder (SSMIS; F-16, -17, and 18)] was used to complement the geostationary IR imagery and examine the storm structure below the cirrus canopy for two TC cases in this study (Hawkins and Velden 2011; Hawkins et al. 2001; Lee et al. 2002). For the ice scattering channels (85, 89, and 91 GHz), the emissivity of water is low, making the ocean surface appear relatively cold, while the TC cirrus canopy is largely transparent. Additionally, scattering by larger snow and ice particles below the cirrus canopy and above the freezing level is more prevalent, making the satellite field of view appear colder. Therefore, this channel is ideal for examining TC inner-core and rainband structures in the middle to upper levels. The 37-GHz channel can detect emissions from below cirrus canopy, but is much less sensitive to precipitation-sized ice particles and more sensitive to low-level rain and cloud liquid water. Thus, this channel has utility for detecting lower to midlevel features in the storm environment. Together, the 85- and 37-GHz channels elucidate important details regarding the nature of the TC diurnal cycle detected in the geostationary IR imagery and provide information as to the approximate depth of the observed diurnal pulses.

Extended best track data (Demuth et al. 2006) was used to examine diurnal tendencies in the radii of 34-, 50-, and 64-kt (1 kt = 0.5144 m s^{-1}) winds for all TC cases in the 10-yr dataset.

Additionally, output from the University of Wisconsin–Madison Cooperative Institute for Meteorological Satellite Studies (UW-CIMSS) advanced Dvorak technique (ADT; Olander and Velden 2007) was used to assess possible linkages between the TC diurnal cycle and satellite-based objective Dvorak intensity estimates.

Water vapor atmospheric motion vectors (AMVs) and upper-level divergence data that are discussed in Chapter 6 are courtesy of UW-CIMSS. Water vapor AMVs are derived using a sequence of three GOES 6.7 μm water vapor images. Features are targeted in the second satellite image (cirrus cloud edges, gradients in water vapor, small cumulus clouds, etc.) are tracked within the first and third images yielding two displacement vectors. These vectors are averaged to derive the final wind vector that is then assigned a height via a two-step process. The first utilizes the measured radiances of the target and is based on the spectral response function of the individual satellite and channel being sampled. The brightness temperature of the target is derived from this radiance measurement. Once determined, the brightness temperature is then compared with a collocated numerical model guess temperature profile, from which an initial height is estimated. The final vector height is derived in the post-processing of the vector field. UW-CIMSS runs the raw winds through two quality control processes to assure vector correctness and uniformity. The first process, called "autoediting", is a two-stage, three-dimensional objective analysis of the wind field (Hayden and Pursor, 1995). This scheme utilizes conventional data assimilation, neighboring wind "buddy" checks, and numerical model analyses for wind vector editing and height adjustments (Velden et al. 1997). The second process is the EUMETSAT "Quality Indicator" (QI) methodology (Holmlund et al., 2001). The QI is a statistically based scheme that highlights internal consistency between vectors without use of a background numerical model. Analyses of upper-level divergence ($x10^{-6}$ s^{-1}) were

derived from gridded AMV output averaged using the 150, 200, 250, and 300 hPa pressure levels and computed using finite differencing of du/dx + dv/dy, where u and v are the wind components and x and y are the horizontal grid spacing.

2.1.2 Hurricane Nature Run

The hurricane nature run that was examined in Chapter 4 was simulated using the Weather Research and Forecasting (WRF) Model version 3.2.1 and is part of a larger 13-month joint observing system simulation experiment (OSSE) nature run that is described in detail by Nolan et al. (2013; and referred to as NRH1 in their paper). NRH1 spans a 13-day period from 29 July 0000 UTC – 11 Aug 0000 UTC 2005 and does not interact with land, unusually cold SSTs, or other synoptic weather systems during the portion of its life cycle that we examined. Track, minimum surface pressure, and maximum 10-m wind speed for the lifecycle of this simulated storm are shown Fig. 2.1, during which time the radius of maximum winds contracts to a minimum radius of 45 km, later expanding to 60 km. The NRH1 9 km nested grid was utilized, which included 61 vertical levels (up to 50 hPa) and employed the WRF 6 class double-moment microphysics scheme (WDM6) [Lim and Hong, 2010], the RRTM-G schemes for both shortwave and longwave radiation (called every 6-min) [Iacono et al., 2008], and the Kain-Fritsch convective parameterization (Kain and Fritsch, 1990; Kain, 2004]). Additionally, the Yonsei University (YSU) planetary boundary layer scheme [Noh et al., 2003; Hong et al., 2006] was used for surface fluxes and turbulent mixing in the boundary layer (the ‘‘TC’’ option for formulas of surface exchange coefficients for momentum, heat, and moisture as a function of wind speed was employed). Finally, for parameterizing ocean cooling, the same mixed layer

model as implemented in WRF 3.2.1 was used with an initial mixed layer depth of 25 m and stratification at the top of the thermocline specified as 0.1 km^{-1}.

2.1.3 Idealized Hurricane Simulations

The idealized hurricane simulations discussed in Chapter 5 (Sec. 5.2) used a version of an idealized HWRF simulation system (Weather Research and Forecasting Model (WRF) 3.4.1) that was modified to give the user control over the development and progression of the solar cycle. This idealized model framework incorporates several standard features, including the Geophysical Fluid Dynamics Laboratory (GFDL) radiation scheme, and three nested domains: outer, intermediate, and inner domains with 27, 9, and 3 km horizontal resolution, respectively. The simulation included weak vertical wind shear (1.4 m s^{-1}), a sea surface temperature (SST) of 30.9°C, employed the moist tropical sounding (Dunion 2011) throughout the domain, and had an initially strong, but slow moving (west motion at 2.1 m s^{-1}) category 3 hurricane on the Saffir-Simpson Hurricane Wind Scale (52 m s^{-1}) with a local time of ~UTC-4 hr, and had a radius of maximum wind of 44 km.

Three experiments (control, day-only, and night-only) were initialized on 04 Sep 0000 UTC and utilized the 3-km inner domain. The control simulation was allowed to run for seven days with no modifications to the standard radiation setup. The day-only experiment included the normal solar cycle through 40 hr (to promote a smoother transition to a constant daytime solar zenith angle) and then remains constant for remainder of the simulation (1600 UTC, local noon at 20°N, 75°W). Finally, the night-only experiment included the normal solar cycle through 28 hr (also to promote a smoother transition to a constant nighttime zenith angle) and then remains constant for remainder of the simulation (0400 UTC, local midnight at 20°N,

75°W). The normal solar cycle prescribed at the beginning of the simulations was allowed to run for at least 24 hr before nighttime-only and daytime-only conditions were set in the respective simulations. Since both of these simulations began at 0000 UTC/2000 LST, nighttime only conditions (local midnight) could be applied 28 hr into the run, while daytime-only (local noon) conditions were applied 12 hr later (40 hr into the simulation). All 3 idealized storms required ~24-48 hr to spin up, maintained category 3 intensity (96-112 kt/49.5-57.5 m s^{-1}) from ~72-108 hr into the simulation, and experienced steady weakening down to category 2 (83-95kt/42.6-49 m s^{-1}) or strong category 1 (80 kt/41 m s^{-1}) intensity by the end of the simulations (Fig. 2.2).

2.1.4 Aircraft Observations

The aircraft observations that are discussed in Chapter 6 included a combination of in situ and radar measurements collected from the two NOAA WP-3Ds (flight-level 2400-3,000 m/8,000-10000 ft) and the NOAA G-IV high altitude jet (flight-level 12,500-14,000 m/41,000-45,000 ft). GPS dropsondes deployed from the WP-3Ds and G-IV jet were used to examine the thermodynamic and kinematic characteristics of a TC diurnal pulse, while the WP-3Ds lower-fuselage (LF) radar and tail Doppler radar (TDR) provided information related to the 3-dimensional reflectivity and kinematics of this feature.

GPS dropsonde data used in this work were from aircraft-deployed Vaisala RD94 dropsondes (Hock and Franklin 1999). These parachuted instruments measure profiles of pressure, temperature, and relative humidity at 2 Hz and wind speed and direction at 4 Hz as they fall from the aircraft flight level to the surface. Estimated typical measurement errors for the Vaisala RD94 dropsonde for pressure, temperature, humidity, and wind are 1.0 hPa, 0.2°C, <5%, and 0.5-2.0 m s^{-1} respectively.

The 2 NOAA WP-3Ds (NOAA 42 and 43) are both equipped with a lower-fuselage (LF) radar, a 5.59 cm C-band radar with a 4.1^{o} (1.1^{o}) vertical (horizontal) beam width and a maximum unambiguous range of 750 km. Additionally, this radar operates at a frequency of 5370 MHz and has a pulse repetition frequency (PRF) of 200 Hz. LF radar images do include a shadow area around the aircraft where radar reflectivity cannot be received due to beam interference from the aircraft fuselage. This region appears as a circular area of near-zero radar reflectivity that is centered on the aircraft position within the storm. One drawback of the LF radar is its large vertical beam width, which causes inadequate illumination of the targets in the beam, especially at ranges >60-90 km (Marks 1985). At close range, there is little loss because the radar beam is narrow enough to be totally within the strong reflectivity region at lower altitudes in the storm. As range increases, the height of the center of the beam increases and more of the beam is unfilled, or filled with the less reflective portion of the storm. This can cause a marked underestimate of a feature's reflectivity values at greater distances from the aircraft.

The NOAA WP-3Ds are also each equipped with a tail Doppler radar (TDR), a 3.22 cm X-band radar with a 1.9^{o} (1.35^{o}) vertical (horizontal) beam width, frequency of 9315 MHz, maximum unambiguous range of 46-94 km, and a PRF of 1600-3200 Hz. The major drawback of the TDR is its 3.22 cm operating wavelength and high PRF. X-Band radars like the TDR are affected by rain attenuation, which limits the maximum range at which Doppler-derived wind estimates can be obtained. This limitation can be mitigated by flying close to the area of interest and reducing the distance the beam has to travel through the intervening rainfall.

2.2 Methodology

2.2.1 2001-2010 Atlantic Major Hurricane Dataset: Selection Criteria

Three search criteria were applied to the 10-yr (2001-2010) Atlantic major hurricane dataset in order to optimize the identification of the TCDC signal in the GOES satellite imagery and are described in detail below. The GOES IR satellite imagery that was used in this study typically detects high-level cirrus in the TC canopy and embedded deep convection. Therefore, in cases of moderate-to-high shear (e.g., >7.5 m s^{-1}), asymmetries in the observed satellite cloud field will often occur and may not necessarily reflect the typical TC outflow pattern. It should be noted that this value falls within the 7-8 m s^{-1} "critical shear" range for weakening versus strengthening North Atlantic TCs (Gallina and Velden 2000) and is slightly less than the mean 200–850-hPa vertical wind shear of the North Atlantic moist tropical sounding (8.2 m s^{-1}; Dunion 2011). Additionally, terrain-induced convection (e.g., related to frictional convergence and surface heating) in the periphery of TCs near land can promote convective development that may not be representative of a TC's natural convective patterns. Finally, weak or incipient TCs often exhibit sporadic and/or asymmetric convective activity that may not reflect the natural convective cycles that are inherent in mature TCs. Based on these considerations, the following criteria were used to sub- sample each 3-h cycle for the storms in the 10-yr dataset: 1) 200–850-hPa vertical wind shear ≤7.5 m s^{-1} [determined from the Statistical Hurricane Intensity Prediction Scheme (SHIPS; DeMaria et al. 2005)]; 2) storm center ≥300 km from land (this criterion was applied for the landmasses of North America, including Cuba and Hispaniola. Smaller islands in the region were not considered to be land.); and 3) Saffir-Simpson storm intensity of category 2 or higher (≥43 m s^{-1}). Additionally, for each TC, a continuous 72-h period was identified that was roughly centered around the time of the storm's peak intensity while also

maximizing the number of usable azimuthal calculations. The 72-h time window was chosen based upon the fact that North Atlantic major hurricanes only maintain category 3 or higher intensity (≥49 m s^{-1}) for an average of ~2.5 days (Jarvinen et al. 1984). The selection criteria described above resulted in 450 individual 3-hourly brightness temperature–brightness temperature trend azimuthal calculation sets for 31 North Atlantic major hurricanes from 2001 to 2010 (Table 1).

2.2.2 Hurricane Nature Run

The NRH1 exhibited a life cycle typical of a North Atlantic Cape Verde-type system, as it underwent genesis from an African easterly wave, intensified into a strong category 3 hurricane (≥49 m s^{-1}) from 05-07 Sept, and eventually recurved after reaching ~65°W. The lifecycle of this sequence spans a 13-day period from 29 July 0000 UTC - 11 Aug 0000 UTC 2005. Dunion et al. (2014) found that the TCDC was most pronounced in mature hurricanes (Saffir-Simpson intensity of category 2 or higher (43 m s^{-1})) that were in relatively low shear environments (≤7.5 m s^{-1} of 200–850-hPa vertical wind shear) and located ≥300 km from land and decided to constrain their storm sample accordingly (see Chapter 2.2.1). This element of the study used identical thresholds to identify the portion of the NRH1 lifecycle that would be most conducive for TCDC processes. Fig. 2.1 shows the track and intensity for the 13-day NRH1 simulation period and indicates that the storm met the minimum distance to land threshold for the entire period and that the intensity requirement was attained from days 5-10. Finally, Nolan et al (2013) showed that the vertical wind shear affecting NRH1 during this 5-day period never exceeded 7.5 m s^{-1}. Therefore, days 5-10 (03 Aug 0000 UTC - 08 Aug 0000 UTC) of the NRH1 simulation were searched for signs of the TCDC.

2.2.3 Idealized Hurricane Simulations

For the idealized hurricane simulations that were examined, the intensity, vertical wind shear, and distance to land criteria that are discussed in Sec. 2.2.1 were employed. The 3 simulations (control, day-only, and night-only) were initialized on 04 Sep, were run for 7 days, and met the TCDC analysis criteria described in Sec. 2.2.1 from days 3-7 in their lifecycles: mature hurricane (Saffir-Simpson intensity of category 2 or higher (43 m s^{-1})) that were in relatively low shear environments (≤7.5 m s^{-1} of 200–850-hPa vertical wind shear), and located ≥300 km from land. Fig. 2.2 shows the intensities (10-m wind speed and pressure) for each of the 3 idealized simulations from 72-hr to 168 hr into the simulations (after the initial 48-72 hr period of vortex spin up) and indicates that all 3 storms met the minimum surface wind speed intensity requirement during this period.

2.3 Tables and Figures

Storm	Year	Dates	Latitude (N)	Longitude (W)	Intensity ($m\ s^{-1}$)	Shear ($m\ s^{-1}$)	TCDC Amplitude (^oC) R=300 km
Erin	2001	09-11 Sep	33.4	63.2	49	6.1	21.5
Felix	2001	13-15 Sep	28.7	45.3	46	5.9	30.3
Iris	2001	08 Oct	17.1	83.9	54	4.9	39.4
Michelle	2001	03 Nov	18.9	84.2	54	4.7	28.4
Lili	2002	01-02 Oct	23.1	85.7	49	3.9	47.2
Fabian	2003	31 Aug-03 Sep	19.0	56.2	61	6.4	33.0
Isabel	2003	12-15 Sep	22.6	61.5	70	3.7	42.9
Kate	2003	03-04 Oct	29.3	48.7	48	4.7	17.9
Frances	2004	31 Aug-02 Sep	20.4	63.7	60	4.5	41.8
Ivan	2004	09-12 Sep	16.2	74.6	68	5.2	30.0
Jeanne	2004	23-25 Sep	26.2	72.0	43	5.7	34.3
Karl	2004	20-22 Sep	20.3	47.1	57	5.6	26.0
Dennis	2005	09-10 July	26.1	84.9	54	5.4	19.8
Emily	2005	15-17 July	16.3	76.6	60	7.6	47.4
Katrina	2005	27-29 Aug	26.0	87.6	65	4.6	34.8
Maria	2005	05 Sep	31.6	56.7	44	7.7	23.7
Rita	2005	21-23 Sep	25.2	88.1	72	4.9	24.7
Wilma	2005	19-20 Oct	17.4	83.0	74	4.3	26.9
Gordon	2006	13-14 Sep	26.2	57.6	45	6.4	41.9
Helene	2006	18-20 Sep	23.8	51.7	49	4.3	21.5
Dean	2007	18-21 Aug	16.8	75.4	69	3.7	34.7
Felix	2007	02-04 Sep	12.9	69.2	56	3.5	64.9
Bertha	2008	07-10 July	22.3	54.7	45	6.5	27.0
Gustav	2008	29 Aug-01 Sep	21.4	79.1	48	6.4	33.1
Ike	2008	04-07 Sep	22.0	58.4	59	5.7	15.2
Paloma	2008	07-08 Nov	18.3	81.3	43	6.4	22.1
Bill	2009	18-21 Aug	19.4	56.1	53	4.2	15.8
Fred	2009	09-10 Sep	14.4	32.7	47	3.7	15.5
Danielle	2010	26-28 Aug	26.3	58.2	50	4.5	32.0
Earl	2010	26-28 Aug	19.5	64.7	56	4.2	39.6
Julia	2010	15 Sep	17.2	31.5	49	5.9	12.4

Table 2.1: 2001-2010 North Atlantic major hurricane cases utilized in this study. The position, intensity, and vertical wind shear represent mean values over the period that was examined. The mean TC diurnal cycle (TCDC) trough-to-peak amplitudes (R=300 km) calculated from the 6-hr geostationary IR brightness temperature differencing imagery is also shown for each storm.

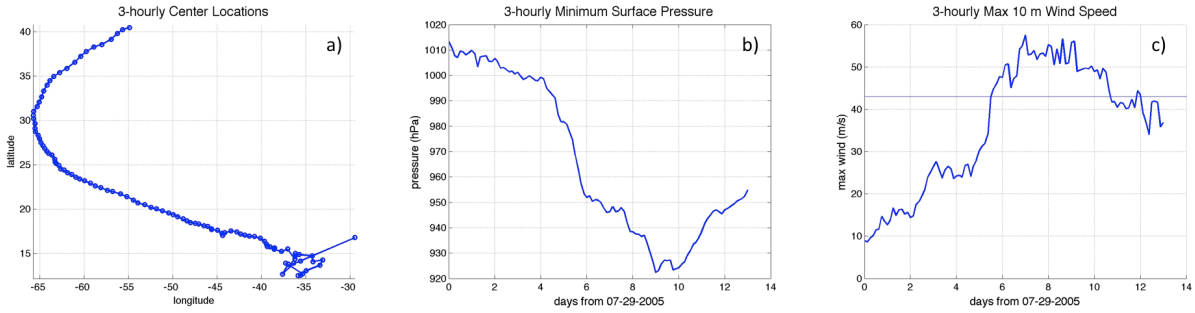

Figure 2.1: 3-hourly (a) track, (b) minimum surface pressure, and (c) maximum 10-m wind speed for the 13-day NRH1 simulation. The light blue line in (c) denotes the Saffir-Simpson category 2 wind speed threshold (43 m s^{-1}).

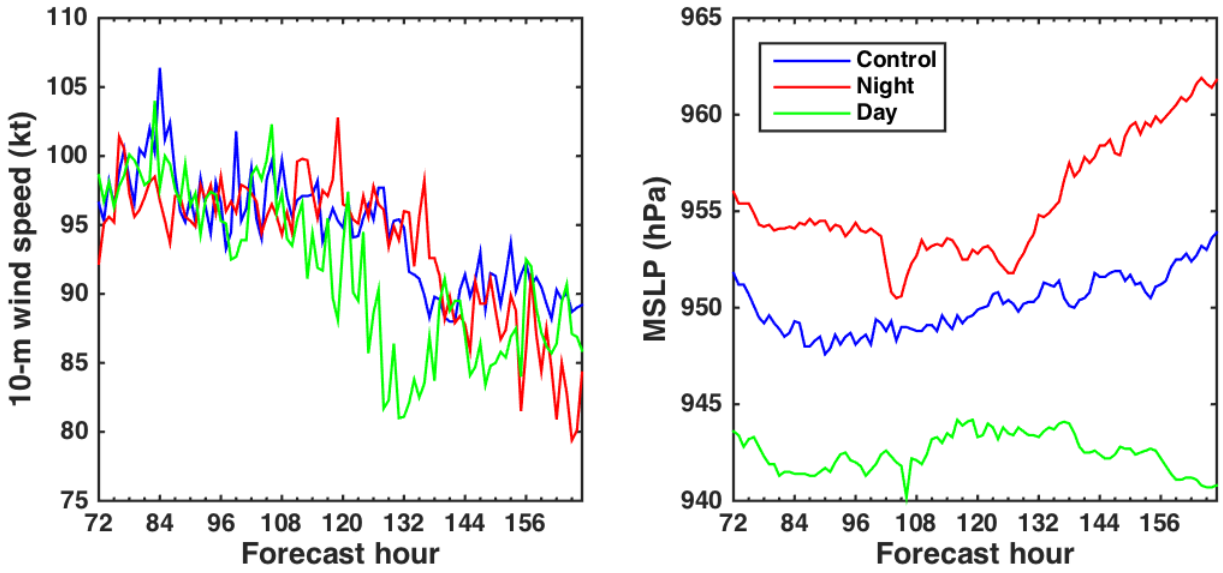

Figure 2.2: 3-hourly maximum 10-m wind speed (kt, left) and minimum surface pressure (hPa, right), for the idealized simulation control run (blue curves), nighttime-only (red curves), and daytime-only (green curves) for the 72-168 hr forecast period (07-11 Sep).

3. Investigating the TC Diurnal Cycle Using Satellite Observations

3.1 Introduction

The summary of previous work that has investigated diurnal convection in the tropics, diurnal fluctuations of the TC cirrus canopy, and diurnal fluctuations of organized versus disorganized convection was outlined earlier in Secs. 1.1-1.4. The current chapter will present two TC case studies from the larger 2001-2010 dataset that exhibited TCDC signals during their lifecycles using the geostationary satellite algorithms and data described in Chapter 2 (Sec. 2.1.1). This chapter also describes mean statistics of the 10-yr TCDC dataset and presents evidence of a diurnal signal in a few parameters that describe and estimate TC structure and intensity. While the exact processes that cause the TCDC and associated diurnal pulses is an emerging area of research, several hypotheses that could explain their development and evolution are posed. Although the main focus of this chapter is to document satellite-based observational aspects and tracking capabilities of TCDC characteristics, its remarkable predictability (timing and propagation) also provides an opportunity to advance our understanding of this phenomenon.

3.2 Case Studies of TCs Exhibiting TCDCs

3.2.1 2007 Hurricane Felix

Figure 3.1 shows an example of the TCDC for 2007 Hurricane Felix on 03 September while it was weakening from a category 5 with an intensity of 72 m s^{-1} to a 59 m s^{-1} category 4 storm. The GOES IR imagery suggests a rapidly expanding cirrus canopy in all quadrants between 1215-1815 UTC and asymmetries were clearly evident in the IR cloud field from

R=100-300 km during this time. These asymmetries were mainly associated with a large area of cold cloud tops (-50 to -70^{o}C) in the western and northern semicircles of the storm that appeared to be separating from the inner core region during the morning hours (Fig. 3.1, upper left; R=~150 km). By the early afternoon local time (Fig. 3.1, upper right), this arc of cold cloud tops had propagated to a radius of ~250-350 km and an expanding gap of relatively warmer cloud tops (~-30 to -40^{o}C) was evident between this feature and the storm's inner core.

Figure 3.1 also shows IR differencing imagery that depicts 6-hr changes in the storm's IR temperature field from 0615-1215 UTC. The imagery indicates a circular ring (i.e. the diurnal pulse; yellow to pink shading) in the cloud field at approximately R=150-250 km that had cooled as much as 20-50^{o}C during this 6-hr period, with areas of warming (cyan to blue shading, 5-30^{o}C) evident behind the diurnal pulse in the inner ~150 km. By 1815 UTC that day (Fig. 3.1, lower right panel), the diurnal pulse had propagated to a radius of ~250-350 km from the center and a broad circular area of warming inner core cloud tops (5-40^{o}C) was located on its inner edge at R=~50-200 km. The arc-like feature of radially propagating cold cloud tops previously noted in the IR satellite imagery was also coincident with the position of the diurnal pulse in the IR differencing imagery. This suggests that it was, in fact, linked to the diurnal pulse seen propagating away from the storm that day. Although the diurnal pulse evolution is somewhat evident in the GOES IR images (Fig. 3.1, upper panels), details and subtleties of its structure and position are better elucidated in the GOES IR differencing images (Fig. 3.1, lower panels).

The 37 and 89/91 GHz microwave satellite images (from the NASA Aqua and DMSP satellites) shown in Fig. 3.2 are within ~1.5 h of the image times shown in Fig. 3.1 and confirm that the arc of cold cloud tops (i.e. diurnal pulse) in the western and northern semicircles of Felix was associated with outwardly expanding deep convection and was not just a shallow layer of

cirrus outflow. The leading edge of this feature was denoted by cyan to pink shading (37 GHz) and brightness temperatures ranging from 175-250 K (89 and 91 GHz) in the microwave imagery and was positioned ~175-200 km from the storm center at 1348 UTC (Fig. 3.2, left panels). By 1829 UTC, it was located at radii ranging from ~200-300 km (Fig. 3.2, right panels). Additional microwave satellite overpasses from NASA TRMM and other DMSP satellites confirmed this radial expansion (not shown). This is a significant observation and suggests that the TCDC may be manifested in a deep layer of the TC environment and therefore may be an important influence on TC structure and possibly even intensity.

The outwardly propagating diurnal pulse and marked warming of the cloud tops at radii inside of the pulse appear to be key elements of the TCDC and suggest that it has a radially dispersive nature. The structure of this propagating feature also suggests that minima and maxima associated with the TCDC (e.g. cirrus canopy areal coverage, convection and precipitation) cannot be adequately described in terms of time alone. Instead, the TCDC is better described in terms of both time and space. In order to effectively capture this diurnal signal, azimuthal calculations of IR brightness temperatures and IR brightness temperature trends were generated for Hurricane Felix every 3-hr from 01 Sep 2045 LST to 04 Sep 0145 LST at 100-600 km radii from the storm center. It should be noted that the SHIPS 200-850 hPa vertical wind shear was quite low (0.5-6 m s^{-1}) throughout this period and consistently below the maximum shear criteria (7.5 m s^{-1}) discussed in Sec. 2.2.1

Figure 3.3 (top panel) shows a time series of azimuthal mean IR brightness temperature (200, 300, 400, and 500 km radii) for Felix from 01-04 September, while the lower panel shows the identical time period, only for calculations of IR brightness temperature trends. The former azimuthal calculations focus on the magnitude of IR brightness temperature fluctuations at

various radii, while the latter calculations focus on the time tendency of this signal. There is some indication that the time tendency variability provides a more robust (i.e. exhibits higher and more consistent amplitude) depiction of the TCDC and will be discussed in further in Sec. 3.3. A clear maximum cooling in the R=200-500 km satellite IR field is evident in both plots ranging from the early morning to late afternoon (local time), followed by a distinct maximum in warming from the early evening to early morning hours. The oscillatory nature of this cooling and warming is quite regular from day to day in these plots and suggests the repeatability of this phenomenon. Also of note is the apparent phase shift in the timing of the TCDC at the various radii (i.e. the peak cooling/warming tended to progress radially outward in time from 200-500 km). These trends suggest that the TCDC signal began at the innermost radii (e.g. <200 km, not shown) and propagated to peripheral radii at a speed of ~5-10 m s^{-1} during the course of several hours.

3.2.2 2005 Hurricane Emily

Figure 3.4 shows an example of the TCDC for 2005 Hurricane Emily on 15 July. Emily was a powerful (category 4, 59 m s^{-1}), compact storm early that day (Fig. 3.4, upper left panel) and similar to the Felix case, exhibited rapid radial growth of its cirrus canopy throughout the late morning and afternoon (Fig. 3.4, upper right panel). Also similar to the Felix case, an arc of cold cloud tops was seen propagating away from Emily's inner core during this time. This diurnal pulse was especially evident in the western, northern, and eastern semicircles of the storm at ~R=150-350 km and a moat of warmer (-30 to -50^{o}C) cloud tops was apparent on the inside edge of that pulse at ~R=150-250 km (Fig. 3.4, upper right panel).

Figure 3.4 (lower left panel) shows IR differencing imagery and depicts changes in Emily's IR temperature field from 0045-0645 UTC. As was seen in the Felix case, the imagery shows a remarkably circular ring feature at approximately R=100-250 km that had cooled 20-60^{o}C during this 6-hr period, with warming of 5-20^{o}C evident on the inside edge of the diurnal pulse in the inner 100 km. By 1445 UTC that day the diurnal pulse had propagated to a radius of ~250-400 km from the center and the inner core cloud tops on its inside edge (0-200 km radius) had warmed by 5-40^{o}C (Fig. 3.4, lower right panel). The GOES IR images from those corresponding times (Fig. 4, upper panels) reveal a storm with a much larger cirrus canopy and a structure that had visibly deteriorated (the NHC Best track intensity for Emily dropped 10 m s^{-1} during that afternoon). Similar to the Felix case, microwave satellite imagery (37 and 85 GHz) from the NASA Aqua, DMSP, and NASA TRMM satellites confirmed that the diurnal pulse that was seemingly propagating away from Emily's inner core in the GOES IR imagery was not just a cirrus outflow feature, but was instead a deep convective feature (Fig. 3.5). Figure 3.5 shows a significant radial expansion of the storm in the 37 GHz and 85 GHz imagery (190-250 K brightness temperatures) on 15 July from 0048-1323 UTC that was approximately collocated with the diurnal pulse signal shown in Fig. 3.4. In fact, the radial extent of the deep convection around the storm [i.e. cyan to pink shading (37 GHz) and ≤250 K brightness temperatures (85 GHz)] expanded by ~125-200 km during that ~12.5-hr period.

Figure 3.6 shows plots derived from azimuthal calculations of GOES IR brightness temperatures and 6-hour IR brightness temperature trends for Hurricane Emily every 3-hr from 14 July 2045 LST to 17 July 1845 LST at 200, 300, 400, and 500 km radii from the storm center. Unlike the Felix case, the SHIPS-analyzed 200-850 hPa vertical wind shear for Emily reached values (9-11 m s^{-1}) above the 7.5 m s^{-1} threshold described in Sec. 2.2.1 for a portion of the

storm's lifecycle that was examined. This segment of Emily's lifecycle was not included in the azimuthal mean statistics of the TCDC presented in the next section. The periods of lower shear ($\leq$7.5 m s^{-1}) at the beginning and end of the Emily time series show distinct diurnal cycle signals in the GOES IR brightness temperature fields, with peak cooling in the early morning to late afternoon hours (local time), followed by distinct maxima in warming during the early evening to early morning hours (Fig. 3.6, solid curves). Similar to the Felix case, the Emily analyses suggest that the radial propagation speed of the TC diurnal pulse signal was ~5-10 m s^{-1}.

Relative to local time, the diurnal variations of warming and cooling in the Emily GOES IR brightness temperature field shown in Fig. 3.6 corresponded remarkably to those found in the Felix case (Fig. 3.3). This further suggests that the TCDC has predictability in both time and space. Interestingly, the period of the Emily lifecycle that exhibited moderate to high vertical wind shear (>7.5 m s^{-1}) was also marked by a diminished TCDC signal (i.e. the brightness temperature magnitudes and time tendency amplitudes were reduced in the satellite IR fields during this time; Fig. 3.6, dashed curves). This could be related to weakening of inner core processes that might be forcing the TCDC and/or to the radial displacement of the cirrus canopy and deep convection in conditions of strong vertical wind shear. Asymmetries in the GOES IR brightness temperature field resulting from the latter process could lead to azimuthal calculations that do not adequately capture diurnal pulses that propagate away from the storm. Still, the TCDC found in the Emily case exhibited notable similarity to that shown for Felix case. These similarities suggest that a robust multi-storm examination of the TCDC could be carried out if the criteria discussed in Sec. 2.2.1 are utilized and if the daily solar cycle is used to normalize the evolution of this phenomenon in time and space.

3.3 TCDC Satellite Analyses

A spectral analysis of the entire 10-yr dataset of IR satellite imagery was performed to identify signals of the TCDC at various radii from the storm center and confirm the cyclic nature of this phenomenon as suggested by the 2005 Hurricane Emily and 2007 Hurricane Felix cases. These analyses were carried out relative to LST on a detrended, concatenated time series created from all storms in the dataset and analyzed using an auto regressive (AR(1)) model. The spectral analyses were tested for significance against a Markov red noise continuum (Gilman et al. 1963). Figure 3.7 shows a spectral analysis of the IR brightness temperatures from R=100-600 km and corroborates some of the findings from Kossin (2002). A clear diurnal cycle (1 cycle per day) is evident in the IR brightness temperature field that appears to be more robust at peripheral radii (e.g. 200+ km), yet is not as readily detectable at 100 km. Surprisingly, the semi-diurnal (2.0 cycles per day) signal that was described by Kossin (2002) was not found at R=100 km in the current dataset. This suggests that if a semi-diurnal cycle is indeed present in TCs at this inner radius, it may either not occur in major hurricanes or is just not readily detectable in the environments of these stronger storms. Figure 3.7 shows that even at the 200 km radius, the TCDC signal is prominent, though it appears to be strongest at the 300 and 400 km radii. This suggests that the outwardly propagating diurnal pulse that has been discussed does not really become a distinct feature until R=~150-200 km. It is not clear if this implies that the TC diurnal pulse tends to form in this intermediate radius range and is not typically found at the innermost radii or if the cyclonic circulation closer to the center is advecting cloud features around the storm and masking an otherwise active diurnal pulse signal in the spectra.

The diurnal cycle power spectrum shown in Fig. 3.7 also indicates that although the peak signal occurs at 300-400 km, this phenomenon is a prominent feature even at large radii (e.g.

500-600 km), far removed from the convective TC inner core region. It is hypothesized that since their convective structure would be more radially confined, smaller sized storms would tend to produce a less detectable diurnal pulse signal at 500-600 km. In fact, each storm may have a preferred radius where the power spectrum peaks and would be dependent on the size of the convectively active inner core region. This is beyond the scope of this research effort, but warrants further investigation.

Based upon the diurnal signal indicated in the spectral analysis of the 2001-2010 dataset, azimuthal mean 6-hr IR brightness temperature trends were calculated at the 400 km radius for a subset (12 storms) of the 31 North Atlantic major hurricanes examined in this study (Fig. 3.8). It should be noted that these cases contained the most complete and continuous 72-hr lifecycles in the 10-yr dataset and were therefore chosen to illustrate the cyclic nature of the TCDC. However, they are also representative of the larger storm sample. Each time series represent continuous 72-hr snapshots for each storm and were examined relative to both LST and hours after sunset in order to optimally capture this diurnal signal. Figure 3.8 shows that a well-defined TCDC with very clear and predictable oscillations in the satellite IR brightness temperature fields emerges, even when numerous TCs are examined. The TC diurnal pulses (i.e. peak cooling in the IR field) typically reached the 400 km radius at ~1100-1700 LST (~17-23 hr after sunset) and were straddled by periods of peak warming from ~2200-0500 LST (~3-10 hr after sunset).

Given the robustness of the TC diurnal signal depicted in Figs. 3.7 and 3.8, mean statistics were then calculated from 31 major Atlantic hurricanes from 2001-2010 using the selection criteria described in Sec. 2.2.1. Figure 3.9 shows the mean azimuthal IR brightness temperatures and IR brightness temperature trends for these TCs every 3-hours at 100-600 km

radii from the storm center relative to LST. The IR brightness temperature trends at the 200-600 km radii (Fig. 3.9) point to a clear TC diurnal signal that is most pronounced (largest amplitudes) at the 300-400 km radii and is supported by the power spectrum analyses shown in Fig. 3.7. The TCDC was not clearly evident at R=100 km, similar to results shown in Fig. 3.7, as well as findings by Kossin (2002).

Several key conclusions can be drawn from the trends of geostationary 6-hour IR brightness temperature trends shown in Fig. 3.9 regarding the nature of the TCDC and its evolution in time and space. As previously mentioned, these 6-hr IR brightness temperature trend plots more effectively captured the TCDC. This figure also confirms the notion that the TCDC and associated diurnal pulses propagate radially outward over time. Table 3.1 summarizes the diurnal pulse evolution relative to both LST and hours after local sunset and specifies the approximate timing of the passage of the TC diurnal pulse (and warming that precedes/follows it) at various TC radii. Fig. 3.10 provides a conceptual graphical representation of the mean TC diurnal pulse evolution over time and space. The diurnal pulses reach the 200 km radius (peak cooling in the IR field) at ~0400-0800 LST (~9-13-hr after sunset), followed by the 300 km radius at ~0800-1200 LST (~13-17-hr after local sunset), and the 400 km radius at ~1200-1500 LST (17-20-hr after local sunset). This implies a diurnal pulse propagation speed of 5-10 m s^{-1}. Each diurnal pulse also appears to be bounded by equally strong peaks in warming that occur ~8-15-hr before and after the passage of the diurnal pulse.

The oscillating peaks of cooling and warming evident in the IR satellite imagery may have important implications for the timing of TC inner core convection (and possibly intensity change and precipitation). For instance, the diurnal pulse reaches R=200 km at ~0400-0800 LST (~9-13-hr after local sunset) and maximum warming (i.e. minimum in deep convection) occurs at

~2000-0000 LST (1-5-hr after local sunset). This corresponds well with Gray and Jacobson's (1977) findings regarding the timing of deep convection minima and maxima over tropical oceanic regions. However, the diurnal pulses pass through outer radii (e.g. 300-500 km) several hours after reaching R=200 km (Fig. 3.9 and Table 3.1). This suggests that Gray and Jacobson's (1977) conclusions, although valid for the TC inner core region, do not adequately describe the TCDC at all radii for a storm. This relates to the fact that TC diurnal pulses propagate away from the TC center and hence, TC convective minima and maxima can be better described in terms of both time and space. Browner et al.'s (1977) findings regarding the minimum (0300 LST) and maximum (1700 LST) extent of the TC cirrus canopy discussed in Sec. 1.2 and shown in Fig. 1.3 also agree with the results shown in Fig. 3.9 and Table 3.1. However, it should be emphasized that the current work also puts these minima and maxima into a spatial context. Instead of a cirrus canopy with a single minimum and maximum extent, it is proposed that TC diurnal pulses may be propagating through a deep layer of the storm that includes the cirrus canopy and lower to middle troposphere.

3.4 The TCDC and TC Structure

The results described in Secs. 3.2 and 3.3 show that the TCDC impacts the thermal structure of the TC cirrus canopy and may impact TC structure through a relatively deep layer of the troposphere below the cirrus canopy. Since several earlier studies have also documented relationships between the areal extent and variance of satellite IR brightness temperature and the size of the TC wind field (Mueller et al. 2006, Kossin et al. 2007, Lee et al. 20101, and Knaff et al. 2014), the possible relationship between the TCDC and TC structure using wind radii information from the Extended Best Track dataset (Demuth et al. 2006) was examined. The

entire 2001-2010 dataset was used to examine diurnal fluctuations in the analyzed radii of 34, 50, and 64 kt 10-m surface winds with data binned into a single 3-hourly 24-hr cycle for these analyses. It should be noted that the mean radii of 34, 50, and 64 kt winds for this limited sample of mature TCs was 230, 120, and 70 km respectively. Table 3.2 shows an analysis of the radius of 50 kt winds derived from the Extended Best Track and suggests that there are diurnal trends in the rate of expansion of the 50 kt wind radius around the storm depending on the time of day. The expansion of the 50 kt wind radius tends to reach a minimum in the early morning hours (~03-09 LST) and peaks in the mid-afternoon to early evening hours (~18-21 LST), which is similar to the TC diurnal pulse timing predicted by the TCDC conceptual clock (Fig. 3.10). This suggests that the radius of 50 kt winds may be linked to radially propagating TC diurnal pulses. Though the trends for the 34 and 64 radii were similar to those of the 50 kt radii, the relationships were not as statistically significant. The weaker signals at these radii may relate to the fact that 34 kt radius is rarely sampled by reconnaissance aircraft and tends to be dominated by persistence from forecast cycle to forecast cycle, while the small mean radius of 64 kt winds (70 km) is in a region of the storm where the TCDC signal is not readily detectable (see Sec. 3.3 discussion). The diurnal fluctuations described here suggest that the surface wind fields of TCs may be influenced by the TCDC and will be discussed further in Chapter 4.

3.5 The TCDC and TC Satellite-Based Intensity Estimates

The Advanced Dvorak Technique (ADT) dataset was used to assess possible linkages between the TCDC and satellite-based estimates of TC intensity. ADT represents an objective, automated version of the operational Dvorak Technique for estimating TC intensity (Olander and Velden 2007). The algorithm utilizes ~11 μm IR imagery from geostationary satellites to

examine various kinematic and thermodynamic properties of the TC cloud pattern. One of the output values from the ADT includes the raw tropical ("T") number and the current intensity (CI) number (with a value range of 1.0-8.0). The former intensity estimate is determined from the analyzed Dvorak scene type (e.g. eye, central dense overcast, embedded center, curved band, and shear) and measured environmental parameters (e.g. scene temperatures and symmetry in the eye and cloudy regions of the storm) and has a final value that is not constrained in any way. The latter value is derived from the initial raw T number, but also includes operational rules and constraints that define how much a T number can change over a specified time interval. The CI number is empirically converted to an equivalent maximum sustained surface wind and a wind-pressure relationship is then used to assign the corresponding minimum sea level pressure (Velden et al. 2006). ADT TC intensity estimates are largely based upon pattern recognition of the IR satellite brightness temperature field and IR temperatures in the eye and surrounding cloud regions of the storm. Therefore, it is hypothesized that the TCDC may also directly influence ADT satellite intensity estimates that are routinely used to determine TC intensity in ocean basins around the world. If this is the case, a spectral analysis of TC ADT estimates should show the existence of a diurnal signal within that dataset. Therefore, spectral analyses were performed on both the T numbers and CI numbers associated with each time series in the 2001-2010 TC dataset using the criteria described in Sec. 3.3. Figure 3.11 indicates that a statistically significant (99% confidence level) diurnal cycle (1 cycle per day) does indeed exist in the Dvorak raw T number intensity estimates.

Curiously, the Dvorak raw T numbers also exhibit a statistically significant cycle that is on the order of 0.5-0.75 per day. This sub-diurnal signal was also evident (95-99% confidence level) in the Fig. 3.7 IR brightness temperature spectral analyses at R=100-600 km and is

especially detectable at R=100-400 km. Given that Dvorak analyses are focused on IR brightness temperature information in the inner storm radii (R=~25-125 km), perhaps it is not surprising that the ADT and 100-400 km IR analyses show similar pattern in their spectra. It is not clear what is causing the 0.5-0.75 cycles per day signal in the Dvorak raw T number spectral analysis and is beyond the scope of this research effort. Future work should include investigating this sub-diurnal signal in the ADT data, as well as possible repeatability in other Dvorak Technique datasets (e.g. those produced at operational forecast centers). Although the spectral analysis of the Dvorak CI number also shows a similar peak at both 1 and 0.5-0.75 cycles per day (95% confidence level), the signal is not as pronounced as that of the Dvorak raw T numbers. It is hypothesized that operational constraints placed on the CI number could act to reduce the natural variability in TC structure that is associated with the TCDC. Therefore the differences between the T number and CI number spectra suggest that there are intensity biases built into the Dvorak technique that warrant further investigation.

3.6 TCDC Mechanisms

The observational evidence from geostationary and polar orbiting microwave satellites shown in Secs. 3.2 and 3.3 suggests that the TCDC manifests itself as a pulse in the cloud field each day that involves a deep layer of the storm extending from the cirrus canopy down to altitudes below the freezing level. Although this indicates that the TCDC may have an important influence on TC structure and possibly intensity, the exact mechanism(s) forcing this phenomenon is (are) not clear. Several hypotheses have been previously presented that attempt to address the causes for observed fluctuations in atmospheric deep convection. The following sections briefly describe these hypotheses that could help address several questions related to

TCDC and TC diurnal pulses, including: where and the how they form in the TC environment, details of their horizontal and vertical structure, and processes that force their radial propagation away from the storm each day. It recognized that a more detailed analyses, including using a combination of satellite data (Chapters 3 and 6), numerical simulations (Chapters 4 and 5), and observations (Chapter 6) will be required to assess the merit of these hypothesized TCDC mechanisms.

3.6.1 Convectively-driven atmospheric gravity waves

The remarkable symmetry of many of the TC diurnal pulses that were observed in this study suggests that they may be a propagating gravity wave feature. During the day, convectively-generated gravity waves are produced in the TC inner core and propagate upward into the stratosphere (e.g. Pfister et al. 1993), but would generally remain undetectable by conventional observations (e.g. satellite imagery). However, it is possible that rapid radiative cooling at the level of the TC cirrus canopy near the time of sunset in concert with vertical wind shear associated with the TC upper-level outflow layer could generate a more statically stable vertical profile that would be capable of reflecting these convectively generated gravity waves (Tripoli and Cotton 1989). During this time, these trapped gravity waves would likely intensify in the troposphere as they propagate away from the storm close to the level of the cirrus canopy and would become more readily detectable (e.g. via satellite imagery) as they move through this cloud layer. These ideas will need to be studied both observationally and theoretically.

3.6.2 Radiatively reduced outflow resistance

Outflow resistance as measured by Inertial Available Kinetic Energy (IAKE) combines the destabilizing effects of convective available potential energy (CAPE) with the stability effects of inertial resistance to the outflow of convection (i.e. "sideways" CAPE), is tied intrinsically to the potential vorticity of the outflow layer (Mecikalski and Tripoli 1998), and is defined as:

$$IAKE = \int_{r=0}^{RNA} \frac{dU_{rad}}{dt}\, dR \qquad (1)$$

where U_{rad} is the radial velocity relative to a given point (in cyclindrical coordinates) and R is the total distance from the cloud plume origin (r=0) to the radius of neutral acceleration (RNA). Since IAKE assumes a straight-line integration path from the outflow plume origin and the RNA in the surrounding environment, an upward adjustment to U_{rad} is applied in Eq. 1 that incorporates the parcel's angular momentum and the environmental tangential velocity that the outflow parcel experiences along its trajectory. Therefore, a TC environment where the tangential wind increases (i.e. potential vorticity lowers) will result in a decrease in U_{rad} and therefore an decrease in IAKE. The potential vorticity of the outflow layer, in turn, is tied to the static stability of that layer, which is modulated diurnally by solar forcing, particularly when filled with outflow cirrus. Convective bands, as well as the developing storm convective core are suppressed by outflow resistance, particularly in the early stages of a TC when the outflow layer has not been strongly modified by the storm's own outflow and so remains particularly resistant to the formation of new outflow. Longwave cooling, beginning just before sunset destabilizes this outflow layer, dramatically reduces the potential vorticity of the layer (i.e. reduces environmental tangential velocity), which increases U_{rad} and hence, increases the IAKE, perhaps making it actually positive. This would lead to the release of outflow, and a response to the convection below, previously limited by the outflow resistance. Measurements of the

potential vorticity evolution in the outflow layer should be made to supply observational confirmation of this potentially advective effect.

3.6.3 Cloud-cloud-free differential heating mechanism

Gray and Jacobsen (1977) described the notion that the cirrus canopy radiationally cools more at night and less during the day than surrounding cloud-free regions. The resulting pressure surfaces created by these temperature contrasts promote enhanced upper-level divergence and low-level convergence during the nighttime and early morning hours and could conceivably promote a period of enhanced upper-level outflow that could force the outward propagating TC diurnal pulses that have been observed moving away from the storm at night. This process would suggest the TC diurnal pulses are, in fact, advectively-driven features. Although Liu and Moncrieff (1998) concluded that this type of process was a secondary influence controlling the convective diurnal cycle in their model simulations, the cloud clusters that they examined were either fast moving or developed randomly in their model domain. It is conceivable that cloud-cloud-free differential heating processes could be more important in a more organized, longer lasting convective system such as a TC.

3.6.4 Direct radiation-convection interactions

This hypothesis was discussed by Kraus (1963), Chen and Cotton (1988), and later by Randall et al. (1991) and offers the idea that during the day, solar warming of the convective region cirrus canopy reduces the local lapse rate and promotes increased static stability in the middle to upper troposphere. Conversely, at night, preferential cooling at the level of the cirrus canopy relative to the lower troposphere decreases the static stability. These diurnal radiative

trends would act to enhance convection during the nighttime and early morning hours and could also enhance upper-level divergence during these times. It is plausible that in the TC peripheral environment (e.g. R=150-200 km), relatively shallow convective areas (e.g. spiral bands) could especially benefit from the reduced mid- to upper-level static stability that direct radiation-convection interaction processes would promote. It is also possible that nighttime and early morning periods of enhanced upper-level divergence could promote the observed TC diurnal pulses by promoting outward radial advection.

3.6.5 Seeder-feeder mechanism

Houze et al. (1981) hypothesized that the enhancement of precipitation in warm-frontal rainbands can result when ice particles from aloft fall into the layer below the -4^{o}C level and aggregate just above the melting level. These "seeder" ice crystals can subsequently, as they descend, help convert cloud water to precipitation via Bergeron-Findeisen processes (Bergeron 1935). Houze et al. 1981 also described a second mechanism by which enhanced mesoscale lifting can increase the amount of "feeder" cloud water by condensation of vapor at low levels. It is possible that ice crystals associated with a radially expanding cirrus canopy in a TC environment (initiated by one of the three processes described in Secs. 3.6.1-3.6.4) could help stimulate convection in peripheral rainbands via the "seeder" mechanism. Additionally, mesoscale lift associated with a radially propagating gravity wave of sufficient depth could promote the "feeder" mechanism.

3.6.6 Summary of TCDC mechanisms

Although the exact nature of the TCDC and associated diurnal pulse are uncertain, more than one of the above-hypothesized mechanisms (or another mechanism not considered here) could be acting together in the TC environment to produce this diurnal phenomenon. This idea is supported by preliminary findings from Sec. 3.2 suggesting that TCDC pulses affect a significant depth of the TC. For example, radial expansion of the cirrus canopy initiated by one or more of the gravity wave or advective processes described above could act in concert with the seeder-feeder mechanism to create a diurnal pulse that extends from the lower troposphere up to the cirrus canopy level. While the observation of the TCDC is easily tracked by satellite and readily predictable in time and space, the causalities are not entirely obvious from a satellite-based perspective. High resolution numerical modeling analyses from a hurricane nature run simulation (Nolan et al. 2013) will be used to examine each of the proposed TC diurnal cycle driving mechanisms in isolation, as well as the possibility that multiple mechanisms are acting in concert to generate this atmospheric phenomenon (Chapter 4).

3.7 Discussion and Conclusions

A satellite-based examination of the TCDC is presented in this chapter that expands on previous studies and attempts to quantify this phenomenon in both time and space. The dataset that was used included storm-centered infrared (IR) and 6-hr IR brightness temperature differencing imagery for continuous 72-hr periods for all North Atlantic major hurricanes from 2001-2010. The IR differencing imagery revealed a distinct diurnal pulse in the investigated storms that begins each evening near the time of local sunset and appears as a radially expanding, quasi-symmetric ring of cooling brightness temperatures with marked warming on its

inside edge. The diurnal pulse appears to steadily move/propagate outward, reaching peripheral radii of the storm by early afternoon local time the following day. The TCDC and associated diurnal pulses were shown to be closely linked to the daily solar cycle and preliminary analyses of microwave imagery suggested that it may involve a deep layer of the troposphere (~200-600 hPa) as it moves/propagates away from the storm each day. Potential links between the TCDC and TC structure and intensity was also supported by analyses of Extended Best Track and ADT datasets. Additionally, geostationary IR imagery was used to examine azimuthal-mean brightness temperatures associated with TC diurnal pulses and suggested that this feature is highly predictable in both time and space. Although the exact nature of the TCDC and diurnal pulses is still unclear, it is hypothesized that the solar cycle is a driving mechanism. The mechanisms controlling its evolution each day are also unclear, though several hypotheses are presented. Several main conclusions can be made from the findings presented in this chapter and the 10-yr dataset used to examine the TCDC:

- This chapter highlights a diurnal cycle pattern in mature TCs that can be described as a dynamic process that evolves in both time and space. A 24-hr conceptual clock has been proposed that approximates its temporal and spatial evolution;
- The TCDC appears to be associated with a pulse in the cloud field that begins near the time of local sunset as a cooling region of inner core cloud tops in geostationary IR differencing satellite imagery. This region of cooling cloud tops subsequently takes on a ring-like appearance as marked cloud top warming begins to occur on its inside edge and it begins to move/propagate away radially from the storm at 5-10 m s^{-1}. A spectral analysis of the raw IR satellite dataset shows that it exhibits a clear diurnal signal;

- The period from local sunset to around sunrise (~0-12 hr after local sunset) is the most optimal time of day for TC inner core deep convection (i.e. relatively colder inner core cloud tops are evident in the IR imagery). The TC diurnal pulse is typically located at R=<200 km from the storm center during this period;
- The period from local mid-morning to late afternoon (~15-23 hr after local sunset) is the least optimal time of day for TC inner core deep convection (i.e. relatively warmer inner core cloud tops are evident in the IR imagery). The TC diurnal pulse is typically located at R=300-600 km from the storm center during this time;
- Microwave satellite imagery suggests that TC diurnal pulses might not be confined to the TC outflow layer, but instead may involve a relatively deep layer (e.g. ~200-600 hPa) of the storm from the upper troposphere to an area near the melting level;
- Diurnal variability in Extended Best Track radii of 50 kt winds was detected and suggests that the TCDC may influence TC structure;
- A spectral analysis of objective ADT data suggests that these satellite-based TC intensity estimates exhibited a statistically significant diurnal signal. A sub-diurnal signal was also found in the ADT data. These results suggest that ADT (and possibly other operational subjective Dvorak Technique) estimates of TC intensity may be impacted by the TCDC and that these estimates may also be associated with predictable biases that are dependent on the local time of day;
- Sunset appears to be a critical time for the initiation of the TCDC and associated diurnal pulses. One or more possible hypothesized mechanisms could be controlling the initiation and subsequent evolution of this phenomenon: convectively-driven atmospheric gravity waves originating in the TC inner core, radiatively-reduced outflow

resistance, cloud-cloud-free differential heating, direct-radiation-convection interactions, or seeder-feeder mechanisms;

This chapter presents evidence for an observable TCDC that is predictable in both time and space that may have implications for TC structure and intensity change. As a compliment to the observational analyses presented in this chapter, subsequent chapters will examine the TCDC from the perspectives of modeling and aircraft observations, with an overarching goal of better understanding and describing this potentially fundamental atmospheric process.

3.8 Tables and Figures

Peak IR Cooling	R=200 km	R=300 km	R=400 km	R=500 km	R=600 km
LST	0400-0800	0800-1200	1200-1500	1500-1800	1600-2000
Hours After Sunset	9-13	13-17	17-20	20-23	21-25

Peak IR Warming	R=200 km	R=300 km	R=400 km	R=500 km	R=600 km
LST	2000-0000	2200-0200	2300-0300	0000-0400	0200-0600
Hours After Sunset	1-5	3-7	4-8	5-9	7-11

Table 3.1: Mean timing of peak cooling and warming at the 200-600 km radii for the 2001-2010 North Atlantic TC dataset relative to local standard time and the number of hours after sunset. The peak cooling represents the approximate timing of the TC diurnal pulse passage at a given radius.

R50 6-hr trend (km)	00 LST	03 LST	06 LST	09 LST	12 LST	15 LST	18 LST	21 LST
Mean	+6.0	+4.3	+4.2	+3.9	+5.2	+6.6	+9.3	+7.0
Standard Error	0.77	0.76	1.02	1.01	0.38	0.91	1.18	0.95

Table 3.2: Diurnal trends (6-hr) of 50 kt wind radii (R50) obtained from the Extended Best Track for the entire 2001-2010 dataset. Trough (09 LST) to peak (18 LST) trends in R50 were significant at the 99.9% level, determined using a two-tailed Student's *t test*.

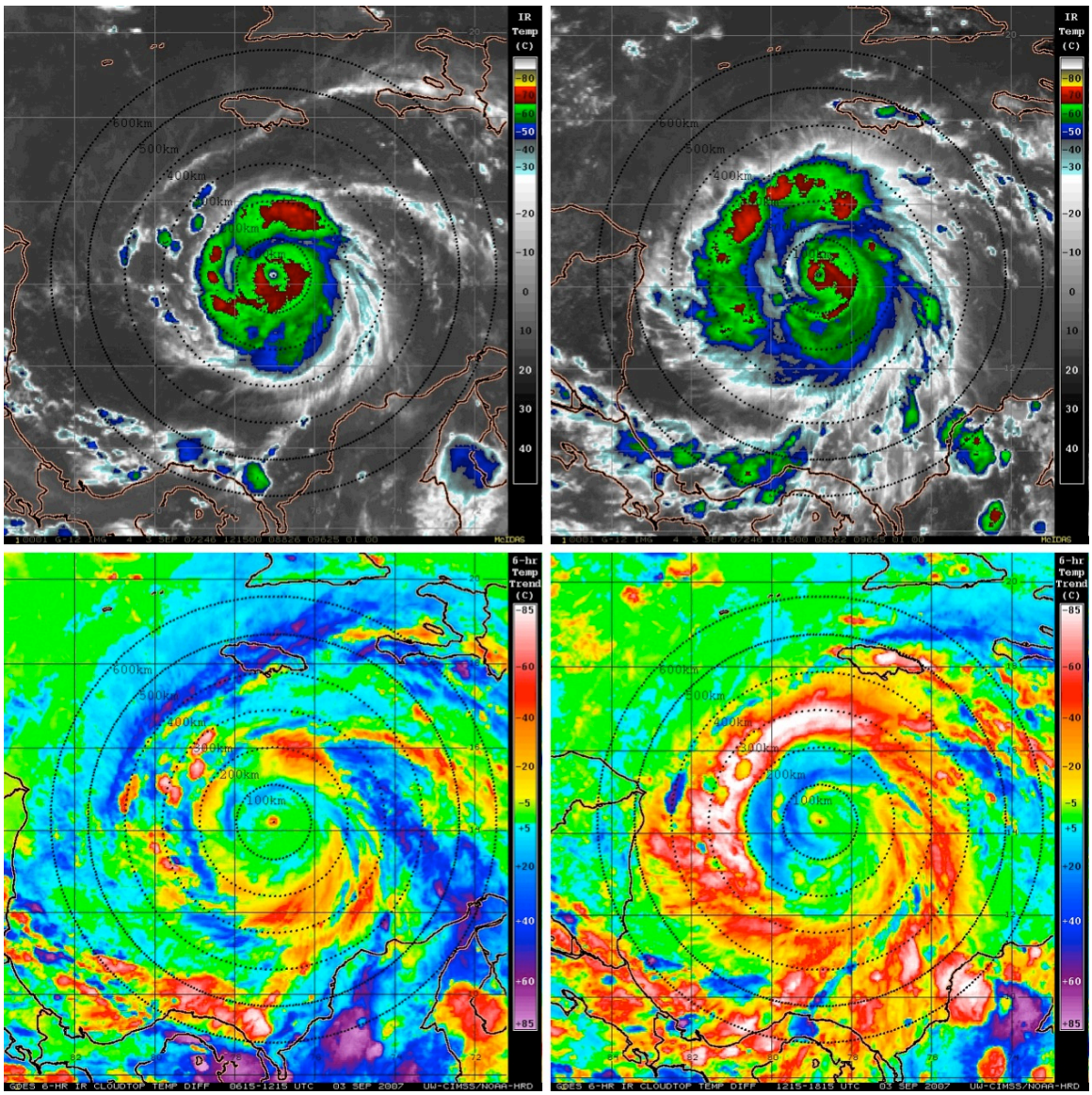

Figure 3.1: (Upper panels) GOES IR imagery showing 2007 Hurricane Felix on 03 Sep valid for (left) 1215 UTC (0715 LST) and (right) 1815 UTC (1315 LST). The corresponding 6-hr GOES IR brightness temperature differencing images for these times are shown in the lower panels. The yellow to pink shading (-10 to -85°C IR cooling tendencies) indicates a diurnal pulse propagating away from the storm during this period. 100-600 km range rings (black dashed curves) from the TC center are overlaid on each of the satellite images. Lines of latitude and longitude are marked at 2 degree intervals.

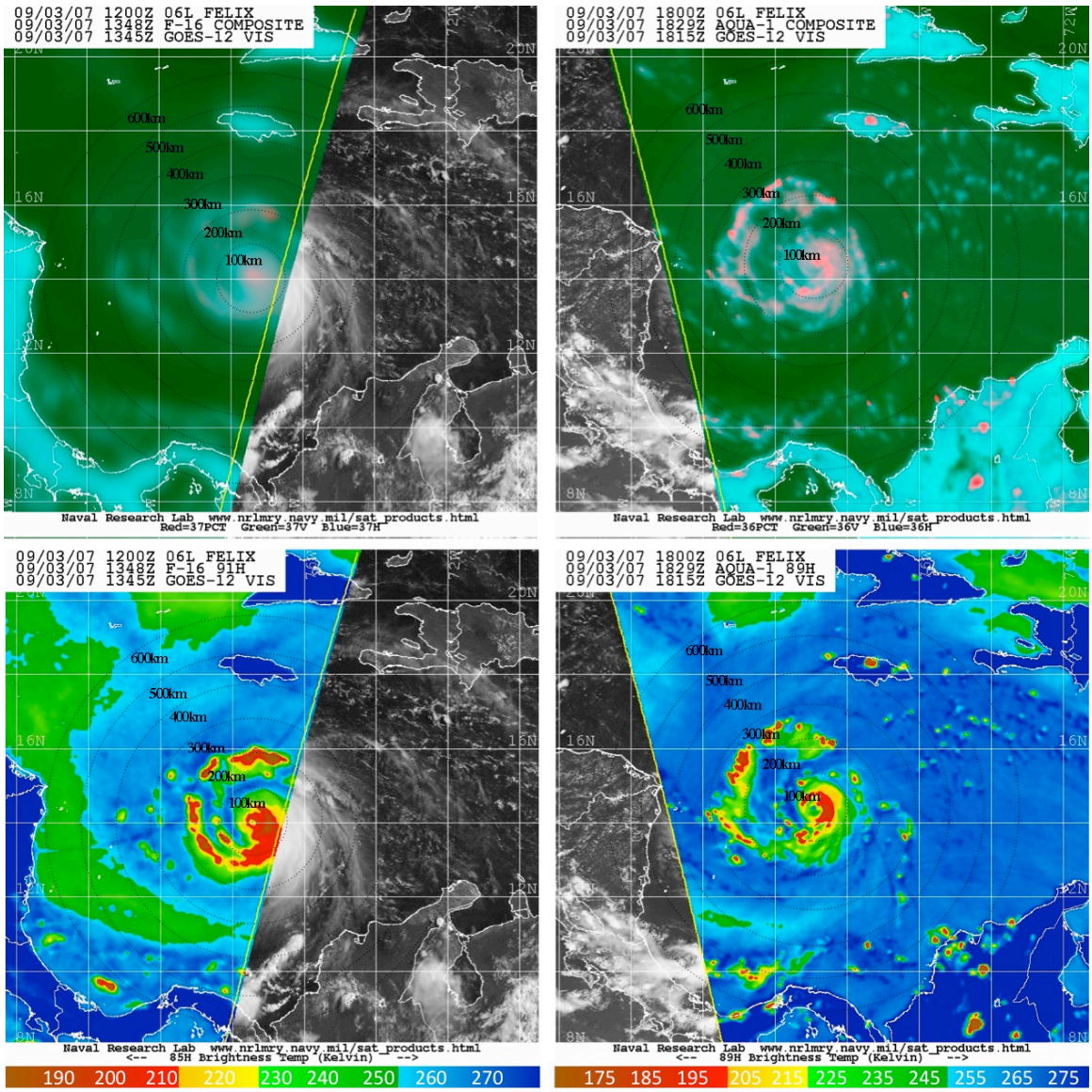

Figure 3.2: (Upper panels) DMSP F-16 SSMIS sensor and NASA Aqua AMSR-E 37 GHz color composite microwave satellite imagery (created from the horizontal and vertical polarizations and polarization-corrected temperatures) for 2007 Hurricane Felix on 03 Sep valid for (left) 1348 UTC (0848 LST) and (right) 1829 UTC (1329 LST). The corresponding 89/91 GHz microwave images for these times are shown in the lower panels. Note that the microwave overpass times are within 90-min of the respective GOES images shown in Fig. 3.1 and that areas outside of the satellite swath were supplemented by GOES visible imagery. 100-600 km range rings (black dashed curves) from the TC center are overlaid on each of the satellite images. Lines of latitude and longitude are marked at 2 degree intervals. Images provided courtesy of the Naval Research Laboratory Monterey.

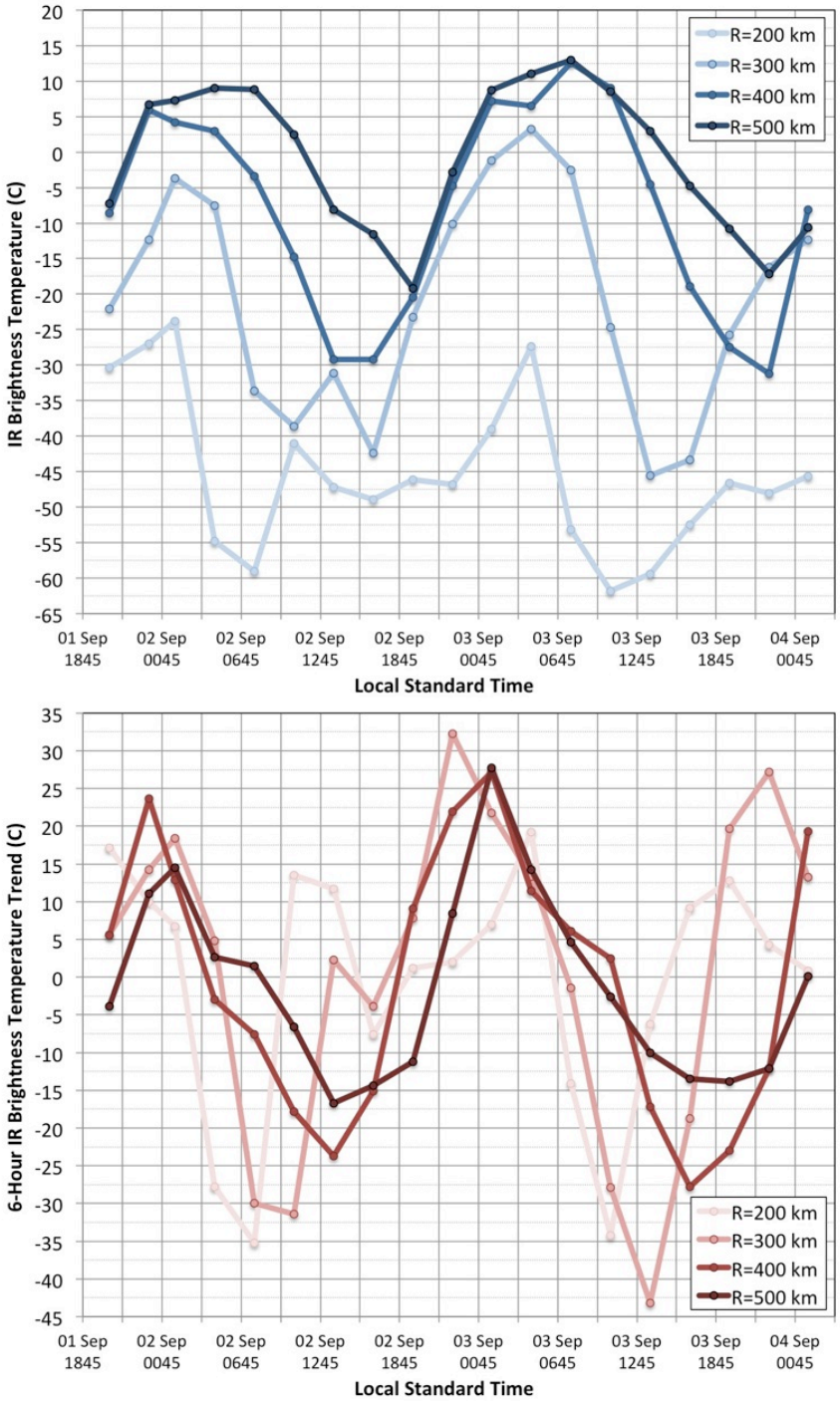

Figure 3.3: Azimuthally averaged 3-hourly GOES (upper panel) IR brightness temperatures and (lower panel) 6-hr brightness temperature trends at the 200, 300, 400, and 500 km radii around 2007 Hurricane Felix from 01 Sep 2045 LST – 04 Sep 0145 LST.

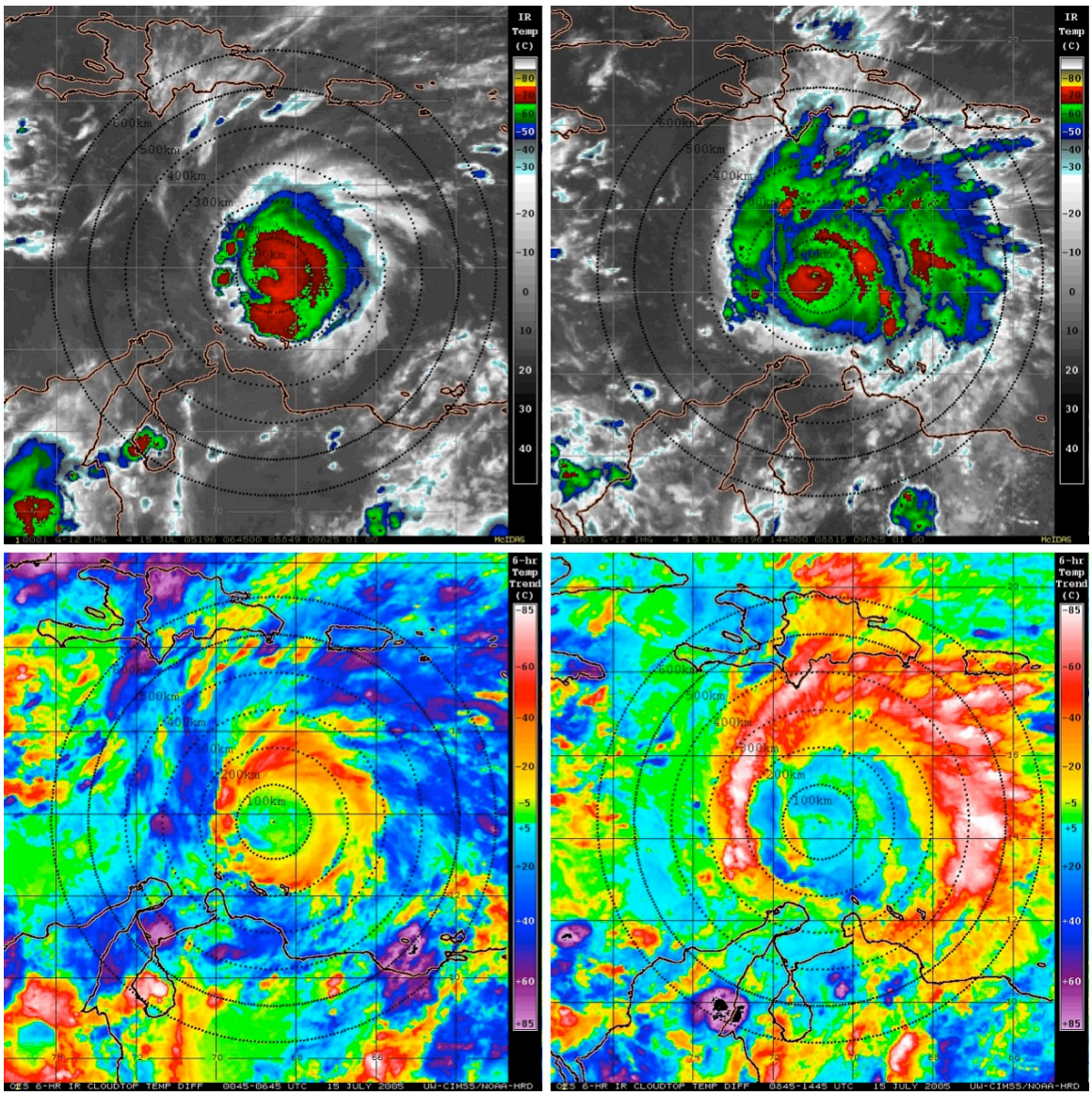

Figure 3.4: As in Fig. 3.1, but for 2005 Hurricane Emily on 15 July valid for (left) 0645 UTC (0145 LST) and (right) 1445 UTC (0945 LST).

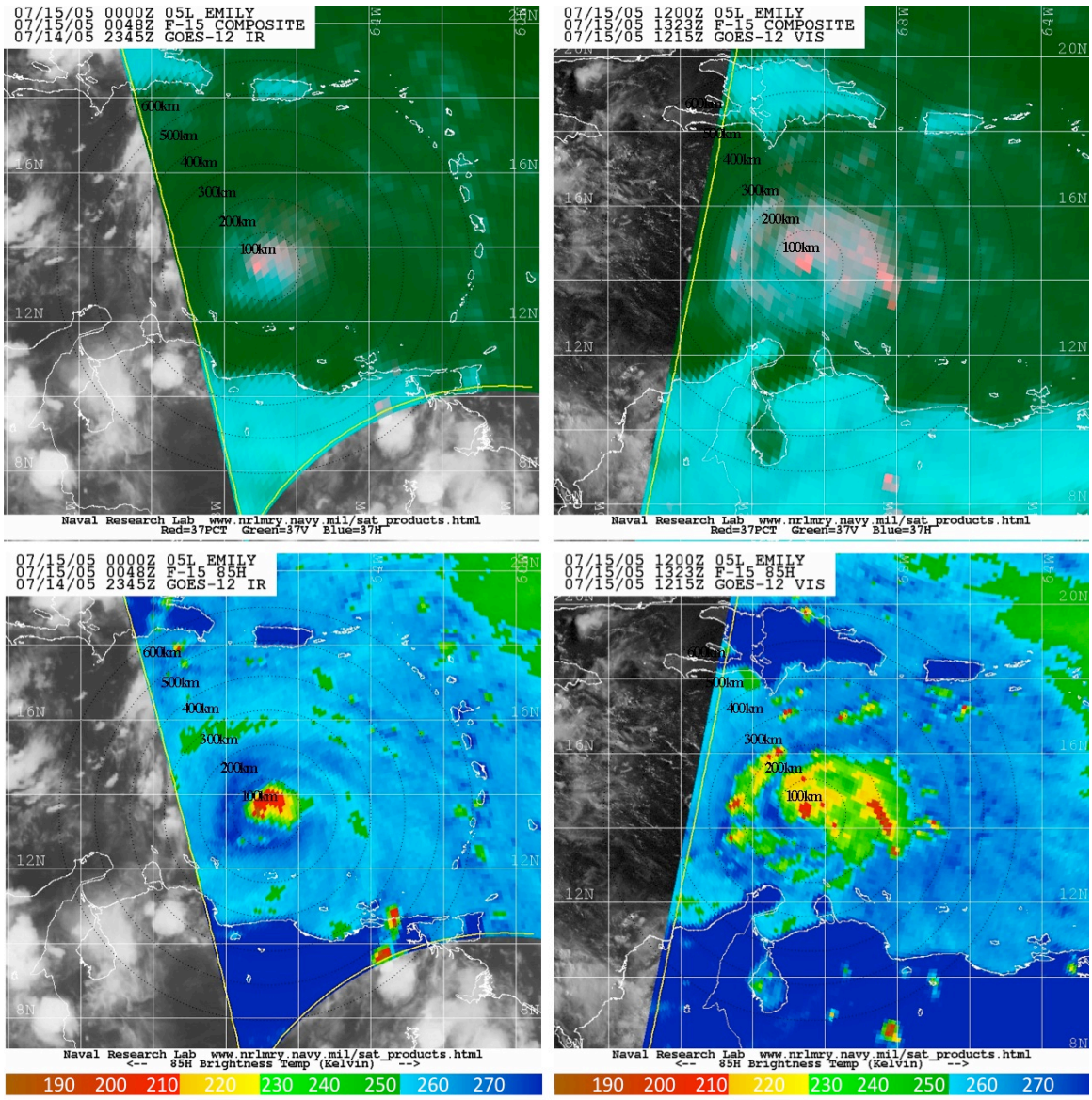

Figure 3.5: As in Fig. 3.2, but for 2005 Hurricane Emily on 15 July valid for (left) 0048 UTC (2048 LST) and (right) 1323 UTC (0823 LST), with the DMSP F-15 SSMIS sensor, and with overpass times that are within ~6-hr and 1.5-hr of the respective GOES images shown in Fig. 3.4. Images provided courtesy of the Naval Research Laboratory Monterey.

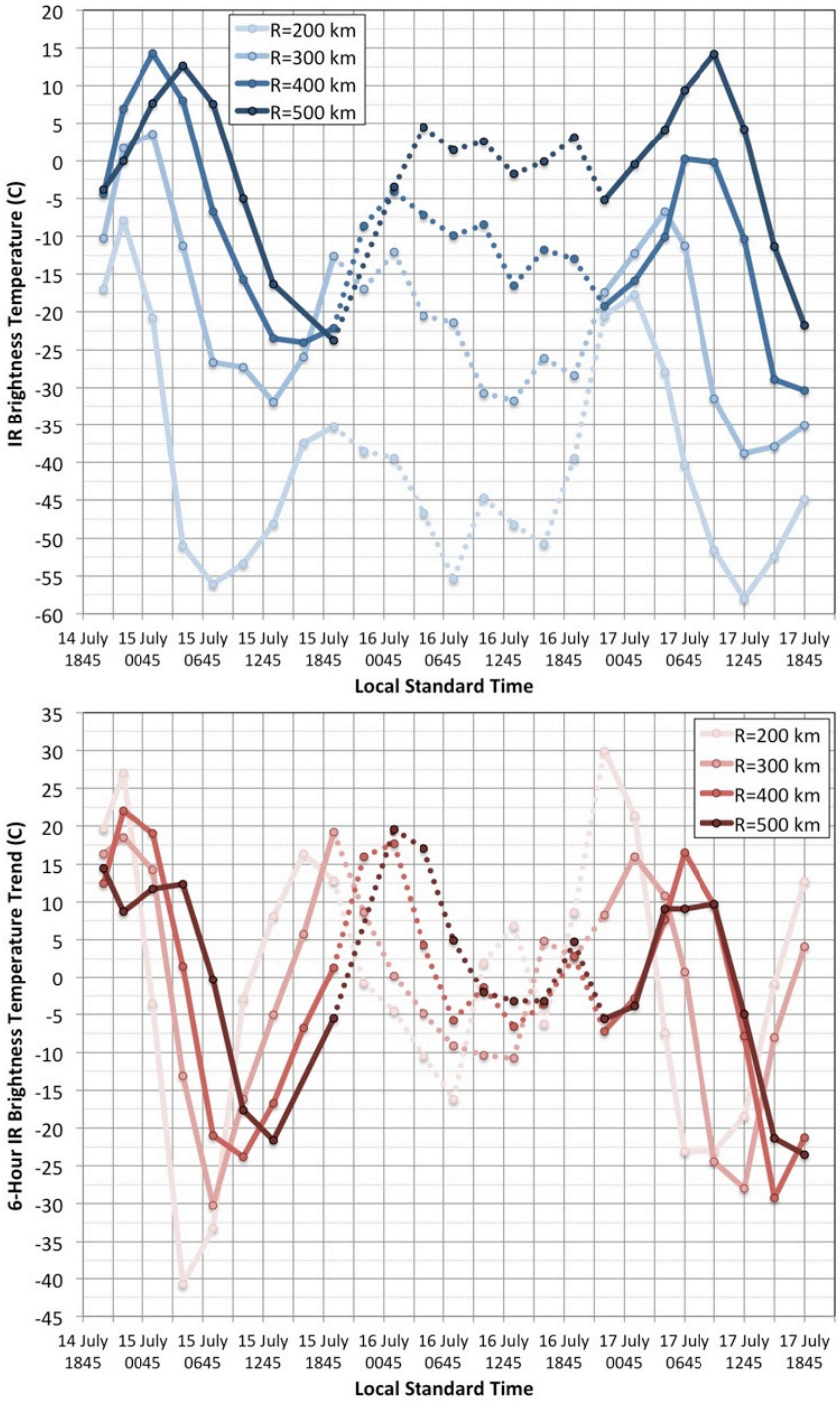

Figure 3.6: Azimuthally averaged 3-hourly GOES (upper panel) IR brightness temperatures and (lower panel) 6-hr brightness temperature trends at the 300, 400, and 500 km radii around 2005 Hurricane Emily from 14 July 2045 LST – 17 July 1845 LST. The dashed curved lines represent periods when the 200-850 hPa vertical wind shear for Emily reached values (9-11 m s^{-1}) above the 7.5 m s^{-1} threshold described in Sec. 2.2.1

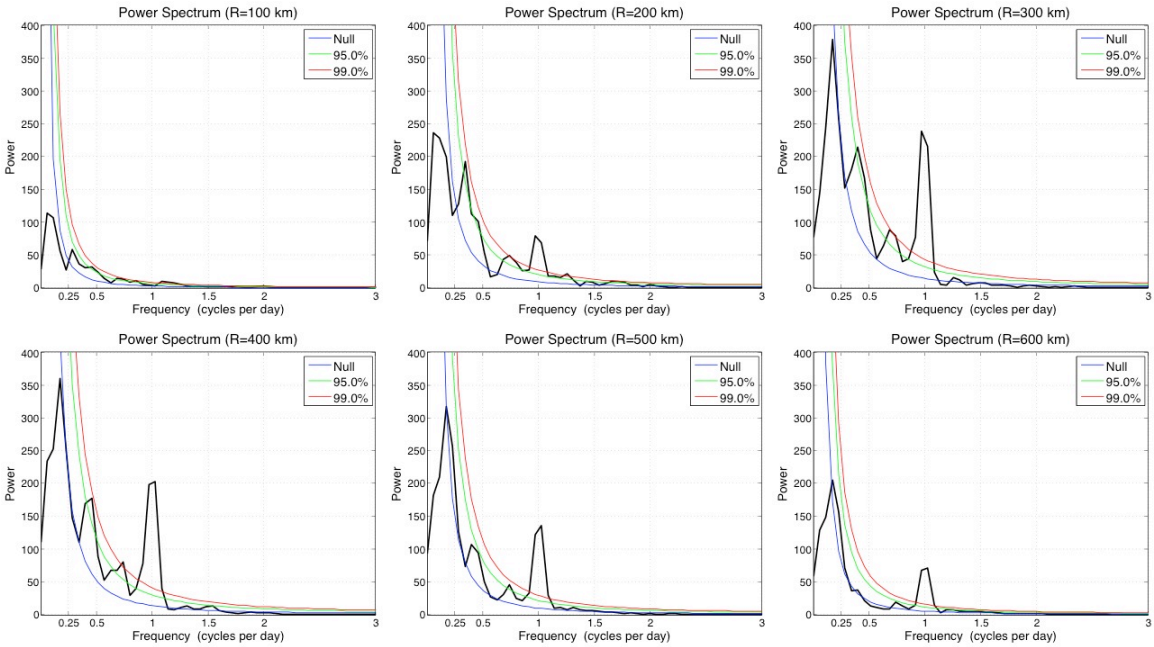

Figure 3.7: Power spectrum of azimuthally averaged geostationary IR brightness temperatures for the 2001-2010 North Atlantic major hurricanes that were investigated (R=100-600 km). The colored curved lines indicated various confidence levels in the analyses (i.e. power values at or above these curves are statistically significant at the respective confidence levels).

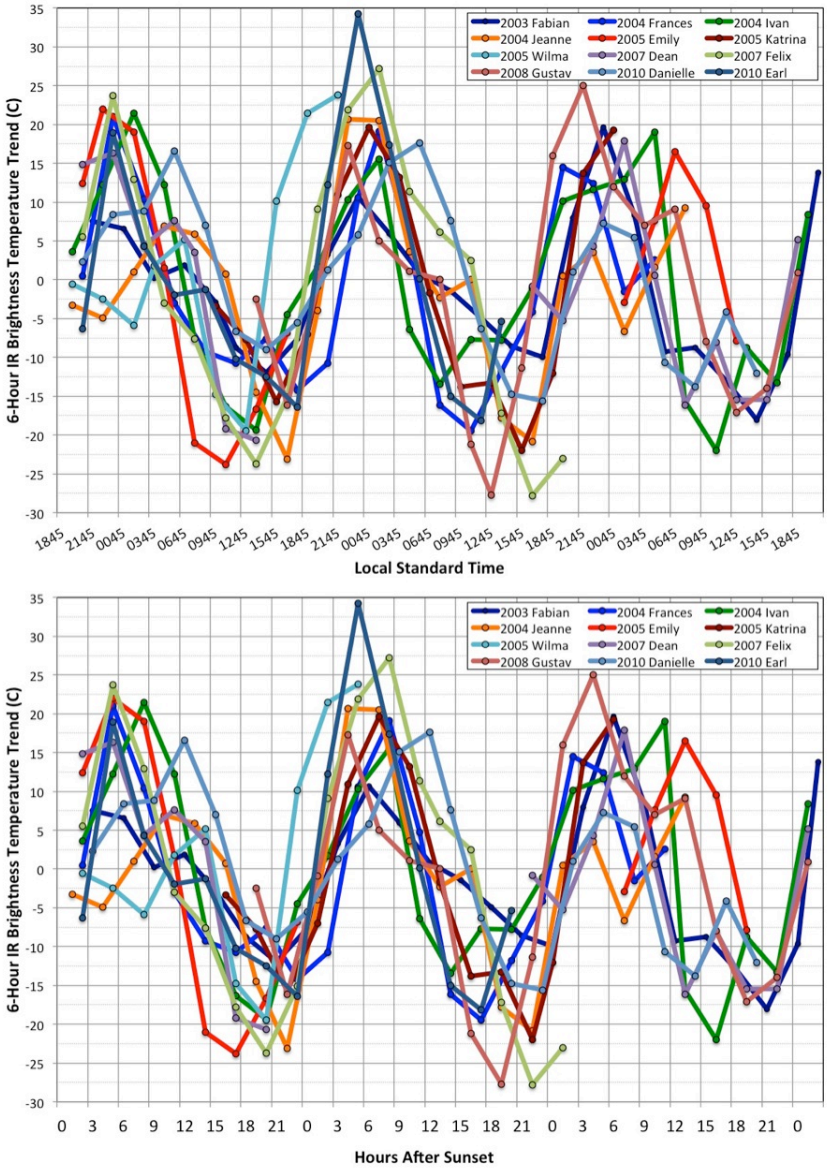

Figure 3.8: Azimuthally averaged 3-hourly geostationary IR 6-hr brightness temperature trends for several North Atlantic major hurricanes at the 400 km radius relative to (upper panel) local standard time and (lower panel) hours after local sunset.

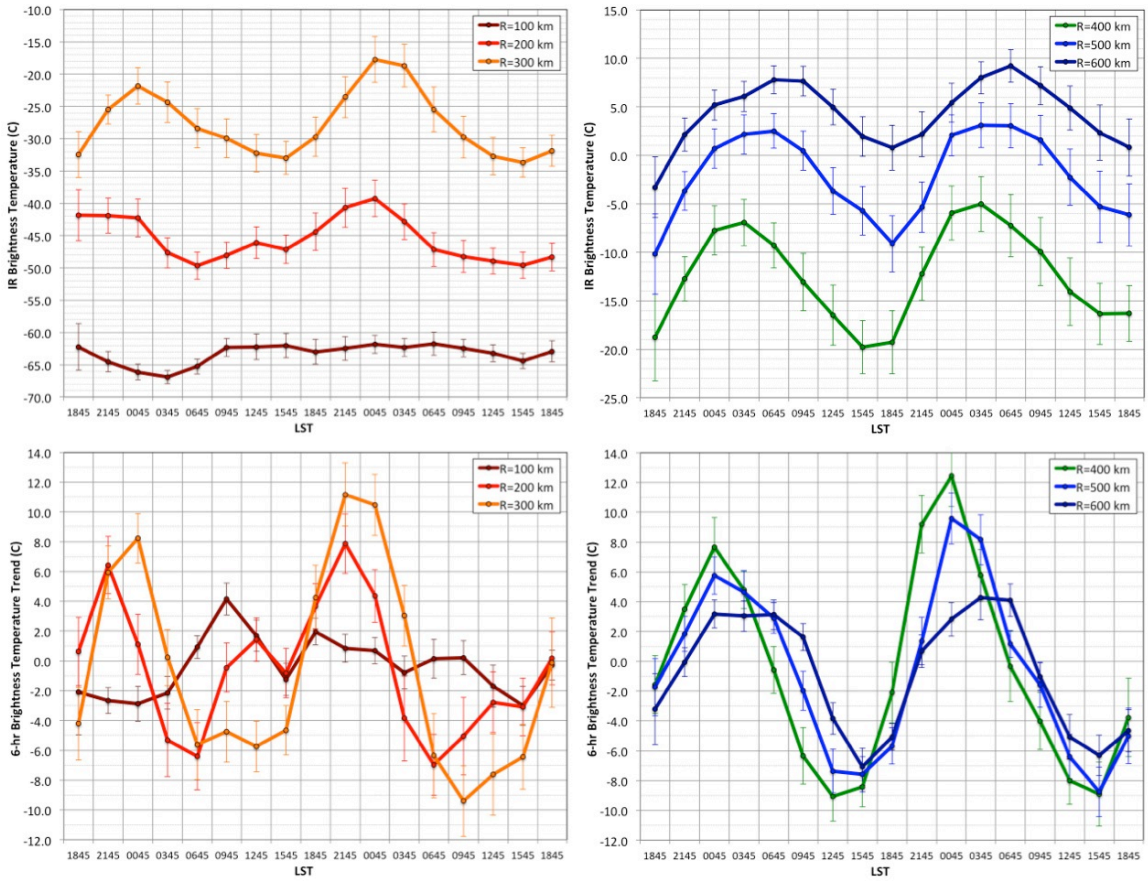

Figure 3.9: (Upper panels) azimuthally averaged 3-hourly geostationary IR brightness temperatures and standard error bars for the (left) 100-300 km radii and (right) 400-600 km radii relative to local standard time for all 31 North Atlantic major hurricanes that were examined. The corresponding azimuthally averaged 6-hr geostationary IR brightness temperature trends are shown in the lower panels.

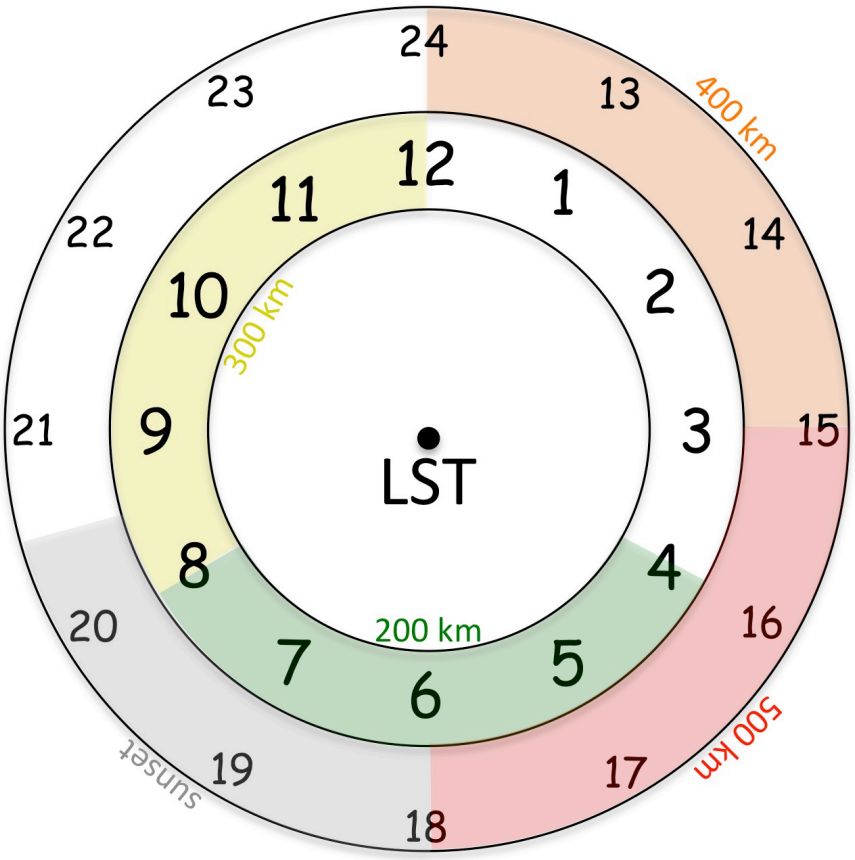

Figure 3.10: 24-hr conceptual clock of the TCDC evolution. Times listed are Local Standard Time (LST) and colored shading denotes the approximate arrival time of the TC diurnal pulse at corresponding radii from the storm center. Arrival times are estimates and may vary depending on storm size and convective structure.

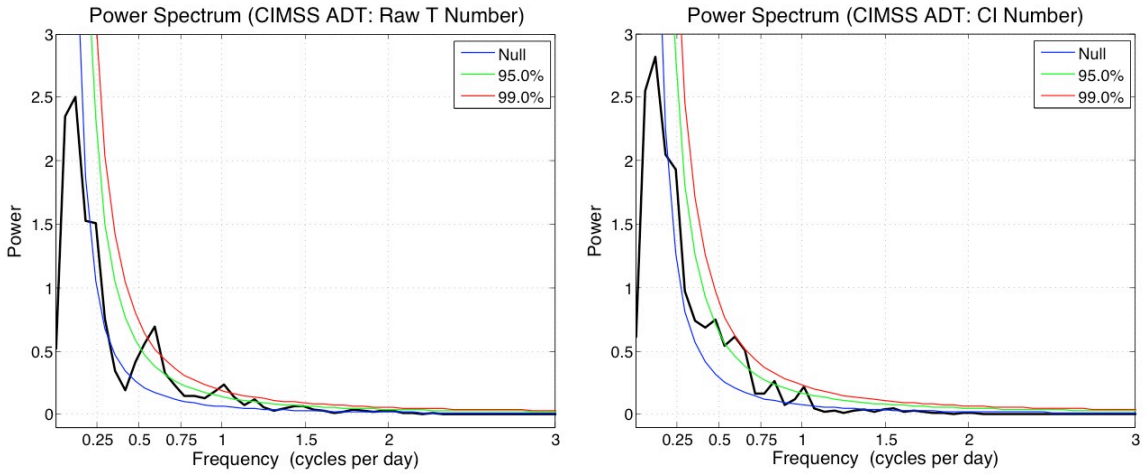

Figure 3.11: Power spectrum of Advanced Dvorak Technique (left) raw T numbers and (right) CI numbers for the 2001-2010 North Atlantic major hurricanes that were investigated. The colored curved lines indicated various confidence levels in the analyses (i.e. power values at or above these curves are statistically significant at the respective confidence levels).

4. Investigating the TC Diurnal Cycle Using a Hurricane Nature Run Simulation

4.1 Introduction

Previous studies have documented diurnal variability of tropical oceanic convection (e.g. Gray and Jacobson 1977, Mapes and Houze 1993, Liu and Moncrieff 1998, and Yang and Slingo 2001) and the tropical cyclone (TC) upper-level cirrus canopy (e.g. Weikmann et al. 1977, Browner et al. 1977, and Kossin 2002). Chapter 3 (see also Dunion et al. 2014) examined the TCDC from a satellite perspective and found cyclical pulses in the satellite infrared cloud field that propagate radially outward from mature TCs. These diurnal pulses begin forming in the storm's inner core near the time of sunset each day and continue to move away from the storm overnight, reaching areas several hundred kilometers from the circulation center by the following afternoon. A 24-h conceptual clock was also presented that describes the TCDC evolution and predicts the approximate arrival time (LST) of TC diurnal pulses at various radii from the storm center each day. This conceptual clock has utility for identifying the position and evolution of TC diurnal pulses in observational datasets and numerical simulations and could also be useful for monitoring the TCDC in operational forecasting environments.

The main goal of this chapter is to examine an idealized hurricane nature run (NRH1) described in Sec. 2.1.2 and in Nolan et al. (2013) to look for signals of the TCDC in the model, characterize these signals in time and space, and investigate possible mechanisms associated with the evolution of this phenomenon. Using criteria described in Sec. 2.2.2, a select period of the nature run is examined when the simulated hurricane was intense, in a low vertical wind shear environment, and sufficiently far from land. When analyses are constrained by these conditions, marked diurnal signals in radiation, thermodynamics, static stability, winds, and

precipitation become evident in the model. Since the TCDC is a diurnal phenomenon, this chapter will begin with a focus on radiation in the NRH1 environment and will include analyses of outgoing longwave radiation (OLR), as well as shortwave, longwave, and total radiation tendencies. Discussion will then shift to include analyses of thermodynamics, static stability, surface pressure, winds, and finally precipitation. There are 3 aspects of the TCDC that are addressed by these discussions: 1) *detection of the TCDC and radially propagating TC diurnal pulses* (i.e. does the NRH1 detect TCDC signals that were described and hypothesized in Chapter 3?); 2) *priming of the TC environment* (i.e. are there diurnally varying aspects of the TC inner core and surrounding environment that promote the occurrence of convectively active, radially propagating TC diurnal pulses?); and 3) *triggering mechanism that leads to the initiation of the TCDC and TC diurnal pulses* (i.e. what processes in the TC environment can trigger the initiation of the TCDC and TC diurnal pulses?). The findings in this chapter confirm the satellite-based TCDC findings discussed in Chapter 3 and have implications for numerical modeling of TCs and furthering our understanding of how the TCDC (and associated diurnal pulses) forms, evolves, and possibly impacts TC structure and intensity.

4.2 Radiation

4.2.1 Outgoing Longwave Radiation (OLR)

OLR represents the total longwave infrared energy radiating from the Earth to space and is affected by the Earth's surface temperature and emissivity, atmospheric temperature, water vapor profile, and cloud cover. It is expected that OLR should correlate highly with the findings in Chapter 3 and in Dunion et al. (2014) that used the 10.7 and 10.8 μm channels on the GOES and Meteosat satellites to detect the TCDC and associated diurnal pulses propagating away from

the storm. Figure 4.1 shows a Hovmoller of OLR for the first 10 days of the life cycle of NRH1 before it began to recurve into the mid-latitudes and weaken below the category 2 TCDC analysis threshold described in Sec. 2.2.1. This figure reveals a marked diurnal oscillation in the OLR pattern that becomes established at a radius (r) range of ~150-450 km beginning on day 5 (03 Aug) and continues through day 10 (08 Aug), the only period in the NRH1 when all three TCDC criteria described in Sec. 2.2.2 are satisfied. This figure also suggests that the OLR signal appears to propagate away from the storm each day. Figure 4.1 includes the same OLR Hovmoller for only the 5-day study period (03-08 Aug) and emphasizes the diurnal fluctuations in OLR, especially at R=150+ km from the storm center. Diurnal fluctuations of ±20-60 W m^{-2} are evident at R=150-250 km, while larger fluctuations of ±45-70 W m^{-2} occur at R=350-450 km (Figs. 4.1 and 4.2). These fluctuations indicate that a distinct radially propagating OLR diurnal cycle signal is evident in NRH1 with R=150-450 km OLR maxima from ~0000-0600 UTC (~2000-0200 LST) and OLR minima from ~1400-2000 UTC (~1000-1600 LST) each day. The diurnal timing of these longwave infrared peaks and troughs and radial propagation speed (5-10 m s^{-1}) is very similar to the TCDC described in Chapter 3 and by Dunion et al (2014). Given the location of NRH1 over the ocean throughout the simulation, this diurnal infrared radiation signal is likely arising through a combination of variations in atmospheric temperature, moisture, and cloud cover. Several of the sections that follow include detailed analyses of these various components of OLR.

4.2.2 Shortwave, Longwave, and Total Radiation

Since the TCDC is a diurnal phenomenon that has been linked to the solar cycle (see Secs. 3.2 and 3.7), analyses were made of shortwave, longwave, and total radiation tendency for

the NRH1 domain from 03-08 August at 200, 700, and 925 hPa (Fig. 4.3). Not surprisingly, the shortwave tendencies show regular oscillations of net warming that are associated with the daily solar cycle and influenced by the 3-dimensional distribution of clouds in the storm. For example, near the outflow layer (~200 hPa), maximum daytime warming takes place from R~50-300 km due to the presence of cirrus clouds (i.e. elevated ice mixing ratio; Fig. 4.4). There is also little warming inside of R~50 km due to the relatively cirrus-free eye region of the storm and a general trend for reduced peak warming with increasing radii (outside of the eye; R~>50 km), which is due to the presence of generally less optically thick clouds with increasing radius from the storm, as suggested by Fig. 4.4. Although shortwave warming (~0.3-1.0 K h^{-1}) occurs near the top of the TC (e.g. 200 hPa) from R~25-450 km, lower to middle levels (e.g. 700 and 925 hPa) experience near zero shortwave warming during the day from just outside the eye to R~150-250 km where ice mixing ratio suggests the presence of a diurnally varying and optically thicker (presumed from analyses of OLR (Fig. 4.1) and ice mixing ratio (Fig. 4.4)) cirrus outflow layer each afternoon that would act to block incoming shortwave radiation (Figs. 4.4 and 4.5).

Although longwave infrared tendencies are generally producing a net cooling in the upper levels across the NRH1 domain, there are preferred times of day when the cooling rate appears to be more pronounced. At 200 hPa, peak longwave cooling occurs in the daytime, reaches a minimum at night, and is correlated with higher values of ice mixing ratio (Fig. 4.5). Although the cloud-free atmosphere is relatively transparent to longwave IR radiation emitted from the Earth, the TC cirrus outflow layer becomes increasingly efficient at absorbing this longwave radiation as these daytime radial surges of high cirrus occur and the layer becomes optically thicker. As indicated by the Stefan-Boltzman Law,,

$$E = \sigma T^4 \qquad (1)$$

, where E is the total energy radiated per unit surface are of a black body across all wavelengths per unit time, σ is Stefan–Boltzman constant (5.670373 x 10^{-8} W m^{-2} K^{-4}), and T is the blackbody's thermodynamic temperature, the energy emitted by an object is proportional to the fourth power of its temperature. In NRH1 simulation, the longwave IR energy that is absorbed by the cirrus outflow layer is re-emitted both back to the Earth and to the top of the atmosphere and because these cirrus clouds are high (e.g. ~300-150 hPa or ~9.5-14 km), and therefore cold, the longwave energy that they radiate to the top of the atmosphere is lower than it would be in the absence of cloud or in an optically thinner layer of cloud. Figure 4.4 indicates that in the late morning/early afternoon, the radial extent of the TC cirrus canopy is greater and contains ice mixing ratio values from z~6-15 km that are a factor of 2-10 times higher than they are in the evening. The optically thicker surges of cirrus clouds from the late morning to early afternoon could explain the daytime peak longwave cooling patterns seen in the upper levels each day (Figs. 4.4 and 4.5).

It is also possible that rapid cooling at the level of the cirrus outflow layer near and after sunset each day could promote conditions that are conducive for trapping gravity waves that emanate from the TC inner core (e.g. Metcalf 1975 and Crook 1988). Although the resolution of the NRH1 simulation that was used (9 km nested grid; see Sec. 2.1.2) may be inadequate to completely resolve gravity waves in the simulated TC (e.g. perturbations in fields of potential temperature and vertical winds), the feature described in the NRH1 vertical wind analyses in Sec. 4.4.4 is noteworthy. This feature is seen as a large, radially propagating, and relatively narrow ring of enhanced vertical wind that has a highly circular in shape.

Total radiation tendencies at 200 hPa suggest that there is a net warming at this level a few hours after 12 UTC each day (approximately local noon) that decreases radially outward

from values of 0.4-0.8 K hr^{-1} at R~50-100 km, to more modest heating rates of 0-0.3 K hr^{-1} from R~150-250 km, to generally no net heating beyond R=250 km (Fig. 4.3). These periods of warming are periodically interrupted by episodes of 0.1-0.8 K hr^{-1} net cooling just before 00 UTC (approximately local sunset) each day and are driven by longwave cooling coupled with an absence of any shortwave warming to balance that cooling. The areal extend of 0.2-0.8 K hr^{-1} nighttime net cooling radially expands from R~50-300 km from 03-04 Aug to R~50-450 km from 06-08 Aug (Fig. 4.3) and may be related to the fact that the NRH1 is generally intensifying over that period (Fig. 2.1). This appears to be linked to the longwave cooling pattern seen at 200 hPa (Figs. 4.2 and 4.3), where areas of cooling expand radially each day and are preferentially occurring in areas of high ice content in the outflow layer (Figs. 4.3 and 4.4). Although this may not be surprising, since the cirrus canopy radiationally cools more at night and less during the day than surrounding cloud-free regions (Gray and Jacobson 1977), there are some notable patterns in the radiation tendencies. First, the maximum net cooling is occurring at night and its signal does not appear to be propagating radially. This suggests that although the longwave radiation tendency is important highly correlated with the OLR signal), the lack of incoming solar radiation may be dominating patterns seen in total radiation tendency and masking any signs of propagation. However, at 200, 700, and 925 hPa, the peak in net radiational cooling at night is reaching farther and farther radially outward each day because the peak diurnal pulse signal at 200 hPa (i.e. more outflow layer cirrus) each afternoon is followed by alternating periods of reduced cirrus in the early evening until the hours leading up to sunrise (Figs. 4.4 and 4.5). The trends of total radiation tendency suggest that upper-level (e.g. 200 hPa) cooling peaks at night and tends to occur farther from the storm over time. However, these peaks in cooling are

consistently located at R~≥100 km and could represent areas where upper-level static stability is preferentially reduced (see Sec. 4.4.3).

Variations in mid-level (e.g. 700 hPa) total radiation tendencies are being driven by complex patterns of shortwave and longwave radiation and exhibit strong radial variability (Fig. 4.3). Net nighttime radiational cooling in the middle levels seems to preferentially occur at two radius ranges: the region of and just outside the relatively cloud-free eye (R~≤50-100 km) where short wave and longwave tendencies influence the total radiation tendencies and R≥200-250 km where shortwave tendencies dominate the total radiation variability. Net nighttime cooling at both radius ranges appear to steadily expand radially outward over the 5-day study period. Additionally, from R~100-200 km, the middle levels experience near-zero radiation tendencies during the day and only very modest cooling (~0.01-0.02 K h^{-1}) at night. These patterns of middle level radiation suggest that lapse rate tendencies are near-neutral (i.e. net zero tendency) throughout the day and that any forcing (e.g. sub-layer warming) that occurs in this radius range may be triggered from below and/or above. These hypothesized middle level patterns in radiation will be discussed further at the end of this section and in Sec. 4.4.3.

Radiation variations at lower levels (e.g. 925 hPa) suggest similar trends to the middle level and are also influenced by a combination of complex shortwave and longwave radiation patterns (Fig. 4.3). However, unlike the middle levels, there is an area of modest (up to 0.1 K h^{-1}) lower level longwave and total radiation warming confined to the region of R~50-150 km just outside the TC inner core. Here, the lower levels warm continuously throughout the study period and tend to exhibit peak warming in the afternoon hours, perhaps indicating that because the inner core region of the storm (i.e.. R≤150 km) tends to be relatively optically thicker than the periphery (i.e.. R>150 km), it is able to trap more of the Earth's emitted longwave radiation.

These trends in low-level radiation suggest that constant warming in this R~50-150 km region of the storm supports instability throughout the day that is most pronounced during the afternoon hours. Beyond R~150 km, patterns in lower level net radiation tendencies are influenced by a combination of shortwave and longwave radiation. However, longwave cooling is dominant in this outer region of the storm and net cooling is occurring over that entire portion of this domain, suggesting that this relatively optically thinner region of the storm is less effectively trapping the Earth's emitted longwave radiation.

The 06 to 07 Aug radius-height cross-sections of radiation tendency shown in Figs. 4.6-4.8 summarize the various aforementioned aspects of the NRH1 3-dimensional radiation profiles and emphasize radiative processes of the background TC environment that may be priming the environment to support TCDC and TC diurnal pulses. This figure includes 2 elevated regions, A and B, that extend from 3-13 km in the vertical and span from R=50-200 km and R=200-400 km in the horizontal respectively. The vertical extent of the 2 regions was chosen to 1) capture the lower extent of persistent warming that occurs throughout the day from R~50-450 km; and 2) capture the extreme upper and lower bounds of the level of neutral buoyancy (LNB) that were found in the NRH1 (describe in Sec. 4.4.3). The horizontal extent of these 2 regions were selected to 1) highlight the regions of the TC inner core (R≤150-200 km) versus the surrounding environment (R~200-450 km); and 2) capture a persistent layer of net warming from R~50-200 km that may be acting to stabilize the inner core and near-inner region of the TC. Regions A and B may represent key areas of the storm where radiation tendencies can lead to marked diurnal fluctuations in static stability (e.g. the LNB and convective available potential energy (CAPE)) and are discussed further in Sec. 4.4.3. While region A corresponds to the approximate radius range of TC diurnal pulse initiation that was noted by in Chapter 3 and in Dunion et al. 2014,

both regions experience patterns of net radiation tendencies that may be important for TCDC processes. For the Figs. 4.6-4.8 plots, nighttime will refer to 2100-0300 LST, dawn is 0600 LST, daytime is 0900-1500 LST, and dusk is 1800 LST. Specific conclusions related to the analyses of radiation in the NRH1 include:

1. Shortwave warming during the daytime and longwave cooling at night are preferentially occurring in the area of the radially descending cirrus outflow layer (i.e. areas of enhanced ice mixing ratio, Fig. 4.4.). The lowering of the TC outflow layer with increasing radius causes relatively more shortwave warming and longwave cooling to occur in region B than in region A.
2. During the day, shortwave warming is greater than opposing longwave cooling in the upper few kilometers of regions A and B (z~10-13 km) and could be a time when the LNB lowers and CAPE is reduced. This may be a key process influencing the daytime evolution of the TCDC and will be discussed more Sec. 4.3.3.
3. During the nighttime, longwave cooling dominates the upper few kilometers of regions A and B (z~8-13 km) and could be a time when the LNB rises and CAPE increases. This may be a key process influencing the nighttime evolution of the TCDC and will be discussed more Sec. 4.3.3.
4. Region A has a layer of persistent net warming (~0.1-0.3 K hr^{-1}) from z~4-6 km that occurs all day, with slightly more warming during the daytime. This warming is occurring just above the melting level and is coincident with the base of the elevated ice mixing ratio shown in Fig. 4.4 (>0.02 g kg^{-1}). This region of high ice content is likely absorbing longwave IR radiation being emitted from the Earth's surface and could be

acting to consistently lower the LNB and reduce CAPE in this area within and just outside the TC inner core.

5. Region B also exhibits a layer of lower level net warming (~0.1-0.4 K hr^{-1}) that persists throughout the day, but unlike the layer in region A, this layer slopes upward with radius from z~4-6 km at R=200 km to z~7-11 km at R=450 km and appears to be linked to the upward sloping anvil cloud base that is evident in the Fig. 4.4 cross-sections. Similar to region A, the elevated ice mixing ratio in this layer is associated with enhanced longwave IR absorption throughout the day and has a total radiation tendency that is coolest (warmest) around local midnight (early to late afternoon). The time of peak cooling and warming likely represent times with elevated LNBs and increased CAPE and lower LNBs and decreased CAPE respectively and will be discussed further in Sec. 4.3.3.

The aforementioned conclusions related radiation tendencies, particularly those in regions A and B in Figs. 4.6-4.8, suggest that the inner 400 km of the NRH1 experiences marked diurnal fluctuations in radiation tendencies that are more pronounced at larger radii (e.g. in region B). These diurnal fluctuations could generate reduced static stability (i.e. a lower LNB and reduced CAPE) in the storm environment that peak from around dusk until dawn and will be discussed further in Sec. 4.4.3. Strikingly similar radiation tendencies to those shown in Figs. 4.6-4.8 were noted throughout the 03-08 Aug study period, suggesting that the 3-dimensional variability of shortwave, longwave, and total radiation tendencies may create an environment each day that primes, or pre-conditions, the TC environment to support the TCDC and associated radially propagating diurnal pulses that have been previously documented. This priming is accomplished via cooling of the middle to upper level environmental profile that would act to destabilize environment. The radiation tendencies shown here (i.e. negative radiation tendencies that are

favored at R≥150-200 km (radially outside of region A)) may also help explain why the TCDC seen in both satellite imagery (e.g. Chapter 3 and Dunion et al. 2014) and in the NRH1 appear to begin each day near R~150-200 km. The TCDC may either be undetectable or simply not originating from the TC inner core region (e.g. R ~ ≤150 km; Rogers et al. 2012). Instead, diurnal radiation tendencies in mature TCs may come together in such a way to preferentially trigger convection in this region of the storm each night near and after the time of local sunset. This will be explored further in Sec. 4.3.3's analyses of static stability

4.3 Thermodynamics and Stability

4.3.1 Potential Temperature

Analyses of NRH1 potential temperature (θ) were conducted to search for signs of the TCDC in the simulated TC's thermodynamic fields. These analyses reveal distinct diurnal signals at various atmospheric levels (e.g. 200, 700, and 925 hPa, and the near-surface) and radii. At upper levels (e.g. 200 hPa), there is no robust diurnal signal in the inner 150 km of the storm. However, there is a distinct diurnal θ pattern just outside of 150 km with maxima around local noon and minima around local midnight (Figs. 4.9 and 4.10). The θ patterns in this region of the storm correspond to the outer edge of the TC inner core, are correlated with upper level shortwave and total radiation tendencies, and are negatively correlated with longwave radiation tendencies (Fig. 4.3). These diurnal θ patterns also appear to be propagating radially away from the TC (Fig. 4.9) and are closely matched in time and space with OLR (Fig. 4.1) and ice mixing ratio (Fig. 4.4). This suggests that diurnal variability at the level of the TC cirrus canopy is driving the upper-level θ patterns at R~150-450 km. Values of θ at upper levels begin cooling each afternoon and reach a minimum around local midnight, which implies that this region of the

storm experiences regular occurrences of destabilization via cooling of the environmental profile in the upper-levels (e.g. an elevated LNB and higher CAPE) from the late afternoon into the evening, which could help promote convection locally (Figs. 4.9 and 4.10).

The middle levels (e.g. 700 hPa) of the NRH1 TC do not exhibit robust diurnal θ fluctuations in the inner 300 km of the storm (Figs. 4.9 and 4.10). There is a modest diurnal signal from R~300-450 km with peak warming (cooling) in the evening to local midnight (pre-dawn hours) and θ fluctuations of ~0.5-1 K.

Diurnal θ patterns are quite evident in the lower levels (e.g. 925 hPa and 40 m) of the NRH1 TC environment, particularly from day 2-5 (05-08 Aug, Figs. 4.9 and 4.10). At 925 hPa and especially 40 m, the diurnal θ signals appear to be propagating away from the storm each afternoon. The 40-m near-surface diurnal fluctuations range from ~0.5-1.5 K and suggest that some kind of outflow boundary that is bringing cooler air to the surface may be propagating away from the storm from the late morning to afternoon each day and occur within 6 hours of corresponding temperature minima in the upper levels (e.g. 200 hPa).

4.3.2 Moisture (mixing ratio)

In order to examine how the TCDC might be affecting the moisture field of the simulated TC and to identify possible signals related to diurnal moisture variability in the storm, mixing ratio is examined. The NRH1 TC exhibits distinct diurnal signals in mixing ratio at all levels (Figs. 4.11 and 4.12). At upper levels (e.g. 200 hPa), these oscillations are most pronounced from R=150-450 km, peak around local noon at inner radii, and appear to slowly propagate away from the storm during the afternoon. Variations in 200 hPa mixing ratio showed a distinct diurnal

pattern that is similar to previously shown patterns of OLR and potential temperature, suggesting that the TCDC signal is characterized by marked changes in both temperature and moisture.

At middle levels of the NRH1 (e.g. 700 hPa), there is a less defined pattern of diurnal mixing ratio throughout the domain (Figs. 4.11 and 4.12). However, at R=150-300 km, there are prominent middle level diurnal peaks in mixing ratio that occur in the late evening through early morning hours each day. These maxima are regularly interspersed by ebbs in mixing ratio that occur in the middle to late afternoon, are 0.5-2.5 g kg^{-1} dryer, and appear to be anti-correlated in time with the upper level values (e.g. 200 hPa).

The lower levels (e.g. 925 hPa and 40-m) show a robust TCDC of mixing ratio that tends to be at a minimum in the late morning to late afternoon hours and are most evident from R~100-300 km (Figs. 4.11 and 4.12). These minima are regularly interspersed by periods of mixing ratio peaks that are significantly moister (~0.5-2.5 g kg^{-1}). Interestingly, the pattern of mixing ratio minima appear to be more pronounced than the maxima and exhibit signs of radial propagation that is particularly pronounced from R=150-350 km. Dunion et al. (2014) noted that large outflow boundaries denoted by arc clouds that are hundreds of kilometers in length tend to form along the leading edge of TC diurnal pulses. These outflow boundaries are associated with convectively-driven downdrafts that originate in the lower to middle levels (e.g. 600-800 hPa) and bring relatively cool, dry air down to the near-surface. Although analyses of θ do not show discernable signatures of convectively-driven downdrafts, radius-height analyses of the NRH1 (shown in Sec. 4.5.2) indicate that diurnal signals of depressed mixing ratio are evident from ~4 km to the surface and are approximately timed to the TC diurnal pulses described in Chapter 3 and by Dunion et al. (2014). This suggests that the diurnal mixing ratio patterns evident in the lower to middle levels of the NRH1 may, in fact, be linked to a squall line feature with outflow

boundaries that propagate away from the NRH1 storm each day and will be discussed more in Secs. 4.4.4 and 4.5.3.

4.3.3 The LNB and Convective Available Potential Energy

CAPE is defined as the amount of energy a parcel of air would have if lifted a certain distance vertically through the atmosphere up to the LNB. Calculations of CAPE in this study assume that a surface parcel is represented by the mean temperature and moisture in the lowest 500 m of each sounding profile that was computed across the NRH1 domain and include irreversible moist-adiabatic processes. CAPE exhibits a distinct TCDC pattern and similar to other parameters that have been previously discussed, a diurnal CAPE signal is evident throughout the study period, and is especially pronounced from 05-08 Aug (Figs. 4.13 and 4.12). CAPE displays TCDC signals that are most pronounced from R~150-300 km, has maximum values in the early morning hours between approximately local midnight and 0900 LST, minimum values from the late morning to late afternoon, and consistently low values (~0-500 J kg^{-1}) inside of R~150 km (Figs. 4.13 and 4.14. Diurnal variations in radiation tendency at critical levels appear to be impacting the environmental temperature profile and resulting LNB. The TCDC signals in CAPE in Figs. 4.13 and 4.14 appear to be in phase with the patterns of middle to upper-level (z~4-10 km) total radiation tendencies discussed in Sec. 4.2.2 and shown in Figs. 4.3 and 4.6-4.8. Maxima in CAPE tend to occur during and shortly after periods of overnight net cooling, while minima occur during and shortly after periods of daytime net heating, suggesting that radiation tendencies in the middle to upper-levels are an important control on diurnal fluctuations of CAPE. It was hypothesized in Sec. 4.2.2 that varying radiation tendencies at various radii from R=50-400 km may have important implications on the LNB and

hence CAPE in the NRH1 environment. Several hypotheses related to the LNB and CAPE are presented and supported by the analyses shown in Figs. 4.13 and 4.14. Throughout the study period, the radius range of R~50-100 km has little to no CAPE (0-500 J kg^{-1}) and LNBs as low as 600-800 hPa that may be related to persistent warming that occurs in the layer from z~4-6 km during both the daytime and nighttime. The magnitude of this warming does fluctuate diurnally and appears to be contributing to the diurnal variability of CAPE (Figs. 4.13 and 4.14) and the LNB (Fig. 4.14). At radii of ~150-350 km, CAPE and the LNB fluctuate diurnally by as much as 1500 J kg^{-1} and 450 hPa respectively and are remarkably in phase throughout the day. As the LNB pressure level increases (decreases), corresponding CAPE values decrease (increase).

Figure 4.15 shows the 3-hourly progression of CAPE in the NRH1 inner core and surrounding environment from 06 Aug 0200 LST to 07 Aug 0200 LST. In the early morning of 06 Aug (0200-0500 LST), a fairly symmetric region of very low CAPE values (~0-500 J kg^{-1}) exists in the inner ~150-200 km of the storm and is immediately surrounded by areas of higher CAPE (~1500-3000 J kg^{-1}) that extend out to the edges of the NRH1 domain. This annulus of inner core low CAPE begins to radially expand near the time of sunrise (~0530 LST) and continues to grow through the early to late afternoon, eventually reaching R~300-400 km. The expanding area of low CAPE during the daytime also concurs with the Fig. 4.6 depiction of marked daytime (nighttime) radiational warming (cooling) in the middle to upper levels (z~6-12 km) and corresponding 0.5-3.5 K diurnal fluctuations in θ shown in Fig. 4.10. Periods of cooling would act to raise the LNB, reducing the total integrated area being used to calculate CAPE, hence, reducing local values of CAPE. Starting in the early evening near the time of local sunset (i.e. ~2000 LST), the low CAPE annulus begins to dissipate along its periphery and continues to wane into the late evening until around local midnight. By the early morning hours

the next day (07 Aug 0200 LST), the shrinking annulus of low CAPE appears to stabilize and once again extends to a radius of only ~150-200 km. Near and just outside this radius range, CAPE values increase from ~0-500 J kg^{-1} to as high as 2500 J kg^{-1} in just a few hours leading up to 0200 LST. This period of enhanced CAPE after sunset in the 150-200 km radius range could be related to the middle to upper level cooling noted in the corresponding areas of regions A and B of Fig. 4.6. The 0-0.5 K hr^{-1} cooling rates that were noted in this area just outside the inner core of the TC would promote reduced lapse rates and increased CAPE locally.

Around the time of local sunrise and through the afternoon to the time of sunset the following day, the annulus of low CAPE once again continues a cycle of radial expansion (not shown). A nearly identical sequence of a diurnally expanding and contracting annulus of low CAPE was also evident the day prior (05-06 Aug, not shown). It is hypothesized that radiational warming and cooling in the TC environment immediately surrounding the TC inner core (e.g. R=150-350 km) are producing striking fluctuations in the LNB each day. These variations in LNB are, in turn, driving diurnal fluctuations in CAPE that dramatically alter the static stability in the NRH1 TC environment and could be a trigger for the formation of diurnal pulses that have been previously discussed. Radiative warming and cooling associated with the TC cirrus canopy and radially sloping TC anvil are hypothesized to be a driving mechanism for the marked diurnal fluctuations in the LNB and CAPE that have been found could help prime the TC environment to support the development of convectively active TC diurnal pulses in the region of the storm just outside the inner core at R~150-300 km).

4.4 Pressure and Wind

4.4.1 Pressure and 10-m Wind

Analyses of pressure and 10-m surface winds in NRH1 were performed to assess the TCDC's relevance to TC intensity and structure forecasts and possible mechanisms for its formation. Surface pressure exhibits a semidiurnal signal (i.e. two daily maxima and minima) that is more easily detected with increasing radius from the storm. These fluctuations are likely related to the semidiurnal tide and are seen as ~1-2 hPa pressure oscillations that occur every ~5-7 hr (Figs. 4.16 and 4.17). Throughout the 03-08 Aug period of study, pressure is on an overall downward trend (i.e. the storm is intensifying), but this background signal of intensity change also includes the higher frequency semidiurnal tide signal. This makes it difficult to extract an obvious TCDC signal, particularly at radii ≥150 km. At all radii (and particularly at R=150 and 300 km), there does appear to be a tendency for relative minima in pressure in the early morning and again in the late afternoon to early evening and relative maxima in the late morning and again in the late evening local time (Fig. 4.17). Analyses of upper-level pressure (e.g. 150-300 hPa, not shown) showed similar trends to the analyses of surface pressure. There is a lack of diurnal surface or upper-level pressure signals in the NRH1 do not support the hypothesized TCDC mechanism discussed in Chapter 3: *cloud-cloud-free differential heating mechanism* (Sec. 3.6.3) and will be summarized in Sec. 4.6.

Surface winds show a clear diurnal signal at radii ranging from ≥50 km (Figs. 4.18 and 4.19). In the inner 200 km of the storm, surface winds tend to peak from the late evening to early morning hours and ebb from the afternoon to late evening. These wind speed oscillations range from ~0.5-2.5 m s^{-1} and tend to be larger with increasing radii. Although the radial and tangential components of the surface wind both exhibit diurnal fluctuations, radial wind has

particularly pronounced signals (Fig. 4.18), suggesting that the diurnal fluctuations of surface wind speed shown in Fig. 4.19 are largely attributable to ebbs and flows radial winds at the surface. These diurnal fluctuations appear to be most pronounced at R~150-350 km where diurnal oscillations in the magnitude of radial inflow are as high as 4-6 m s^{-1}. The tendency for surface wind diurnal oscillations to be more pronounced at larger radii has implications for TC structure (e.g. significant wind radii). This is particularly so for the radii of 34 and 50 kt winds, which in the North Atlantic, average ~155 and 85 km respectively (Demuth et al 2006).

The analyses of surface pressure in the NRH1 shows a clear signal of the semidiurnal tide that makes it difficult to discern any clear TCDC signals in these fields. However, analyses of 10-m surface winds show a strong diurnal signal with periods of stronger winds and more vigorous low-level inflow in the early morning hours that are interspersed with periods of weaker winds and reduced lower level inflow from the mid morning to early afternoon. These trends in surface wind suggest potential links between the TCDC and TC intensity and structure.

4.4.2 Radial Wind (Near Surface to Upper-Level)

Radial wind (V_r) tendencies in the NRH1 exhibit distinct diurnal patterns throughout the troposphere (Figs. 4.20 and 4.21). In the upper troposphere (e.g. 200 hPa), there appear to be daily bursts of outflow outside of ~100-150 km that develop in the early morning hours each day and steadily propagate away from the storm (at speeds similar to those described in Secs. 3.2.1 and 3.2.2), reaching R=450 km in the afternoon. These daily maxima in outflow steadily strengthen through the study period, are strongest from R~200-400 km, and have peak values of ~15-20 m s^{-1}. The 200 hPa radial outflow bursts are also regularly interrupted by outflow minima that peak from the late evening to early morning hours each day and are roughly a factor

of two weaker (Figs. 4.20 and 4.21). These surges in V_r are coincident in time with the diurnal patterns shown in OLR (Fig. 4.1), as well as 200 hPa ice mixing ratio, θ, and mixing ratio, suggesting that TC diurnal pulses are associated with marked upper-level signals in both thermodynamics and kinematics. Although there does not appear to be a robust upper-level diurnal signal in radial winds inside of ~150 km, diurnal outflow variability beyond this radius is marked and may have important implications for TC intensity and structure.

In the middle levels of the atmosphere (e.g. 700 hPa), there is a distinct diurnal pattern of enhanced inflow (2-5 m s^{-1}) each day that peak in the early morning and are concentrated at R=150-300 km (Figs. 4.20 and 4.21). These inflow surges occur prior to and radially inward of the 200 hPa outflow bursts that were previously discussed and are interspersed by periods of weak or even near-zero inflow that peak from the late evening to early morning hours each day. Finally, on the inside edge of these inflow bursts (R~25-150 km) there are areas of outflow ranging from 0.5-3 m s^{-1}. The diurnal patterns of inflow and outflow suggest that there are favored times of day (approximately midnight to 0600 LST) when local middle level convergence is maximized and could represent times when the TC is more susceptible to middle level ventilation (i.e. the flux of cooler, drier middle level air into a TC; Tang and Emanuel 2012).

At the lower levels, diurnal tendencies of V_r are evident from R=100-450 km (Figs. 4.20 and 4.21). Peak inflow (~12-18 m s^{-1}) tend to occur in the late evening to early morning hours and are interrupted by periods of relatively weaker inflow (5-12 m s^{-1}) that reach a minimum from the late morning to afternoon hours. These peaks and ebbs in low-level V_r appear to propagate away from the storm each day and the flow patterns suggest that TC inflow and surface fluxes (not shown) are maximized just before and after local midnight from R=100-200

km and peak at larger radii (200+ km) in the early to late morning. It should be noted that diurnal peaks in low-level inflow coincide with peaks in low-level moisture that were discussed in Sec. 4.3 and shown in Fig. 4.9.

Interestingly, the phasing of maximum near-surface inflow and maximum upper-level outflow are slightly offset in time (Figs. 4.20 and 4.21). The maximum near-surface inflow occur in the late evening to early morning hours, while the peak upper-level outflow tend to occur in the mid-morning to late afternoon. This temporal offset of several hours suggests that surges in low-level inflow proceed/follow surges in upper level outflow and that the mechanism(s) driving the TCDC do not initiate radial flow simultaneously throughout the depth of the storm. Perhaps radiative effects initiate enhanced outflow near the level of the outflow layer each day and there is a lag between this onset and the onset of enhanced radial inflow.

4.4.3 Tangential Wind (Near Surface to Upper-Level)

Tangential winds (V_t) in the NRH1 exhibit marked diurnal signals throughout the troposphere and are most pronounced in the upper levels (e.g. 200 hPa). Figure 4.22 shows the occurrence of episodic oscillations in upper-level V_t that are particularly apparent from R=150-450 km. Peaks in upper-level V_t occur in the middle to late afternoon at R=300 km (Fig. 4.22 and 4.23) and in the late afternoon to early evening at R=450 km and similar to radial wind, V_t peaks are regularly interrupted by lulls that are a factor of 1.5-5 times weaker at radii ranging from 200-450 km.

The middle levels (e.g. 700 hPa) of the NRH1 show a relatively more muted V_t diurnal signal that is more pronounced at larger radii (Fig. 4.22). Figure 4.23 shows these subtle diurnal oscillations with maxima that occur in the early to middle afternoon and minima around local

midnight. Lower level (e.g. 925 hPa and 40 m) diurnal fluctuations in V_t, although not as pronounced as at upper levels, are clearly evident from R=150-450 km and are particularly robust at R=300 km (Figs. 4.22 and 4.23). Here, peak values of V_t tend to occur in the late morning to early afternoon and reach a minimum in the evening, propagating at speeds similar to those described in Secs. 3.2.1 and 3.2.2. These analyses suggest that there are favored times of day for maximum and minimum values in the magnitude of V_t in the upper, middle, and lower levels of the NRH1 TC.

4.4.4 Vertical Wind

Vertical wind (w) in the NRH1 shows a distinct diurnal pattern that appears to propagate away from the storm each day at speeds similar to previously discussed variables (Fig. 4.24). At upper levels (e.g. 200 hPa), peaks in w appear at R=150-200 km in the late morning and propagate to peripheral radii through the early to late afternoon. Maxima in w range from ~0.1-0.5 m s^{-1}, while interspersed minima reach magnitudes close to zero and are occasionally even negative (Figs. 4.24 and 4.25). Although the diurnal signal of w is evident at R~150-450 km, Figs. 4.24 and 4.25 show that the magnitudes of the peaks are highest at closer radii and lower with increasing radius from the storm.

Diurnal signals of w in the lower to middle levels are less defined than in the upper levels (Figs. 4.24 and 4.25). However, 2-dimensional map analyses of w throughout the study period indicate that this parameter marks the position of the diurnal pulses quite clearly and is seen as a narrow (~10-20 km wide) ring of enhanced w that radially propagates away from the storm and has a s line-like appearance (Fig. 4.26). The relatively limited radial width of this feature coupled with slight azimuthal asymmetries in the NRH1 diurnal pulse signal (i.e. enhanced w)

appear to be somewhat muting the *w* signal when it is azimuthally averaged (e.g. Figs. 4.24 and 4.25). Fig. 4.26 shows a 6-hourly progression of a diurnal pulse on 06 Aug from 0600 UTC (0200 LST) to 1800 UTC (1400 LST) and shows a semi-circular signal in *w* that is propagating away from the storm each day, reaches R~300 km in the afternoon, and is evident through a deep layer of the troposphere from 150-925 hPa (not shown). This figure suggests that diurnal pulses are associated with distinct peaks in *w* with updrafts that range from ~1-3 m s^{-1} and trailing 0.5-2 m s^{-1} downdrafts that appear to be favored behind the diurnal pulse. The couplets of highly symmetric updrafts and downdrafts suggest that these diurnal pulses may be a squall line feature or gravity wave moving/propagating away from the storm each day. The timing of these propagating diurnal pulse signals in *w* also correspond well with the TCDC clock presented in Chapter 3 and by Dunion et al. (2014). Similar analyses made on 04, 05, and 07 Aug (not shown) indicate a nearly identical diurnal pulse signature in *w* that is highly symmetric and is also propagating away from the storm. Analyses of *w* support the following hypothesized TCDC mechanisms discussed in Chapter 3: *convectively-driven atmospheric gravity waves* (Sec. 3.6.1) and seeder-feeder mechanism (Sec. 3.6.5) and will be summarized in Sec. 4.6.

4.5 Precipitation

4.5.1 Rain Rate

Rain rate shows a distinct TCDC pattern and is especially evident from R=100-300 km (Figs. 4.27 and 4.28). Similar to analyses of temperature, moisture, and winds, radially propagating signals in rain rate can be seen throughout the study period, but are particularly robust from 05-08 Aug (Fig. 4.27 and 4.28). Peaks occur in the late evening to early morning hours in the inner core (e.g. R=100-150 km) and in the early to late morning farther from the

storm (e.g. R=200-250 km, Fig. 4.28). Conversely, rain rate minima occur in the late morning to middle afternoon at R=100-150 km and in the late afternoon to late evening at R=200-250 km. These patterns in rain rate suggest that the TCDC may have important implications for quantitative precipitation forecasting and TC structure.

4.5.2 Simulated Radar Reflectivity

Analyses of simulated radar reflectivity show a robust propagating diurnal signal that extends throughout the troposphere (Fig. 4.29). Diurnal oscillations in this parameter range from ~10-30 dBZ and are especially evident from R=100-300 km (Figs. 4.29 and 4.30). Not surprisingly, these patterns of reflectivity closely resemble those of rain rate and given the diurnal signal of reflectivity, it is plausible that aircraft equipped with radar (e.g. C-band or Doppler) could be used to track the evolution of the TCDC in the future and is further discussed in Chapter 6. Additionally, given the common practice of empirically estimating rainfall from land-based radar, the TCDC could be an important consideration regarding the analysis of quantitative precipitation forecasts for landfalling TCs.

4.5.3 Q-Condensate

Figure 4.31 shows NRH1 azimuth-radius analyses of Q-condensate and vertical wind during the most pronounced day of diurnal reflectivity fluctuations (06 Aug). This figure suggests that an area of enhanced moisture and vertical winds forms outside the eyewall (R~75-150 km) around local midnight that day. This feature appears to be elevated above the surface, has a vertical extent of ~2-14 km, and clearly propagates away from the storm throughout the day, reaching radii of approximately 200, 250, and 300 km at 0600, 1200, and 1800 LST

respectively. This region of enhanced moisture and vertical winds may, in fact, be linked to a diurnal pulse that is propagating away from the storm and during the afternoon, becomes coupled with a trailing downdraft and area of suppressed low-level moisture. This area behind the diurnal pulse extends from the surface to ~ 3 km and may be the signature of a cold pool. In fact, the entire propagating feature (TC diurnal pulse and cold pool) looks remarkably similar to a squall line. If TC diurnal pulses do indeed behave like squall line features that propagate away from the storm each day, some kind of common lifting mechanism, such as a gravity wave, frontal feature, or outflow boundary is suggested. Also, since squall lines develop in regions of optimal moisture, stability, and lift, it is possible that the priming of the environment just outside the inner core (R~150-350 km) during the nighttime that was discussed in Sec. 4.4.3 (i.e. elevated LNB and enhanced CAPE) could support the existence of a convectively active, long lived (several hours) squall line feature. Finally, squall lines sustain themselves by producing their own lift via outflow boundaries. Dunion et al. 2014 noted that arc clouds (i.e. outflow boundaries) often appear to form along the leading edges of TC diurnal pulses, which further supports this idea that TC diurnal pulses associated with the TCDC behave like squall lines. These ideas will be explored more in Chapter 6's discussion of 2014 Hurricane Edoaurd. Whatever this feature is, it repeats over multiple days of the NRH1 study period and appears to have origins in a deep (but elevated) layer at radii where radiation tendencies support reduced static stability near and after sunset each day. The TCDC conceptual clock (Fig. 3.10) also suggests that as this feature propagates away from the storm during the early to late morning, it is located at R~200-300 km. Analyses of the LNB (Sec. 4.3.3, Fig. 4.14) indicate that this timing coincides with diurnal minima in LNB heights (z~500-600 hPa) in this region of the peripheral TC environment, which could act to limit its vertical extent as it propagates away from the storm.

Although the exact mechanism causing the diurnal features described above is not clear, their regular diurnal occurrence does suggest that radiation tendencies that are being driven by the solar cycle may be a key controlling factor.

4.6 TCDC Mechanisms

Analyses of radiation, thermodynamics, kinematics, and precipitation in the NRH1 that were presented in Secs. 4.2-4.5 suggest a complex and dynamic background environment that varies throughout the day and also fluctuates greatly with radius and height. Several findings from this chapter can be linked to the TCDC mechanisms that were proposed in Chapter 3 (Sec. 3.6):

1. *Convectively-driven atmospheric gravity waves (Sec. 3.6.1)*: it was hypothesized in Chapter 3 that the combination of rapid cooling of the cirrus outflow layer and vertical wind shear associated with radial outflow in this layer could promote ducting of radially propagating gravity waves. NRH1 analyses show evidence of both of these key processes: radiation tendencies (Figs. 4.3, 4.6-4.8) reveal that the outflow layer experiences rapid cooling near the time of sunset and is focused in regions of cirrus cloud (Fig. 4.4). Additionally, after reaching a minimum in the middle to late evening, upper level radial outflow is influenced by the TCDC and rapidly increases in the late evening to early morning hours, eventually peaking in the mid-morning to afternoon. During this period, radial outflow becomes almost a factor of 2 stronger and would act to dramatically increase vertical wind shear across the outflow layer. In this scenario, the primed TC environment supports TC diurnal pulses that produce enhanced radial outflow and vertical wind shear in the storm. Analyses of w showed a radially propagating semi-

circular ring of enhanced vertical winds that was ~10-20 km wide and had a squall line-like appearance (Zipser 1977) that was also noted in cross sections of Q-condensate and *w* (Fig. 4.31). This feature was observable through a deep layer of the atmosphere (150-925 hPa) and for several hours and on multiple days as it propagated from just outside the TC inner core out to a radius of ~300 km. Unfortunately, gravity wave signatures in other parameters (i.e. perturbations in surface pressure, wind velocity, and temperature; Nappo 2013) were not identified in the NRH1. It is possible that the limited resolution of the NRH1 domain that was used in this study (9 km nested grid) may not have been adequate to resolve propagating gravity wave features in the NRH1 simulation or that a gravity wave feature simply did not exist in the simulation.

2. *Radiatively reduced outflow resistance (Sec. 3.6.2):* near the time of sunset (~1800 LST), shortwave warming in the middle to upper levels of the storm rapidly declines and longwave cooling begins to dominate the total radiation tendency signal (Figs. 4.6-4.8). From approximately dusk until dawn, the radius range from ~150-350 km in regions A and B in these figures experiences net cooling from z~8-12 km that could act to destabilize the NRH1 outflow layer, thereby reducing $d\theta/dz$ in that layer and hence reducing potential vorticity. This reduction in PV would lead to enhanced inertial available potential energy (IAKE), which would lead to a radial release in outflow (Sec. 3.6.2). The region of the NRH1 environment from R~200-400 km experiences a period of net cooling from z~10-13 km that spans from dusk until dawn, is most pronounced at around local midnight (0.1-0.7 K hr^{-1}), and could represent a period when static and hence, inertial stabilities are markedly reduced in this region of the storm. Indeed, 10-20 m s^{-1} surges in radial outflow at the level of the cirrus canopy were observed to peak in

the mid-morning to early afternoon R~150-450 km and lagged by several hours the nighttime net radiational cooling that was seen.

3. *Cloud-cloud-free differential heating mechanism (Sec. 3.6.3)*: this hypothesis relates to how the TC cirrus canopy radiationally cools more at night and less during the day compared to surrounding cloud-free regions. Indeed, shortwave warming and longwave radiational cooling in the upper-levels of the NRH1 TC were enhanced in areas of high ice mixing ratio (i.e. in regions of ice cloud). During the day, shortwave warming was greater than opposing longwave cooling in the upper few kilometers of regions A and B (~150-350 km) from z~10-12 km in Figs. 4.6-4.8 and was noted to be a time when the LNB lowered several hundred hPa and CAPE was reduced to 0-500 J kg^{-1} in this area of the storm. During the nighttime, longwave radiational cooling dominated the total radiation tendencies in the storm environment and the region of the NRH1 from R~200-400 km experienced a period of net cooling from z~10-12 km that spanned from dusk until dawn and was most pronounced at around local midnight (0.1-0.7 K hr^{-1}). During these periods, the LNB rose several hundred hPa, CAPE increased by a factor of 3-10 times, and upper-level radial outflow began to markedly ramp up at R~200-450 km. However, no definitive upper level pressure anomalies were detected in the NRH1 to further support the hypothesis that the aforementioned conditions were leading to enhanced upper-level divergence. However, analyses of surface and upper level pressure in the NRH1 did not reveal any notable diurnal signals in the model domain (R=0-450 km). This does not support the notion that temperature contrasts that arise from preferred shortwave warming of the TC outflow layer during the day and longwave cooling at night (relative to surrounding cloud-free environment) is impacting pressure surfaces at these

levels. It should be noted, however, that the extensive radial extent of the NRH1 cirrus canopy at all times of day (Fig. 4.4), suggests that the model domain may not be large enough to properly assess surface and/or upper level pressure perturbations that may exist in the simulation.

4. *Direct radiation-convection interactions (Sec. 3.6.4):* similar to the previously hypothesized mechanism, the shortwave radiational warming in the upper-levels of the NRH1 TC were enhanced in areas of high ice mixing ratio (i.e. in regions of ice cloud). During the day, shortwave warming was greater than opposing longwave cooling in the upper few kilometers of regions A and B (~150-350 km) from z~10-12 km in Figs. 4.6-4.8 and experienced net radiation warming of 0.2-0.8 K hr^{-1}. These daytime periods where also times when the LNB dropped several hundred hPa and CAPE decreased by a factor of 3-10 times to values of 0-500 J kg^{-1}. Interestingly, the lower to middle levels of the NRH1 (i.e. z~4-10 km) contained a 2-3 km thick layer of net radiational warming (0.1-0.4 K hr^{-1}) throughout the entire day that was located at z~5-6 km from R~50-200 km (Fig. 4.6). This layer of constant warming begins to slope radially upward from z~5-6 km at R=200 km to z~8-10 km at R=450 km, is almost entirely linked to longwave IR warming (i.e. there is almost no daytime shortwave warming from R~50-450 km in the z~5-10 km layer, Figs. 4.6-4.8), and is presumably linked to IR surface emissions that are being absorbed by the lower extent of the TC's cirrus anvil (Figs. 4.4 and 4.6-4.8). At night, longwave radiational cooling dominated the total radiation tendencies in the storm environment and the region of the NRH1 from R~200-400 km experienced a period of net cooling from z~10-12 km that spanned from dusk until dawn and was most pronounced at around local midnight (0.1-0.7 K hr^{-1}). During these periods, the LNB

rose several hundred hPa and CAPE increased by a factor of 3-10 times. Additionally, rain rate and simulated radar reflectivity tended to peak during this same evening to early morning timeframe, suggesting that enhanced convection was also occurring at this time. Peaks in upper-level radial outflow closely followed these periods of nighttime maxima in rain rate and simulated radar reflectivity and suggest that radiationally-driven instability at night leads to enhanced convection, which, in turn promotes enhanced upper level divergence in the NRH1.

5. *Seeder-feeder mechanism (Sec. 3.6.5)*: this hypothesized mechanism proposes that enhancement of precipitation in warm-frontal rainbands can result when ice particles from aloft fall into the layer below the -4^{o}C level and aggregate just above the melting level. These "seeder" ice crystals can subsequently, as they descend, help convert cloud water to precipitation. Analyses of ice mixing ratio in Fig. 4.4 suggest that there are diurnal surges in the cirrus outflow layer that are coupled with surges in upper level outflow that occur in the mid-morning to afternoon and are accompanied by significant increase in the radial extent of the TC's cirrus canopy that contain ice mixing ratio values from z~6-15 km that are a factor of 2-10 times higher than they are in the evening to early morning hours. These surges are presumed to be TC diurnal pulses and could act to "seed" the region of the NRH1 just outside the TC inner core from R~150-200 km. As seen in Fig. 4.31, this region of the storm experienced diurnal fluctuations in both Q-condensate and vertical winds that may benefit from diurnal surges in ice mixing ratio that were emanating from the storm's inner core. It was also hypothesized that mesoscale lift associated with a radially propagating gravity wave of sufficient depth could promote the "feeder" mechanism. Analyses of *w* that showed a radially

propagating semi-circular ring of enhanced vertical winds that was observable through a deep layer of the atmosphere (150-925 hPa) could provide just such a "feeder" mechanism.

4.7 Discussion and Conclusions

The goal of this chapter was to examine a hurricane nature run (NRH1) simulation to look for signals of the TC diurnal cycle (TCDC) in the model, characterize these signals in time and space, and identify possible mechanisms associated with its evolution. This element of the TCDC research finds a marked radially propagating diurnal signal in a simulated TC that becomes robust when the storm reaches category 2 intensity ($\geq$43 m s^{-1}), is embedded in a low vertical wind shear environment ($\leq$7.5 m s^{-1}), and is sufficiently removed from land ($\geq$300 km). When these thresholds described in Sec. 2.2.1 are satisfied, various diurnal signals in thermodynamics, static stability, winds, and precipitation become apparent in and around the storm environment. Details of these signals are discussed in the context of both time and space and may be applicable to other simulated TCs where the employed model includes a solar cycle and the simulated storm satisfies the aforementioned conditions. Additionally, complex interactions between shortwave and longwave radiation in the region of the TC inner core and near environment (e.g. R=50-350 km) cause marked diurnal fluctuations in static stability that promote convection at certain times of day, which may favor the formation of convectively active TC diurnal pulses each day. Figure 4.32 presents a schematic that summarizes diurnal background states for parameters of radiation, thermodynamics, kinematics, and precipitation that were discussed in this chapter. This schematic highlights relative diurnal trends of these parameters at various levels in the evening to early morning hours when the TCDC and TC

diurnal pulses are first beginning to evolve versus the mid-morning to afternoon hours, when TC diurnal pulses have propagated several hundred kilometers from the NRH1 inner core. Figure 4.33 presents a TCDC-centric schematic summarizing the daytime evolution of TC diurnal pulses, seen as radially propagating squall line features with associated gust fronts (i.e. arc clouds), highlights relative minima and maxima of radial outflow and inflow during different times of day, and indicates enhanced vertical winds at the location of the squall line. Key findings from the NRH1 analyses reveal the following:

1. *OLR and Upper-Level Ice Mixing Ratio*: OLR analyses show a distinct diurnal oscillation that appears to propagate away from the storm each day (~5-10 m s^{-1}), beginning at R~150 km and eventually reaching R~450 km. Peak OLR cooling occurs from ~0600-1800 LST and has similar timing to previously discovered radially propagating diurnal pulses that have been detected in infrared satellite imagery (e.g. Chapter 3 and Dunion et al. 2014). Complimentary analyses of ice mixing ratio at ~200 hPa support the OLR patterns and suggest that a distinct radially propagating diurnal signal is present in the upper-level outflow layer of the storm.
2. *Thermodynamics*: detailed analyses of potential temperature and mixing ratio reveal a TCDC signal that involves a relatively deep layer of the storm and its surrounding environment. Analyses of potential temperature indicate pronounced diurnal signals that extend from the TC outflow layer down to the near-surface, especially at radii of 150 km and outward. Examination of mixing ratio indicates a propagating diurnal signal that is particularly pronounced near the TC outflow layer and at lower levels (~925 hPa to the near surface). The upper-level trends are similar to those seen on OLR, ice mixing ratio,

and potential temperature, suggesting that diurnal pulses are characterized by marked changes in both temperature and moisture. Diurnal oscillations in low-level (e.g. 925 hPa to the near surface) moisture appear to manifest as periodic minima in moisture that are concentrated at radii of ~100-300 km and extending from ~4 km to the surface. As discussed by Dunion et al. 2014, these minima may be linked to large arc cloud features (hundreds of km in length) and appear to form along the leading edge of TC diurnal pulses. This suggests that TCDC moisture signals may be linked to squall line features with associated outflow boundaries that propagate away from the NRH1 storm each day and that the TCDC affects a deep layer of the atmosphere from the TC outflow layer down to the near-surface.

3. *LNB and CAPE:* Middle to upper-level (z~4-12 km) diurnal fluctuations of shortwave and longwave radiation in the TC inner core and surrounding environment appear to have profound affects on the LNB and hence, CAPE in the storm each day. Although shortwave and longwave radiation tendencies consistently support very low CAPE (~0-500 J kg^{-1}) inside the TC inner core (R~≤150 km), the region just outside the inner core (R~150-350 km) experiences marked diurnal fluctuations of the LNB and CAPE. These parameters fluctuate by as much as 450 hPa and 1500 J kg^{-1} respectively and favor a convectively primed (i.e. more convectively favorable) environment in the late evening to early morning hours in this region of the storm. This nighttime enhancement of CAPE at R~150-350 km could favor the formation of convectively active TC diurnal pulses at this radius range and could explain why TC diurnal pulses as seen in both satellite imagery and the NRH1 appear to form at R~150 km after sunset each day.

4. *Pressure and 10-m Surface W*inds: An examination of pressure and winds in the NRH1 was made to assess possible relevance to forecasting of TC intensity and structure. An anticipated semidiurnal tide signal was revealed in surface pressure that favored relative pressure minima in the early morning and again in the late afternoon to early evening and relative pressure maxima in the late morning and again in the late evening. Surface winds showed a clear diurnal signal and indicated that there are marked periods of alternating enhanced (evening to early morning hours) and suppressed (mid-morning to afternoon hours) surface winds and low-level inflow each day, particularly along the periphery and just outside the storm's inner core (R~100-350 km). These findings suggest that the TCDC has implications for TC intensity and structure (e.g. radii of 34 and 50 kt winds). These aspects of the TCDC will be investigated in future studies.
5. *Radial winds*: Radial winds in the NRH1 show significant diurnal oscillations near the level of the outflow layer with regular outward bursts evident at R~150 km in the morning hours each day that steadily propagate out to peripheral radii (e.g. R=450 km) during the afternoon. These outflow maxima are interrupted by lulls in outflow that peak in the late evening and are a factor of two weaker than the periods of maximum outflow. Middle level (e.g. 700 hPa) radial wind also has a diurnal inflow peak in the mid-morning and appears to occur prior to and radially outward of the aforementioned upper-level outflow bursts. These diurnal patterns of middle level inflow suggest that the morning could be a time when the TC is more susceptible to middle level ventilation.
6. Low-level (~925 hPa to the surface) radial winds in the NRH1 also indicated that peak inflow at R~100-200 km occurs in the early morning hours and is interspersed by periods of relatively weaker inflow that are weakest in the late morning to afternoon. The

temporal phasing of maximum near-surface inflow and maximum upper-level outflow are offset by ~12 hr, suggesting a possible cause-and-effect relationship where surges in lower level inflow precede/follow surges in upper-level outflow by approximately half a solar day.

7. *Tangential Winds*: Diurnal patterns of tangential wind exhibit marked diurnal signals throughout the troposphere and are most pronounced in the upper-levels (e.g. 200 hPa). Peaks in upper-level tangential wind occur from the mid-afternoon to early evening at R~300-450 km and are interspersed by lulls that are 1.5-5 times weaker. There do appear to be certain times of day when maximum and minimum values in the magnitude of tangential wind are favored throughout the troposphere.
8. *Vertical Winds*: the NRH1 exhibits a clear diurnal signal of vertical winds near the level of the TC outflow layer (~200 hPa), but in the mean, these diurnal signals are less defined in the lower (e.g. 925 hPa to the near-surface) and especially middle (e.g. 700 hPa) levels. Interestingly, 2-dimensional plots of vertical wind made during several of the days of NRH1 peak intensity reveal narrow (~10-20 km wide), highly symmetric rings of enhanced vertical winds that propagate away from the storm each day. These rings of enhanced vertical winds appear to involve a deep layer of the troposphere and the timing of their propagation closely matches the TCDC conceptual clock presented in Chapter 3. These features are also similar in appearance to the 37 and 85 GHz microwave convective rings (i.e. diurnal pulses) that were described in that chapter and may be a signature of the diurnal pulse. However, given the limited width of these ring of enhanced vertical motion, they may be difficult to consistently track using simple azimuthal mean analyses.

9. *Precipitation*: Analyses of NRH1 rain rates and simulated radar reflectivity showed a strong outwardly propagating diurnal signal. Maxima (minima) in precipitation peak in the late evening to early morning (late morning to middle afternoon) in the inner core and in the early to late morning (late afternoon to late evening) farther from the storm (e.g. R=200-450 km). These trends suggest that the TCDC may have implications for quantitative precipitation forecasting and TC structure. Analyses of Q-condensate and vertical wind suggested that TC diurnal pulses might behave like squall lines that are accompanied by outflow boundaries (i.e. arc clouds).
10. *TCDC Mechanisms*: Analyses of the radiation, thermodynamics, and kinematics in the NRH1 suggest a complex and dynamic environment that varies throughout the day and also fluctuates greatly with radius and height. Analyses of longwave, shortwave and total radiation tendency, ice mixing ratio, static stability (the LNB and CAPE), vertical wind, and radial wind in the NRH1 simulation indicate that there is evidence supporting various aspects of all of Chapter 3's hypothesized TCDC driving mechanisms: a) convectively-driven atmospheric gravity waves, b) radiatively reduced outflow resistance, c) cloud-cloud-free differential heating mechanism, d) direct radiation-convection interactions, and e) seeder-feeder mechanism. However, no single mechanism was clearly identified as the primary forcing for the TCDC and associated TC diurnal pulses.

Analyses presented in this chapter and summarized in Figs. 4.32 and 4.33 suggest that aspects of each of the previously described 5 proposed TCDC mechanisms are present in the NRH1 TC simulation. However, an examination of radiation, ice mixing ratio (a proxy for the TC outflow layer), static stability, and winds suggest that nighttime longwave cooling and

daytime shortwave warming that are particularly favored in the TC outflow layer may be critical factors influencing the evolution of the TCDC.

Enhanced nighttime longwave cooling of the cirrus outflow layer begins near the time of sunset may initiate the TCDC and could act in 2 ways: first to prime the inner core (R≤150 km) atmosphere by rapidly destabilizing (reducing $d\theta/dz$) the top of the TC outflow layer . When the mean flow Richardson number is <0.25, gravity wave reflection at a viscous boundary layer is favored (Nappo 2013). Therefore, nighttime reductions in $d\theta/dz$, would establish conditions that could support reflection of gravity waves, reduction of upper-level potential vorticity, increased IAKE that would favor a release of outflow, lower pressure in the upper levels (hence reduced divergence), and enhanced inner core convection. Second, this nighttime longwave cooling would rapidly prime (destabilize) the region just outside the TC inner core (R~150-350 km), thereby elevating the level of the LNB and hence, increasing CAPE in this region of the storm where deep convection doesn't always occur and TC diurnal pulses appear to initiate.

Beginning around the time of local sunrise, daytime shortwave warming that is also favored in regions of the cirrus outflow layer would begin to dominate the aforementioned nighttime longwave cooling processes and could lead to the culmination of the TCDC each day. This shortwave warming could act in 2 ways: first to rapidly stabilize (by increasing the vertical gradient of potential temperature) the top of the TC outflow layer in the inner core region (R≤150 km). This would establish conditions that could support gravity waves that more easily propagate upward (rather than radially outward) into the stratosphere, an increase of upper-level potential vorticity, reduced IAKE that would favor more restricted outflow as the day progresses, higher pressure in the upper levels (hence increased divergence), and reduced inner core convection. Second, this shortwave warming would rapidly stabilize the region just outside the

TC inner core (R~150-350 km), thereby lowering the level of the LNB, reducing CAPE, and suppressing convection in this region of the storm. Assuming that the 3 TCDC analysis conditions continued to be satisfied, these daytime processes would begin to wane in the late afternoon and around the time of sunset, nighttime longwave dominated processes would once again begin to dominate.

The following chapter will include applying the findings in this study to idealized vortex simulations with varying solar cycles to further investigate the TCDC.

4.8 Figures

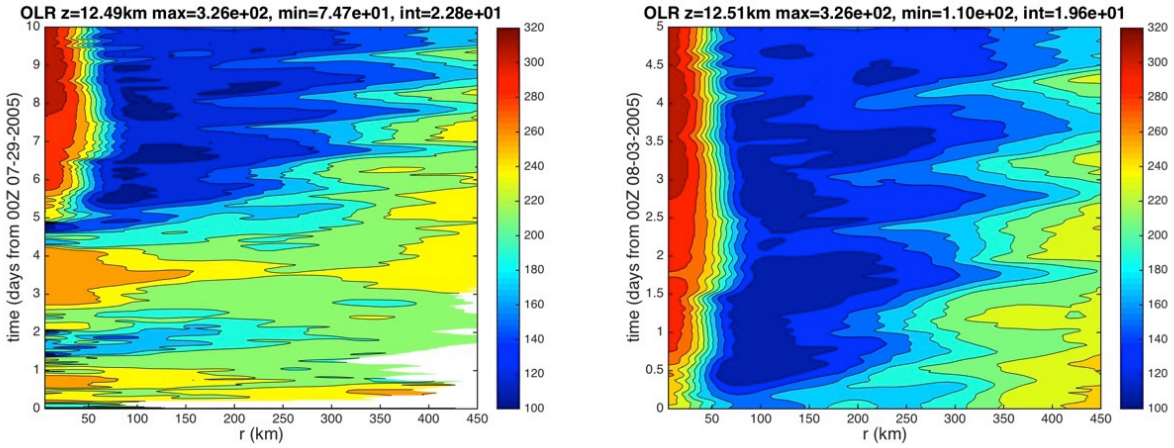

Figure 4.1: Hovmollers of azimuthally averaged OLR (W m s^{-2}) calculated for (left) the period from 29 Aug-08 August of the NRH1 and (right) only for the 03-08 August NRH1 study period. Radii are analyzed relative to the TC center and extend out to 450 km.

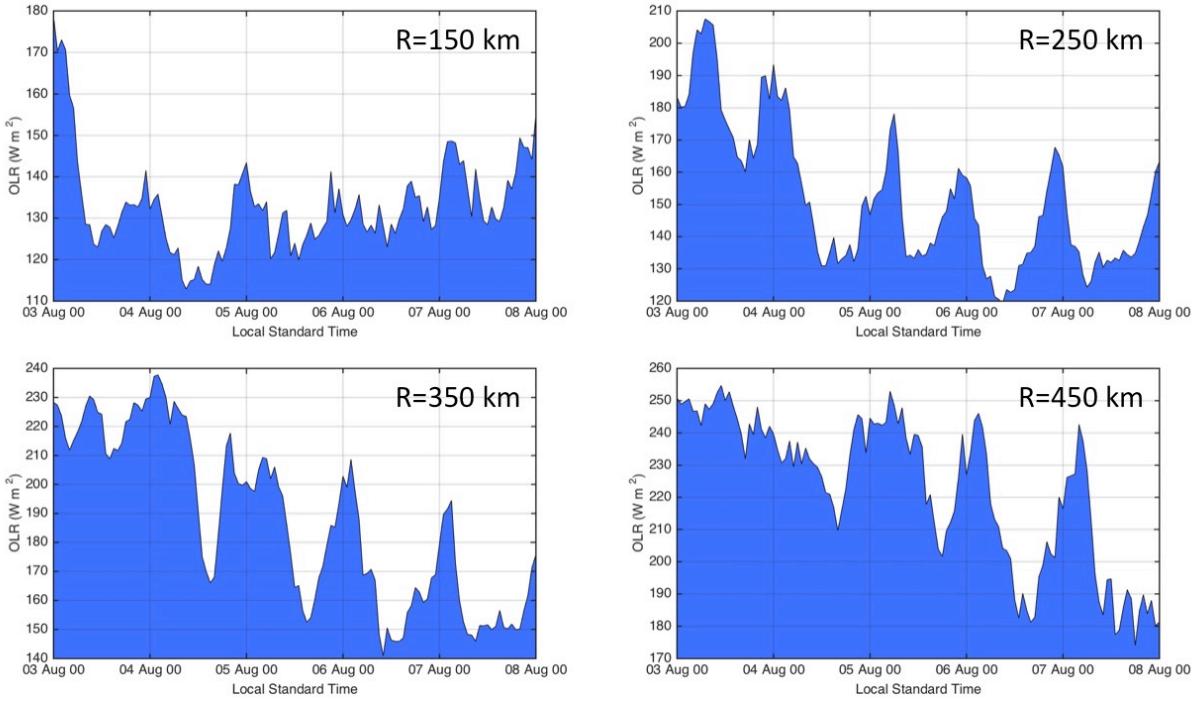

Figure 4.2: Azimuthally averaged OLR (W m s^{-2}) derived from the 03-08 August NRH1 study period at the 150, 250, 350, and 450 km radii.

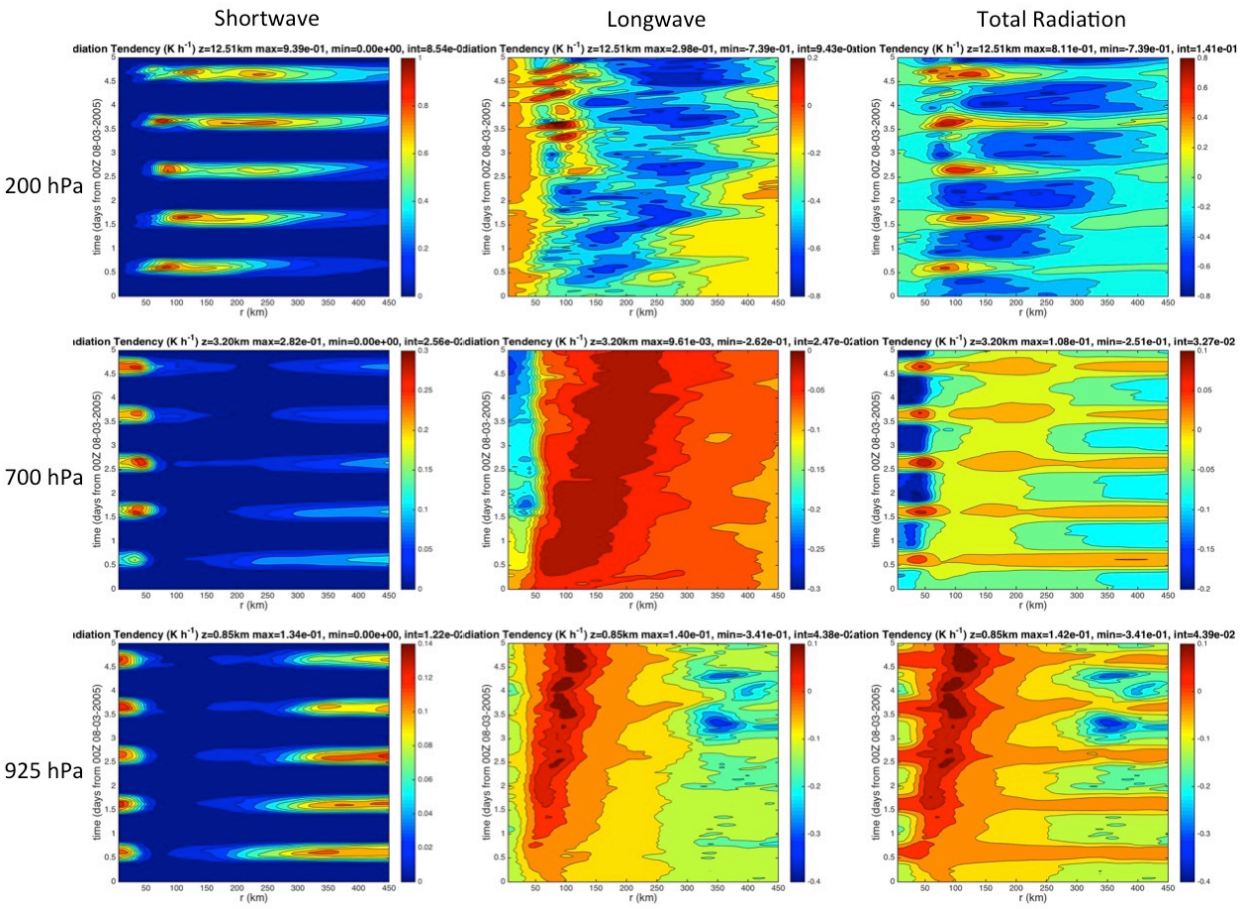

Figure 4.3: Hovmollers of azimuthally averaged shortwave, longwave, and total radiation tendencies (K h^{-1}) derived from the NRH1. Analyses are derived over the 03-08 August study period and show the 200, 700, and 925 hPa pressure levels. Radii are analyzed relative to the TC center and extend out to 450 km.

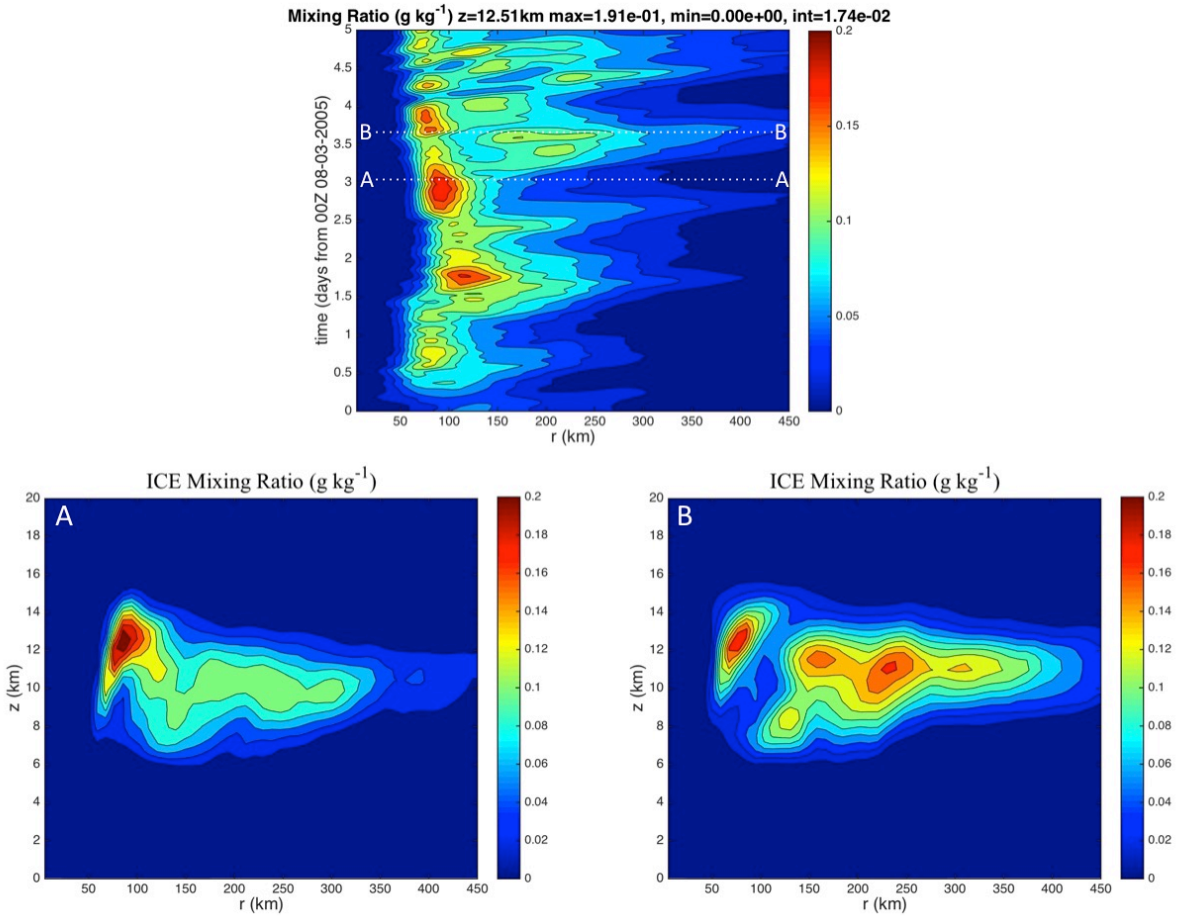

Figure 4.4: Hovmoller of azimuthally averaged ice mixing ratio (g kg^{-1}) derived from the 03-08 August NRH1 study period for 200 hPa (top). Radius-height cross-sections of azimuthally averaged ice mixing ratio derived from the NRH1 on (A) 06 Aug 0100 UTC (2100 LST) and (B) 06 Aug 1600 UTC (1200 LST) are also shown. The white dashed lines indicated the times along the Hovmoller plot when both cross-sections were derived. Radii in all plots are analyzed relative to the TC center and extend out to 450 km.

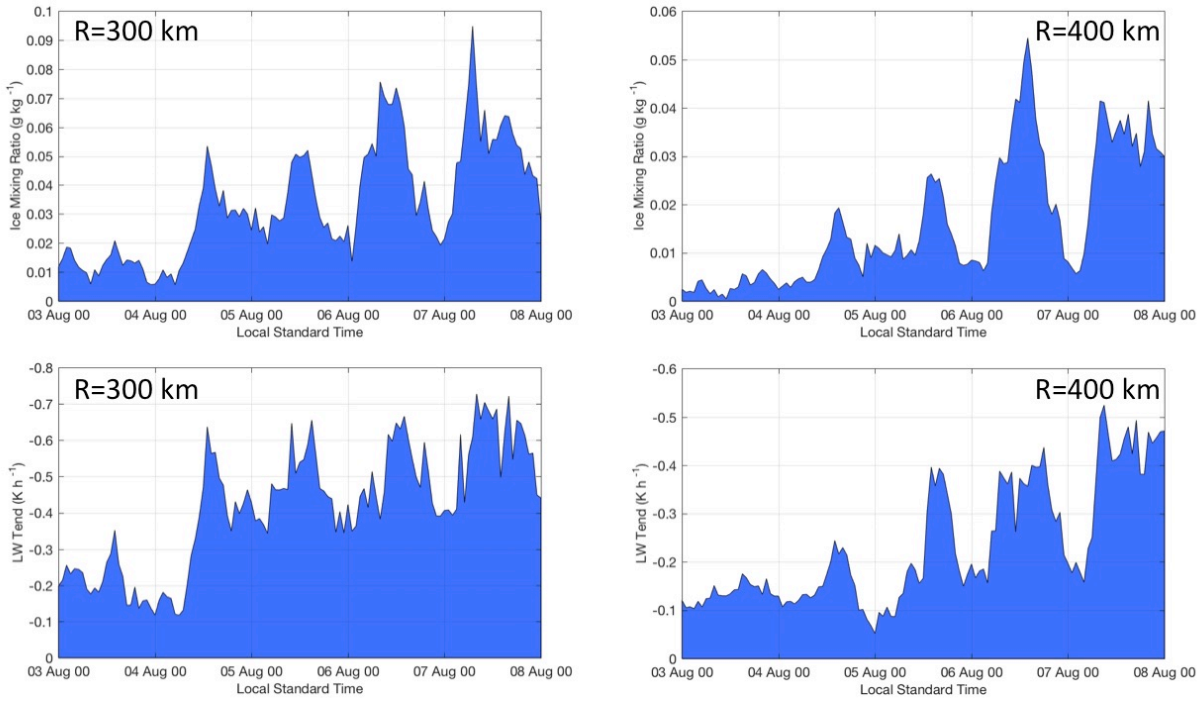

Figure 4.5: 200 hPa azimuthally averaged (top) ice mixing ratio (g kg^{-1}) and longwave radiation tendency (K h^{-1}) derived from the 03-08 August NRH1 study period at 300 and 400 km radii.

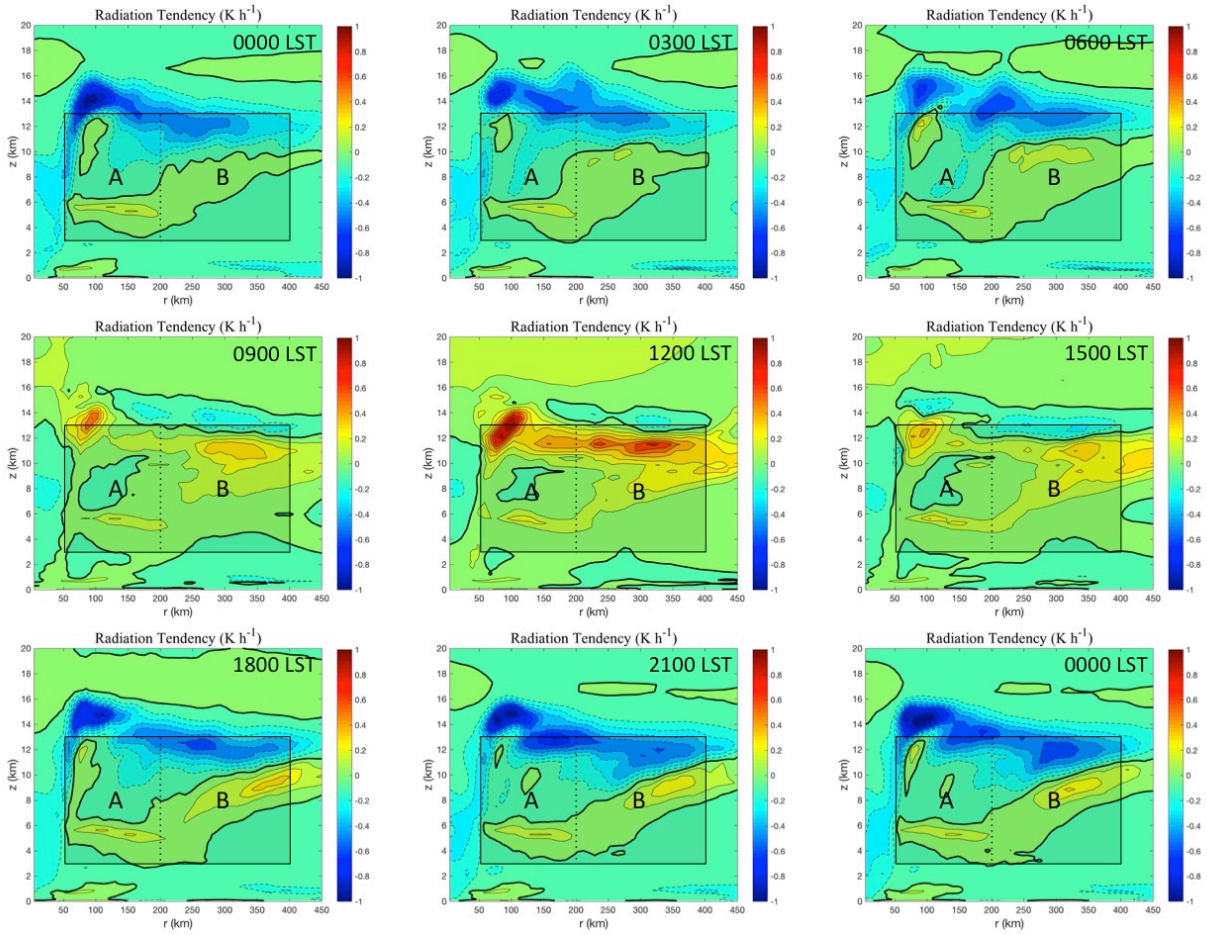

Figure 4.6: 3-hourly radius-height cross-sections of azimuthally averaged total radiation tendency (K h^{-1}) derived from the NRH1 from 06 Aug 0000 LST to 07 Aug 0000 LST. The shaded boxes highlight the regions from z=3-13 km from R=50-200 km (A) and R=200-400 km (B). The bold contours denote regions of zero net radiation tendencies. Radii are analyzed relative to the TC center and extend out to R=450 km.

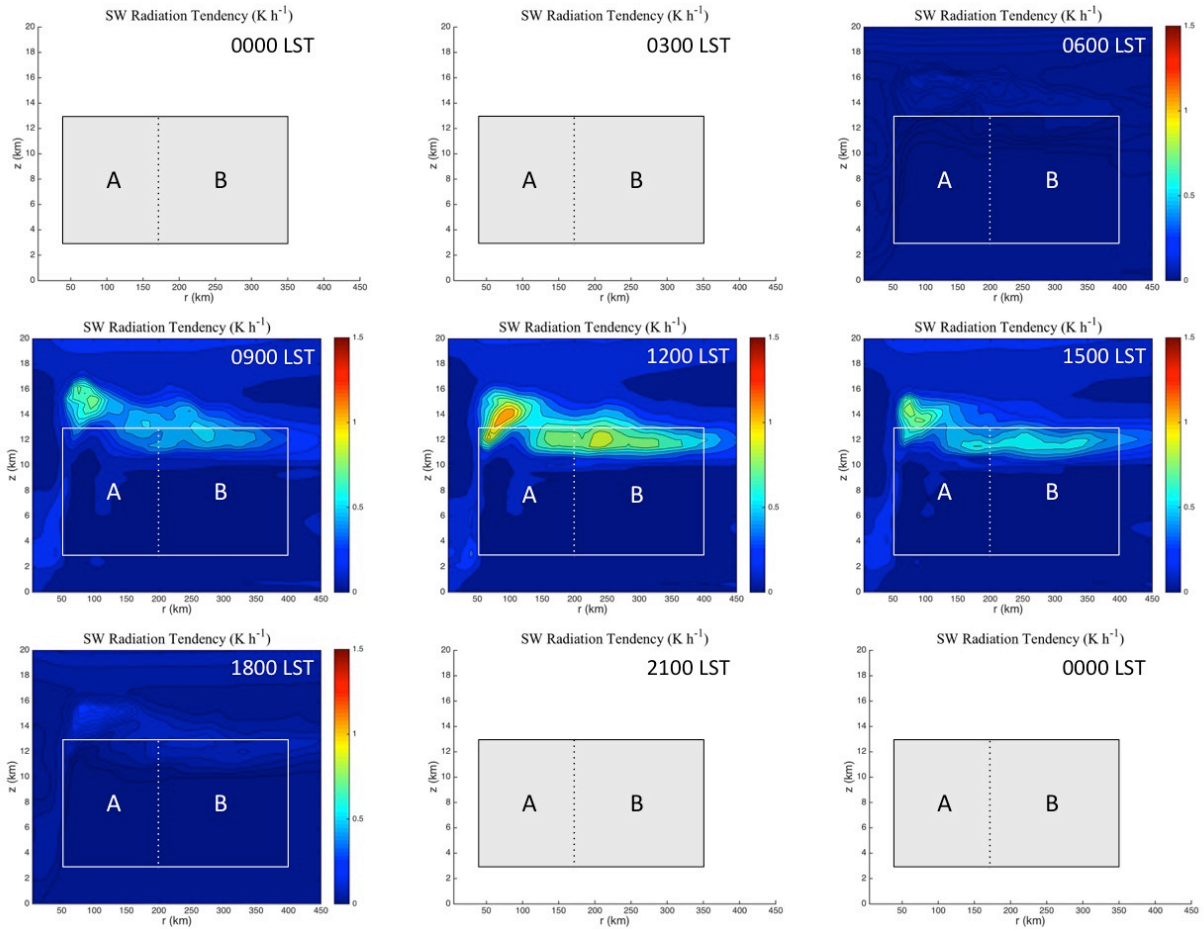

Figure 4.7: 3-hourly radius-height cross-sections of azimuthally averaged shortwave radiation tendency (K h^{-1}) derived from the NRH1 from 06 Aug 0000 LST to 07 Aug 0000 LST. The shaded boxes highlight the regions from z=3-13 km from R=50-200 km (A) and R=200-400 km (B). The bold contours denote regions of zero net radiation tendencies. Radii are analyzed relative to the TC center and extend out to R=450 km.

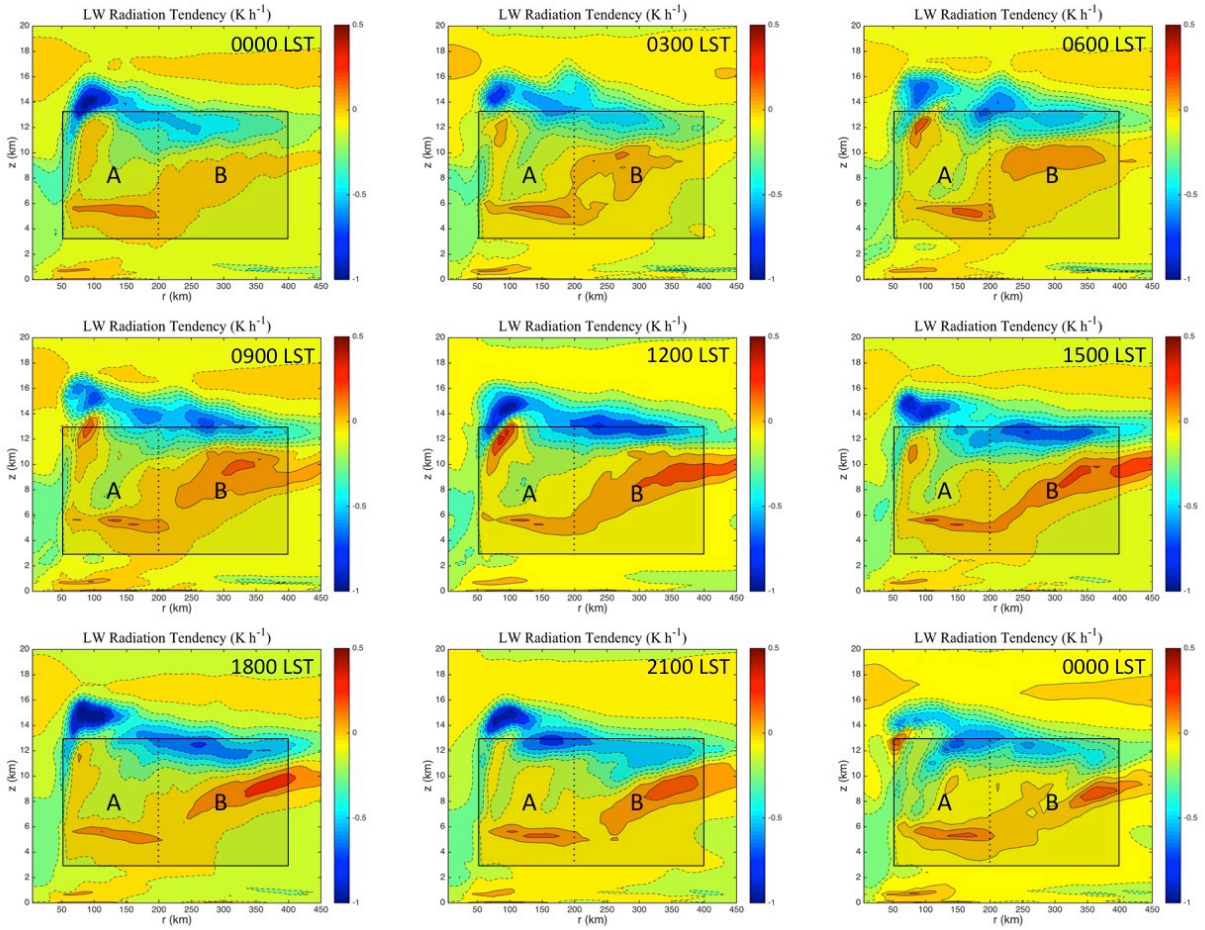

Figure 4.8: 3-hourly radius-height cross-sections of azimuthally averaged longwave radiation tendency (K h^{-1}) derived from the NRH1 from 06 Aug 0000 LST to 07 Aug 0000 LST. The shaded boxes highlight the regions from z=3-13 km from R=50-200 km (A) and R=200-400 km (B). The bold contours denote regions of zero net radiation tendencies. Radii are analyzed relative to the TC center and extend out to R=450 km.

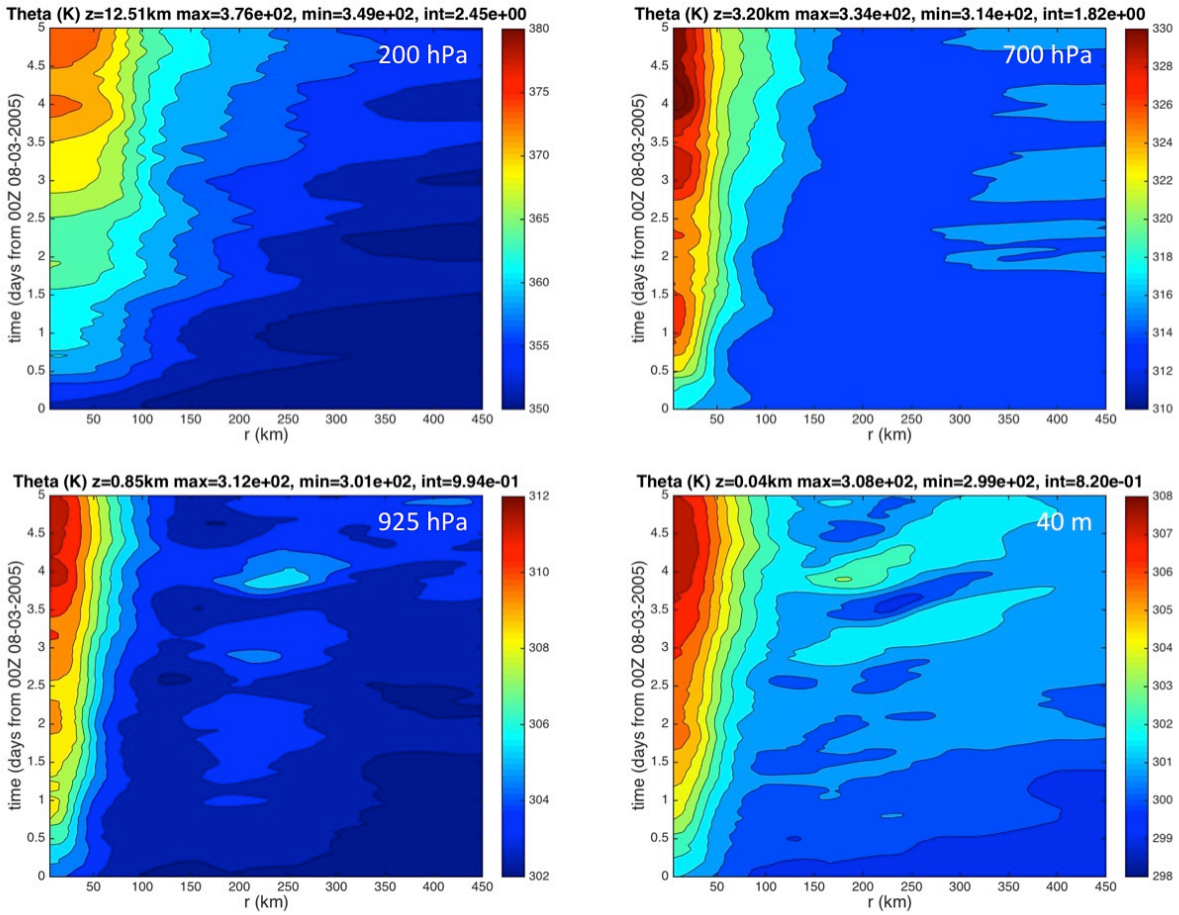

Figure 4.9: Hovmollers of azimuthally averaged potential temperature (K) derived from the 03-08 August NRH1 study period for 200 hPa, 700 hPa, 925 hPa, and 40 m. Radii are analyzed relative to the TC center and extend out to 450 km.

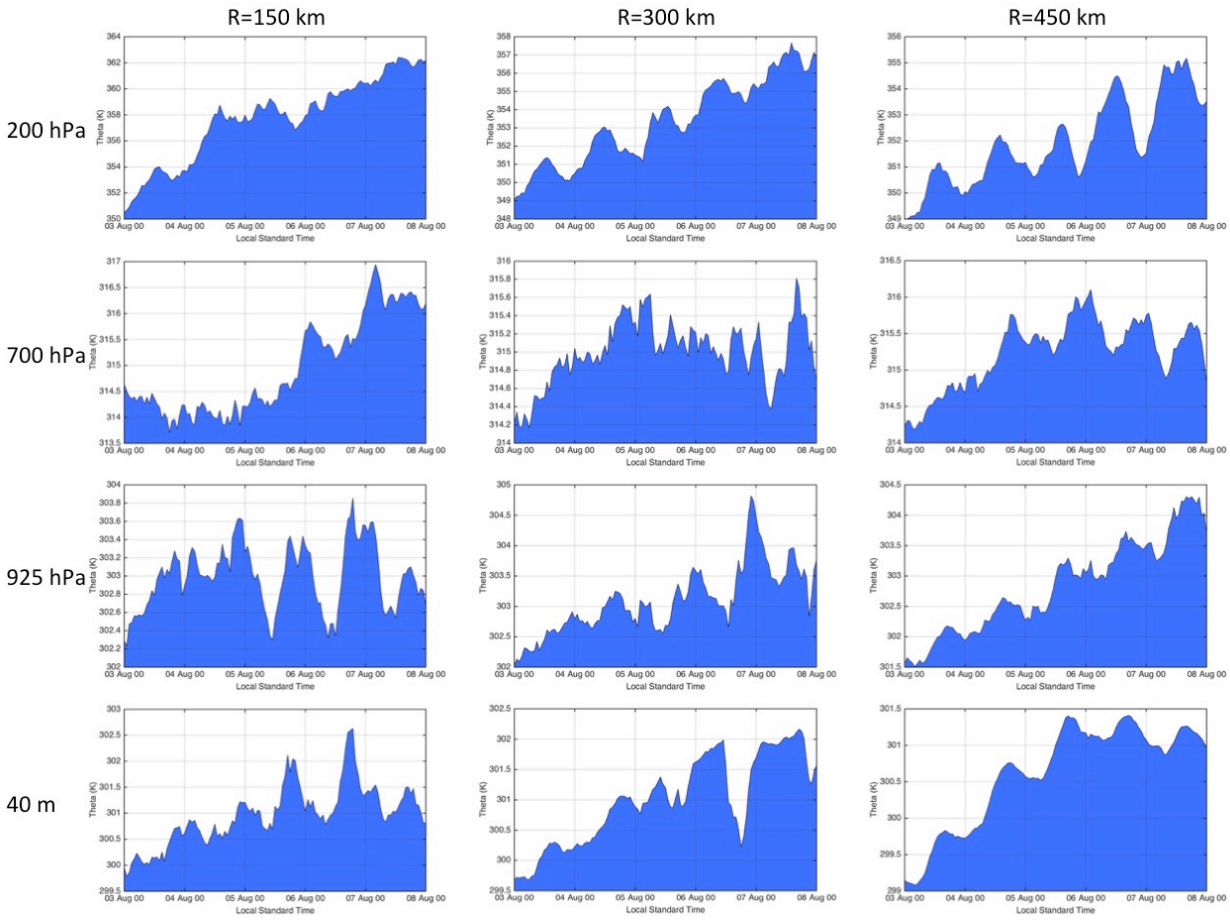

Figure 4.10: Azimuthally averaged potential temperature (K) derived from the 03-08 August NRH1 study period for the 200 hPa, 700 hPa, 925 hPa, and 40 m vertical levels. Analyses include the 150, 300, and 450 km radii.

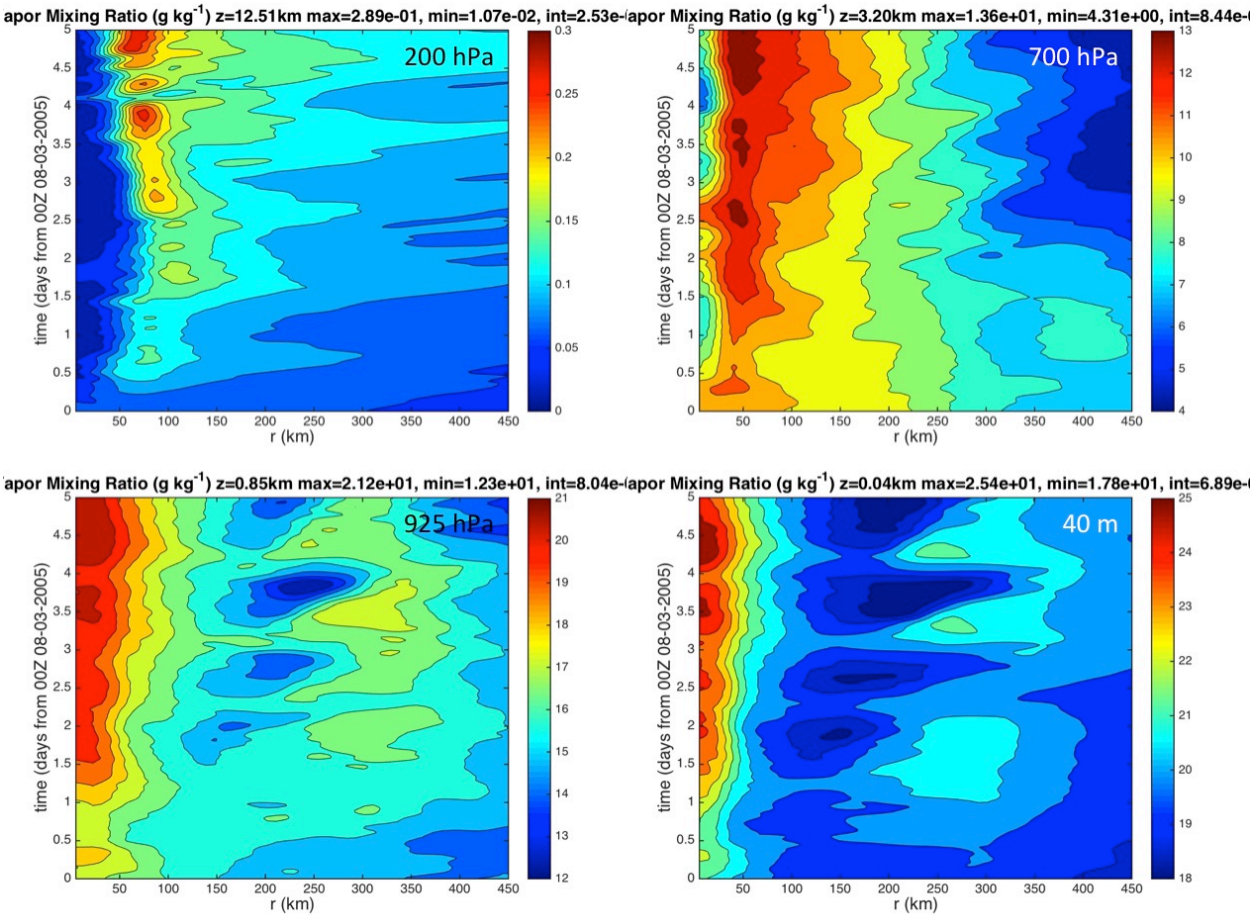

Figure 4.11: Hovmollers of azimuthally averaged mixing ratio (g kg^{-1}) derived from the 03-08 August NRH1 study period for 200 hPa, 700 hPa, 925 hPa, and 40 m. Radii are analyzed relative to the TC center and extend out to 450 km.

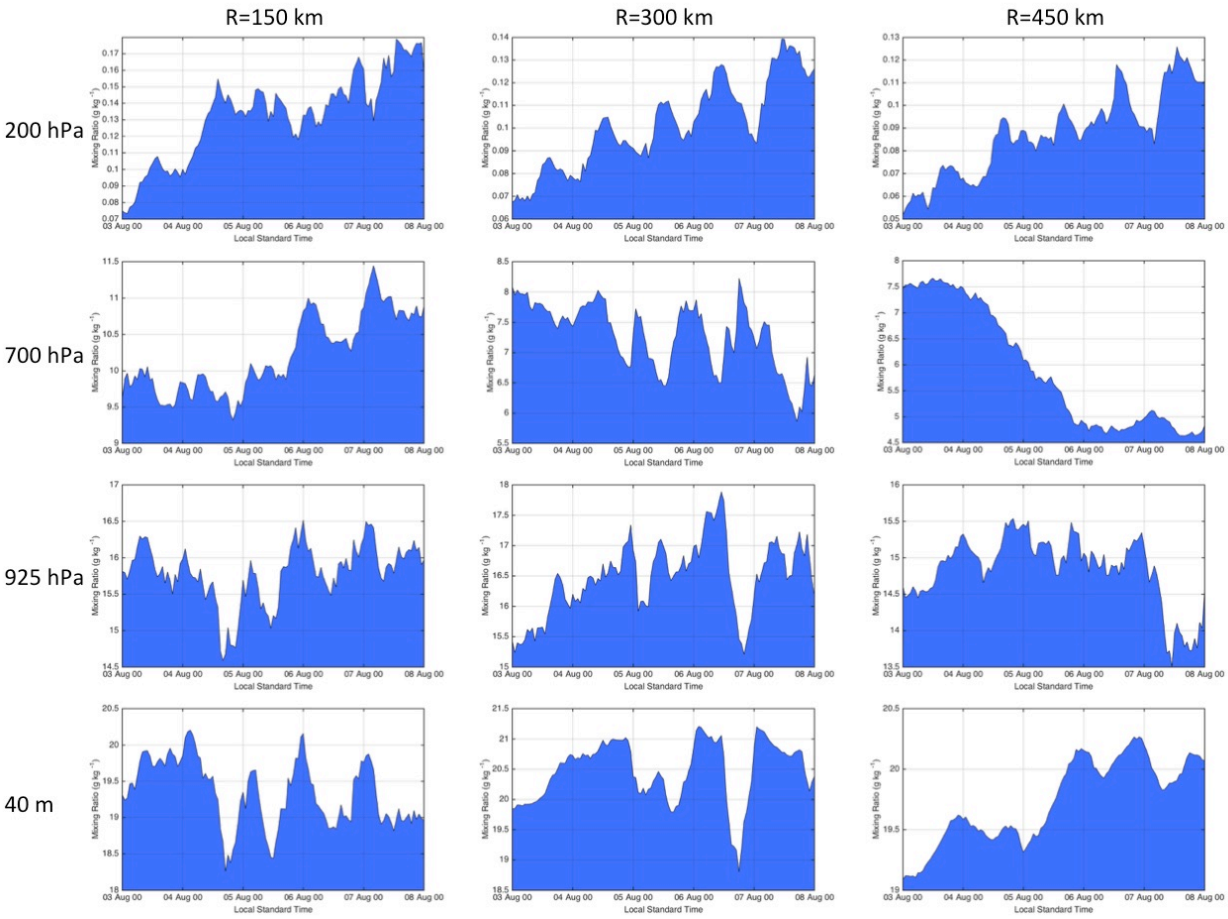

Figure 4.12: Azimuthally averaged mixing ratio (g kg^{-1}) derived from the 03-08 August NRH1 study period for the 200 hPa, 700 hPa, 925 hPa, and 40 m vertical levels. Analyses include the 150, 300, and 450 km radii.

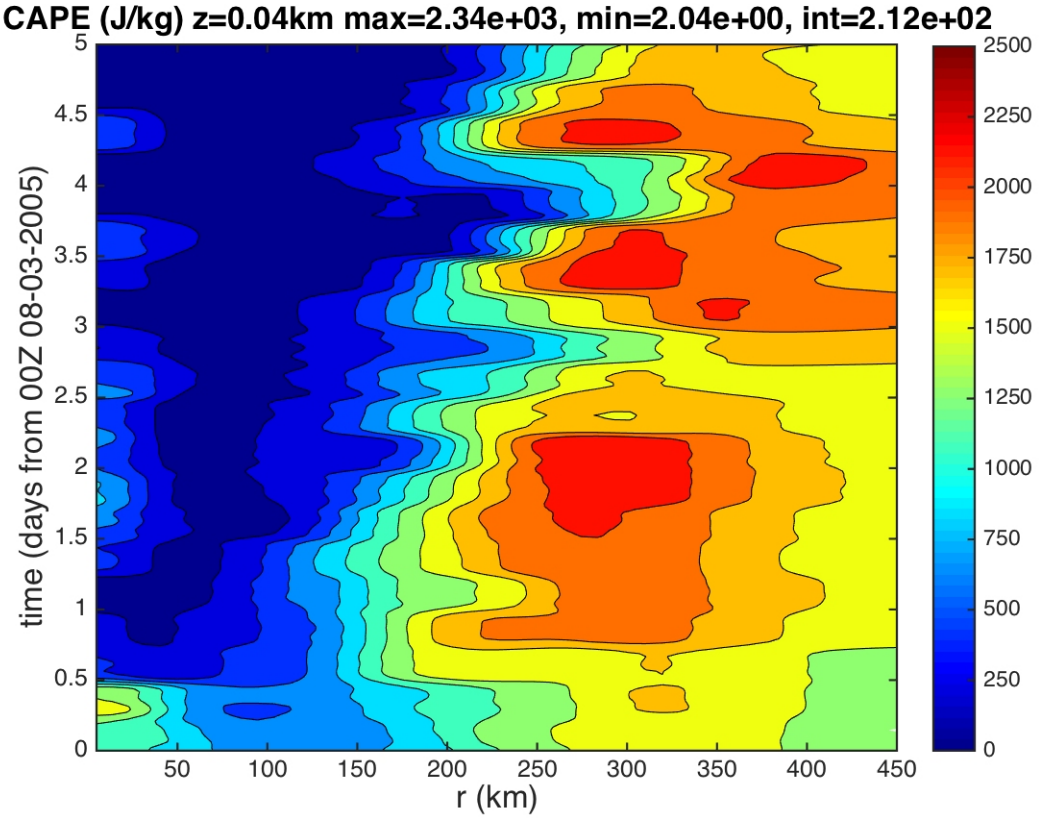

Figure 4.13: Hovmoller of azimuthally averaged CAPE (J kg^{-1}) derived from the 03-08 August NRH1 study period. Radii are analyzed relative to the TC center and extend out to R=450 km.

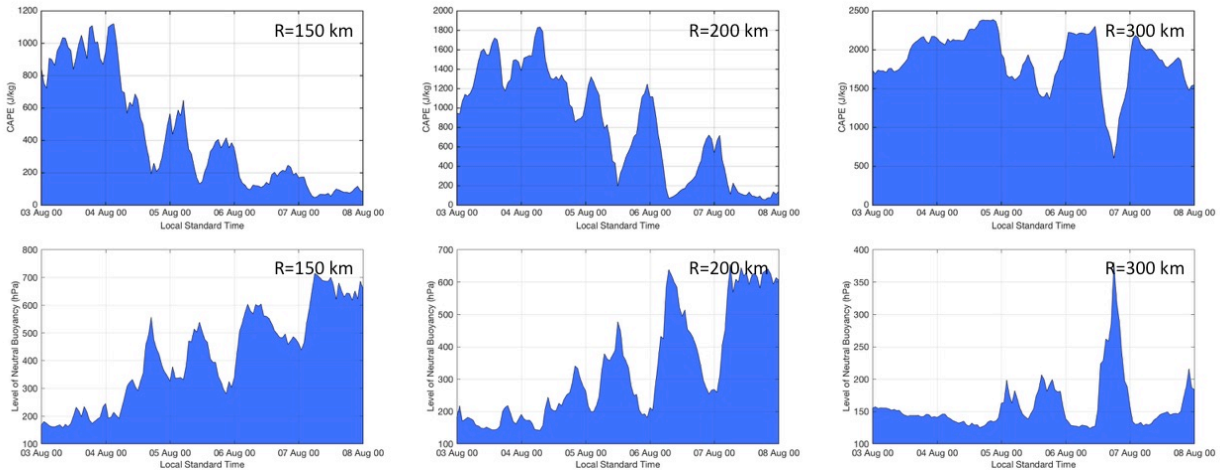

Figure 4.14: Azimuthally averaged CAPE (top) and the level of neutral buoyancy (LNB) derived from the 03-08 August NRH1 study period at the 150, 200, and 300 km radii.

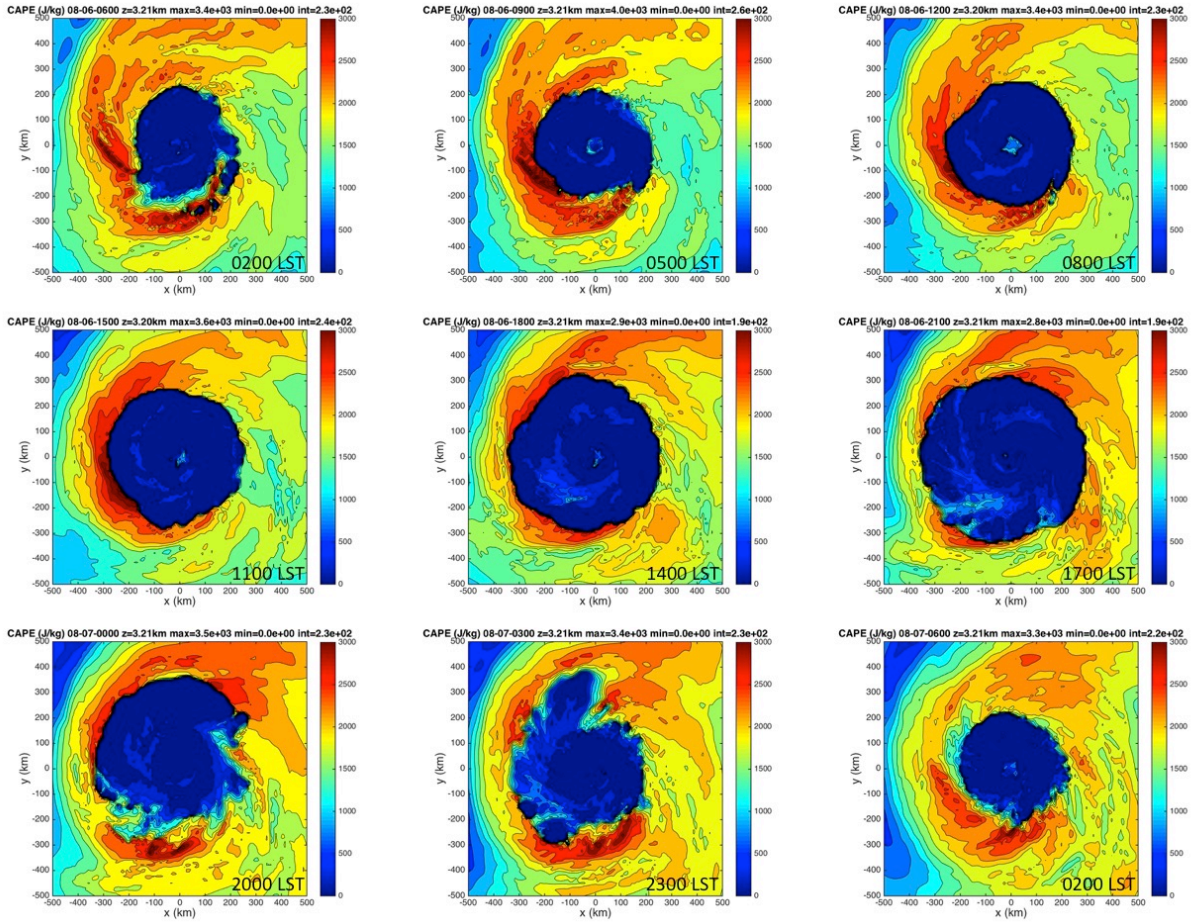

Figure 4.15: CAPE (J kg^{-1}) derived from the NRH1 for 06-07 August. Images are 3-hourly from 06 Aug 0200 LST (0600 UTC) to 07 Aug 0200 LST (0600 UTC).

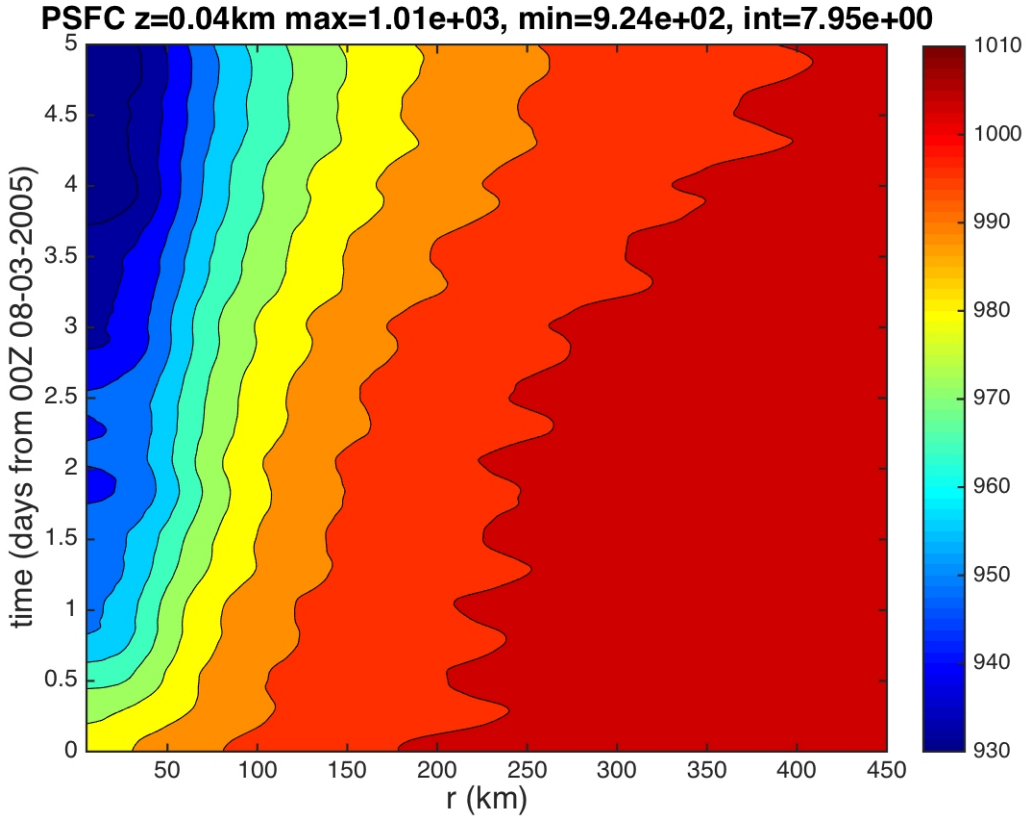

Figure 4.16: Hovmoller of azimuthally averaged surface pressure (hPa) derived from the 03-08 August NRH1 study period. Radii are analyzed relative to the TC center and extend out to R=450 km.

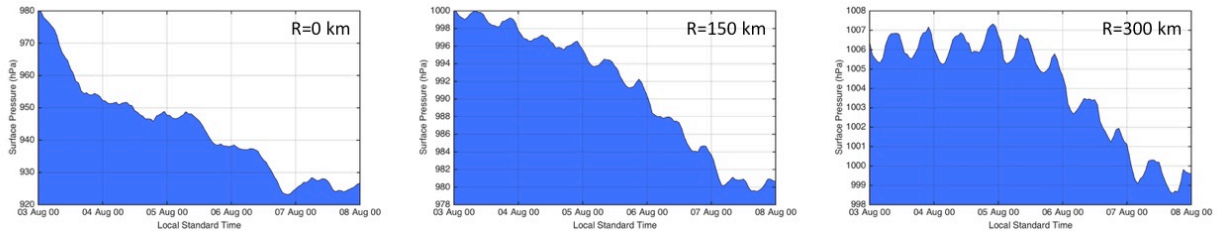

Figure 4.17: Plots of azimuthally averaged surface pressure (hPa) derived from the 03-08 August NRH1 study period for the 0,150, and 300 km radii.

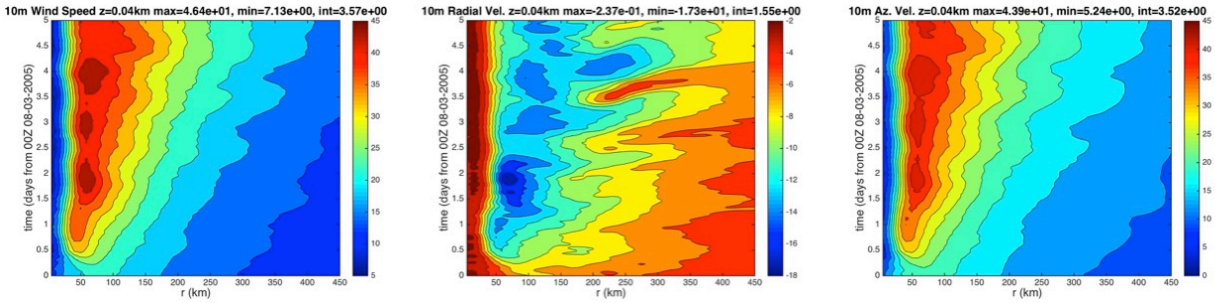

Figure 4.18: Hovmollers of azimuthally averaged 10-m surface winds (m s^{-1}) derived from the 03-08 August NRH1 study period for (a) wind speed, (b) radial wind speed, and (c) tangential wind speed. Radii are analyzed relative to the TC center and extend out to R=450 km.

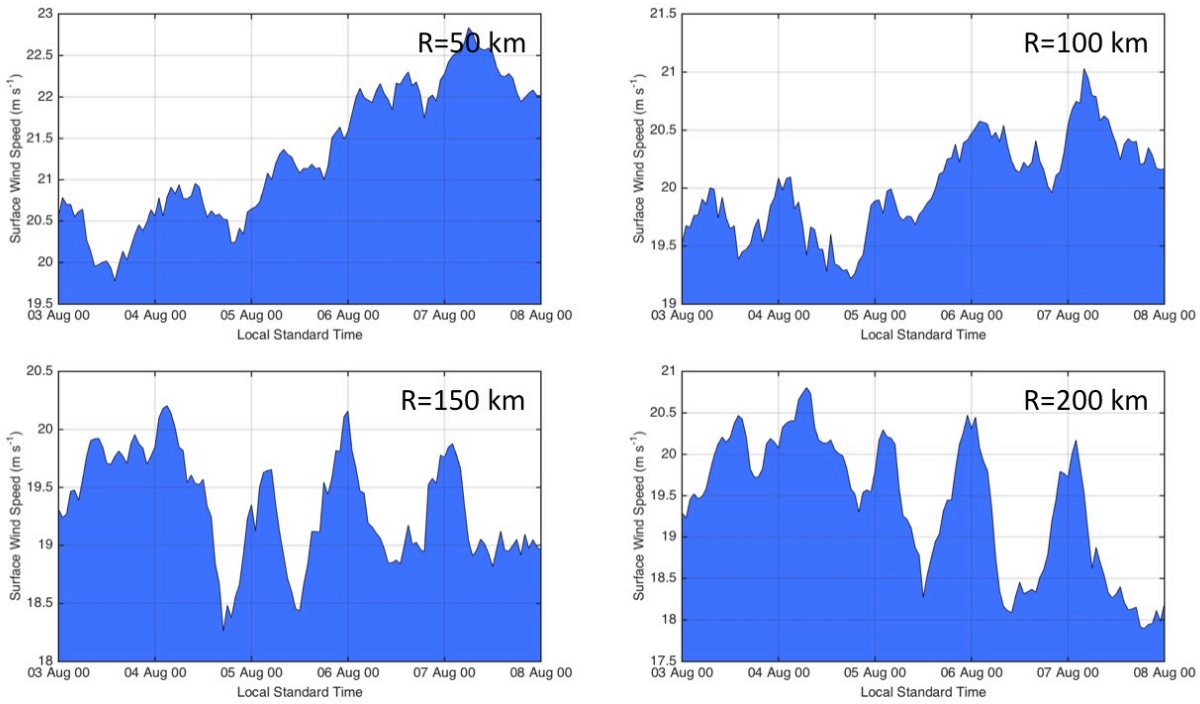

Figure 4.19: Plots of azimuthally averaged 10-m surface winds (m s^{-1}) derived from the 03-08 August NRH1 study period for 50, 100, 150, and 200 km radii.

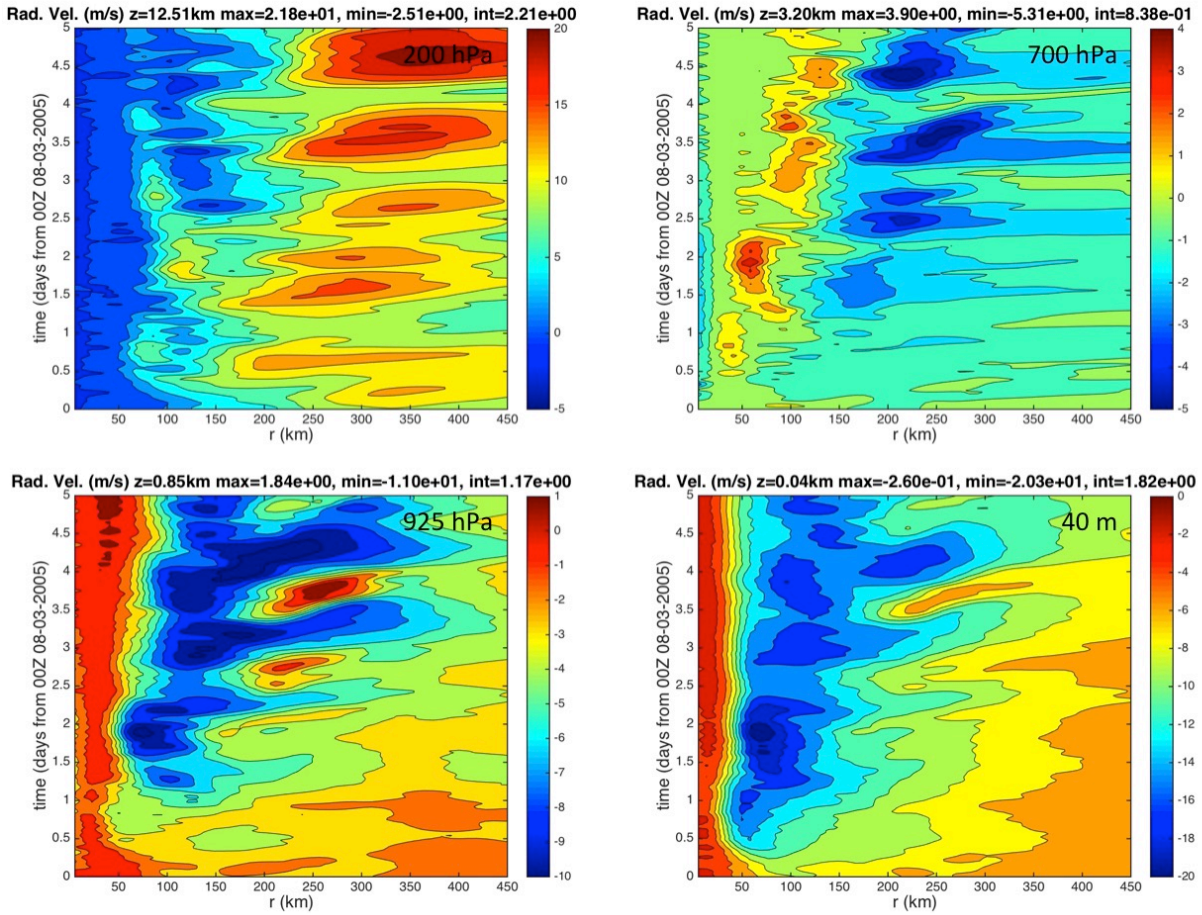

Figure 4.20: Hovmollers of azimuthally averaged radial wind (m s^{-1}) derived from the 03-08 August NRH1 study period for 200 hPa, 700 hPa, 925 hPa, and 40 m. Radii are analyzed relative to the TC center and extend out to 450 km.

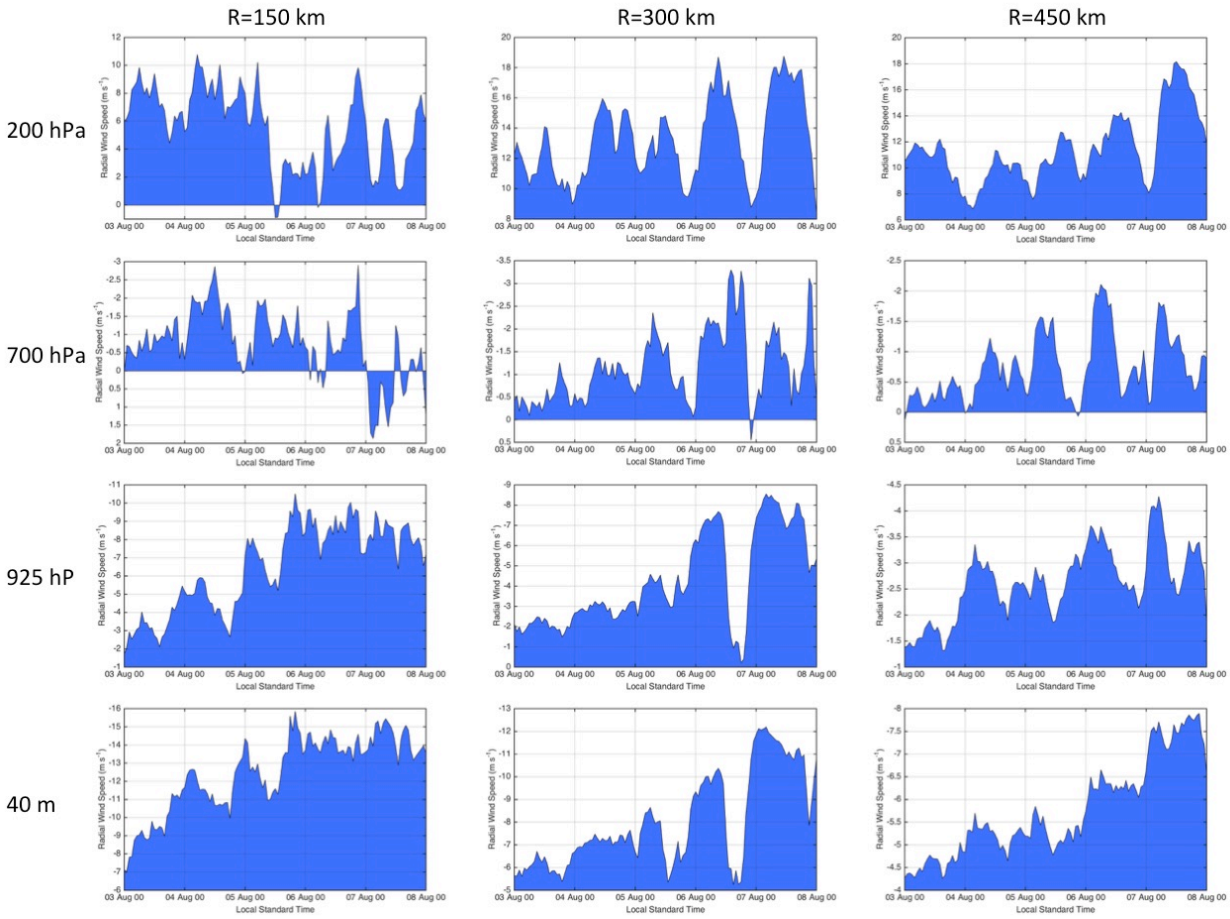

Figure 4.21: Plots of azimuthally averaged radial wind (m s^{-1}) derived from the 03-08 August NRH1 study period for the 200 hPa, 700 hPa, 925 hPa, and 40 m vertical levels. Analyses include the 150, 300, and 450 km radii.

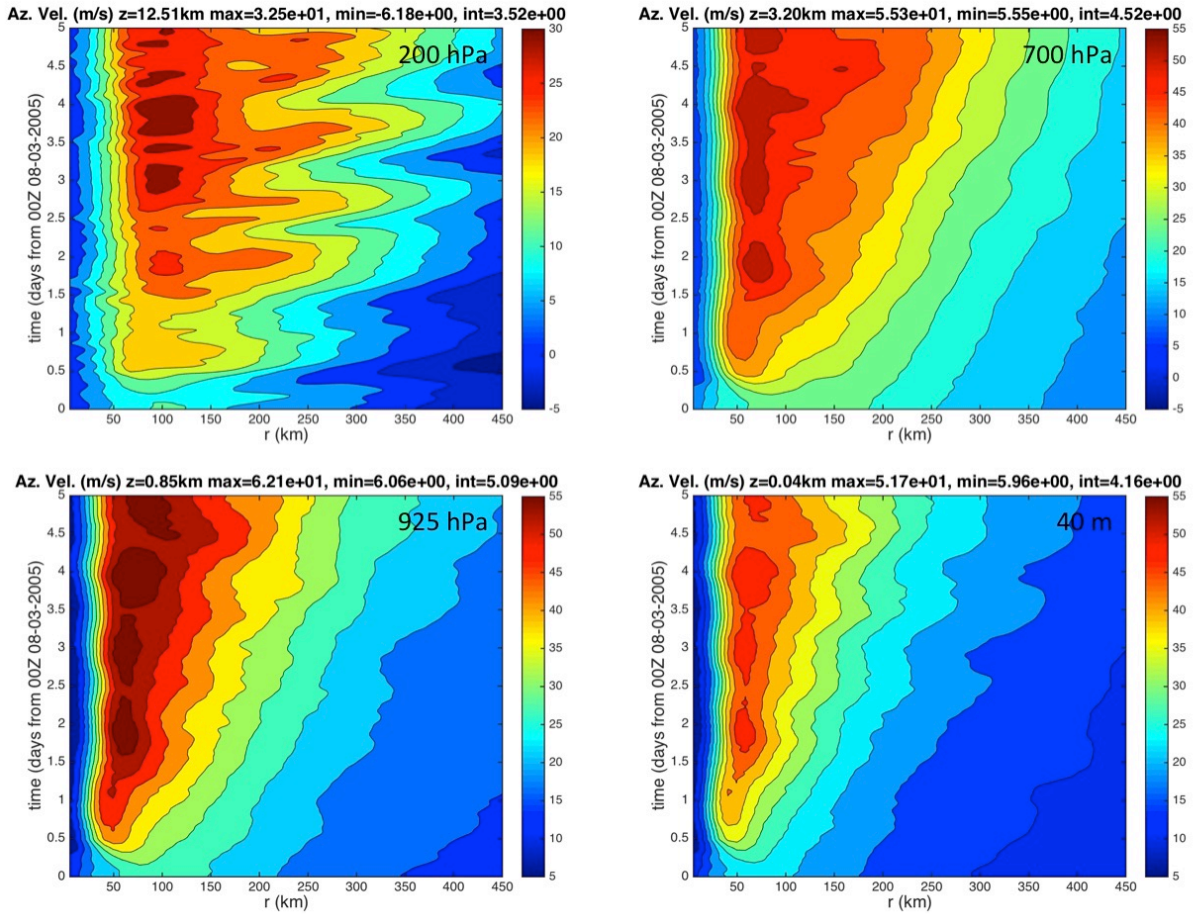

Figure 4.22: Hovmollers of azimuthally averaged tangential wind (m s^{-1}) derived from the 03-08 August NRH1 study period for 200 hPa, 700 hPa, 925 hPa, and 40 m. Radii are analyzed relative to the TC center and extend out to R=450 km.

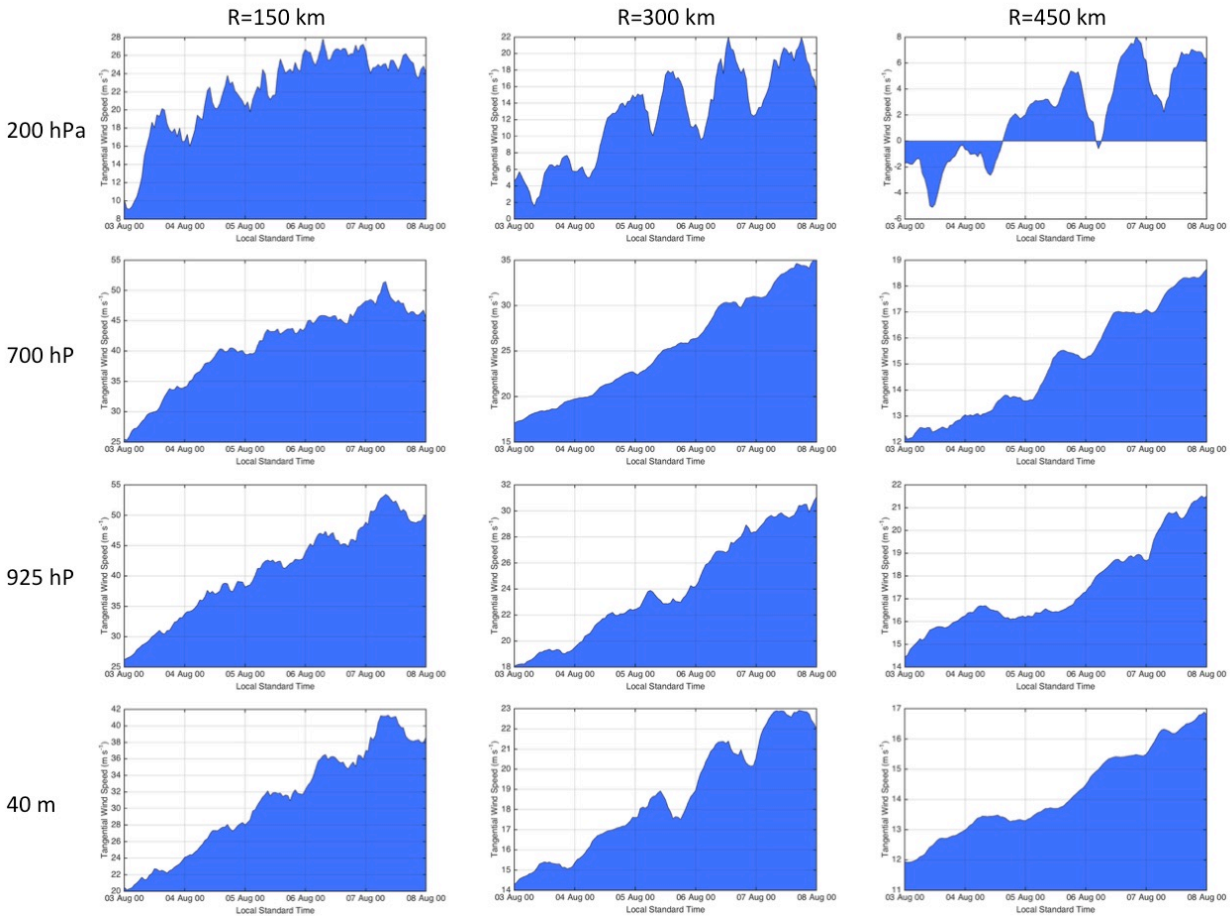

Figure 4.23: Plots of azimuthally averaged tangential wind (m s^{-1}) derived from the 03-08 August NRH1 study period for the 200 hPa, 700 hPa, 925 (hPa), and 40 m vertical levels. Analyses include the 150, 300, and 450 km radii.

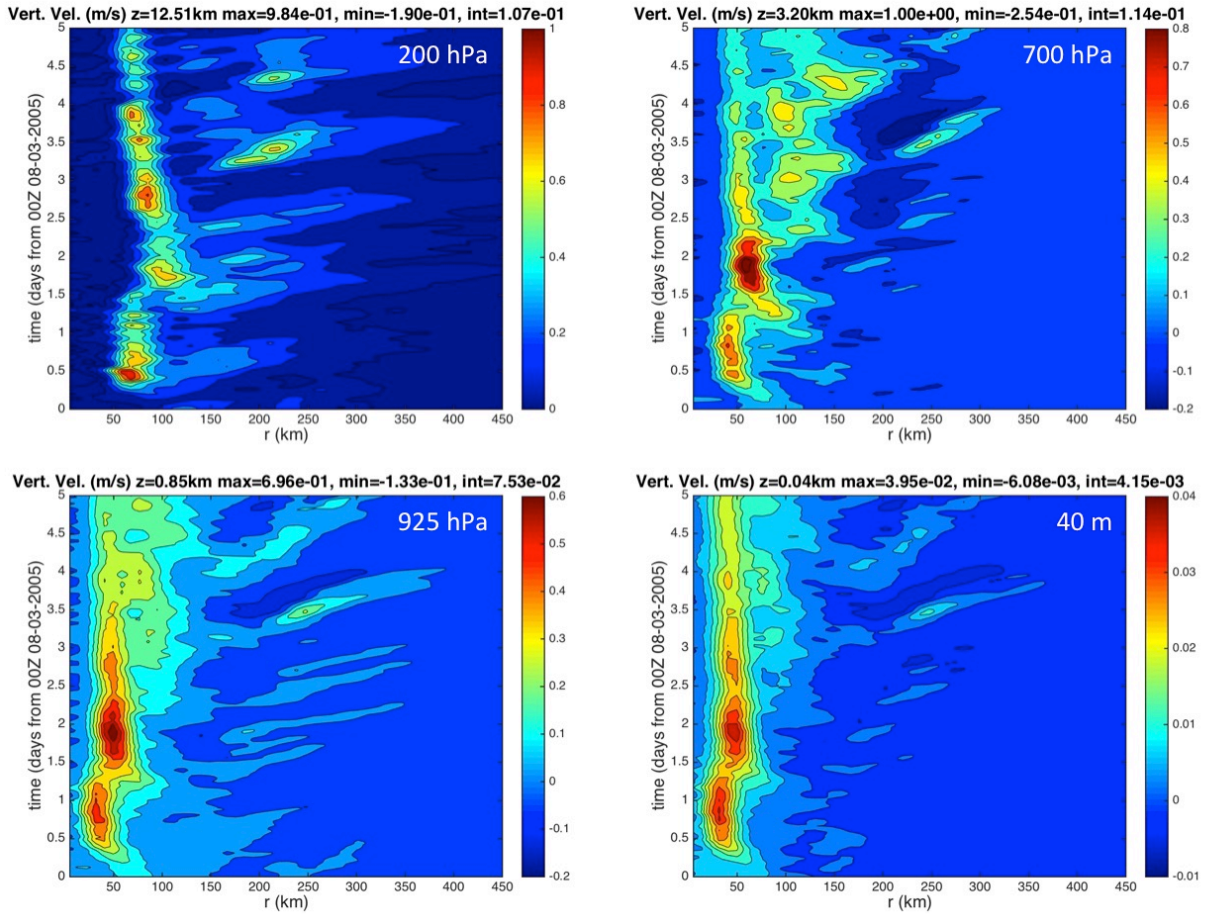

Figure 4.24: Hovmollers of azimuthally averaged vertical wind (m s^{-1}) derived from the 03-08 August NRH1 study period for 200 hPa, 700 hPa, 925 hPa, and 40 m. Radii are analyzed relative to the TC center and extend out to 450 km.

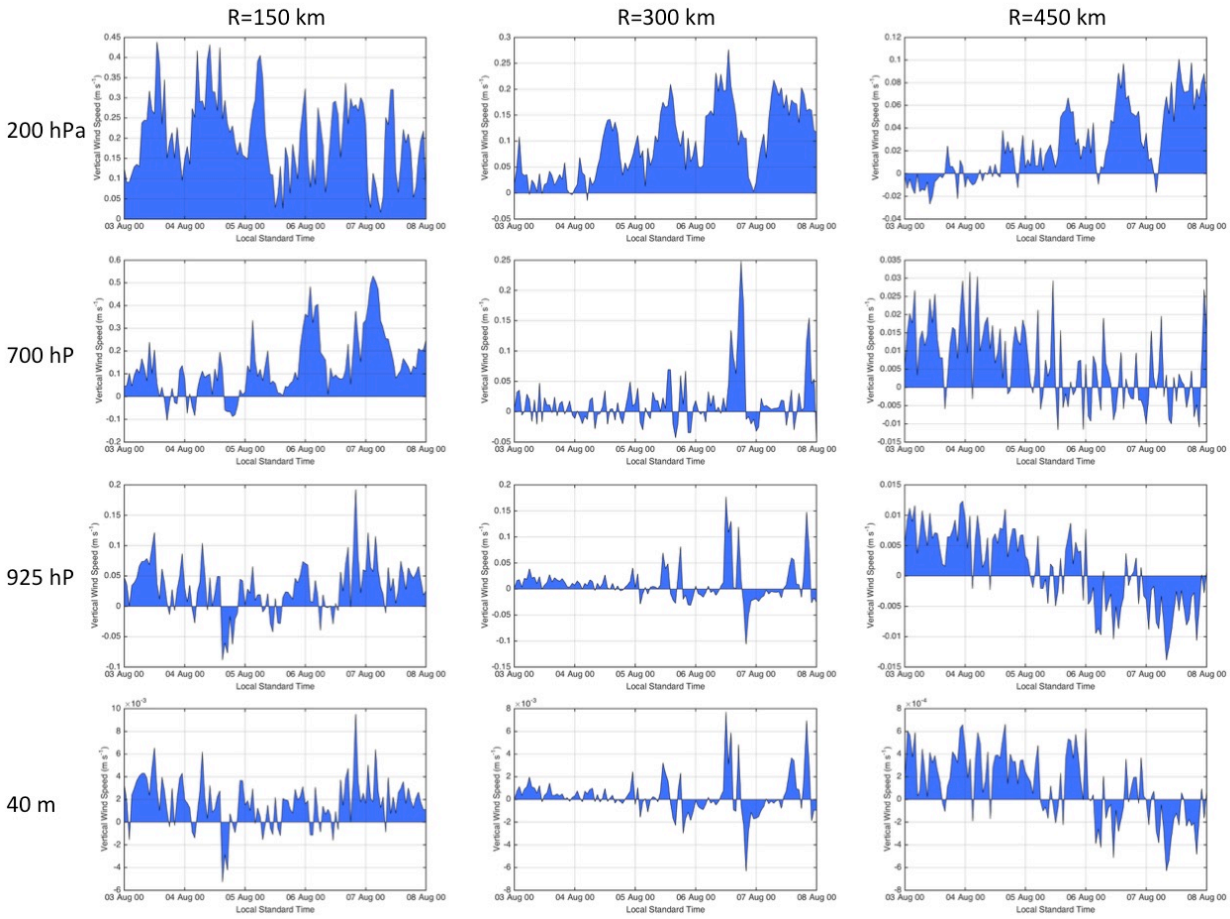

Figure 4.25: Plots of azimuthally averaged vertical wind (m s^{-1}) derived from the 03-08 August NRH1 study period for the 200 hPa, 700 hPa, 925 (hPa), and 40 m vertical levels. Analyses include the 150, 300, and 450 km radii.

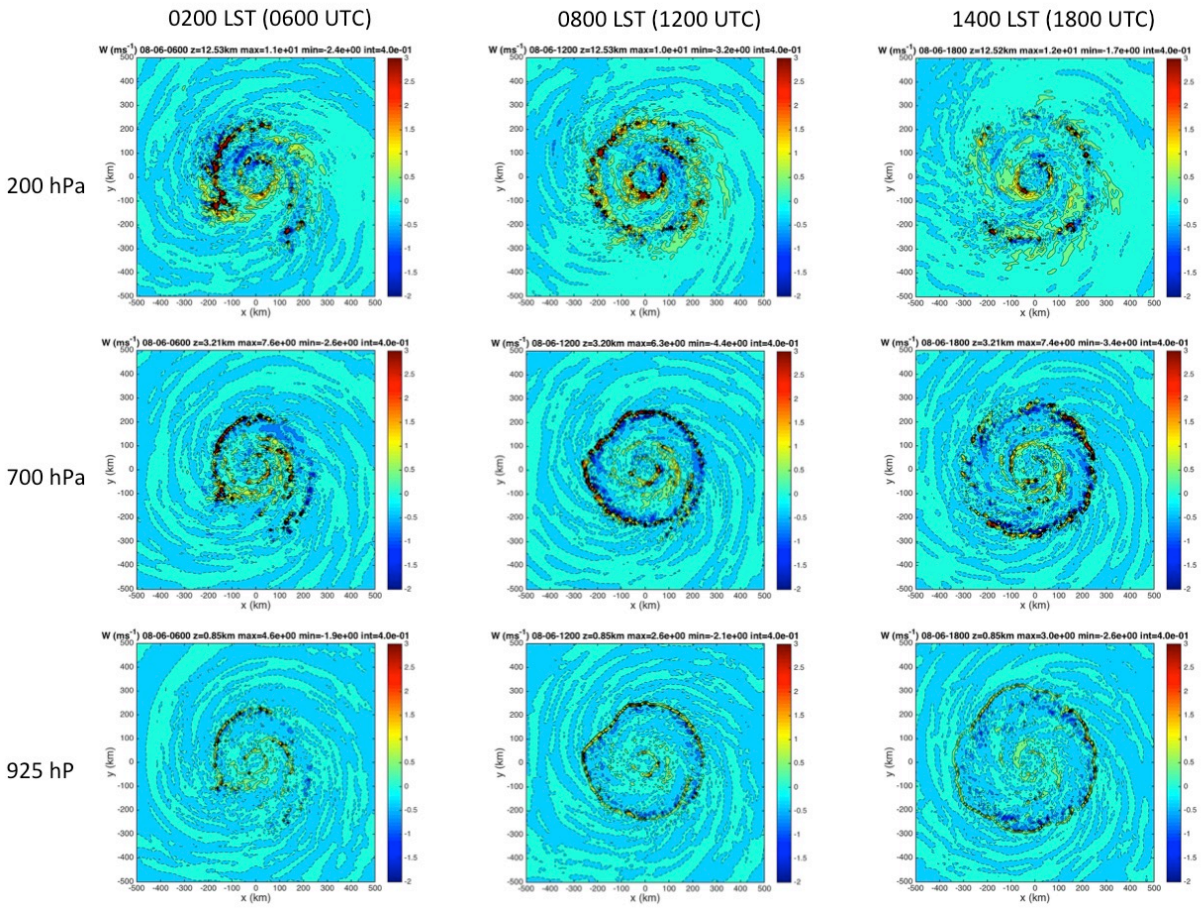

Figure 4.26: Plots of vertical wind (m s^{-1}) derived from the NRH1 from 0200-1400 LST (0600-1800 UTC) on 06 August at 200 hPa, 700, and 925 hPa. A relatively deep layer semi-circular feature is indicated 200-300 km outside of the eyewall that has 1-3 m s^{-1} vertical motion and is propagating away from the TC.

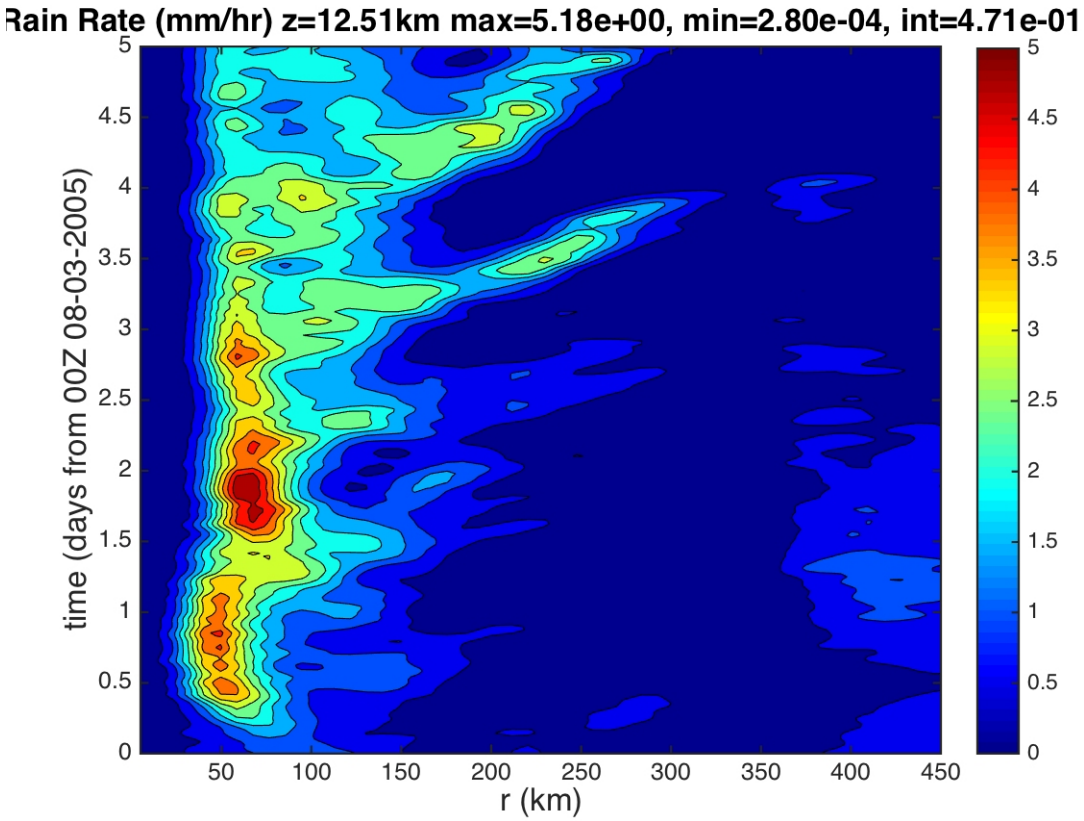

Figure 4.27: Hovmoller of rain rate (mm h^{-1}) derived from the 03-08 August NRH1 study period. Radius is analyzed relative to the TC center and extends out to R=450 km.

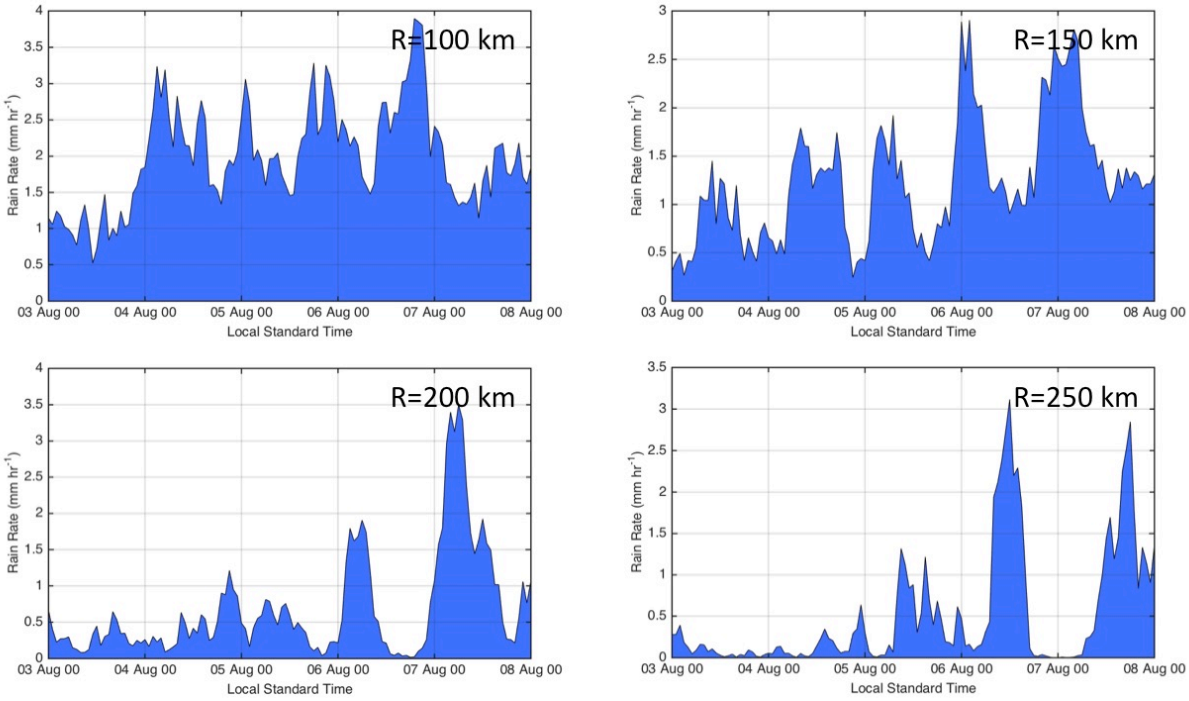

Figure 4.28: Plots of azimuthally averaged rain rate (mm hr^{-1}) derived from the 03-08 August NRH1 study period at the 100, 150, 200, and 250 km radii.

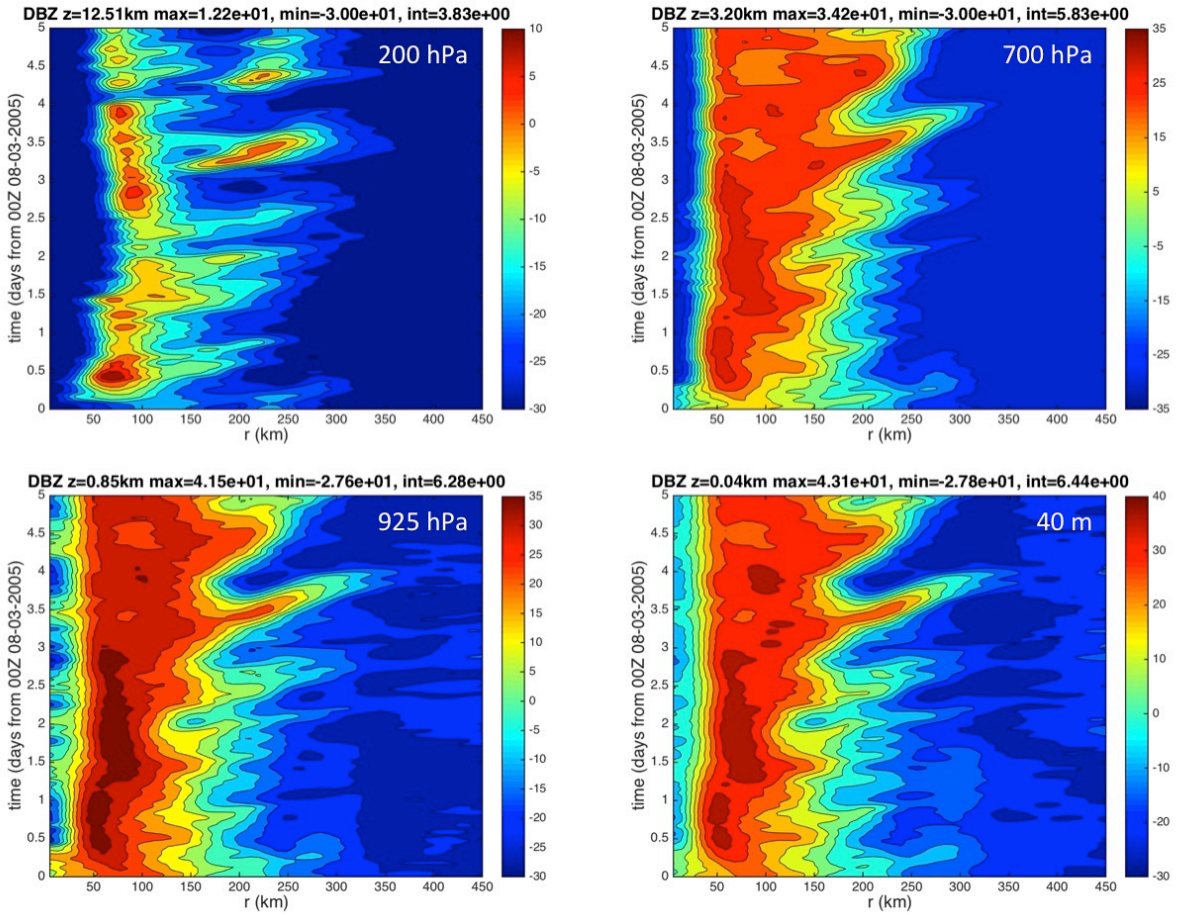

Figure 4.29: Hovmollers of simulated radar reflectivity (dBZ) derived from the 03-08 August NRH1 study period for 200 hPa, 700 hPa, 925 hPa, and 40 m. Radii are analyzed relative to the TC center and extend out to R=450 km.

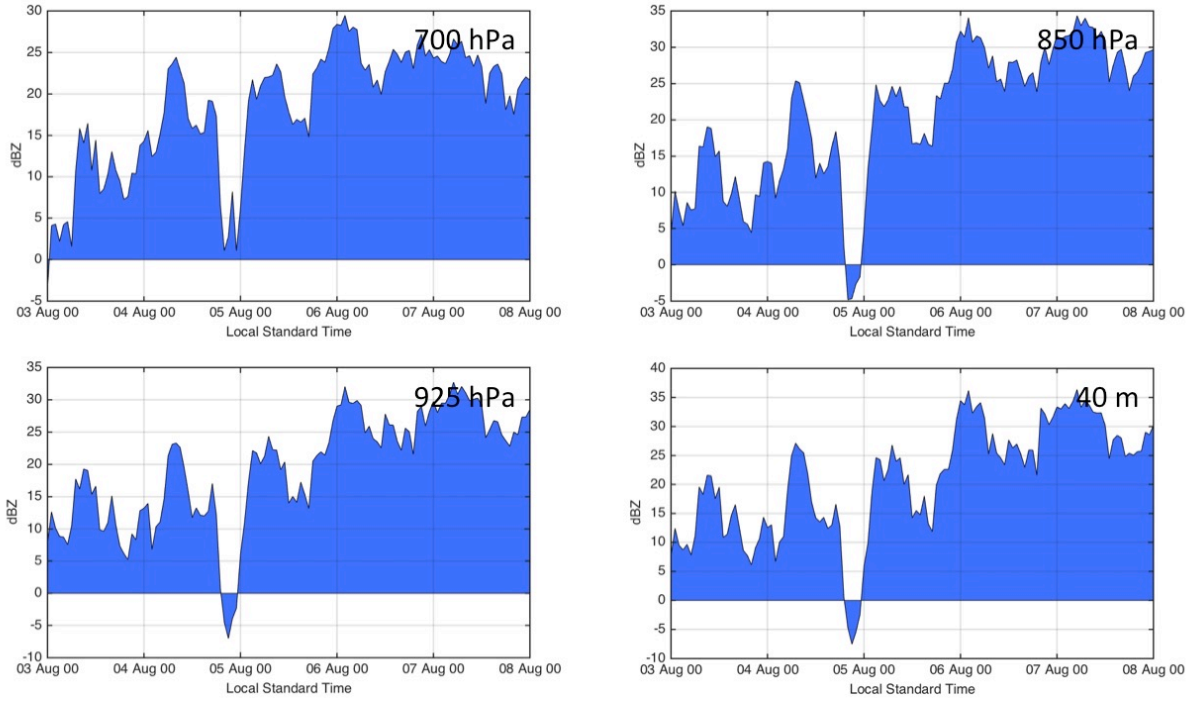

Figure 4.30: Plots of simulated radar reflectivity (dBZ) derived from the 03-08 August NRH1 study period for the 700 hPa, 850 hPa, 925 (hPa), and 40 m vertical levels and analyzed at the 150 km radius.

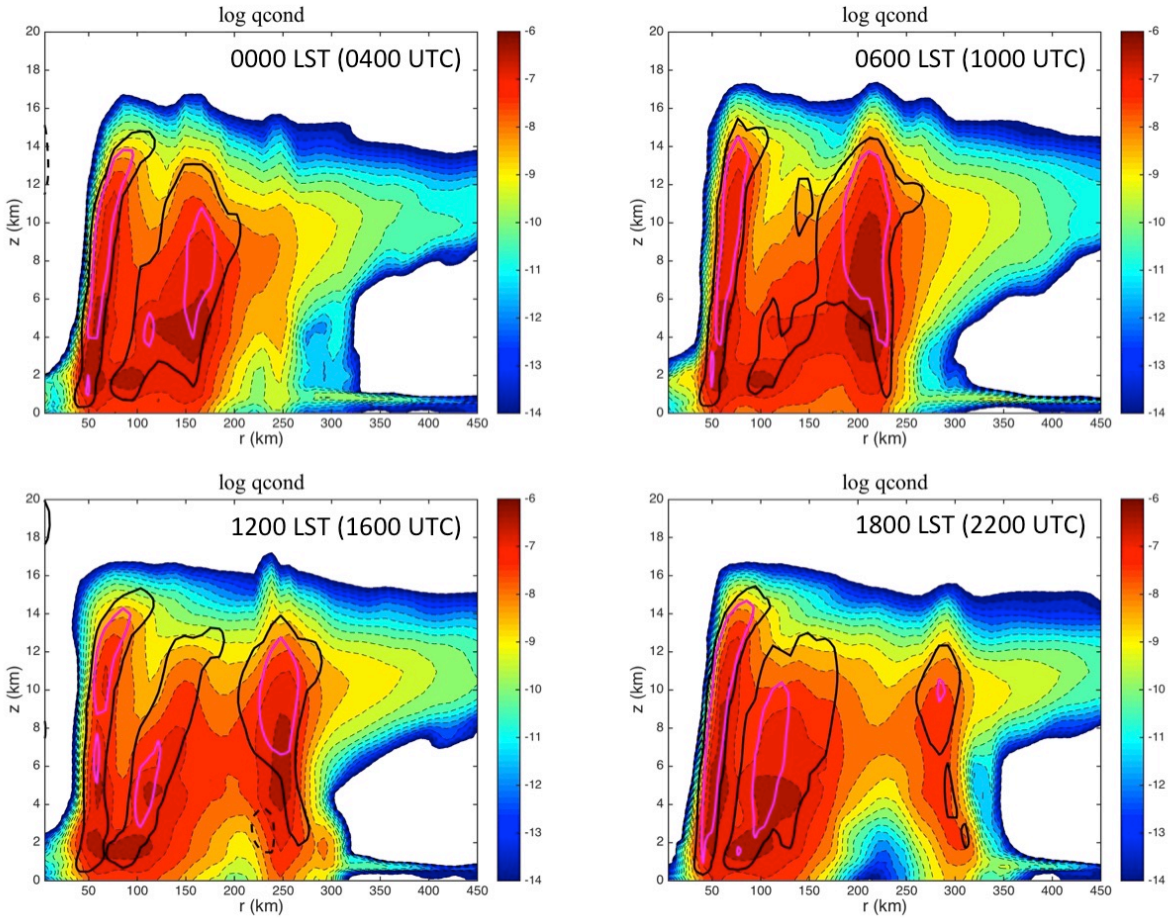

Figure 4.31: 6-hourly radius-height plots of Q-condensate from the NRH1 on 06 August from 0000-1800 LST (0400-2200 UTC). Dashed black, solid black, and magenta contours indicate azimuthal mean vertical winds of -0.25 ms^{-1}, +0.25 ms^{-1}, and +0.5 ms^{-1} respectively.

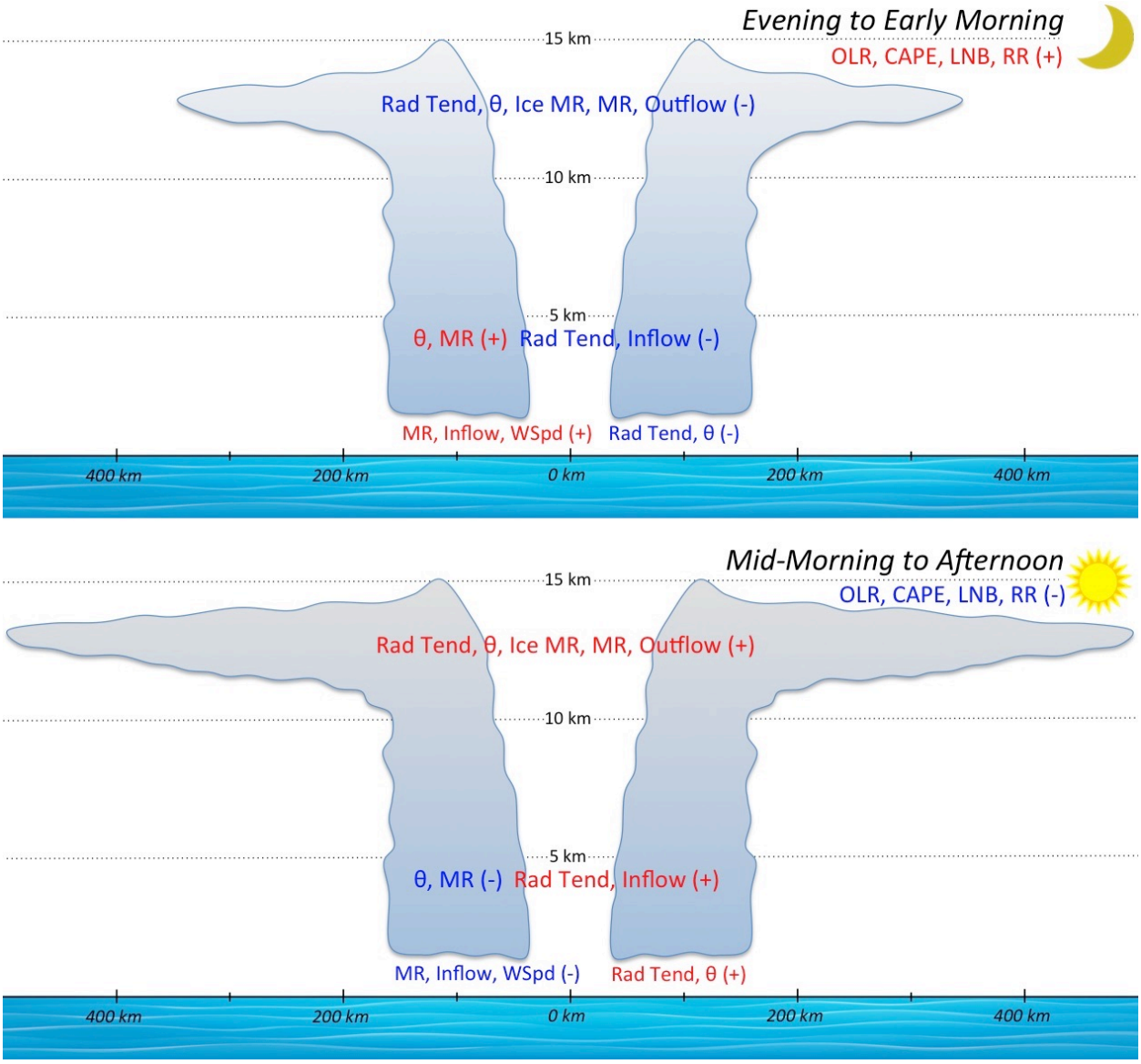

Figure 4.32: Schematic showing a TC in the (top) initial (i.e. nighttime) and (bottom) later (i.e. daytime) stages of the TCDC. The cross sections show background state parameters of total radiation tendency (Rad Tend, K hr^{-1}), θ (K), ice mixing ratio (Ice MR, g kg^{-1}), Vr-indicated inflow/outflow (inflow/outflow, m s^{-1}), and surface wind speed (WSpd, m s^{-1}) at different levels of the storm. Single level/layer values of OLR (W m^2), CAPE (J kg^{-1}), LNB) (height), and rain rate (mm h^{-1}) are labeled at the top right of each plot. Red (blue) lettering indicates diurnal maxima (minima) of the various parameters. The (bottom) nighttime cross section has an outflow layer with a larger radial extent and higher values of ice mixing ratio (darker shading at the top of the storm) compared to the (top) nighttime cross section.

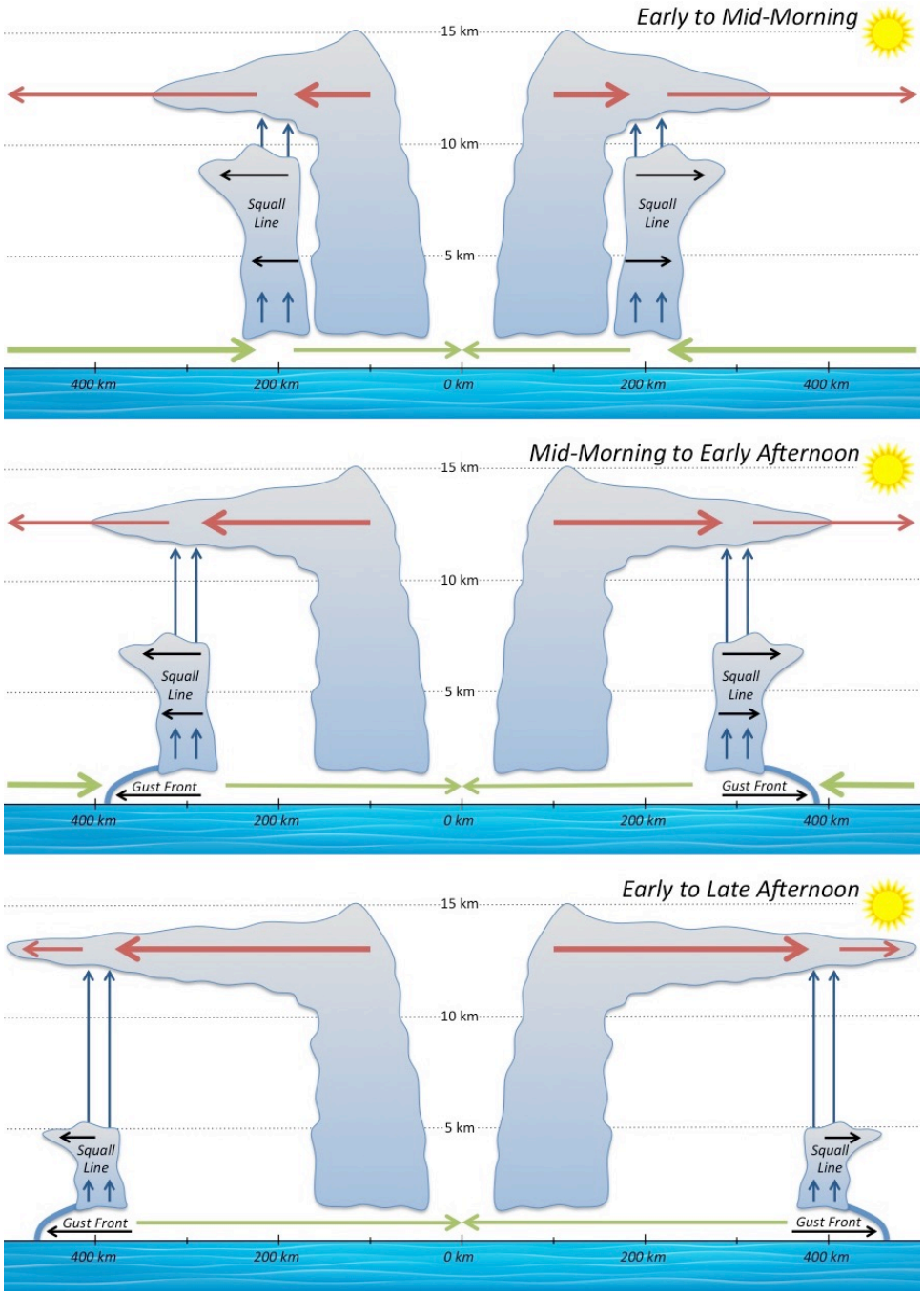

Figure 4.33: Schematic showing the evolution of a radially propagating TC diurnal pulse from the early morning to late afternoon. Upper level radial outflow (red arrows), lower level radial inflow (green arrows), and enhanced vertical wind at the location of the TC diurnal pulse (i.e. squall line, blue arrows) are shown. Gust fronts favored to form along the leading edge of the squall line beginning in the mid-morning to late afternoon when it is located at R~300-400 km are shown. Thickness of the radial outflow and inflow lines indicate relative strength at different times of day relative to the position of the squall line. The depth of the squall line is also suggested to lessen as it propagates away from the storm due to a lowering LNB that reaches a minimum in the afternoon.

5. Investigating the TC Diurnal Cycle Using an Idealized Hurricane Model

5.1 Introduction

This chapter will highlight the TCDC using idealized hurricane simulations in the WRF model. The main goal of the idealized hurricane simulation discussions will be to test the hypothesis that by varying the solar cycle in an idealized numerical simulation of a mature TC, the thermodynamic and kinematic TCDC signals that were identified in Chapter 4 analyses of the NRH1 simulation will be altered and perhaps provide insight regarding how these signals are manifested in the model. This was addressed using 3 versions of the idealized model described in Secs. 2.1.3 and 2.2.3: 1) a control run with a normal solar cycle; 2) a daytime-only experiment (with a constant local noon solar zenith angle starting at 40 hr into simulation; Sec. 2.1.3); and 3) a nighttime-only experiment (with a constant local midnight solar zenith angle starting at 28 hr into simulation; Sec. 2.1.3). Discussion will include thermodynamic and kinematic differences between these 3 idealized simulations, as well as comparisons of these simulations to the NRH1 that was highlighted in Chapter 4.

5.2 Idealized Hurricane Simulations

5.2.1 Intensity

The idealized hurricane simulations that are described here were all strong category 3 (52 m s^{-1}) hurricanes at time=0 and were located in favorable environments of low vertical wind shear, high SSTs, and a moist middle to lower level atmosphere (Secs. 2.1.3 and 2.2.3). However, each storm exhibited unique trends in intensity (defined by maximum 10-m surface winds minimal surface pressure (Fig. 5.1). It should be noted that simulation experienced an

initial vortex spin up in the first 24-48 hr and quickly reached category 3 intensity shortly after 72 hr. The control run experienced its peak lifecycle wind intensity (106 kt) at ~84 hr and lowest pressure (948 hPa) ~6 hr later. The maximum wind speed trends show 3 distinct periods of intensity for this run: a fairly steady state period of category 3 intensity from ~87-126 hr, followed by steady weakening from 126-141 hr, followed lastly by an interval of fairly steady category 2 intensity. The daytime-only simulation showed a similar 2-step trend in maximum surface winds with timing that was very similar to the control run. However, there were 2 interesting differences between the control and daytime-only simulations: first, the surface winds in the daytime-only run decreased more rapidly during the latter half of the simulation; and second, the minimum surface pressure in the daytime-only run was by far the lowest of any of the 3 runs throughout the 168 hr simulation period. Similar to the control run, the nighttime-only simulation exhibited a period of fairly steady state surface wind intensity during the initial half of the simulation (~72-135 hr). However, after this period, the storm weakened fairly rapidly from a category 3 to a category 1 hurricane and continued weakening until the end of the simulation.

Each of the 3 simulated idealized hurricanes that were analyzed exhibited unique trends in intensity (defined by maximum surface wind and minimum surface pressure), but no diurnal variability of intensity was noted in any of the storms. Although the idealized simulation control run exhibited the strongest surface wind intensity, the daytime-only simulation reached the lowest surface pressure. The nighttime-only simulation experienced the steadiest weakening during the latter ~36 hr of its simulation, eventually became the weakest of the 3 simulated hurricanes, and also had the highest surface pressures throughout the 168 hr simulation period.

5.2.2 Thermodynamics

Analyses of the idealized hurricane simulations were made to investigate possible diurnal signals at various atmospheric levels (e.g. 150, 200, 700, and 925 hPa) and radii. For the control run, there were distinct upper level (e.g. 150 and 200 hPa) diurnal fluctuations in temperature from R=100-500 km that were especially pronounced at 150 hPa and appeared to be radially propagating (~5-10 ms^{-1}) at 200 hPa (Fig. 5.2). The enhanced TCDC signal at 150 hPa could be related to the simulated TC having an outflow layer that is concentrated slightly above 200 hPa, a hypothesis that is corroborated by analyses of radial wind in the next section. The TCDC patterns in these analyses suggest that preferred daytime shortwave warming and nighttime longwave cooling of the TC cirrus canopy is occurring at the upper-levels of the TC (see cloud-cloud-free differential heating mechanism; Sec. 4.6). Similar to the NRH1 TC, these diurnal oscillations were more pronounced outside the TC inner core (e.g. R~150-500 km) and ranged from ~2-3 K.

Diurnal signals in temperature were not discernable in the upper-levels for the constant day simulation, but were surprisingly detectable from 0-96 hr in the constant night simulation (Fig. 5.2). For the daytime-only run, it is hypothesized that since shortwave warming is always greater than longwave cooling (Sec. 4.2.2), in the absence of nighttime conditions constant daytime shortwave warming that is concentrated in the area of the cirrus canopy (beginning at 40 hr) results in widespread middle to upper level warming as the simulation progresses with temperatures that quickly become the warmest of the 3 runs (see Sec. 4.2.2). As discussed in Sec. 4.3.3, this middle to upper level warming could result in a warming environmental profile that would lower the LNB and hence lower CAPE (not shown), particularly at R≥ 150 km.

For the nighttime-only run, there were indications of a diurnal temperature pattern at 200 hPa in the first 96 hours of the simulation that appears to reach out farther radially with time, but becomes undetectable past 96 hr. Since the normal solar cycle was employed in the constant night case for the first 28 hr of the simulation (to promote a smoother transition of the simulation to a constant daytime solar zenith angle; Sec. 2.1.3), it appears that the TCDC and associated TC diurnal pulse were initiated in this early period, but were not able to maintain a robust and detectable signal once the environment experienced constant night conditions (beginning at 28 hr in to the simulation). It is hypothesized that during the initial 28 hr period when a normal solar cycle was used in the nighttime-only run, the TCDC forcing mechanisms discussed in Chapter 3: radiatively reduced outflow resistance (Sec. 3.6.2), cloud-cloud-free differential heating mechanism (Sec. 3.6.3), and direct radiation-convection interactions (Sec. 3.6.3) may have been taking root and will be discussed and will be summarized in Sec. 5.2.5. As discussed in Sec. 4.3.3, middle to upper level cooling in the nighttime-only run could also result in reduced static stability by raising the level of neutral buoyancy and hence increasing CAPE (not shown), particularly at $R \geq 150$ km.

Temperature analyses in the lower to middle levels (e.g. 700 and 925 hPa) suggest that at 700 hPa, none of the 3 simulations has a robust diurnal temperature signal (Fig. 5.3). Also, at 925 hPa only the control run has a discernable diurnal signal that is most pronounced at R~200-450 km and is similar to NRH1 analyses that were discussed in Chapter 4.3.1. It is appears that at these peripheral radii, the cooling that is occurring from the mid-morning to early afternoon from 48-144 hr is coincident with periods of enhanced radial wind (discussed in the next section). This cooling could be related to radial surges in the cirrus canopy that are reducing

shortwave radiation or to radially propagating outflow boundaries that appear to be linked to TC diurnal pulses (Sec. 4.3.1).

Analyses of mixing ratio in the idealized hurricane simulations were also made at various atmospheric levels (e.g. 150, 200, 700, and 925 hPa) and radii. For the control run, there was a distinct diurnal pattern in moisture that, similar to the NRH1 (Chapter 4.3.2), was detectable in the upper-levels (e.g. 150 and 200 hPa), not present in the middle levels (e.g. 700 hPa), and again detectable in the lower levels (e.g. 925 hPa; Figs. 5.4 and 5.5). Also similar to the NRH1 analyses, the upper and lower level diurnal variations were most concentrated at R~150-450 km. Upper level TCDC moisture fluctuations were not readily detectable in either the daytime-only and nighttime-only simulations (Figs. 5.4 and 5.5), suggesting that even when a normal solar cycle is applied to the initial 28-40 hr of the simulations, diurnal surges in the cirrus canopy that were discussed in Chapter 4 are not occurring (or are not detectable) in these simulations. The lower to middle levels of the daytime-only run were the moistest of the 3 simulations at all radii and could be related to its relatively warmer temperatures and hence, increased capacity to hold moisture. Although this would suggest that the environment outside of the inner core (e.g. R≥150-500 km) might be more conducive for convective development in this region where convectively active TC diurnal pulses radially propagate, this was not the case and is shown in the next section. This suggests that similar to the NRH1 discussed in Chapter 4 (and indicated in Fig. 5.2), preferred middle to upper level shortwave warming of the daytime-only TC outflow layer during the day is acting to stabilize the overall environment, even when relatively moist conditions exits in the lower to middle levels.

Thermodynamic analyses of the 3 idealized simulations suggest that a constant day TC environment is not conducive to producing TCDC signals, even when a normal solar cycle is

applied to the initial 40 hr of the run. It is hypothesized that constant-daytime conditions act to continuously stabilize the TC environment, hence suppressing convection. Although constant night conditions do appear to be able to sustain a detectable TCDC pattern in temperature for a few days (if a normal solar cycle is applied for the first 28 hr of the simulation), that signal quickly diminishes over time. It is hypothesized that nighttime radiation tendencies act to prime (i.e. destabilize) the TC environment and may be important for initiating the TCDC thermodynamic signal in the TC inner core and that a fluctuating solar cycle is a necessary ingredient for sustaining it over time and propagating that signal to peripheral radii. This will be discussed further in the analyses of precipitation that are presented in Sec. 5.2.4.

5.2.3 Winds

Analyses of radial winds (V_r) in the idealized hurricane simulations were made to investigate possible diurnal signals at various atmospheric levels (e.g. 150, 200, 700, and 925 hPa) and radii. Like the NRH1 (Chapter 4.4.2), the control run has a robust diurnal signal in the upper levels (150 hPa) with bursts of outflow that occur in the morning/early afternoon and are approximately a factor of 2 stronger than interspersed diurnal minima (Fig. 5.6). There is also a notable diurnal pattern of V_r at 200 hPa with peaks in radial outflow that tend to occur in the mid-morning to afternoon hours, but is not as well defined as the patterns at 150 hPa, simply suggesting that the outflow layer in the idealized TCs is concentrated slightly above 200 hPa. The constant-day and especially constant-night simulations do occasionally exhibit bursts and lulls in upper level outflow, but these fluctuations do not have a regular diurnal signature as seen in the control run (Fig. 5.6). These surges in V_r appear to be related to bursts in inner core convection (discussed in the next section) that may be partly related to the timing of when the

prescribed solar cycles switched from a normal cycle to a nighttime-only (28 hr) or daytime-only (40 hr) cycle in the respective simulations.

Analyses of V_r in the middle levels (e.g. 700 hPa) has no obvious diurnal signal in the control run, though there are periods of near zero inflow that are interspersed with times of weak outflow (~1-3 m s^{-1}; Fig. 5.7). The constant-day and constant-night simulations both show slight diurnal fluctuations of inflow and outflow, but only during the initial 24-40 hours when the runs incorporate a normal solar cycle (Fig. 5.7). Similar to temperature (Sec. 5.2.2), middle level diurnal signals in V_r disappear shortly after the solar cycle is removed and held constant at local noon and local midnight respectively. None of the middle level analyses suggest a diurnal signal in V_r that could be linked to changes in TC structure or intensity (e.g. diurnal surges in middle level inflow that could promote ventilation at these levels). Analyses of V_r in the lower levels shows a more robust diurnal signal in the control run and marked diurnal signals in the first few days of the constant-day and constant-night simulations. However, the diurnal patterns in these latter two simulations begin to wane and lower level inflow (e.g. 4-8 m s^{-1} inflow) becomes less radially extensive within a few days of the normal solar cycle being removed from the model run (e.g. after 72-84 hr; Fig. 5.7). Figure 5.7 suggests that the TCDC provides a mechanism for the storm to periodically "reach out" to the surrounding environment via surges in the radial extent of lower level inflow. During these times, the TC would be most vulnerable to effects of an unfavorable surrounding environment (e.g. low entropy air) when radial entrainment would be favored. In contrast, there are periods in the control run when diurnal surges in lower level V_r are at a minimum (mid-morning to afternoon) or in the daytime-only and nighttime-only simulations when there is no longer a robust signal in V_r (after ~72 and 84 hr respectively). These times in the simulations could represent intervals when the TC is most protected or insulated from the

potentially negative influences of a hostile surrounding environment. Since the moist tropical sounding (Dunion 2011) was used in the 3 idealized simulations (Sec. 2.1.3), the surrounding environments of these storms were not hostile (i.e. contained relatively high entropy air). However, future work could include prescribing a moist tropical sounding in the inner core region of the storm and a Saharan Air Layer or mid-latitude dry air intrusion sounding (Dunion 2011) at the radius range of ~250-500 km as a means to explore the impact of diurnal fluctuations of V_r on TC structure and intensity.

The NRH1 TC exhibited marked diurnal fluctuations of tangential wind (V_t) that were evident throughout the troposphere and at radii ranging from 150-450 km. None of the 3 idealized hurricane simulations showed robust diurnal fluctuations of V_t and it is not entirely clear why in the case of the control run this is so (Figs. 5.8 and 5.9). Analyses of vertical wind (w; Figs. 5.10 and 5.11) also do not show clear TCDC signals in azimuthally averaged fields. One possible explanation relates to the discussion of vertical wind in the NRH1 (Chapter 4.4.4). Although diurnal w signals in the NRH1 TC were not consistently well defined when averaged azimuthally, 2-dimensional map analyses showed distinct rings of enhanced w propagating away from the storm each day (and hypothesized to be TC diurnal pulses that were discussed in Chapter 3). This discrepancy was caused by the fact that the signal of enhanced w in the NRH1 TC diurnal pulse was relatively narrow in width (~10-20 km) and not perfectly circular in shape (Fig. 4.26). This, in turn, caused the TCDC signal in w to be essentially undetectable when azimuthal calculations at various radii were made. Figure 5.12 shows 2-dimensional map analyses of w for the 3 idealized hurricane simulations at 0500, 0800, and 1100 LST. Though not as symmetric and defined as the NRH1 TC diurnal pulse signature, the control run and nighttime-only runs do show signs of a radially propagating feature in the w field that is

hundreds of kilometers in length, eventually reaches R~300 km and is especially evident in the western semicircle of the storm. The radial position of this feature closely matches the TC diurnal clock presented in Chapter 3 (Fig. 3.10) and it has a radial speed of ~5-7 m s^{-1}, which is similar to the propagation speed of satellite-observed and NRH1-observed diurnal pulses discussed in Chapters 3 and 4 respectively. Although there are some bands of enhanced w (1-3 m s^{-1}) at R~100-150 km in the daytime-only simulation a radially propagating diurnal pulse feature is not evident in this simulation and is consistent with the analyses of thermodynamics, V_r, and V_t, where the daytime-only simulation did not appear to support distinct TCDC signal. From the discussion in Sec. 4.3.3, it is hypothesized that constant shortwave warming of the TC cirrus outflow layer (e.g. z~8-14 km) would increase static stability outside the TC inner core (R≥150 km) by lowering the level of neutral buoyancy and hence lowering CAPE (not shown). Persistent daytime conditions would therefore promote a prolonged period of low CAPE that would not support convectively active TC diurnal pulses in this environment just outside the TC inner core.

5.2.4 Precipitation

Precipitation analyses of the 3 idealized TC simulations did not reveal the same robust radially propagating TCDC signals that were seen in the NRH1 (Sec. 4.5). However, there were some notable characteristics of the precipitation fields in these simulations (Fig. 5.13). For the control run, the 925 hPa inner core (R~50-150 km) precipitation tends to peak a few hours after 0000 UTC (evening to early morning) throughout the simulation and relative minima tend to occur in the mid-morning to afternoon, which is similar to the NRH1 analyses discussed in Sec.

4.5. These diurnal oscillations do become less defined later in the forecast, particularly around 120 hr when the hurricane starts to steadily weaken.

For the daytime-only idealized simulation, there is also an evening to early morning peak in precipitation shortly after 24 hr 0000 UTC that is followed by a relative minimum in the late morning to early afternoon (Fig. 5.13). It is perhaps not surprising that these diurnal fluctuations look similar to the control run, since the normal solar cycle was being applied until 40 hr into the simulation. After 40 hr however, the daytime-only run no longer exhibits diurnal precipitation variability and instead shows an extended period of enhanced inner core precipitation from ~48-96 hr that is followed by a period from ~96-168 hr that has the lowest precipitation values of any of the 3 simulations. It is possible that after the normal solar cycle was turned off, constant shortwave heating, as was discussed in Secs. 4.2.2 and 4.3.3, would have preferentially warmed the TC cirrus canopy over time (i.e. middle to upper levels of the TC), thereby steadily increasing static stability and eventually stifling inner core deep convection. In this scenario, a TCDC was initially established in the storm, but environmental conditions were not primed (i.e. conducive) to support its radial propagation. Although the current framework of this simulation did not allow for detailed analyses of radiation and static stability, this will be addressed in future work.

The nighttime-only simulation also exhibits an evening to early morning peak in precipitation shortly after 24 hr 0000 UTC that is followed by a relative minimum in the late morning to early afternoon (Fig. 5.13). Since nighttime-only conditions are not set until 28 hr into the simulation (Sec. 2.1.3), it is not surprising this period exhibits diurnal fluctuations in precipitation that are similar to the control run. However, unlike the control run, the period starting just after 48 hr does not continue to exhibit TCDC signals. In fact, from ~60-144 hr, the

nighttime-only run has an inner core region that is marked by fairly continuous 925 hPa precipitation that is generally more rigorous than both the control and the daytime-only runs. It is possible that after the normal solar cycle was turned off, in the absence of any shortwave warming, constant longwave cooling (discussed in Secs. 4.2.2 and 4.3.3) would have preferentially cooled the TC cirrus canopy (i.e. middle to upper levels of the TC), thereby reducing static stability and promoting a sustained period of inner core deep convection.

5.2.5 TCDC Processes

Analyses of thermodynamics and kinematics in 3 idealized hurricane simulations that are presented in Secs. 5.2.2-5.2.4 suggest several elements of the simulations that may have implications related to the representation of TCDC processes in the different model runs. First, similar to the NRH1, the idealized hurricane control run establishes marked TCDC signals in thermodynamics and winds that can be seen through a deep layer of the atmosphere. Second, the use of a normal solar cycle during the initial 28 and 40 hr of the daytime-only and nighttime-only simulations appears to have had lingering affects on each simulation, even 1-2 days after being set to constant day (or night) solar zenith angles. It is hypothesized that this lag relates to nighttime initiation of the TCDC during the time of a normal solar cycle that once started, continues overnight and into the next day, even if environmental conditions become less primed (i.e. conducive) support TCDC processes (e.g. if a constant-day solar cycle is prescribed to the simulation). Third, it appears that during and a few days after the period of the simulation when there is a normal solar cycle, temperature, moisture, radial wind, and vertical wind begin to exhibit diurnal fluctuations in the nighttime-only runs. Hovmollers of these parameters suggest that TCDC forcing mechanisms discussed in Chapter 3: radiatively reduced outflow resistance

(Sec. 3.6.2), cloud-cloud-free differential heating mechanism (Sec. 3.6.3), and direct radiation-convection interactions (Sec. 3.6.3) may have begun to be established. It is hypothesized that in the nighttime-only run, after the normal solar cycle was turned off and in the absence of any shortwave warming, constant longwave cooling (Secs. 4.2.2 and 4.3.3) would have preferentially cooled the TC cirrus canopy (i.e. middle to upper levels of the TC), thereby reducing static stability and promoting a sustained period of inner core deep convection in the storm. This longwave cooling would also destabilize the environment just outside the inner (R~150-350 km) core, elevating the level of neutral buoyancy and hence increasing CAPE, thereby promoting the formation of TC diurnal pulses. Lastly, only modest TCDC signals were found in the daytime-only run and only in the lower levels of the storm. It is possible that constant shortwave warming of the TC cirrus outflow layer (e.g. z~8-14 km) could increase static stability in the radius range of ~150-300 km by lowering the level of neutral buoyancy and hence lowering CAPE. Persistent daytime conditions would therefore promote a prolonged period of low CAPE that would not support convectively active TC diurnal pulses in this environment just outside the TC inner core.

The timing of the prescribed solar cycles in the 3 idealized simulations and differing affects of a normal solar cycle versus constant daytime versus constant nighttime conditions on shortwave and longwave radiation balances are likely promoting the expected TCDC signals in the control run, less robust TCDC signals in the nighttime-only simulations, and relatively muted signals in the daytime-only simulations.

5.3 Discussion and Conclusions

This chapter investigates aspects of the TCDC that include examining idealized hurricane simulations with normal, daytime-only, and nighttime-only solar cycles and comparing those simulations to NRH1 analyses discussed in Chapter 4 to identify similarities and differences that arise when the solar cycle is altered. Results show that the normal solar cycle is expectedly important for maintaining many of the TCDC signals that were seen in the NRH1 (Chapter 4). While an altered solar cycle simulation that begins with a normal solar cycle and transitions to a nighttime-only environment is only able to maintain TCDC signals for a relatively short time, equivalent daytime-only simulations have less detectable TCDC signals that may be related to differences in shortwave warming/longwave cooling that lead to differences in static stability in the storm environment. Several main conclusions can be made from the findings presented in this chapter:

- The 3 idealized model simulations exhibited unique trends in maximum surface winds and minimum surface pressure. The control run had the strongest surface winds, the daytime-only simulation reached the lowest surface pressure and the nighttime-only simulation experienced the steadiest weakening during the final ~36 hr of its lifecycle. The nighttime-only TC also became the weakest of the 3 simulated hurricanes and had the highest surface pressures throughout the 168 hr simulation period.
- Similar to findings in Chapters 3 and 4, the idealized hurricane control run establishes marked TCDC signals in thermodynamics and winds that can be seen through a deep layer of the atmosphere (~150-925 hPa).
- The normal solar cycle that was prescribed during the initial 28 and 40 hr of the daytime-only and nighttime-only idealized simulations appears to have had lingering

affects on these runs, with TCDC signals being detectable even 1-2 days after those simulations were set to constant day (or night) solar zenith angles. This may relate to nighttime initiation of the TCDC during the time of a normal solar cycle that once started, continues overnight and into the next day, even if environmental conditions become less primed to support TCDC processes.

- TCDC signals in the nighttime-only simulation are more robust and persist longer into the forecast than the daytime-only run. Once shortwave IR was turned off in this run, in the absence of any shortwave warming, constant longwave cooling preferentially cools the TC cirrus canopy, thereby cooling the environmental profile (and likely elevating the LNB, hence increasing CAPE) and promoting a sustained period of inner core deep convection. This cooling would also destabilize the environment just outside the TC inner core, elevating the level of neutral buoyancy and hence increasing CAPE, thereby promoting the formation of TC diurnal pulses in this region of the storm.
- TCDC signals in the daytime-only simulation are less robust and did not last as long into the simulation as the nighttime-only run. Constant shortwave warming of the TC cirrus outflow layer could warm the environmental profile in the radius range of ~150-300 km by lowering the LNB and hence lowering CAPE. Persistent daytime conditions would therefore promote a prolonged period of low CAPE where as was seen in 2-D analyses of vertical wind, the environment just outside the TC inner core could produce some rainband formation in the inner 100-150 km, but would not be sufficiently primed to support convectively active TC diurnal pulses that could propagate several hundred kilometers from the storm.

- Periods of diurnal surges in lower level radial inflow in the control run and the first 72-84 hr of the daytime-only and nighttime-only runs could represent times when the TC would be most vulnerable to effects of an unfavorable surrounding environment (e.g. intrusions of low entropy air) when radial entrainment would be favored.
- Times of diurnal minima in lower level radial inflow in the control run and the periods after these TCDC signals wane in the daytime-only and nighttime-only runs (after 72-84 hr) could represent intervals when the TC is most protected or insulated from the potentially negative influences of a hostile surrounding environment (e.g. intrusions of low entropy air) when radial entrainment would be reduced.

5.4 Figures

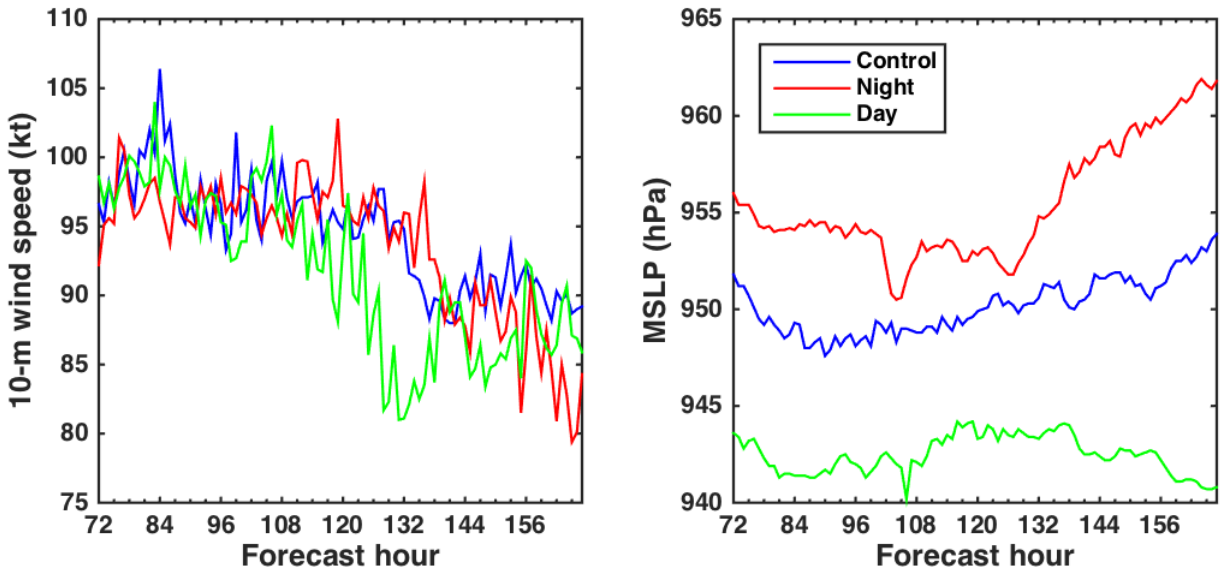

Figure 5.1: 3-hourly maximum 10-m wind speed (kt, left) and minimum surface pressure (hPa, right), for the idealized simulation control run (blue curves), nighttime-only (red curves), and daytime-only (green curves) for the 72-168 hr forecast period (07-11 Sep).

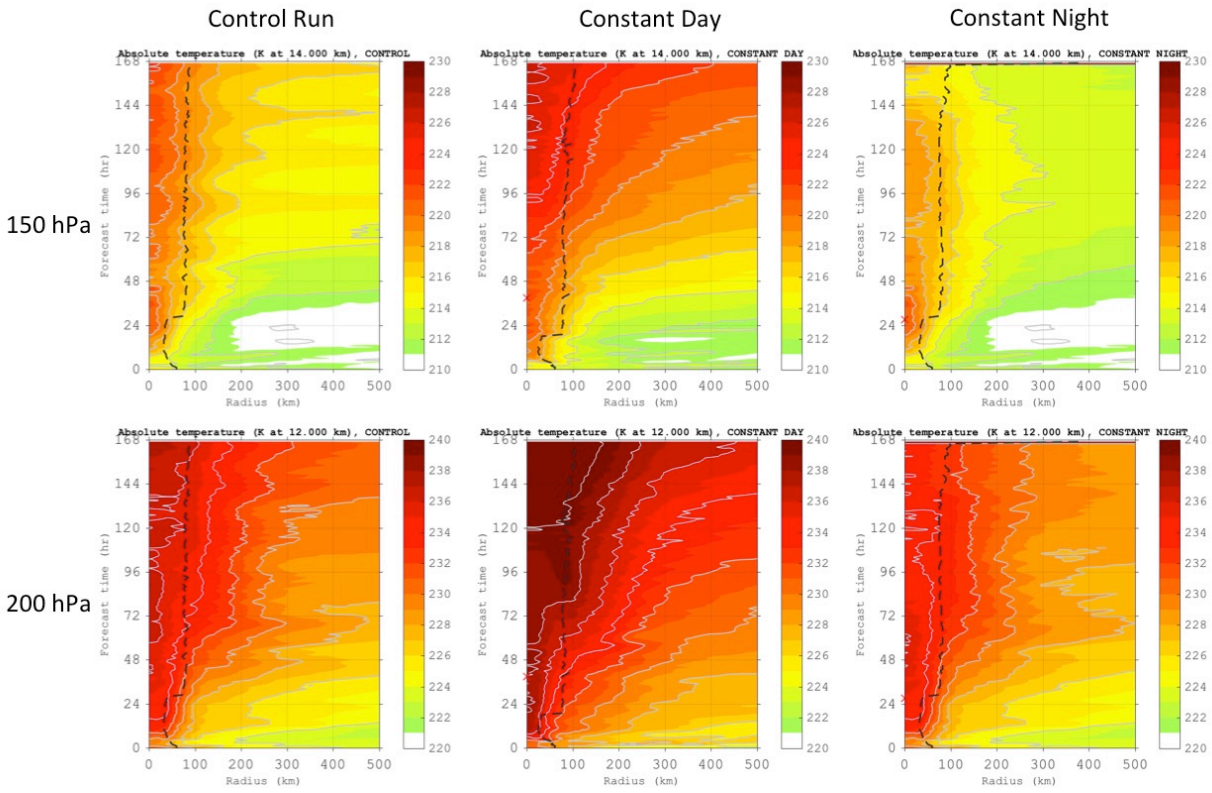

Figure 5.2: Hovmollers of azimuthally averaged temperature (K) derived from the idealized TC simulation for the control run, constant day, and constant night simulations. Red "X"s signify the time that the solar cycle was turned off in the daytime-only (40 hr) and nighttime-only (28 hr) simulations. Analyses and forecasts are derived from the 02-09 Sep 0000 UTC study period and show the 150 hPa (~14 km) and 200 hPa (~12 km) pressure levels. Radii are analyzed relative to the TC center and extend out to 500 km.

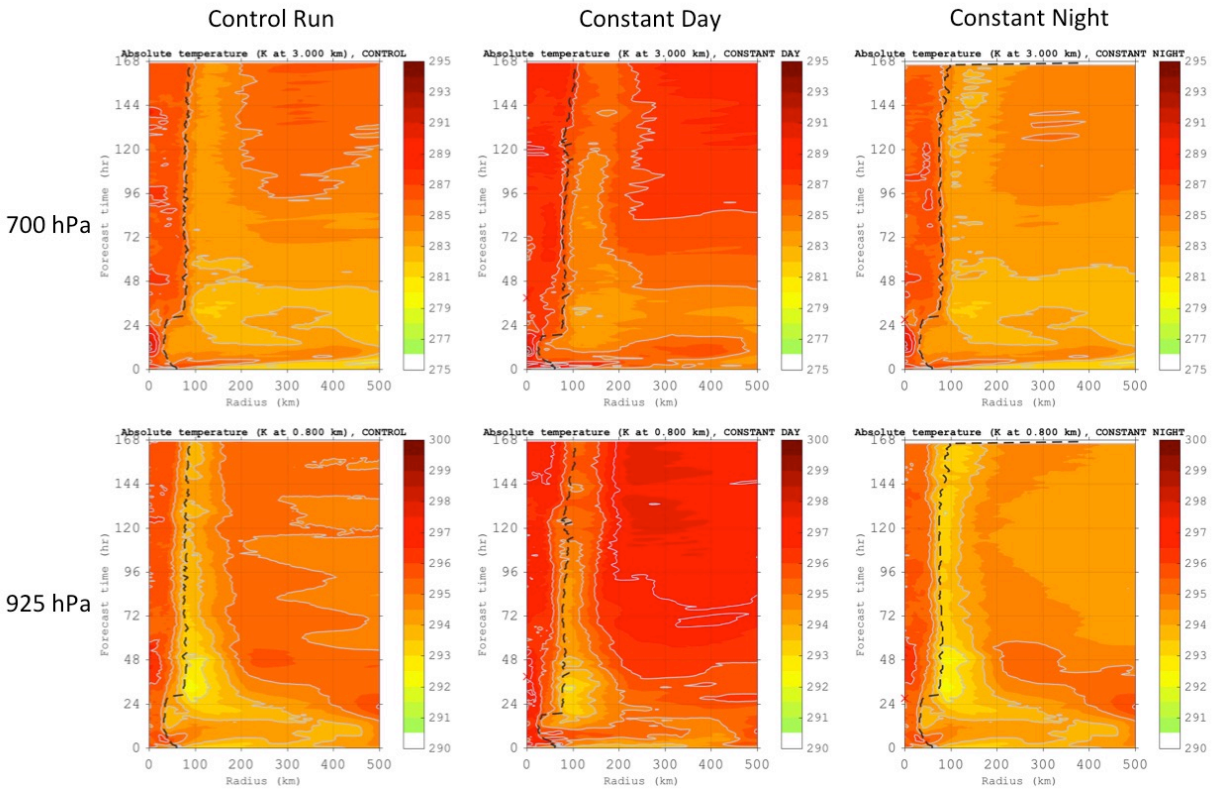

Figure 5.3: Hovmollers of azimuthally averaged temperature (K) derived from the idealized TC simulation for the control run, constant day, and constant night simulations. Red "X"s signify the time that the solar cycle was turned off in the daytime-only (40 hr) and nighttime-only (28 hr) simulations. Analyses and forecasts are derived from the 02-09 Sep 0000 UTC study period and show the 700 hPa (~3 km) and 925 hPa (~0.8 km) pressure levels. Radii are analyzed relative to the TC center and extend out to 500 km.

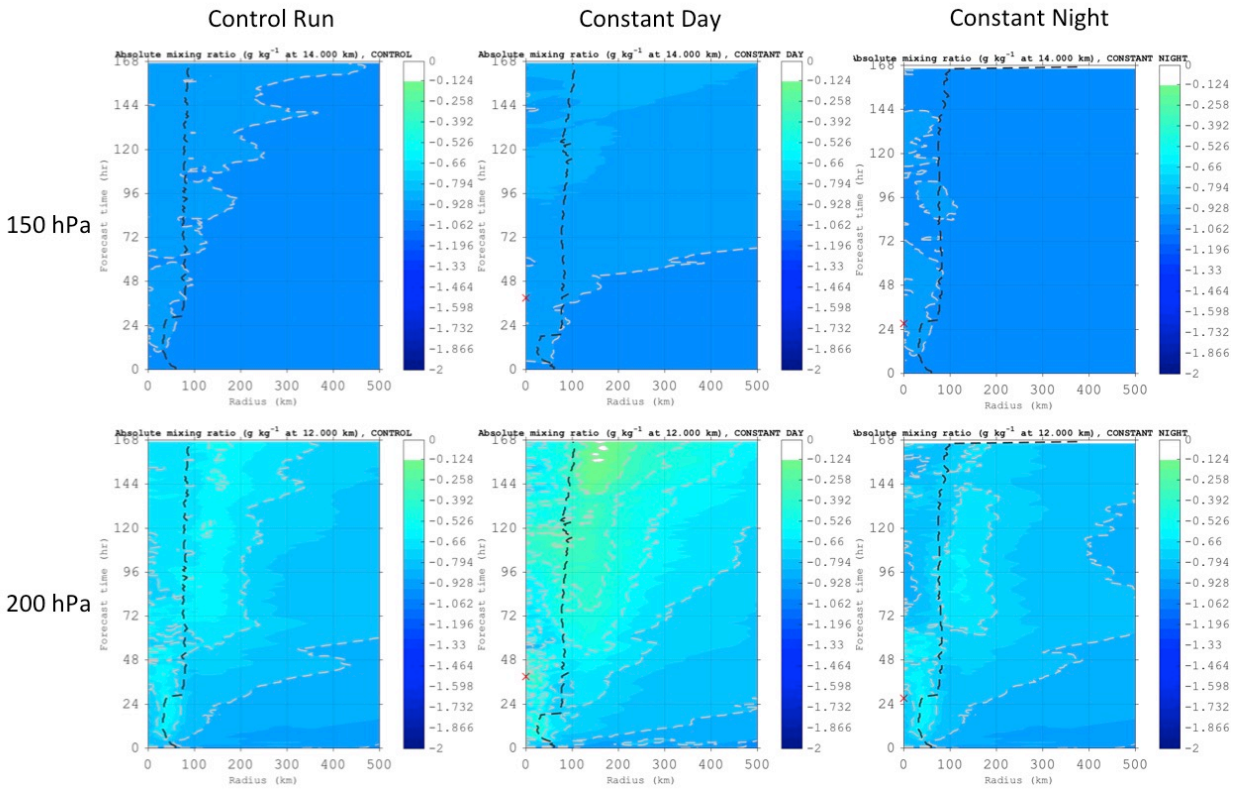

Figure 5.4: Hovmollers of azimuthally averaged mixing ratio (g kg^{-1}) derived from the idealized TC simulation for the control run, constant day, and constant night simulations. Red "X"s signify the time that the solar cycle was turned off in the daytime-only (40 hr) and nighttime-only (28 hr) simulations. Analyses and forecasts are derived from the 02-09 Sep 0000 UTC study period and show the 150 hPa (~14 km) and 200 hPa (~12 km) pressure levels. Radii are analyzed relative to the TC center and extend out to 500 km.

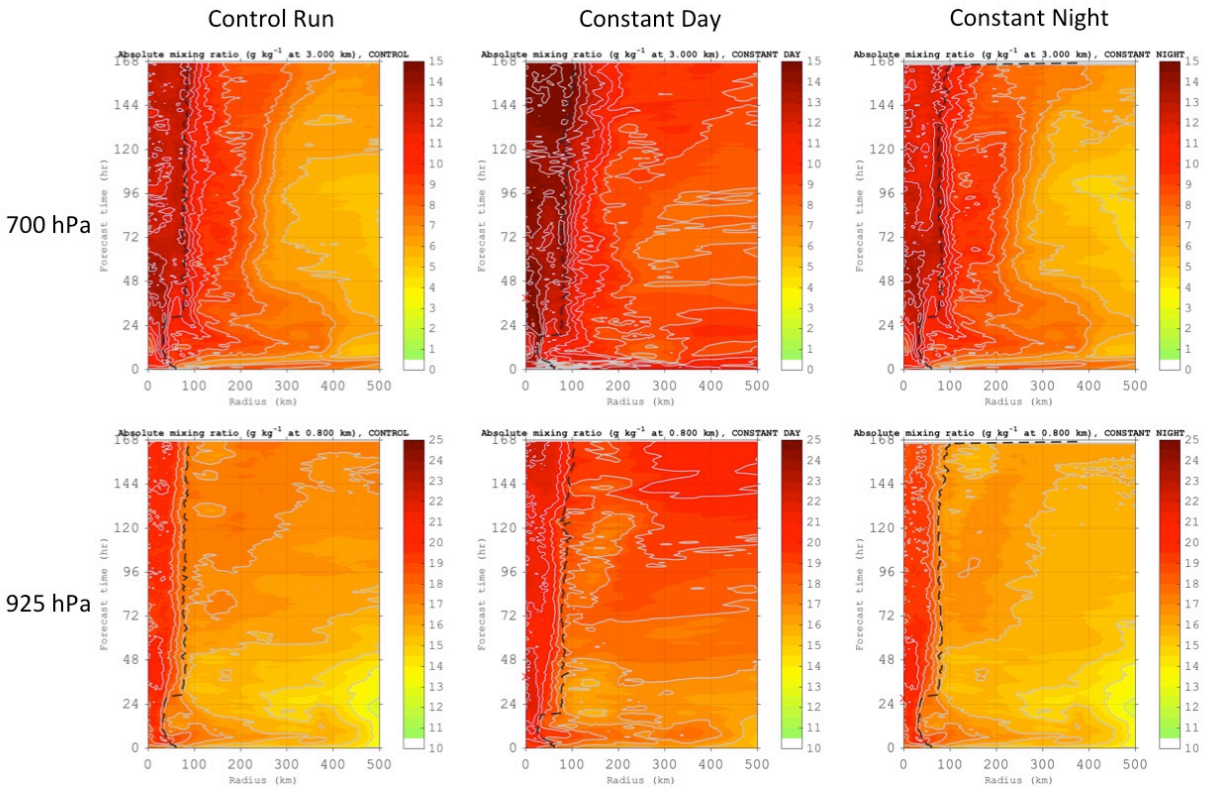

Figure 5.5: Hovmollers of azimuthally averaged mixing ratio (g kg^{-1}) derived from the idealized TC simulation for the control run, constant day, and constant night simulations. Red "X"s signify the time that the solar cycle was turned off in the daytime-only (40 hr) and nighttime-only (28 hr) simulations. Analyses and forecasts are derived from the 02-09 Sep 0000 UTC study period and show the 700 hPa (~3 km) and 925 hPa (~0.8 km) pressure levels. Radii are analyzed relative to the TC center and extend out to 500 km.

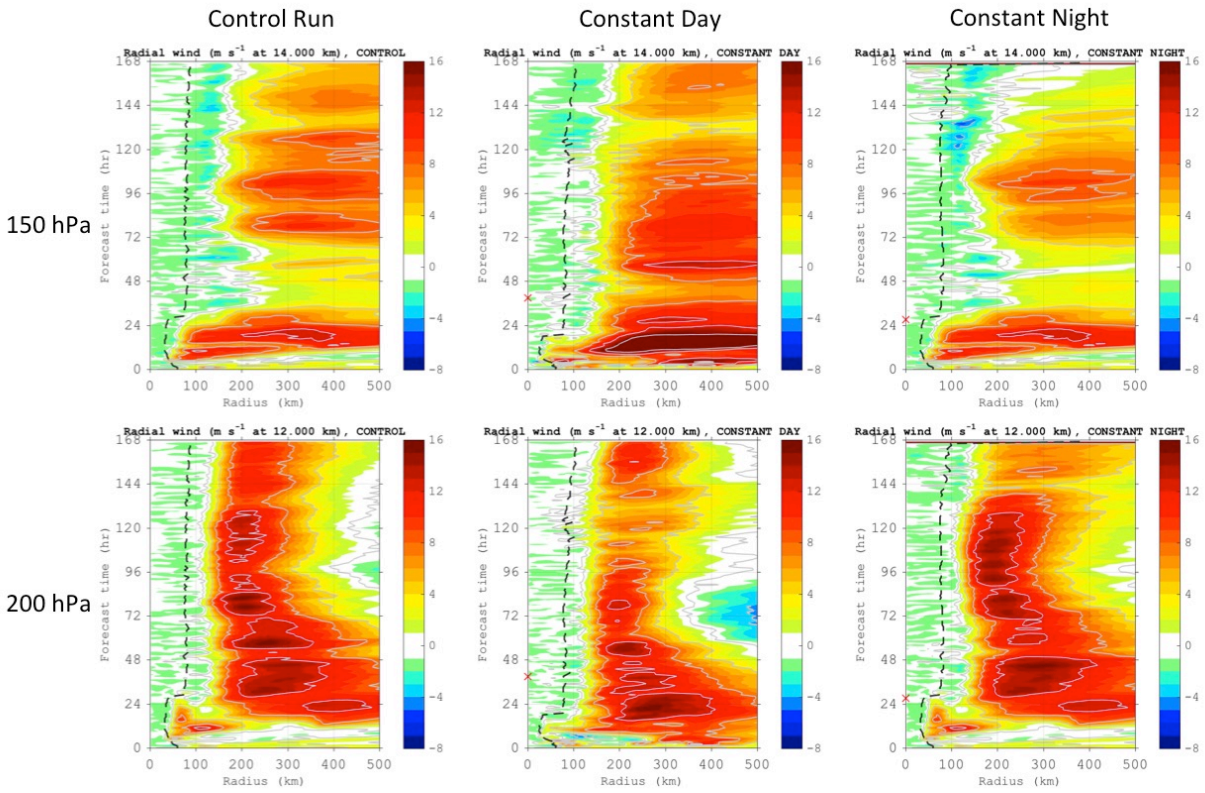

Figure 5.6: Hovmollers of azimuthally averaged radial wind (m s^{-1}) derived from the idealized TC simulation for the control run, constant day, and constant night simulations. Red "X"s signify the time that the solar cycle was turned off in the daytime-only (40 hr) and nighttime-only (28 hr) simulations. Analyses and forecasts are derived from the 02-09 Sep 0000 UTC study period and show the 150 hPa (~14 km) and 200 hPa (~12 km) pressure levels. Radii are analyzed relative to the TC center and extend out to 500 km.

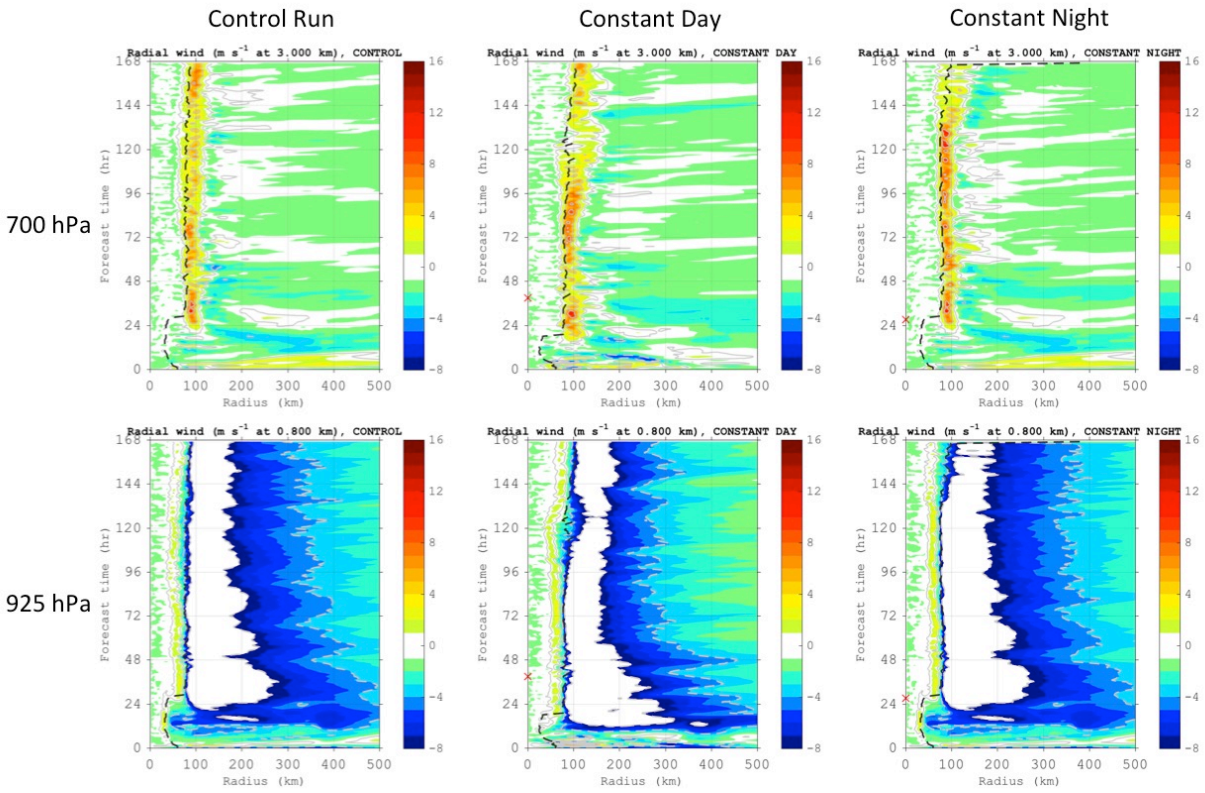

Figure 5.7: Hovmollers of azimuthally averaged radial wind (m s^{-1}) derived from the idealized TC simulation for the control run, constant day, and constant night simulations. Red "X"s signify the time that the solar cycle was turned off in the daytime-only (40 hr) and nighttime-only (28 hr) simulations. Analyses and forecasts are derived from the 02-09 Sep 0000 UTC study period and show the 700 hPa (~3 km) and 925 hPa (~0.8 km) pressure levels. Radii are analyzed relative to the TC center and extend out to 500 km.

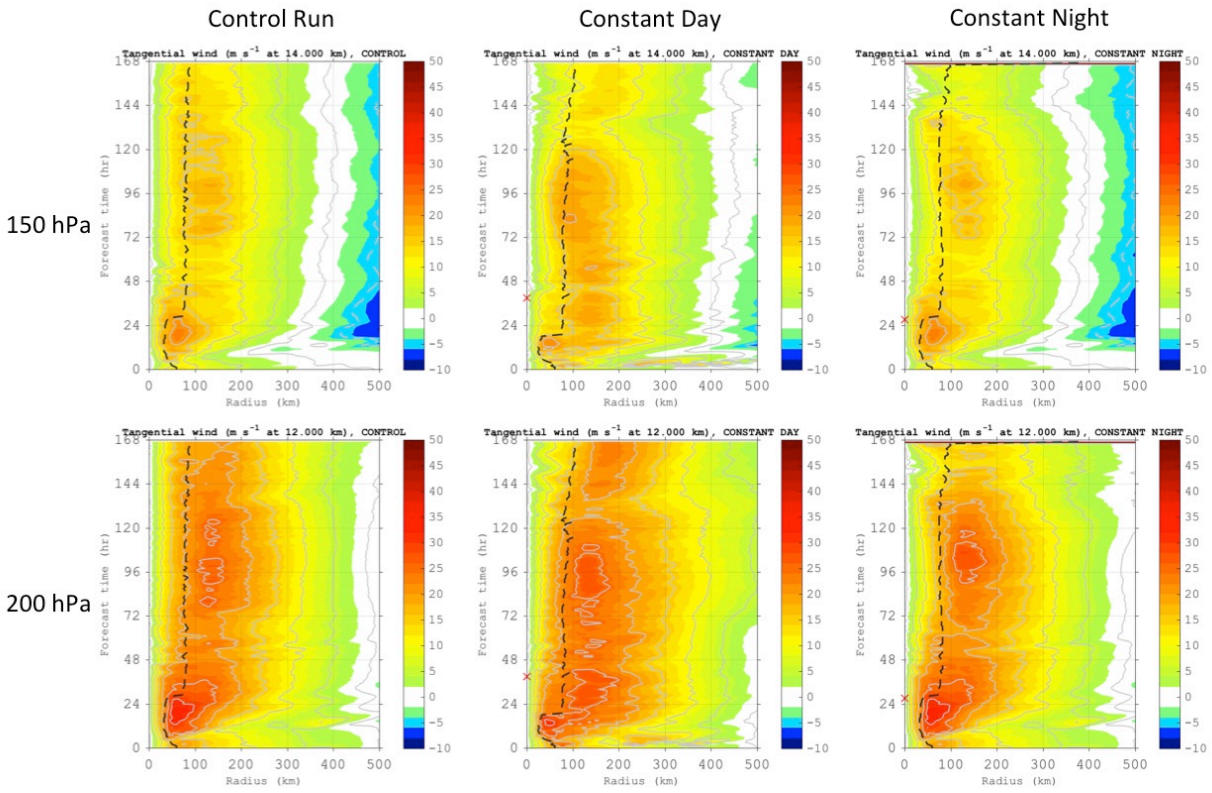

Figure 5.8: Hovmollers of azimuthally averaged tangential wind (m s^{-1}) derived from the idealized TC simulation for the control run, constant day, and constant night simulations. Red "X"s signify the time that the solar cycle was turned off in the daytime-only (40 hr) and nighttime-only (28 hr) simulations. Analyses and forecasts are derived from the 02-09 Sep 0000 UTC study period and show the 150 hPa (~14 km) and 200 hPa (~12 km) pressure levels. Radii are analyzed relative to the TC center and extend out to 500 km.

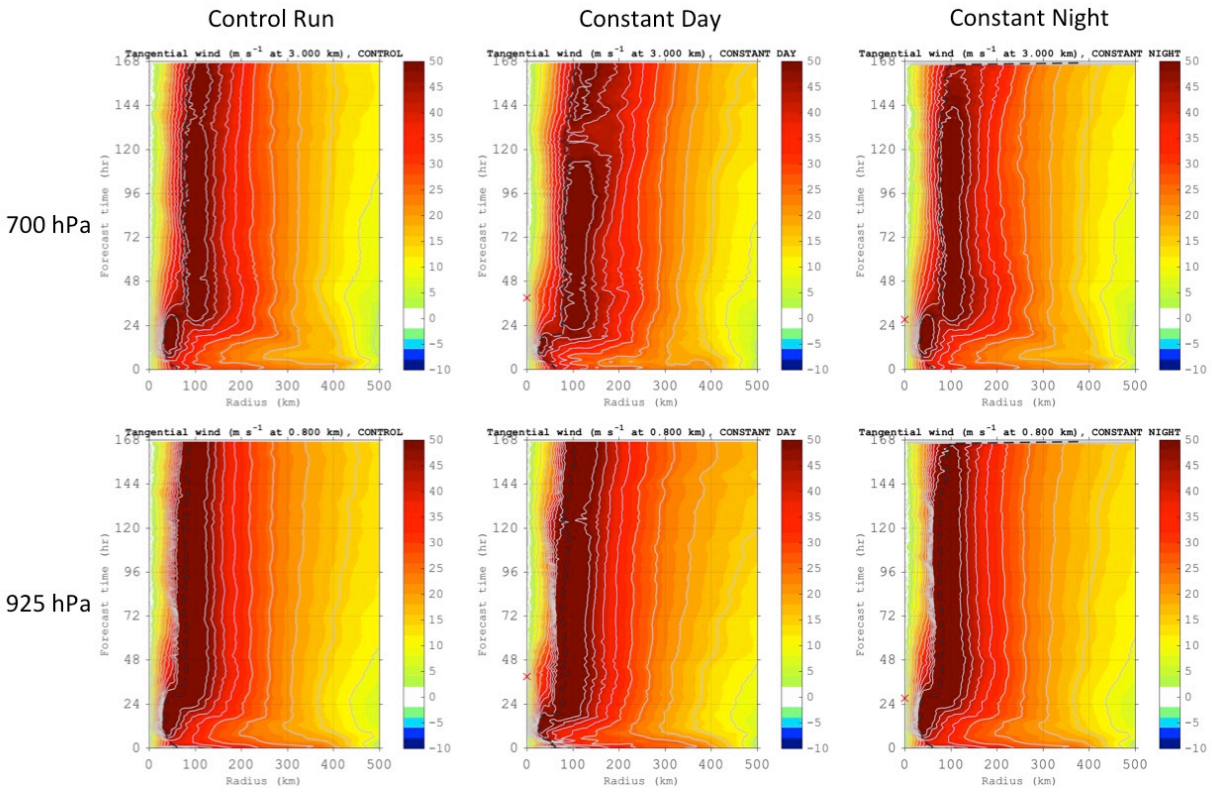

Figure 5.9: Hovmollers of azimuthally averaged tangential wind (m s^{-1}) derived from the idealized TC simulation for the control run, constant day, and constant night simulations. Red "X"s signify the time that the solar cycle was turned off in the daytime-only (40 hr) and nighttime-only (28 hr) simulations. Analyses and forecasts are derived from the 02-09 Sep 0000 UTC study period and show the 700 hPa (~3 km) and 925 hPa (~0.8 km) pressure levels. Radii are analyzed relative to the TC center and extend out to 500 km.

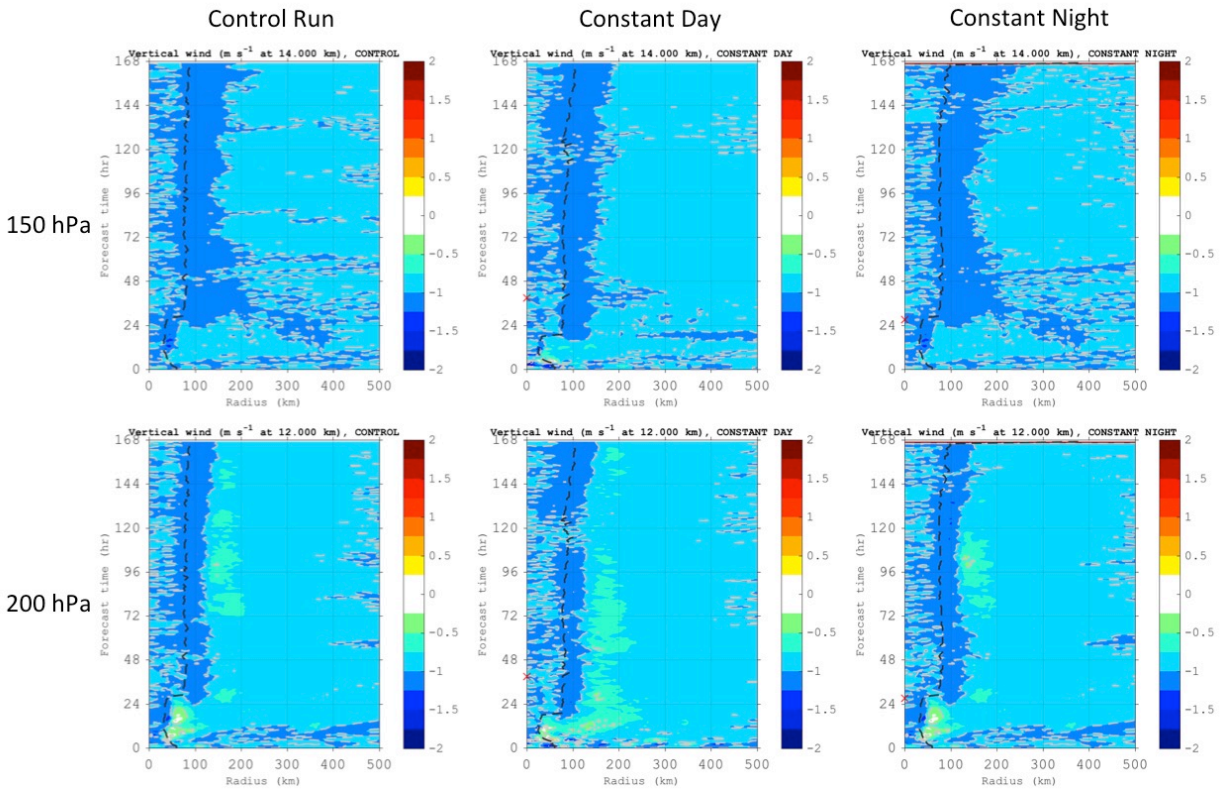

Figure 5.10: Hovmollers of azimuthally averaged vertical wind (m s^{-1}) derived from the idealized TC simulation for the control run, constant day, and constant night simulations. Red "X"s signify the time that the solar cycle was turned off in the daytime-only (40 hr) and nighttime-only (28 hr) simulations. Analyses and forecasts are derived from the 02-09 Sep 0000 UTC study period and show the 150 hPa (~14 km) and 200 hPa (~12 km) pressure levels. Radii are analyzed relative to the TC center and extend out to 500 km.

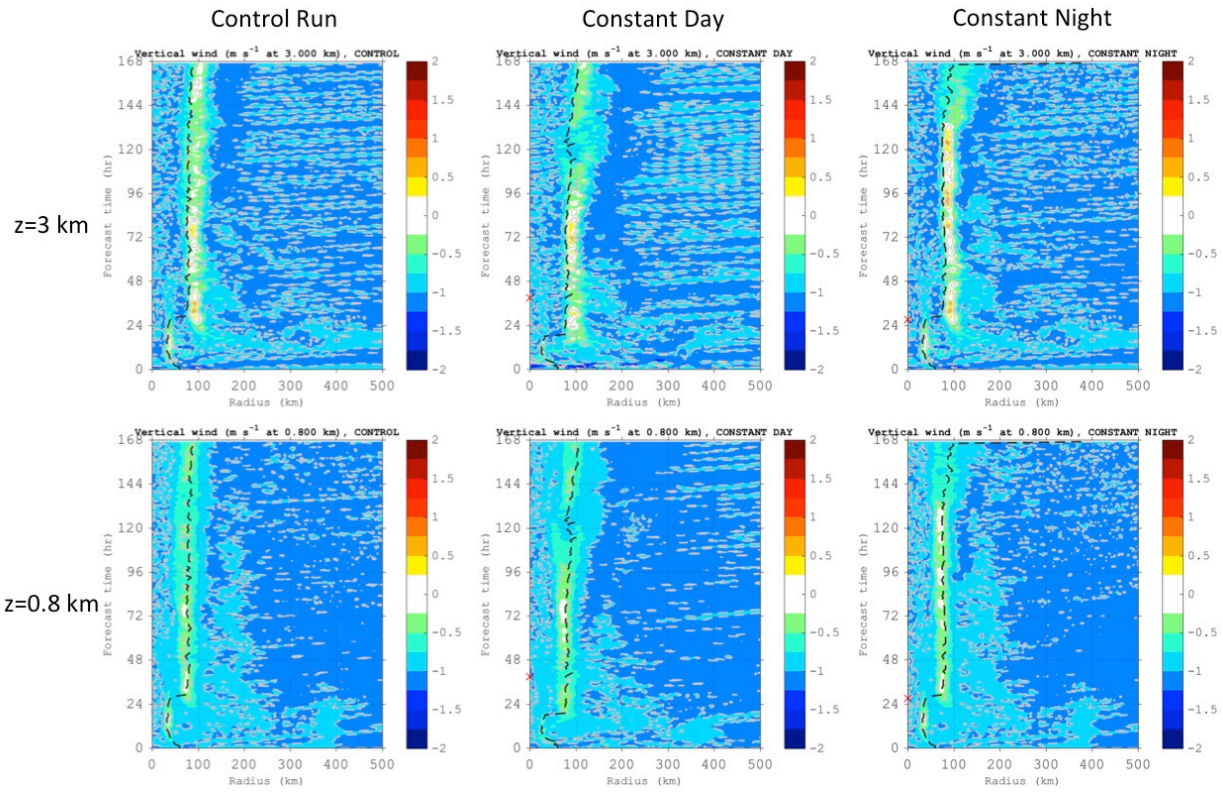

Figure 5.11: Hovmollers of azimuthally averaged tangential wind (m s^{-1}) derived from the idealized TC simulation for the control run, constant day, and constant night simulations. Red "X"s signify the time that the solar cycle was turned off in the daytime-only (40 hr) and nighttime-only (28 hr) simulations. Analyses and forecasts are derived from the 02-09 Sep 0000 UTC study period and show the 700 hPa (~3 km) and 925 hPa (~0.8 km) pressure levels. Radii are analyzed relative to the TC center and extend out to 500 km.

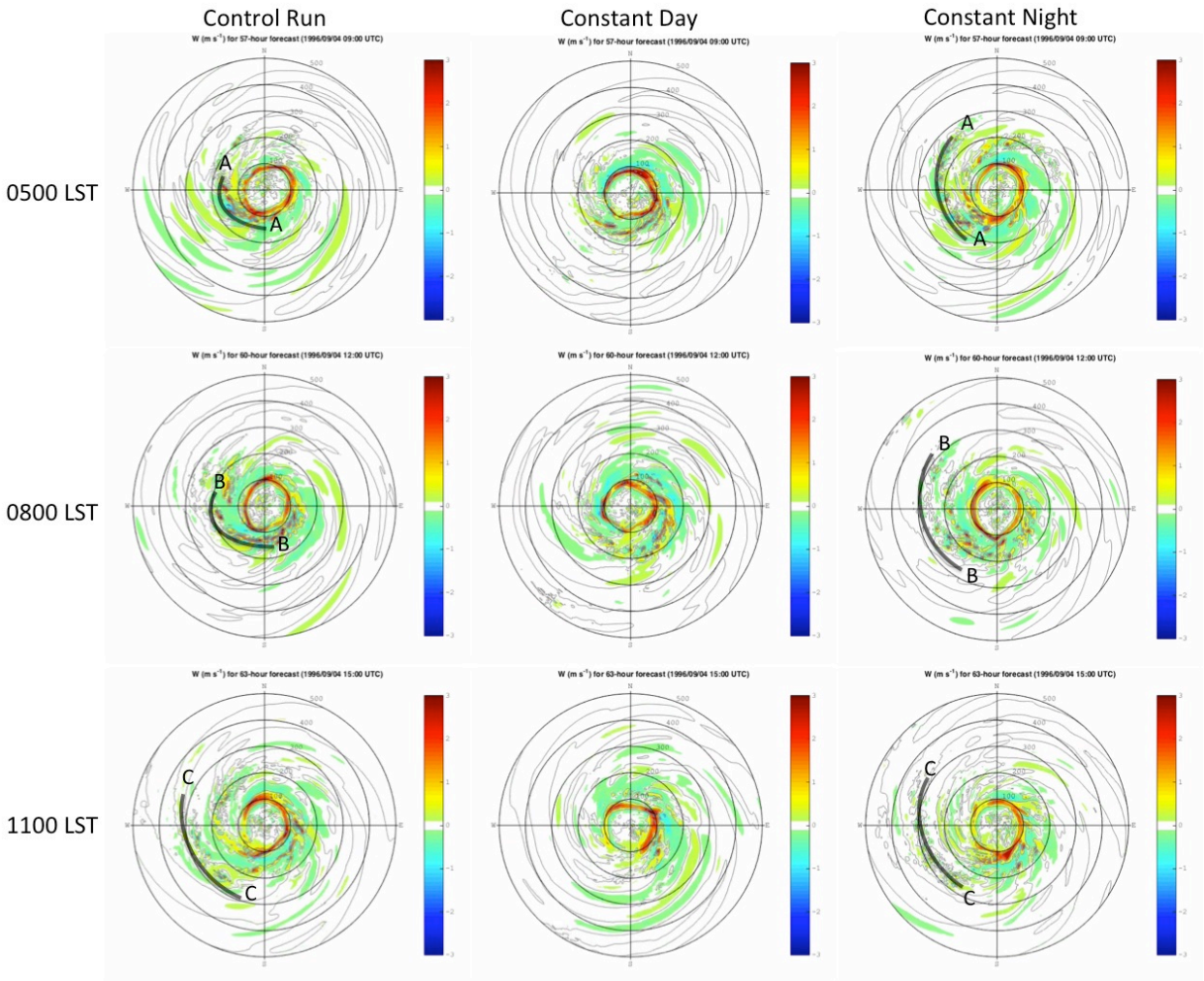

Figure 5.12: Plots of vertical wind (m s^{-1}) derived from the idealized TC simulation for the control run, constant day, and constant night simulations from 0500-1400 LST (0900-1800 UTC) on 04 Sep at 700 hPa (~3 km). A, B, and C mark the leading edge of an arc-shaped feature with enhanced vertical winds that was propagating away from the control run and constant night simulated TC at 0500, 0800, ad 1100 LST respectively.

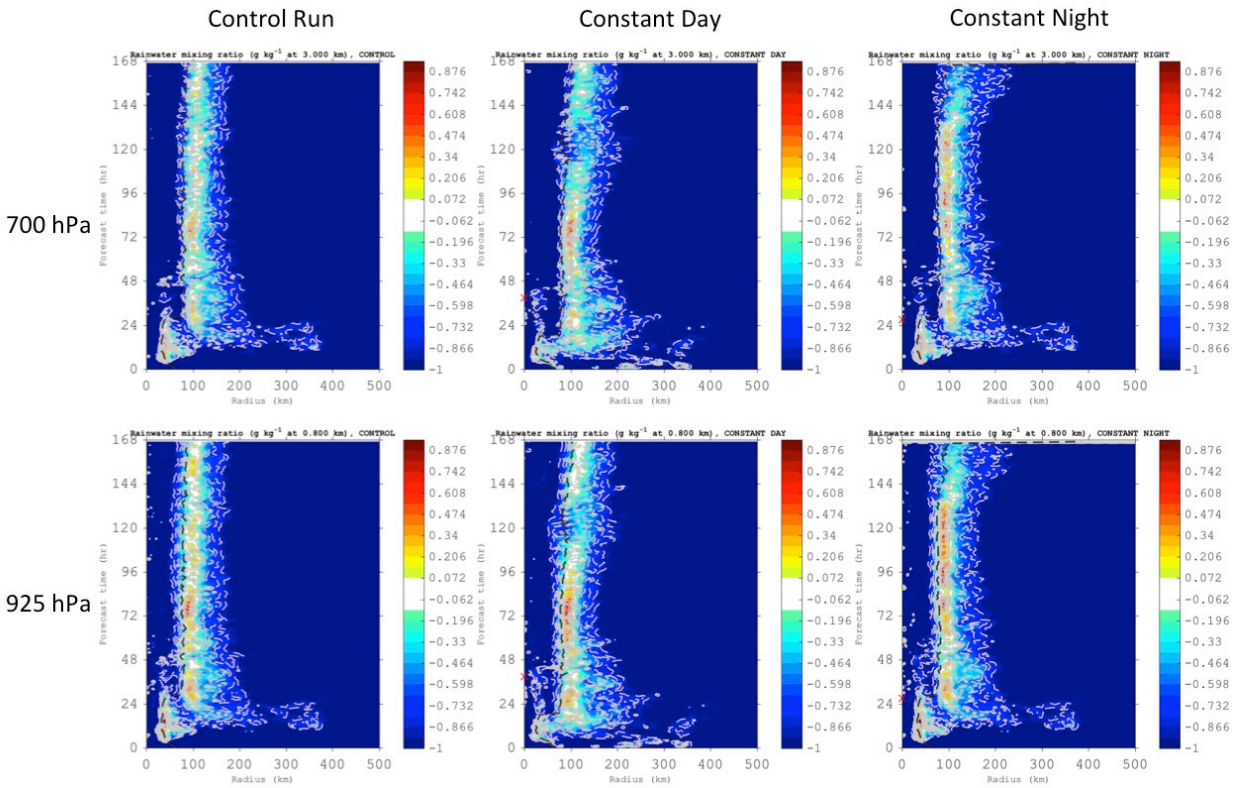

Figure 5.13: Hovmollers of azimuthally averaged rainwater mixing ratio (g kg^{-1}) derived from the idealized TC simulation for the control run, constant day, and constant night simulations. Analyses and forecasts are derived from the 02-09 Sep 0000 UTC study period and show the 700 hPa (~3 km) and 925 hPa (~0.8 km) pressure levels. Radii are analyzed relative to the TC center and extend out to 500 km.

6. Investigating the TC Diurnal Cycle Using Observations

6.1 Introduction

This chapter will examine a combination of satellite-derived water vapor AMVs (described in Sec. 2.1.1) and aircraft observations collected in the inner core and surrounding environments of 2010 Hurricane Earl and 2014 Hurricane Edouard while they were exhibiting detectable TCDC signals in GOES and 37 GHz microwave satellite imagery (described in Chapter 3). For Hurricane Earl, analyses will be focused on data collected on 31 Sep 2010 when the NOAA G-IV jet was collecting GPS dropsonde observations in the environment of the storm. Hypothesized links between the storm's TCDC and upper-level outflow and divergence that were discussed in Chapters 3 and 4 (Sec. 4.4) will also be examined. Finally, analyses of Earl's TCDC using a combination 37 GHz microwave imagery, GOES visible and IR satellite imagery, and GPS dropsondes deployed from a NOAA IFEX G-IV mission will be made to investigate the evolution and thermodynamic/kinematic structure of Earl's TC diurnal pulse in the context of the analyses and hypothesized mechanisms discussed in Chapters 3 and 4.

For Hurricane Edouard, analyses will focus on 16 Sep 2014 when the NOAA Hurricane Research Division and NOAA NESDIS were conducting research missions with 2 NOAA WP-3Ds and collecting GPS dropsonde and radar observations in the storm. Analyses of Earl's TCDC and evidence that the storm's TC diurnal pulse was coupled to a large arc cloud feature will be presented using a combination of data from 37 GHz microwave imagery, GOES visible and IR satellite imagery, and GPS dropsondes deployed from a NOAA IFEX WP-3D mission. WP-3D LF radar (reflectivity) and tail Doppler radar (TDR; reflectivity and winds) data will be used to provide further insight into the TCDC by characterizing the 3-dimensional structure and

evolution of Edouard's TC diurnal pulse and apparent impact on the TC environment as it propagated away from the storm that day.

6.2 2010 Hurricane Earl

6.2.1 Hurricane Earl's TC Diurnal Cycle

Figure 6.1 shows the TCDC for 2010 Hurricane Earl on 31 Aug during a period of steady state category 4 intensity (59 m s^{-1}). Earl was one of the TCs used in the TCDC 10-yr major hurricane dataset discussed in Chapter 3 and exhibited a TCDC evolution that was quite similar to the Hurricane Emily (2005) and Felix (2007) TCDC cases discussed in Chapter 3.2. GOES IR imagery showed a rapidly expanding cirrus canopy in all quadrants as a TC diurnal pulse propagated away from the storm and marked asymmetries in Earl's IR cloud field as the diurnal pulse reached peripheral radii (e.g. R=300-500 km). It should also be noted that the timing of the radial progression of this diurnal pulse closely matched the TCDC conceptual clock presented in Chapter 3.3. Figure 6.2 shows 37 GHz microwave satellite images (from the TRMM and WindSat satellites) at ~0030 and 0630 LST and corresponding 6-hr GOES IR brightness temperature trend images that are within 55 min of the 37 GHz image times. At around the time of local midnight, Earl's cloud field was relatively symmetric and compact in both the IR and microwave images and a nascent diurnal pulse appeared to be forming at R~150-200 km, which, as predicted by the TCDC conceptual clock, corresponds to the period ~4 hr before TC diurnal pulses typically reach R=200 km (Fig. 3.10). The 37 GHz imagery indicates that Earl's low to mid-level cloud field was largely contained within a radius of ~200-250 km. Just 6 hours later (~0630 LST), a definitive diurnal pulse was evident at R~200-300 km in the IR brightness temperature trend imagery and the 37 GHz imagery showed that Earl's low to mid-level cloud

field had expanded to a radius of ~250-350 km. This TCDC sequence is strikingly similar to that shown for 2007 Hurricane Felix (Chapter 3.2.1, Figs. 3.1 and 3.2) and 2005 Hurricane Emily (Chapter 3.2.2, Figs. 3.4 and 3.5) and corroborates the observation that the TCDC and associated radially propagating TC diurnal pulses are not confined to the upper-level cirrus canopy. Instead, the TCDC affects a relatively deep layer of the atmosphere (dynamically and thermodynamically) and is linked with marked changes in TC structure, which is consistent with findings in Chapters 3 and 4. It should be noted that although the 37 GHz microwave satellite imagery is more effective than GOES IR imagery at capturing the lower to middle level evolution of TC diurnal pulses, unlike GOES, these microwave satellites cannot provide nearly continuous coverage over targets of interest. Microwave satellite passes are inherently intermittent and in the case for Earl on 31 Aug 2010, there were coverage gaps of ~5-10 hr before and after the 37 GHz images shown in Fig. 6.2 which did not allow for a detailed examination of Earl's TCDC evolution.

Figure 6.3 shows a time series of the TCDC for Hurricane Earl at R=300, 400, 500, and 600 km from 30 Aug – 01 Sep. Similar to the 2007 Hurricane Felix (Chapter 3.2.1, Fig. 3.3) and 2005 Hurricane Emily (Chapter 3.2.2, Fig. 3.6), Earl exhibited a strong TCDC signal with a clear maximum cooling in the R=300-600 km satellite IR field that peaks from the early morning to late afternoon (local time) and is followed by a distinct maximum in warming from the early evening to early morning hours. A phase shift in the timing of the TCDC at the various radii (i.e. the peak cooling/warming tended to progress radially outward in time from 300-600 km), indicates that the TCDC signal began at the innermost radii (e.g. <300 km, not shown) and propagated to peripheral radii at a typical TC diurnal pulse propagation speed of ~5-10 m s^{-1}

during the course of several hours and is similar to the results discussed in Chapter 3 and shown in Fig. 3.9.

6.2.2 Water Vapor AMVs and Upper Level Divergence

Figure 6.4 shows a 6-hourly sequence of Hurricane Earl's TCDC on 31 Aug and includes corresponding UW-CIMSS water vapor AMVs and analyses of upper-level (150-300 hPa) divergence. Near the time of local midnight, the TC diurnal pulse discussed in the previous section was just beginning to appear in the 6-hr GOES IR brightness temperature trend imagery at R~150-200 km. Concurrent water vapor AMVs indicated largely cyclonic upper-level (100-350 hPa) flow in the inner 400 km of Earl's circulation, with some outflow in the northeast and southwest quadrants outside of 400 km. At this time, upper-level divergence was well established over the storm (though slightly offset to the east of the center), with peak values of 30 to <40 $x10^{-6}$ s^{-1}. Divergence was especially established northeast, east, and southeast of Earl's center, while upper-level convergence was evident ≥300 km west of the storm. This pattern of restricted divergence west of the Hurricane Earl is likely related to the ~10-15 kt of westerly/southwesterly vertical wind shear that was affecting the storm during this time (as indicated by the SHIPS model; Sec. 2.2.1).

By 0600 LST that day, the diurnal pulse had propagated to R~200-300 km and water vapor AMVs indicate enhanced outflow near and just ahead of the TC diurnal pulse. This was especially evident in the western and southern semicircles of Earl at and beyond R=200 km. Although water vapor AMVs in the eastern semicircle of the storm still did not indicate a robust outflow pattern, the AMVs in this region did appear to have become slightly more divergent. The upper-level divergence analysis at this time indicated that the magnitude and areal extent of

divergence associated with Earl had markedly increased in all quadrants around the storm, especially in the eastern semicircle. The upper-level convergence in the western semicircle was now located ≥350 km from the center of circulation.

At 1200 LST, Earl's TC diurnal pulse had propagated to a radius of ~400-550 km (Fig. 6.4), which was well-predicted by the TC diurnal clock (Chapter 3.3, Fig. 3.10). Water vapor AMVs continued to show enhanced outflow north, east, and south of the storm, with outflow still somewhat radially inhibited on the west side (likely related to the aforementioned vertical wind shear). The magnitude and areal extent of upper-level divergence continued to increase and a marked growth and expansion was evident over the 12 hr period from 0000 to 1200 LST. Figure 6.5 quantifies the upper-level divergence associated with Earl from 30 Aug – 01 Sep at various radii from the storm. This analysis shows that on both 30 and 31 Aug, divergence peaked in the early to mid-afternoon and was at a minimum in the late evening to early morning hours and corresponds to the water vapor AMVs and divergence analyses in Fig. 6.4. It is hypothesized that the TCDC and radially propagating diurnal pulses promote enhanced upper-level outflow and divergence that rapidly increases each morning and peaks in the afternoon, which would indicate that this may be a favorable time of day for promoting upper level outflow and subsequent TC intensification. NRH1 analyses in Chapter 4 and the TCDC schematic shown in Fig. 4.32 show that the upper level outflow does indeed tend to peak from the mid-morning to afternoon and that diurnally fluctuating surface winds reach a maximum at R~50-200 km several hours later, in the evening to early morning hours. Future work will include performing more in-depth analysis of the 10-year major hurricane satellite dataset described in Chapter 3 to more robustly test this hypothesis.

6.2.3 NOAA IFEX G-IV Observations

The NOAA G-IV high altitude jet was tasked by NOAA's National Hurricane Center to fly a synoptic surveillance mission around Hurricane Earl on 31 Aug and deployed 33 GPS dropsondes during this 8.5 hr flight. The main objective of these NHC-tasked G-IV missions is to sample the storm's surrounding environment with GPS dropsondes and improve numerical guidance for hurricanes that threaten the United States, Puerto Rico, the U.S. Virgin Islands, and Hawaii (Aberson 2010). Figure 6.6 shows the G-IV flight track and indicates that the aircraft sampled the environment several hundred kilometers east and north of the storm and also performed a circumnavigation around the TC inner core at R~200-300 km. As previously discussed in Secs. 6.2.1 and 6.2.2, a marked diurnal pulse that was closely following the TC diurnal clock (Chapter 3, Fig. 3.19) was noted in the satellite imagery on this day and was accompanied by enhanced upper-level divergence. Figure 6.7 shows 6-hr GOES IR brightness temperature trend imagery at 1945 UTC (1545 LST) that afternoon along with corresponding GOES visible and IR imagery and locations of 4 GPS dropsondes that were deployed from the G-IV. At this time, the TC diurnal pulse discussed in Sec. 6.2.1 was in the later stages of its evolution and was located at R~450-600 km. Although the limited duration of this G-IV mission and relatively short period of GPS dropsonde sampling did not allow for an examination of the evolution of Earl's TC diurnal pulse, it did offer an opportunity to observe a snapshot of this feature during the later stages of its daily evolution.

Though targeting observations of Earl's TCDC was not an objective of the synoptic surveillance mission flown on 31 Aug, the G-IV did serendipitously sample the environment along and radially inward of the propagating diurnal pulse noted in the GOES satellite imagery (Fig. 6.7). Since the G-IV was flying at ~12,500-14,000 m during this mission, GPS dropsondes

that were deployed near Earl's TC diurnal pulse that day offered a unique opportunity to examine the environment associated with these features through a nearly complete depth of the troposphere. Several of the G-IV GPS dropsondes that were launched that afternoon indicated unusual (compared to the moist tropical sounding; Dunion 2011) thermodynamic and kinematic profiles in this region of Earl's surrounding environment. Figure 6.8 shows that these G-IV GPS dropsondes sampled layers with relatively strong (1.5-3.7^{o}C) middle level temperature inversions (yellow shading in Fig. 8's skew-t plots) with bases ranging from 455-530 hPa that were accompanied by a dewpoint profile that mirrored the temperature profile (e.g. as the temperature rapidly increased with height above the base of the inversion, the dewpoint also rapidly increased with height). Additionally, the 100+ hPa layer above the inversion bases were all saturated with respect to ice and contained marked shifts in both wind speed and direction with height (with enhanced outflow indicted above the temperature inversion). These G-IV GPS dropsonde soundings may have captured a few key characteristics of the TCDC and associated diurnal pulses that have been described in previous chapters.

As discussed in Chapter 4 (Sec. 4.2.2), TC diurnal pulses are associated with surges in the cirrus canopy with enhanced ice mixing ratio that can extend hundreds of kilometers from the storm center. Chapter 3 (Sec. 3.6.5) also discusses that over time some of these radially propagating ice particles could eventually fall into the layer below -4^{o}C and aggregate just above the melting level. It is hypothesized that sublimation in these areas can produce temperature inversions (through cooling by latent heat of sublimation) similar to those seen in Fig. 6.8, especially during the day and when strong winds and a significant dry layer exists in the sounding. Indeed, all of soundings in Fig. 6.8 show 35-55 kt winds at the level of their 455-530 hPa temperature inversions with dry layers immediately below that ranged from 20-40% RH,

which is ~25-40% dryer than the moist tropical sounding (Dunion 2011). The ~455-530 hPa temperature inversions that were identified in the Fig. 6.8 soundings had temperatures at their bases that ranged from -5.1 to -15.9^{o}C and all were immediately topped by a deep layer of relative humidity that was ~100% with respect to ice and at least 150 hPa thick. These profiles resemble the "onion" soundings described by Zipser (1977) that are often seen in the downdraft trailing stratiform region of squall lines (Bryan and Parker 2010), suggesting that the observed TC diurnal pulse may have squall line-like characteristics (Sec. 4.5.3). In these squall line "onion" soundings (and in Fig. 6.8's soundings), there is a nearly saturated and approximately moist-adiabatic layer above the melting level (top of the "onion") overlying a sub-saturated and nearly mixed layer below the melting level that is nearly saturated at its base (root of the "onion").

Another characteristic of TC diurnal pulses seen in the Hurricane Earl G-IV soundings relates to surges in radial wind (Sec. 4.4.2; Figs. 4.20 and 21) and associated enhancement of upper-level outflow and divergence (Sec. 6.2.2). Interestingly, the 4 soundings in Fig. 6.8 all indicated a marked drop in wind speed (10-20 kt) with height between the bottom and top of their mid-level temperature inversions. However, the winds above the inversions also had a stronger radial component, indicating enhanced outflow radially inward of (drops 15 and 17, Figs. 6.7 and 6.8) and especially near (drops 12 and 13, Figs. 6.7 and 6.8) the environment of the satellite-observed TC diurnal pulse. Although the 150, 200, and 250 hPa winds (the approximate upper level outflow layer) in these 4 GPS dropsonde profiles all clearly indicate outflow with winds that are 7-20 m s^{-1} stronger than the moist tropical sounding (Dunion 2011), the 2 soundings that were closer to Earl's TC diurnal pulse (drops 12 and 13) had relatively enhanced outflow (Table 6.1). In fact, the 150-250 hPa winds in these 2 soundings were ~1.5-3 times

stronger than the corresponding upper level winds in drops 15 and 17. This further supports the idea that the environment near TC diurnal pulses is associated with enhanced upper level outflow. Sec. 6.3.3 uses aircraft radar observations collected in the environment of 2014 Hurricane Edouard to further examine this TCDC characteristic.

Ice particles that are hypothesized to be falling from the TC outflow layer would be especially favored during the afternoon hours (i.e. when the Hurricane Earl G-IV GPS dropsonde observations were collected) when TC diurnal pulses with enhanced ice mixing ratio are propagating away from the TC inner core. These processes were found in the NRH1 and highlighted in Sec. 4.2.2 and the TCDC schematic shown in Fig. 4.32. Additionally, soundings that contain strong winds and significant dry layers near the melting level (i.e. the G-IV GPS dropsonde profiles shown in Fig. 6.8) could promote ice sublimation in this region of the storm. The G-IV GPS dropsonde data discussed in this section showed profiles of RH that were saturated with respect to ice over a relatively deep layer (150+ hPa) and were underlain by middle level temperature inversions that may have been created/enhanced by latent cooling associated with ice sublimation. These observations provide indirect evidence of Sec. 3.6.5's hypothesis (seeder-feeder mechanism) that enhanced ice mixing ratio associated with TC diurnal pulses could promote convection in these radially propagating features. The G-IV GPS dropsonde data suggesting that the aircraft may have sampled "onion" soundings behind a squall line-like feature (i.e. the diurnal pulse) supports the findings and discussions of NRH1 moisture, wind, and precipitation presented in Secs. 4.3.2, 4.4.4, and 4.5.3 and the TCDC schematic shown in Fig. 4.32. G-IV GPS dropsondes deployed in the environment of Hurricane Earl also suggest that the environments of TC diurnal pulses are associated with enhanced upper level outflow and confirms the analyses presented in Sec 4.4.2.

6.3 2014 Hurricane Edouard

6.3.1 Hurricane Edouard's TC Diurnal Cycle

Figure 6.9 shows the TCDC for 2014 Hurricane Edouard on 16 Sep during the time of its peak intensity (category 3; 54 m s^{-1}). Although TCDC signals (e.g. a diurnal pulse and radially expanding cloud shield) are evident in the GOES IR and 6-hr IR brightness temperature trend imagery, the diurnal pulse indicated by yellow to pink shading in the latter images is somewhat less defined and less symmetric compared to those seen in the 2005 Emily, 2007 Felix, and 2010 Earl cases. It should be noted that for the Edouard case, the 200-850 hPa vertical wind shear as analyzed by the SHIPS model ranged from 7.5-8.5 m s^{-1}, which is slightly higher than the TCDC criteria defined in Sec. 2.2.1 ($\leq$7.5 m s^{-1}). Therefore, it is hypothesized that moderate southeast shear on 16 Sep may have been slightly inhibiting the TCDC signal in Hurricane Edouard. Nonetheless, Fig. 6.10 confirms that a robust TCDC signal was still detectable at R=300, 400, and 500 km around the storm and that the diurnal pulse radial propagation closely matched that of the mean 2001-2010 dataset and the TCDC conceptual clock presented in Sec. 3.3.

Figure 6.11 shows 37 GHz microwave satellite images from the WindSat and GCOM sensors on 16 Sep at 0627 LST (1027 UTC) and 1205 LST (1605 UTC) and corresponding 6-hr GOES IR brightness temperature trend images that are within 12-min of the 37 GHz image times. At 0627 LST, Edouard was fairly symmetric and most of its 37 GHz-sensed cloud field (cyan to pink shading) was contained within the inner 200-300 km of the storm center. The corresponding GOES imagery showed a TC diurnal pulse from the previous day located in the western semicircle of Edouard at R~400-550 km and a newer TC diurnal pulse located at R~200-250 km (again closely matching the TCDC conceptual clock discussed in Sec. 3.3). By 1215 LST, GOES imagery indicated that the TC diurnal pulse had propagated to a radius of ~250-350

km (Fig. 6.11). Interestingly, the matching 37 GHz image showed that this TC diurnal pulse was especially prominent in the northern semicircle of the storm (cyan to pink shaded arc-shaped feature in the image that was also apparent in the visible portion of the image), was hundreds of kilometers in length, only ~25-50 km wide, and had propagated to R~200-300 km. These microwave images once again support the hypothesis that the TCDC affects a relatively deep layer of the atmosphere and is linked with marked changes in TC structure. Visible imagery in Fig. 6.12 further suggests that the TC diurnal pulse evident in the GOES 6-hr IR brightness temperature trend and 37 GHz microwave imagery was coupled with a large arc cloud feature that was hundreds of kilometers in length and was propagating away from the TC inner core region at ~5-10 m s^{-1}. This feature was well sampled on 16 Sep by two NOAA WP-3Ds (NOAA 42 and 43) that were conducting NOAA IFEX and NESDIS research missions, details of which are highlighted in the next section. This possible link between the TC diurnal cycle and arc cloud features was also discussed by Dunion et al. 2014 and in Chapter 4 (Secs. 4.3.1 and 4.3.2).

6.3.2 NOAA IFEX WP-3D Observations: GPS Dropwindsondes

Two NOAA WP-3Ds (NOAA 42 and 43) were conducting research missions into Hurricane Edouard on 16 Sep and captured several aspects of the storm's TC diurnal cycle. NOAA 42 was deployed to Bermuda and was conducting a combination NOAA IFEX Model Evaluation Experiment and COYOTE Unmanned Aircraft System (UAS) Experiment, while NOAA 43 was base from St. Croix, USVI and was conducting a NOAA NESDIS Ocean Winds Experiment (Fig. 6.13). Noting the different latitude and longitude scales on the flight track plots, NOAA 43's pattern was focused more of the inner core region of Edouard, while NOAA 42 sampled a combination of the inner core and surrounding environment of the storm out to

R~200-300 km. During its ~9 hr mission (flight-level 3,000 m/10,000 ft), NOAA 42 deployed 24 GPS dropsondes to sample the inner core region of Edouard (e.g. R=≤150 km), as well as the region just outside the inner core (R=150-200 km).

Figure 6.14 shows GOES visible imagery for this day at 1245 LST (1645 UTC) and indicates that several of the WP-3D GPS dropsondes that were deployed sampled the region behind a large arc cloud feature (and collocated TC diurnal pulse) that was propagating away from Edouard and was especially evident in the northern semicircle of the storm (Figs. 6.11 and 6.12). Additionally, Fig. 6.14 suggests that these GPS dropsondes sampled the atmosphere ~3-4 hours after the passage of the arc cloud feature. It is hypothesized that this arc cloud formed when the radially propagating diurnal pulse reached an area of middle level (e.g. ~600-800 hPa) dry air, which would initiate convectively driven downdrafts (Knaff and Weaver 2000). Convection was confirmed to be associated with the radially propagating arc cloud by WP-3D radar data and is discussed more in the next section. These downdrafts would transport relatively cooler, dryer air from the mid-levels down to the boundary layer and possibly even down to the surface, thereby stabilizing the environment. Upon reaching these lower levels, these downdrafts begin to spread out horizontally and could promote locally enhanced outflow as they propagate away from the convective region where they originated. Figure 6.15 confirms the presence of middle level dry air around Edouard (total precipitable water (TPW) values of 40 to <50 mm) that is located at R~250-350 km and is within ~50-75 km of the GPS dropsondes that are shown. Dunion (2011) suggested that 45 mm is a reasonable TPW threshold value for discerning moist tropical air masses from environments with substantially dry air in the lower to middle levels (e.g., Saharan Air Layer and mid-latitude dry air intrusion air masses). The presence of this satellite-indicated middle level (e.g. 600-800 hPa dry air was confirmed by WP-3D dropsonde

data and will be discussed next. Finally, similar to work by Knaff and Weaver (2000) who examined a large outflow boundary feature (i.e. arc cloud) emanating from 1995 Hurricane Luis, it is hypothesized that these thermodynamic and kinematic modifications to the TC environment represent a short-term impact (e.g. <12 hr) and recovery to a more typical tropical environment (e.g. the moist tropical sounding) may take several hours.

The 4 GPS dropsonde locations highlighted in Figs. 6.14 and 6.15 were deployed behind the TC diurnal pulse (and associated arc cloud feature) to the east of and around the northern semicircle of Edouard and all captured unusual thermodynamics in their sounding profiles that are not typical of a moist tropical environment (Dunion 2011). GPS dropsondes #1 and #2 were launched ~190 km east and northeast of Edouard respectively and ~150 km behind the TC diurnal pulse/arc cloud feature and showed an unsaturated boundary layer profile that was close to dry adiabatic from ~940 hPa to the surface (Figs. 6.14 and 6.16). Table 6.2 indicates that these 2 GPS dropsondes indicated low-level moisture (e.g. 850 hPa) that was comparable to or even moister than the mean moist tropical sounding (Dunion 2011). However, surface moisture in these soundings was 71% RH, which is significantly dryer than the moist tropical sounding (83% RH; Dunion 2011) and is hypothesized to be linked to the arc cloud seen in Fig. 6.14. It should be noted that the surface temperatures were slightly warmer that the moist tropical sounding, indicating that the moisture component of the surface RHs were dominating the low RH values. GPS dropsondes #3 and #4 were launched ~200 km to the northwest of Edouard and were only ~50 km radially inward of the propagating diurnal pulse/arc cloud feature (Fig. 6.14). GPS dropsonde #3 was ~28% RH dryer than the moist tropical sounding in the low-levels (e.g. 850 hPa), showed a nearly dry adiabatic lapse rate from ~975 hPa to the surface, was >1^{o}C cooler than the moist tropical sounding at the surface, and indicated a nearly dry adiabatic lapse

rate from ~975 hPa to the surface. GPS dropsonde #4 was nearby to GPS dropsonde #3 and was markedly cooler (2.2^{o}C) than the moist tropical sounding at the surface and cooler than any of the other GPS dropsonde soundings that have been shown. Unfortunately, these soundings that all sampled behind the Edouard's TC diurnal pulse were launched too low in the atmosphere to confirm if "onion" soundings similar to those found in the G-IV GPS dropsonde data from Hurricane Earl were present.

The 4 GPS dropsondes that have been discussed were representative of other GPS dropsondes (not shown) launched from NOAA 42 during the 16 Sep mission and suggest that the lower to middle level thermodynamic environment just outside the storm's inner core and behind Edouard's TC diurnal pulse/arc cloud feature was markedly impacted by the convectively driven downdrafts that occurred in association with the arc cloud (convection associated with this feature is confirmed by WP-3D radar data and is discussed in the next section). Although it is not clear what the recovery time is for this modified atmosphere (i.e. the time to return to a more typical moist tropical atmosphere), these GPS dropsonde soundings suggest that arc cloud events like these can act to stabilize the atmosphere by bringing cool, dry air into the low-levels and boundary layer and can affect the peripheral TC environment for several hours, which has also been discussed in previous studies (Knaff and Weaver 2000). It is hypothesized that these highly visible large arc cloud events may be the lower to middle level portion (e.g. near-surface to 600 hPa) of the deep layer TC diurnal pulses that have been identified using satellite imagery (Chapter 3) and analyses from the NRH1 (Chapter 4) and may be a fundamental component of the TCDC, especially when the TC is surrounded by middle level dry air. This suggests that the stabilizing affects of arc cloud features may occur at predictable times of day, especially in the mid-morning to afternoon when TC diurnal pulses are located at R~250-400 (Fig. 3.10) and

particularly when middle level dry air is present at this radius range. The TCDC and radially propagating TC diurnal pulses could provide a mechanism for the TC to reach out to this peripheral dry air and stabilize the environment just outside the TC inner core via the initiation of convectively driven downdrafts. In this paradigm, a TC that is insulated (i.e. maintaining separation from) lower to middle level dry air could suddenly begin interacting with that dry air as a TC's convectively active diurnal pulse radially propagates through the surrounding environment. The squall line-like appearance of these TC diurnal pulses and arc cloud features (with associated cold pools) were also identified in analyses of vertical wind and simulated radar reflectivity in the NRH1 (Secs. 4.4.4. and 4.5.2), suggesting that aircraft radar may be able to detect these features as well. This prospect will be examined in the next section.

6.3.3 NOAA IFEX WP-3D Observations: LF Radar and TDR Data

The two NOAA WP-3D (NOAA 42 and 43) IFEX missions that were flown into Hurricane Edouard on 16 Sep were both equipped with a lower-fuselage (LF) radar and a tail Doppler radar (TDR), which are described in detail in Sec. 2.1.4. Although the WP-3D LF radar has historically been used as a real-time tool for targeting features in the TC environment (e.g. TC eyewalls and outer rainbands) and for hazard avoidance, it is being increasingly used as a research tool as well. NOAA HRD routinely processes storm-centered LF radar images with a domain of 360 x 360 km (Fig. 6.17, left panel), but this domain size would typically only be able to capture a TC diurnal pulse in the early stages of its evolution (e.g. ~0400-1200 LST when the diurnal pulse is in its early evolution and is located at R~200-300 km; Fig. 3.10). Though the 360 x 360 km LF radar domain does, in fact, capture a portion of Edouard's TC diurnal pulse in extreme northwest corner of Fig. 6.17's 1323 LST radar image, it is not possible to discern that

the arc of high reflectivity in the western semicircle of Edouard at R=~150-250 km is part of a much larger, semicircular feature that extends for hundreds of kilometers around the storm. A special expanded LF radar analysis domain was created (660 x 660 km) in order to detect TC diurnal pulses/arc cloud features throughout their evolution, including the mid- to late morning and afternoon hours local time when TC diurnal pulses are typically at R=300-500 km (Fig. 3.10). Indeed, this larger 660 x 660 km domain (Fig. 6.17) shows the presence of a large, convectively active, semicircular ring of high reflectivity at R~150-350 km that is hypothesized to be a TC diurnal pulse and corresponds to the position of Edouard's TC diurnal pulse/arc cloud feature shown in Figs. 6.9, 6.11, and 6.12.

Figure 6.18 shows a series of LF radar images from NOAA 42 on 16 Sep from 1120-1528 LST. These images indicate that the semicircular ring of 20-40 dBZ reflectivity at R~150-350 km seen in Fig. 6.17 is steadily propagating away from the storm at a speed of 3-5 m s^{-1}, which is slightly slower (perhaps due to the moderate southeasterly shear affecting the storm that day), but similar to the TC diurnal pulse speed discussed in Chapter 3 (~5-10 m s^{-1}). As Figs. 6.9, 6.11, and 6.12 suggest, the moderate 7.5-8.5 m s^{-1} southeasterly shear that was affecting Edouard on 16 Sep appears to have favored a more well-defined TC diurnal pulse around the downshear northern semicircle of the storm and a more suppressed TCDC signal in the storm's upshear southern semicircle. The LF radar reflectivity pattern in Fig. 6.18 confirms these satellite-based observations and shows that in the northern semicircle of the storm, the TC diurnal pulse was more discernable and propagated farther away from the storm over the ~4.5 hr that it was observed. Although this hypothesized TC diurnal pulse feature was associated with significant reflectivity (35-40 dBZ) and was likely a low to mid-level feature based on corresponding GOES visible imagery (Figs. 6.12 and 6.14), the WP-3D LF radar is not able to

provide height information regarding the features that it detects. Therefore, data from the WP-3D TDR was used to further examine the TC diurnal pulse seen in the LF radar data.

NOAA 42's TDR provided detailed 3-dimensional analyses of reflectivity and winds made during 2 transects through Hurricane Edouard's TC diurnal pulse on 16 Sep during NOAA IFEX mission 20160916H1. Both of these transects sampled the region of the TC diurnal pulse in the NW quadrant of Edouard (Fig. 6.19) and were made during the initial (A-B; 1320-1416 UTC) and final (C-D; 1720-1812 UTC) passes though the storm.

For the initial NOAA 42 pass (A-B), the GOES imagery in Fig. 6.19 indicated that NOAA 42 passed through Edouard's TC diurnal pulse at R~175-250 km. The aircraft's LF radar confirmed that a ~20 km wide arc-shaped convective feature was located at R~150 km, slightly radially inward from the satellite-indicated TC diurnal pulse position, and was associated with reflectivity values of 30-40 dBZ. Figure 6.20 shows 3-dimensional TDR analyses for this initial pass (A-B) of reflectivity, wind speed, radial wind speed, and vertical wind speed from R=0-300 km and z=0-15 km. There are several notable features in the reflectivity and radar-derived wind fields near the radius of the TC diurnal pulse that was identified (Fig. 6.20). At R~150 km, TDR reflectivity indicated that the high reflectivity noted in the LF radar was a low to mid-level feature that only extended from ~0.5-6 km and was associated with an area of enhanced wind speed (40-50 m s^{-1}) that sloped radially outward with height. Additionally, there was a marked shift in radial wind flow that occurred at the radius of the radar-indicated TC diurnal pulse. Outside of R~150 km, there was a deep layer of enhanced middle to upper-level (z~5-10 km) radial outflow that extended out to R~300 km, as well as a relatively deep layer (z~0.5-5 km) of 5-15 m s^{-1} inflow that sharply descended and narrowed at R~150 km. Inside of R~150 km, outflow in the middle to upper-levels (z~5-11 km) was weaker and was mainly concentrated

above z~7 km. 5-10 m s^{-1} lower to middle level (z~0.5-5 km) inflow was evident from R~20-150 km, but was not as strong and vertically uniform as was noted outside of R=150 km. Fig. 6.20's analysis of vertical wind confirms that the area near R=150 km had vertical motions of up to 5-10 m s^{-1} that extended from z~2-6 km, supporting the hypothesized mechanism that TC diurnal pulses could be associated with a "feeder" mechanism where enhanced mesoscale lifting can increase the amount of "feeder" cloud water by condensation of vapor at low levels. (Sec. 3.6.5). There was also a vertically narrow layer of enhanced updrafts (1-3 m s^{-1}) and downdrafts (1-4 m s^{-1}) at z~4.5-5 km from R~175-250 km, just outside of the radar-indicated TC diurnal pulse position and close to the approximate satellite-indicated TC diurnal pulse location. Below this vertically thin updraft/downdraft layer and at the same ~175-250 km radial range, a broad area of 1-4 m s^{-1} downdrafts that were evident down to z=0.5 km (the lowest level that TDR data can be collected) was also noted in the TDR analysis. These patterns could be related to the seeder feeder mechanism discussed in Sec. 3.6.5 where ice sublimation could be occurring in this region of the GOES IR satellite-indicated diurnal pulse that is accompanied by a surge in ice mixing ratio in the outflow layer. As previously discussed, some of these "seeder" ice crystals fall into the layer below the -4^{o}C level, and aggregate just above the melting level (Houze et al. 1981). The latent cooling from this sublimation could act to destabilize the atmosphere in this region of the storm where ice sublimation is favored by promoting a statically unstable condition of relatively cooler air overlaying relatively warmer air and could explain the enhanced updrafts and downdrafts seen in the TDR data.

Figure 6.19 indicates that NOAA 42 final TDR pass through the storm (C-D) included a short southeast-northwest leg that extended out to R~190 km and was followed by a short east-northeast to west-southwest leg that ended at R~310 km. This left turn ~1/2 way through the

outbound radial leg is not typical when TDR cross sections are a WP-3D mission objective and was made partly for hazard avoidance considerations. In fact, the source of this hazard avoidance concern was the TC diurnal pulse that was being flown through, as it was associated with some of the highest reflectivity (~35-42 dBZ) that was encountered during the NOAA 42 mission that day. Nonetheless, even when the WP-3D radial leg is not perfectly straight (as in this case), robust TDR analyses can still be generated from the NOAA HRD analysis software. Figure 6.19 also indicates that the TC diurnal pulse feature that was flown through ~3 hours earlier (A-B) had radially propagated ~30-50 km (~3-5 m s^{-1}) and was located at R~200 km when the WP-3D encountered it the second time (C-D). Figure 6.21 shows 3-dimensional TDR analyses for this final pass of reflectivity, wind speed, radial wind speed, and vertical wind speed from R=0-300 km and z=0-15 km. There are several aspects of these analyses that are similar to the analyses shown in the Fig. 6.20 transect. At the LF radar-indicated TC diurnal pulse radius (R~200 km), TDR reflectivity once again indicated that the high reflectivity noted in the LF radar was a low to mid-level feature that only extended from ~0.5-6 km and was associated with enhanced winds (Fig. 6.21). However, reflectivity and vertical wind at the TC diurnal pulse radius were relatively weaker than they were in the earlier transect through the TC diurnal pulse (Fig. 6.20). This suggests that although the TCDC was still evolving, perhaps the TC diurnal pulse and associated radially propagating arc cloud were slowly dissipating over time. Also similar to the earlier NOAA 42 transect that was shown, Fig. 6.21 indicates that a notable shift in radial wind flow occurred at the radius of the radar-indicated TC diurnal pulse. Outside of the TC diurnal pulse radius (R~200 km), there was once again a deep layer (5+ km) of enhanced middle to upper-level (z~5-10 km) radial outflow that extended out to R~300 km and a relatively deep layer (z~0.5-5 km) of 5-15 m s^{-1} inflow that sharply descended and narrowed at R~200 km.

Inside of R~200 km, outflow in the middle to upper-levels (z~5-10 km) was not as well sampled by the TDR, presumably due to a lack of radar scatterers. Still, it appeared that outflow in this part of the storm was relatively weaker than it was outside of the LF radar-indicated TC diurnal pulse at R~200 km. Also similar to the previous WP-3D pass, the lower to middle level (z~0.5-5 km) inflow inside of R~200 km was overall weaker and significantly vertically narrower than it was outside of R=200 km. Finally, a broad region of 1-5 m s^{-1} downdrafts ~0-50 km outside the radius of the radar-indicated diurnal pulse was again noted in the TDR analysis. The conclusions drawn from these TDR analyses suggest that the TCDC is linked to diurnal ebbs and flows in total, radial, and vertical wind, as well as radar reflectivity and support the findings from the hurricane nature run analyses that are presented in Chapter 4 (Secs 4.4 and 4.5.2). The TDR cross-sections that are shown were collected in the late morning to early afternoon and are similar to the corresponding mid-morning to afternoon schematic of the TCDC presented in Chapter 4 (Figs. 4.32 and 4.33), with well defined upper-level outflow, a TC diurnal pulse with squall line-like characteristics that is propagating away from the storm, and lower level inflow that is relatively diminished radially inward of the TC diurnal pulse.

6.4 Discussion and Conclusions

This chapter includes an observationally based perspective on the TCDC and utilizes a combination of in situ and radar observations collected from multiple aircraft during missions flown into two Atlantic hurricanes (2010 Earl and 2014 Edouard). The main objectives of this chapter include 1) using observational data to confirm several TCDC characteristics that were identified in earlier chapters that examined satellite data (Chapter 3) and output from NRH1 simulation (Chapter 4); 2) confirming or discounting the TCDC mechanisms that were proposed

in Chapter 3; and 3) identifying other aspects of the TCDC that may not be well-represented in satellite data and/or model simulations.

The 2 hurricane environments that were selected for analysis in this section both exhibited distinct TCDC signals that were similar to the case studies presented in Chapter 3 and analyses of the NRH1 in Chapter 4. The TC diurnal pulses in these hurricanes were observed using GOES IR and microwave satellite imagery and exhibited marked TCDC signals in their cloud fields that radially propagated away from the inner core each day at speeds similar to those described in Chapter 3 and were well-predicted by the TCDC conceptual clock presented in that same chapter. A combination of observations from satellite water vapor AMVs, GPS dropsondes deployed from the NOAA G-IV jet and 2 WP-3Ds, and LF radar and TDR data from the WP-3Ds corroborated several hypotheses and conclusions related to TCDC driving mechanisms and general characteristics that were made in Chapters 3 and 4. These observations also provided new insights regarding the structure of TC diurnal pulses and their squall line-like qualities, how they impact the TC environment as they propagate away from the storm each day, and how they can be tracked in real-time. The observations of thermodynamics, winds, and TCDC evolution that shown in this chapter are well represented by the TCDC schematics presented in Chapter 4 (Figs. 4.32 and 4.33). Key findings from the satellite and aircraft observational analyses that were discussed in this chapter include:

- Analyses of GOES water vapor AMVs, AMV-based analyses of upper-level divergence, and NOAA G-IV GPS dropsonde observations in Hurricane Earl suggested that radially propagating diurnal pulses promote enhanced upper-level outflow and divergence that rapidly increase each morning and peak in the afternoon as the TC diurnal pulse propagates away from the storm;

- Satellite AMVs and AMV-based analyses of upper-level divergence indicate that the afternoon may be a diurnally favorable time of day for the enhancement of TC outflow and possible TC intensification. These analyses are supported by the discussion in Chapter 4 (Sec. 4.4.2), where robust surges in the simulated TC outflow layer were found to occur each day and peaked from the late morning through the afternoon hours;
- GPS dropsondes deployed from a NOAA WP-3D during 2010 Hurricane Earl suggest that the region radially inward of a TC diurnal pulse exhibits atmospheric profiles that resemble the "onion" soundings that are often seen in the downdraft trailing stratiform region of squall lines, suggesting that the observed TC diurnal pulse may have squall line-like characteristics. Like "onion" soundings, the G-IV GPS dropsonde soundings in Earl showed a nearly saturated and approximately moist-adiabatic layer above the melting level overlying a sub-saturated and nearly mixed layer below the melting level that is nearly saturated at its base.
- Large arc cloud events may represent the lower to middle level portion of the deep layer TC diurnal pulses that have been identified using satellite imagery (Chapter 3) and analyses from the NRH1 (Chapter 4) and could be a fundamental component of the TCDC and TC diurnal pulses, especially when lower to middle level dry air that can initiate convectively driven downdrafts is located in the peripheral environment of the storm (e.g. R~200-400 km). The stabilizing affects of the convectively driven downdrafts that form arc cloud features may occur at predictable times of day, especially in the mid-morning to afternoon when TC diurnal pulses are located at R~250-400 km and potentially moving through areas of middle level dry air (i.e. convectively-driven downdrafts can form);

- GPS dropsondes deployed from a NOAA WP-3D suggest that the thermodynamic environment just outside the Hurricane Edouard's inner core and behind its radially propagating TC diurnal pulse/large arc cloud feature was impacted by convectively driven downdrafts that brought significantly dryer air into boundary layer. These observations suggest that large arc cloud events that are associated with TC diurnal pulses can act to stabilize the atmosphere by bringing cool, dry air into the low-levels and boundary layer that can affect the peripheral TC environment for several hours and could be important for TC intensity change;
- WP-3D LF radar and TDR data suggest that Hurricane Earl's TC diurnal pulse appears as a ~20 km wide semicircular ring in radar reflectivity that extends from ~0.5-6 km in the vertical and steadily propagates away from the storm. These radar features are associated with enhanced winds/vertical winds and shifting radial flow where the strength and depth of the lower level inflow and middle to upper-level outflow layers increases outside (radially) the radar-indicated TC diurnal pulse location;
- GPS dropsonde and WP-3D TDR data that were examined suggest that sublimation is prevalent in the region of satellite-indicated TC diurnal pulses (i.e. during times of enhanced ice content in the TC environment), especially during the day and when strong winds and a significant dry layer existed in the sounding profile. This supports the proposed seeder-feeder forcing mechanism presented in Chapter 3 (Sec. 3.6.5) and corroborated in Chapter 4 and could be driving the TCDC via diurnal surges in cirrus canopy ice content;
- The "seeding" mechanism proposed in Chapter 3 (Sec. 3.6.5) could result in the formation of the convectively active radar-indicated diurnal pulse and coupled arc cloud

features that were seen in 2014 Hurricane Edouard. The time involved in the seeding process (i.e. the time it takes for outflow level ice particles to reach the layer just above the freezing level) would involve a time lag, whereas the middle to upper level satellite-indicated TC diurnal pulse is radially "ahead" of the convectively active radar-indicated TC diurnal pulse;

- G-IV GPS dropsonde and WP-3D TDR data suggested that regions of suspected sublimation (and associated latent heat release) near TC diurnal pulses were associated with strong middle level temperature inversions that were overlain by 150+ hPa layers that were saturated with respect to ice and underlain by a shallow layer of enhanced updrafts and downdrafts near the melting level. These regions of sublimation near the TC diurnal pulse support the idea that abundant ice particles are coincident with TC diurnal pulses, which would support the TCDC "seeder" mechanism (Sec. 3.6.5);

6.5 Tables and Figures

Drop #	Time (UTC) (LST)	Pressure (hPa)	WSpd (m s^{-1})	WDir (deg)	WSpd (m s^{-1}) MT Sounding	WDir (deg) MT Sounding
12	2029 1629	175 200 250	24.4 24.1 17.7	215 203 202	n/a 3.6 2.1	n/a 309 305
13	2046 1646	175 200 250	17.1 17.1 17.2	182 184 158	n/a 3.6 2.1	n/a 309 305
15	2059 1659	175 200 250	15.0 16.2 18.4	203 190 185	n/a 3.6 2.1	n/a 309 305
17	2120 1720	175 200 250	8.8 10.9 15.4	193 224 188	n/a 3.6 2.1	n/a 309 305

Table 6.1: Wind speed (WSpd) and direction (WDir) at 175, 200, and 250 hPa, for 4 GPS dropsondes launched during a NOAA G-IV synoptic surveillance mission into Hurricane Earl on 31 Aug 2010 (mission 20100831N1). The moist tropical sounding (Dunion 2011) is included for reference (note: this sounding only includes sounding data at mandatory levels and therefore does not have data at 175 hPa). The four GPS dropsondes that are depicted correspond to drop points 12, 13, 15, and 17 in Figs. 6.7-6.9.

Drop #	Time (UTC)	Pressure (hPa)	T (C)	RH (%)	T (C) MT Sounding	RH (%) MT Sounding
1	1605	750	11.9	73	n/a	n/a
		850	18.1	78	17.6	80
		950	22.3	78	n/a	n/a
		Surface	26.9	71	26.8	83
2	1626	750	11.9	77	n/a	n/a
		850	16.7	97	17.6	80
		950	21.9	90	n/a	n/a
		Surface	27.7	71	26.8	83
3	1745	750	12.7	72	n/a	n/a
		850	20.9	52	17.6	80
		950	22.3	89	n/a	n/a
		Surface	25.7	84	26.8	83
4	1752	750	11.7	80	n/a	n/a
		850	16.8	83	17.6	80
		950	22.8	70	n/a	n/a
		Surface	24.6	79	26.8	83

Table 6.2: Temperature and humidity data at 750, 850, and 950 hPa, and the surface for 4 GPS dropsondes launched during a NOAA WP-3D (NOAA 42) Model Evaluation-COYOTE mission into Hurricane Edouard on 16 Sep 2014 (mission 20140916H1). The moist tropical sounding (Dunion 2011) is included for reference (note: this sounding only includes sounding data at mandatory levels and therefore does not have data at 750 or 950 hPa). The four GPS dropsondes that are depicted correspond to drop points 1-4 in Figs. 6.14-16.

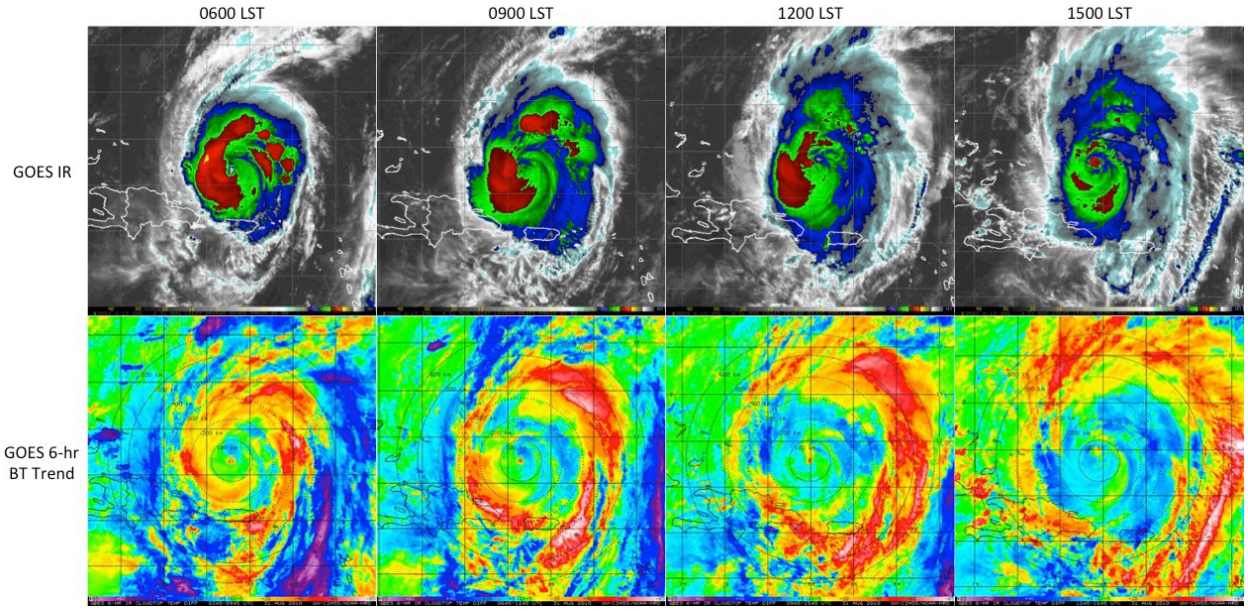

Figure 6.1: (Upper panels) GOES IR imagery showing 2010 Hurricane Earl on 31 Aug valid every 3-hours from 0600-1500 LST. The corresponding 6-hr GOES IR brightness temperature trend images for these times are shown in the lower panels. The yellow to pink shading (-10 to -85^{o}C IR cooling tendencies) indicates a diurnal pulse propagating away from the storm during this period. 100-600 km range rings (black dashed curves) from the TC center are overlaid on each of the satellite images. Lines of latitude and longitude are marked at 2 degree intervals.

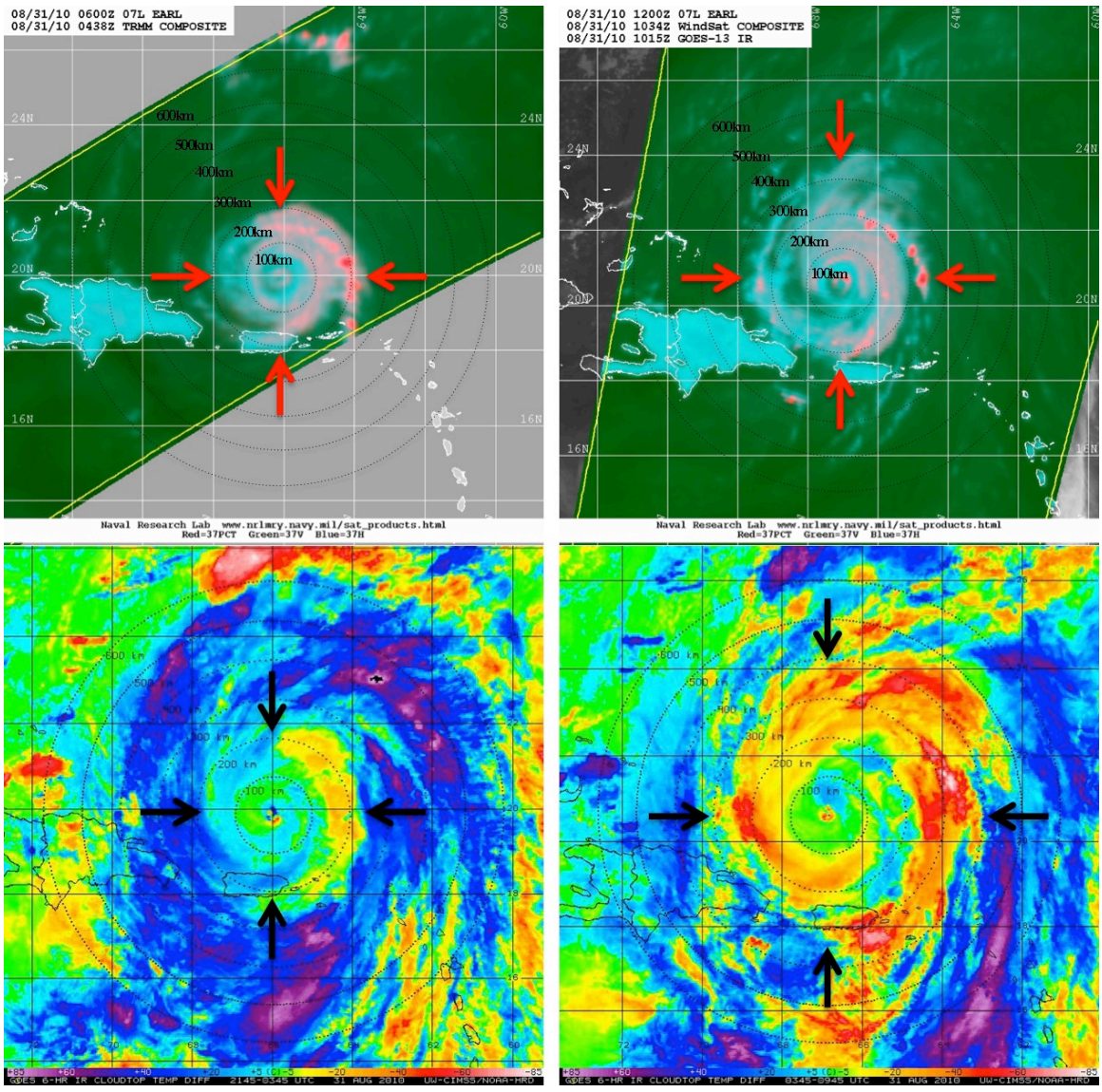

Figure 6.2: (Upper panels) NASA TRMM sensor and NOAA, Department of Defense, and NASA WindSat 37 GHz color composite microwave satellite imagery for 2010 Hurricane Earl on 31 Aug valid for (left) 0438 UTC (0038 LST) and (right) 1034 UTC (0634 LST). The corresponding 6-hr GOES IR brightness temperature trend images are shown in the lower panels. The microwave overpass times are within 55 minutes of the GOES images and areas outside of the TRMM and Wind Sat satellite swaths were supplemented by GOES visible imagery. 100-600 km range rings (black dashed curves) from the TC center are overlaid on each of the satellite images and black/red arrows denote the satellite-estimated positions of the TC diurnal pulse north, east, south, and west of the storm center. Lines of latitude and longitude are marked at 2 degree intervals. Microwave images provided courtesy of the Naval Research Laboratory Monterey.

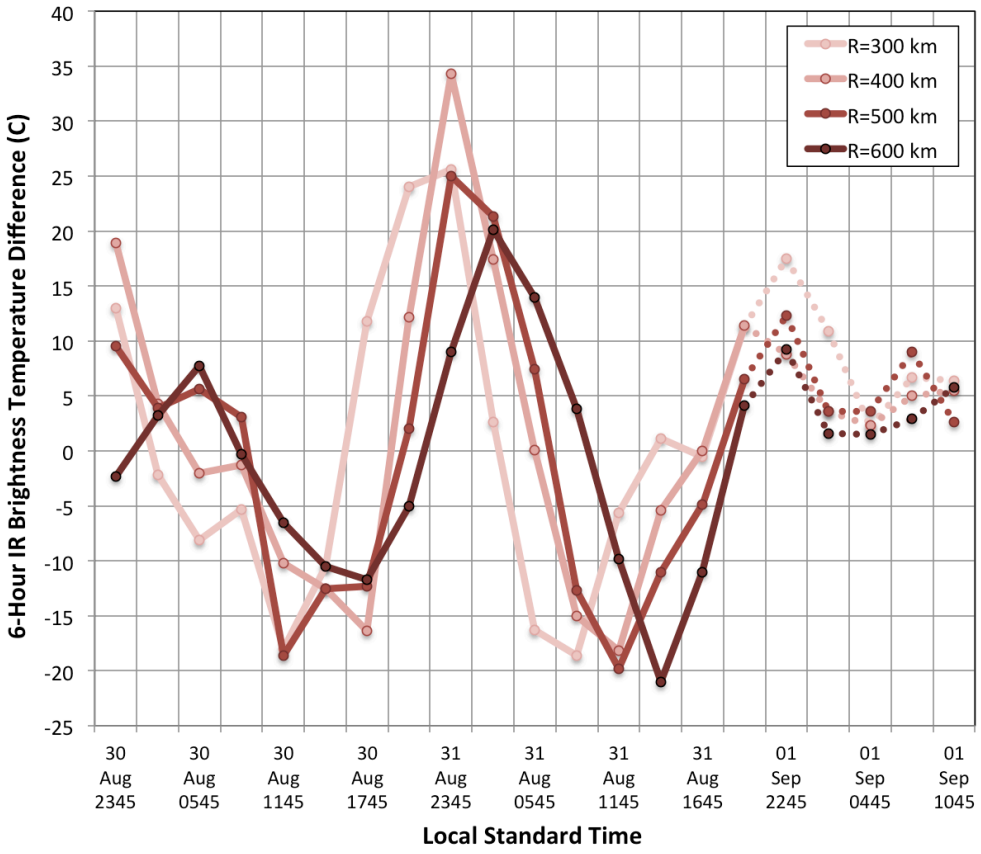

Figure 6.3: Azimuthally averaged 3-hourly 6-hr brightness temperature trends at the 300, 400, 500, and 600 km radii around 2010 Hurricane Earl from 30 Aug 2345 LST – 01 Sep 1045 LST. The dashed curved lines represent periods when the 200-850 hPa vertical wind shear for Earl reached values (8-13 m s^{-1}) above the 7.5 m s^{-1} threshold described in Sec. 2.2.1.

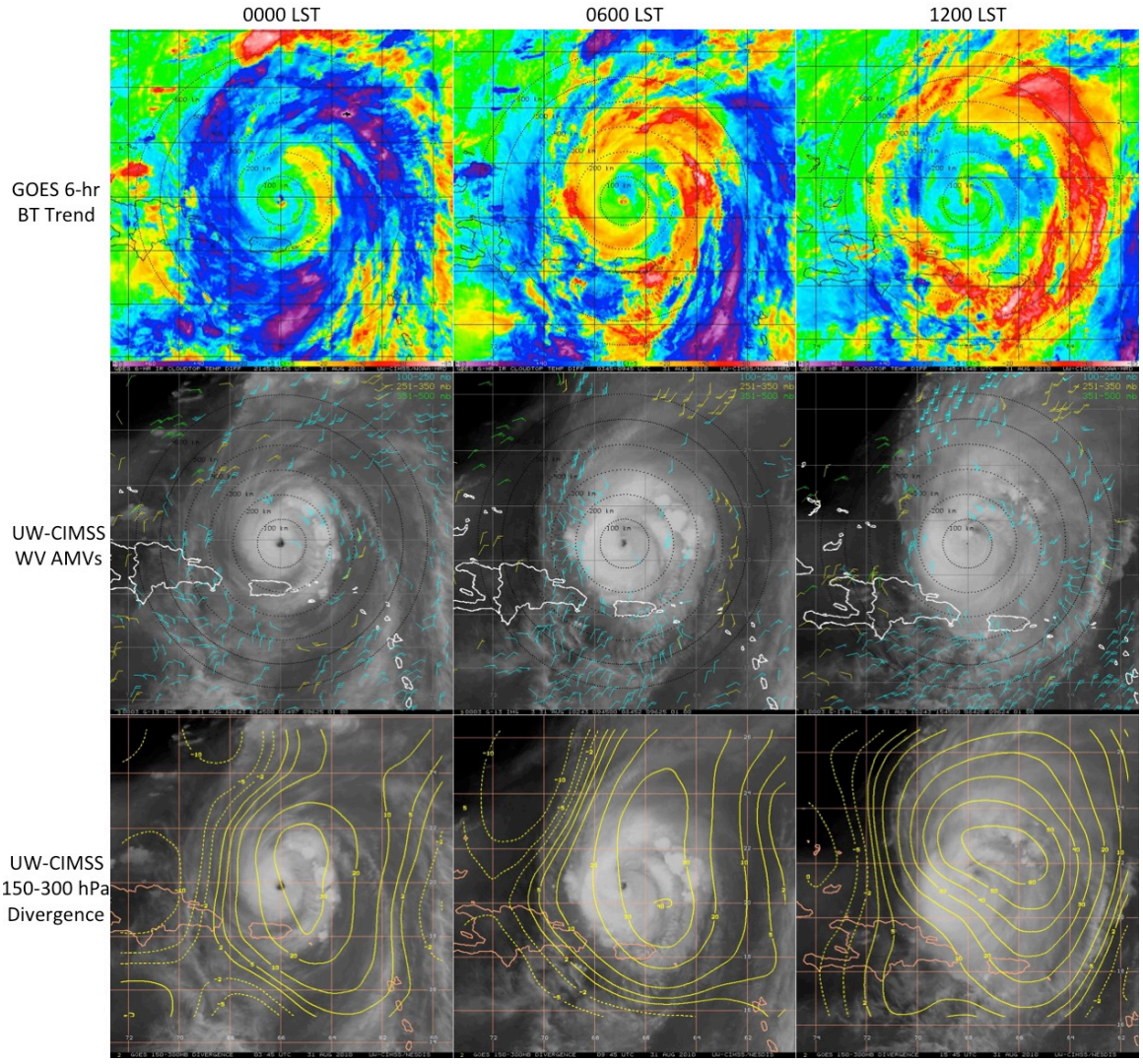

Figure 6.4: (Upper panels) 6-hr GOES IR brightness temperature differencing, (middle panels) UW-CIMSS water vapor AMVs (kt; 100-500 hPa), and (lower panels) UW-CIMSS 150-300 hPa divergence ($x10^{-6}$ s^{-1}) for 2010 Hurricane Earl on 31 Aug at 0000, 0600, and 1200 LST. Upper-level divergence (convergence) is indicated by the solid (dashed) curves. 100-600 km range rings (black dashed curves) from the TC center are overlaid on each of the satellite images. Lines of latitude and longitude are marked at 2 degree intervals.

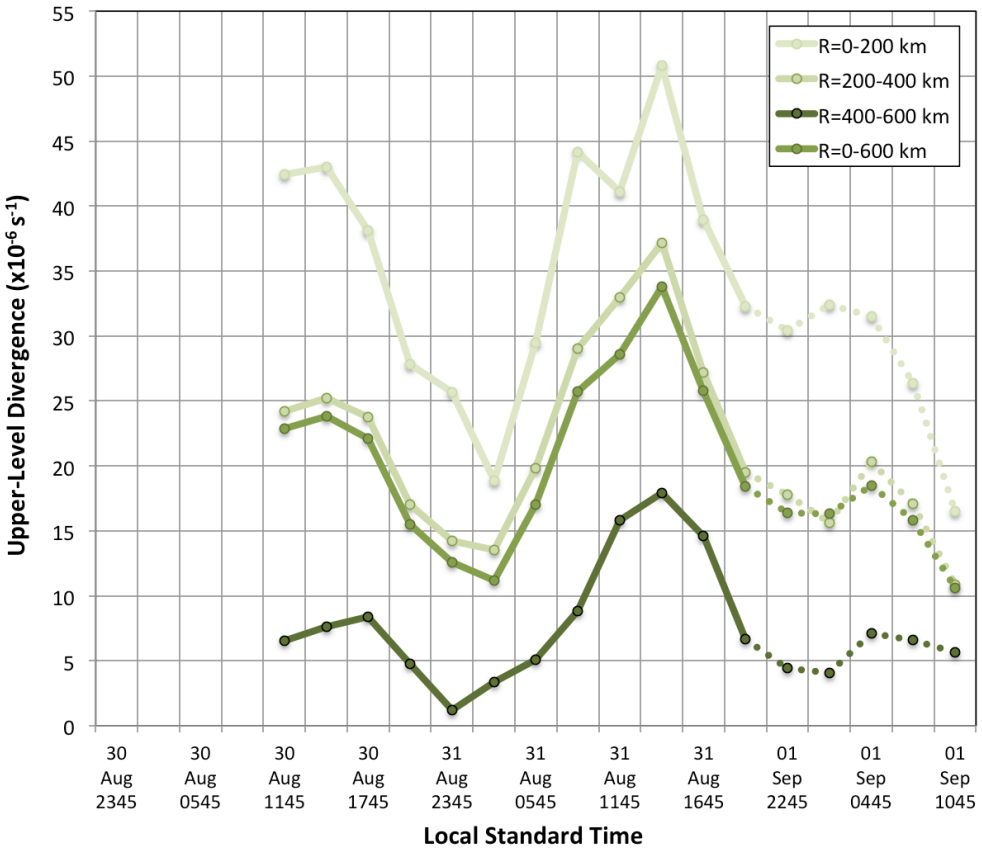

Figure 6.5: Azimuthally averaged upper-level divergence (150-300 hPa) for several radii annuluses around 2010 Hurricane Earl from 30 Aug 2345 LST – 01 Sep 1045 LST. The dashed curved lines represent periods when the 200-850 hPa vertical wind shear for Earl reached values (8-13 m s^{-1}) above the 7.5 m s^{-1} threshold described in Sec. 2.2.1. Data courtesy of the University of Wisconsin-CIMSS (note that upper-level divergence information was not available prior to 30 Aug 1145 UTC).

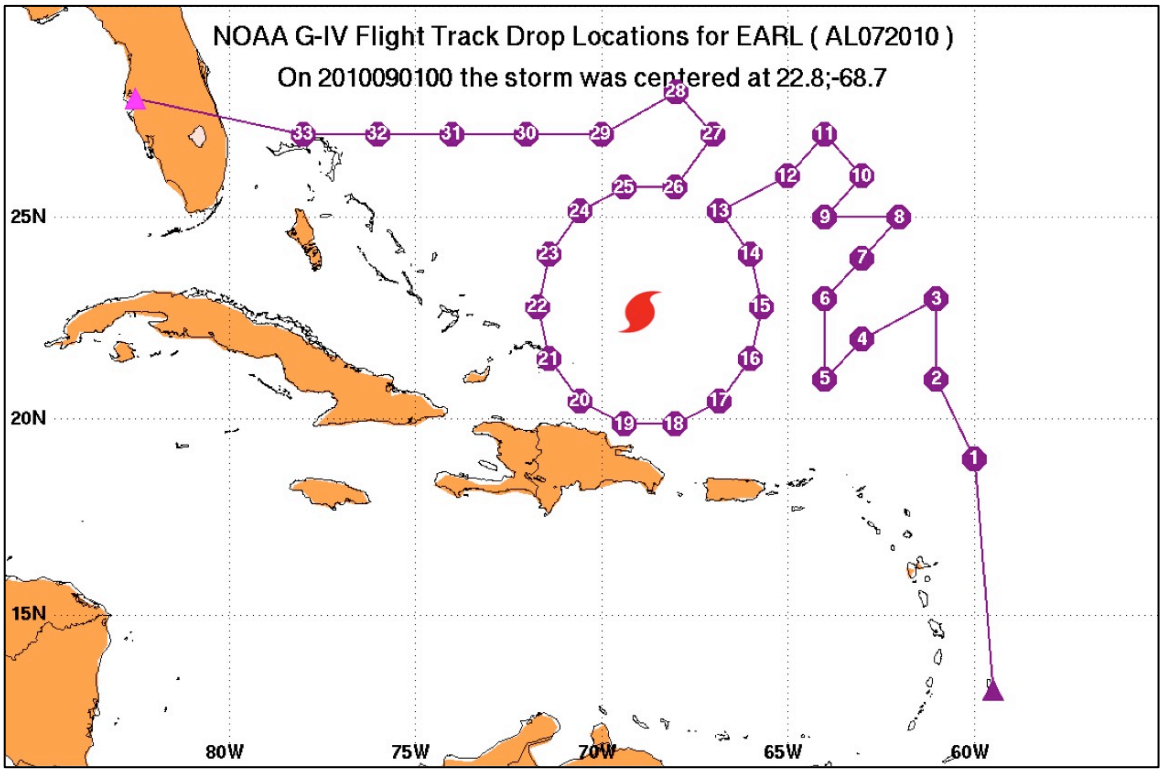

Figure 6.6: Track and GPS dropsonde points for NOAA G-IV Synoptic Surveillance mission 20100831N1 tasked by the NOAA National Hurricane Center and flown in the environment of Hurricane Earl from 31 Aug-01 Sep. Take-off was from Barbados with a landing at MacDill AFB in Tampa, FL and included 33 GPS dropsondes launched from 31 Aug 1807 UTC to 01 Sep 0045 UTC. The hurricane symbol denotes the center of Earl at 2200 UTC, approximately half way through the G-IV mission.

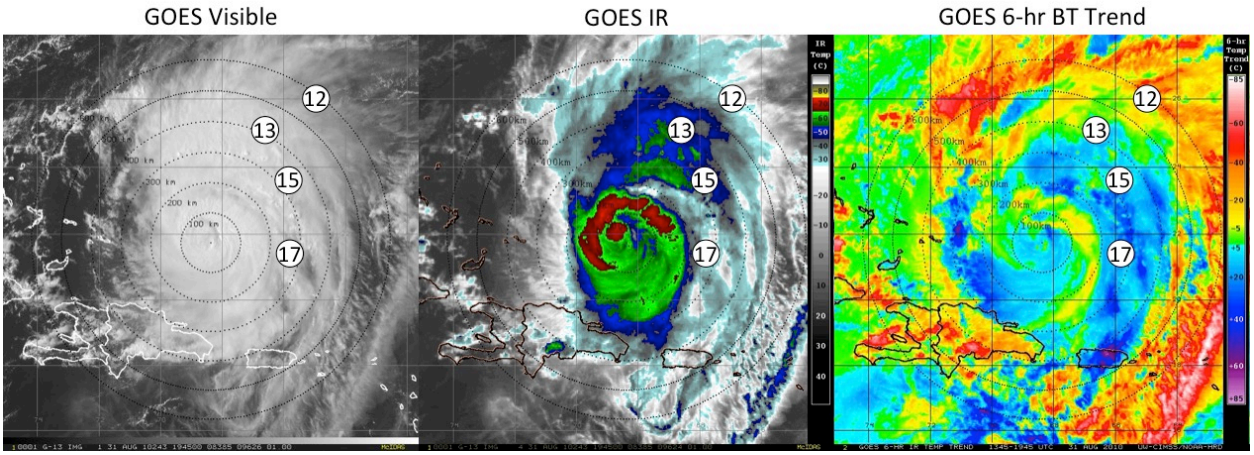

Figure 6.7: GOES visible (left), GOES IR (middle) and 6-hr GOES IR brightness temperature trend imagery showing 2014 Hurricane Earl on 31 Aug at 1945 UTC (1445 LST). For the latter image, the yellow to pink shading (-10 to -85°C IR cooling tendencies) indicates a diurnal pulse propagating away from the storm during this time. Drop points 12, 13, 15, and 17 from NOAA G-IV mission 20100831N1 (Fig. 6.6) and 100-600 km range rings (black dashed curves) from the TC center are overlaid on each of the satellite images. Lines of latitude and longitude are marked at 2 degree intervals.

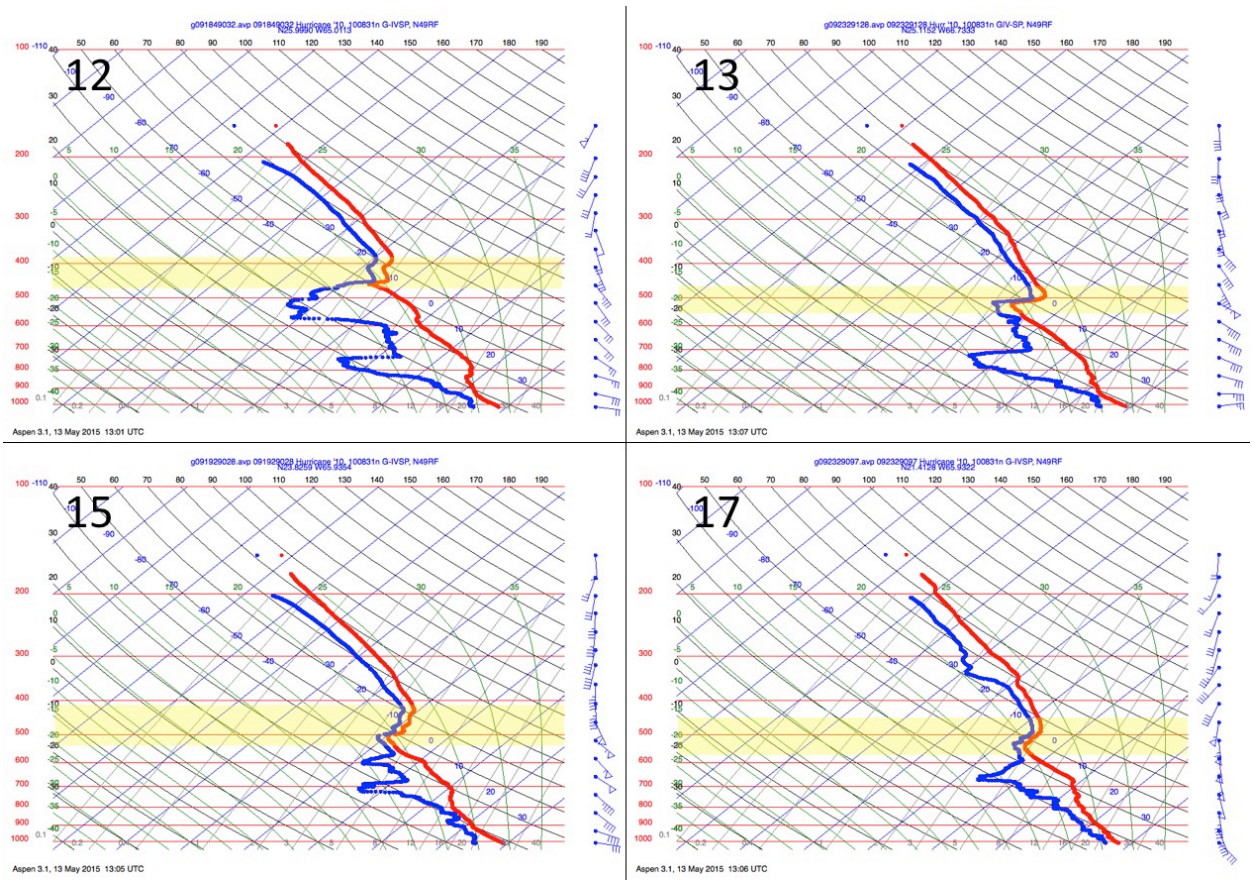

Figure 6.8: NOAA G-IV GPS dropsonde skew-t profiles from Synoptic Surveillance mission 20100831N1. The four GPS dropsondes that are depicted correspond to drop points 12 (2029 UTC/1629 LST), 13 (2046 UTC/1646 LST), 15 (2059 UTC/1659 LST) and 17 (2120 UTC/1720 LST) shown in in Figs. 6.6 and 6.7. The yellow shading highlights the locations of distinct middle level thermodynamic and wind discontinuities in each profile. The melting levels for these 4 soundings range from ~590 600 hPa.

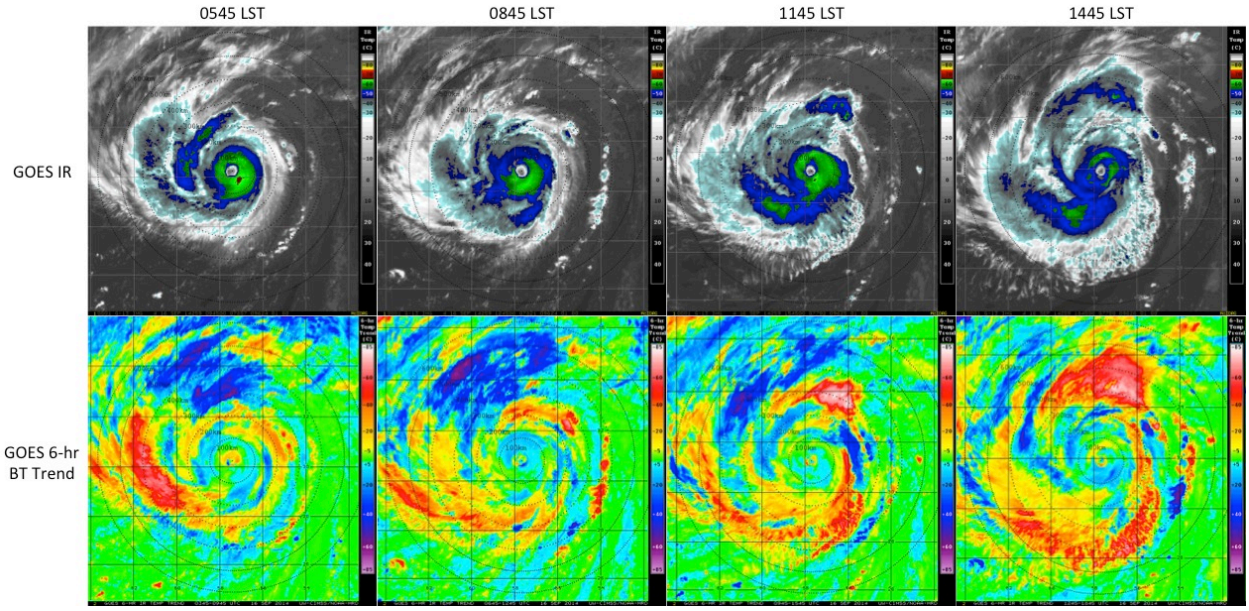

Figure 6.9: (Upper panels) GOES IR imagery showing 2014 Hurricane Edouard on 16 Sep valid every 3-hours from ~0600-1500 LST. The corresponding 6-hr GOES IR brightness temperature trend images for these times are shown in the lower panels. The yellow to pink shading (-10 to -85^{o}C IR cooling tendencies) indicates a diurnal pulse propagating away from the storm during this period. 100-600 km range rings (black dashed curves) from the TC center are overlaid on each of the satellite images. Lines of latitude and longitude are marked at 2 degree intervals.

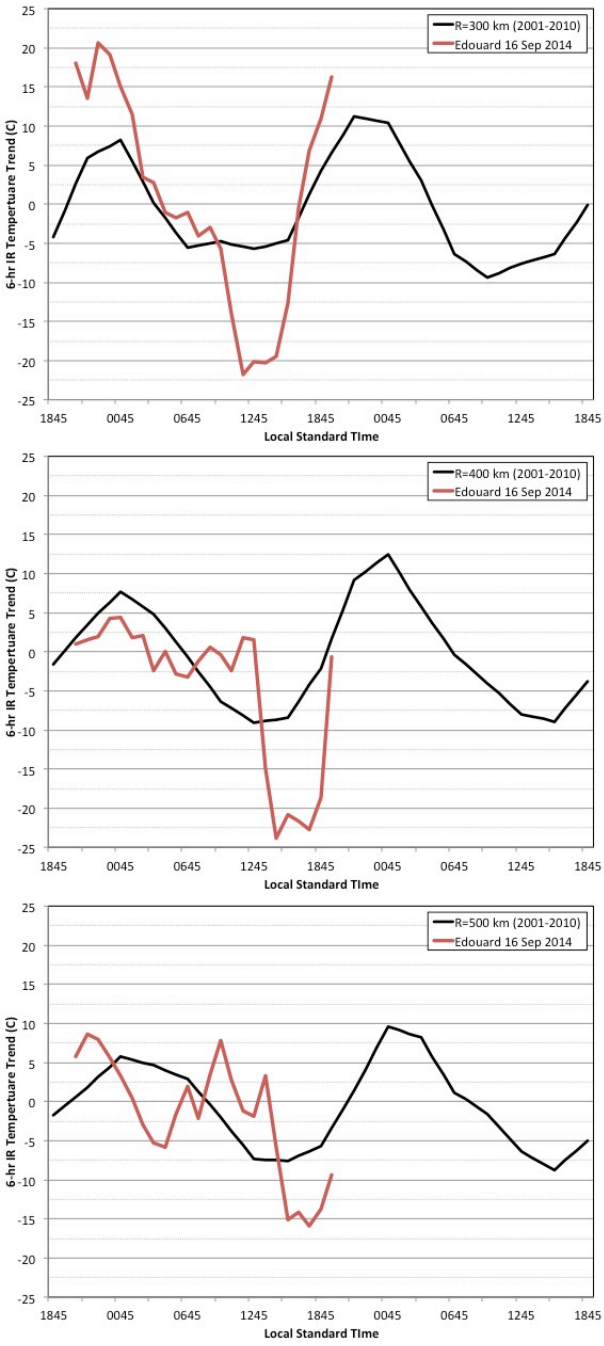

Figure 6.10: Azimuthally averaged 3-hourly 6-hr brightness temperature trends at the 300 km (top), 400 km (middle), and 500 km (bottom) radii. The red curves show Edouard's TCDC at the respective radii, while the black curves represent the corresponding mean 2-day TCDC pattern derived from the 2001-2010 major hurricane dataset discussed in Chapter 3.

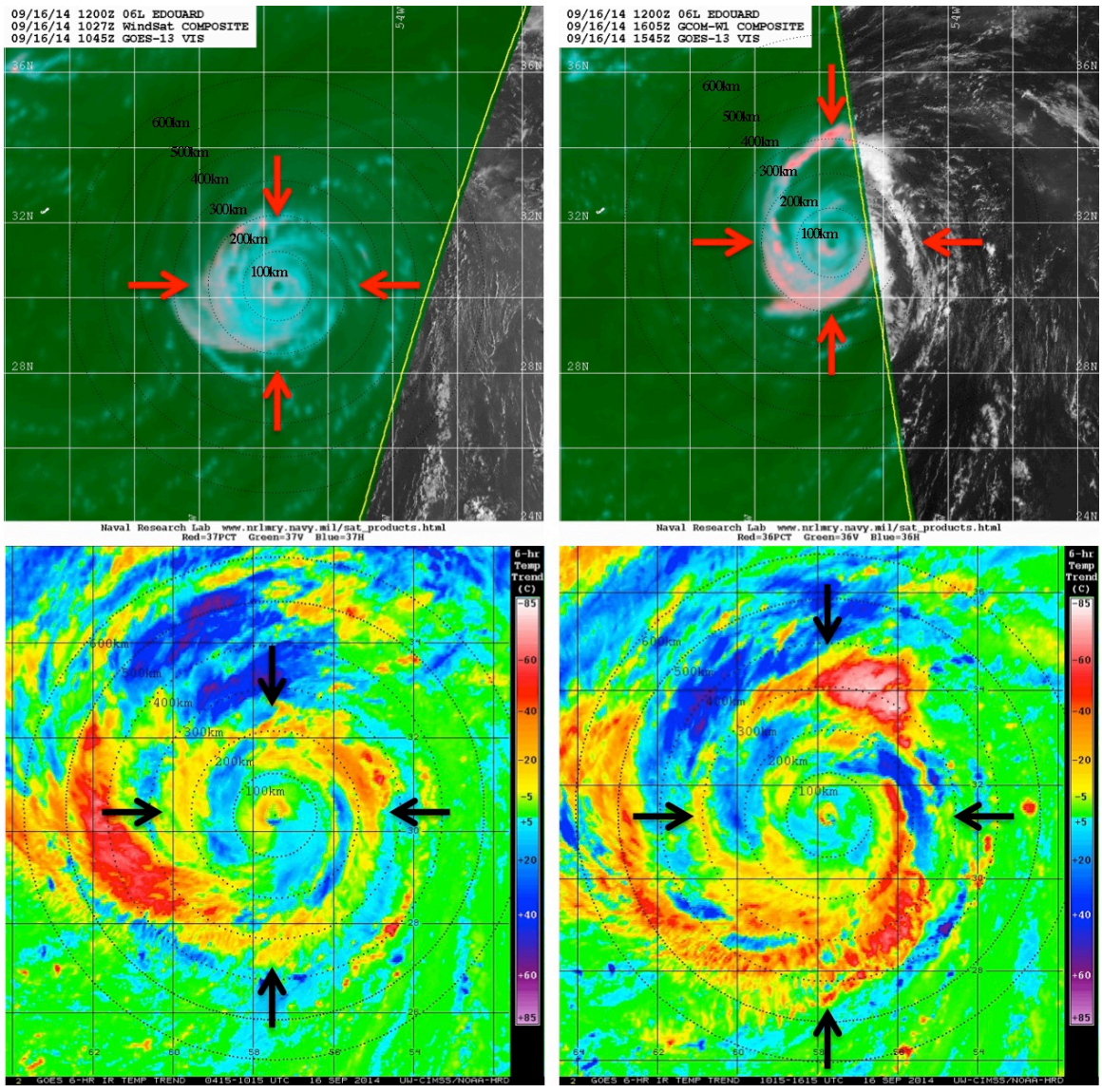

Figure 6.11: As in Fig. 6.2, but NOAA, Department of Defense, and NASA WindSat sensor and Japan Aerospace Exploration Agency GCOM-W satellite AMSR2 sensor 37 GHz color composite microwave satellite imagery for 2014 Hurricane Edouard on 16 Sep valid for (left) 1027 UTC (0627 LST) and (right) 1605 UTC (1205 LST). The microwave overpass times are within 12 minutes of the GOES images.

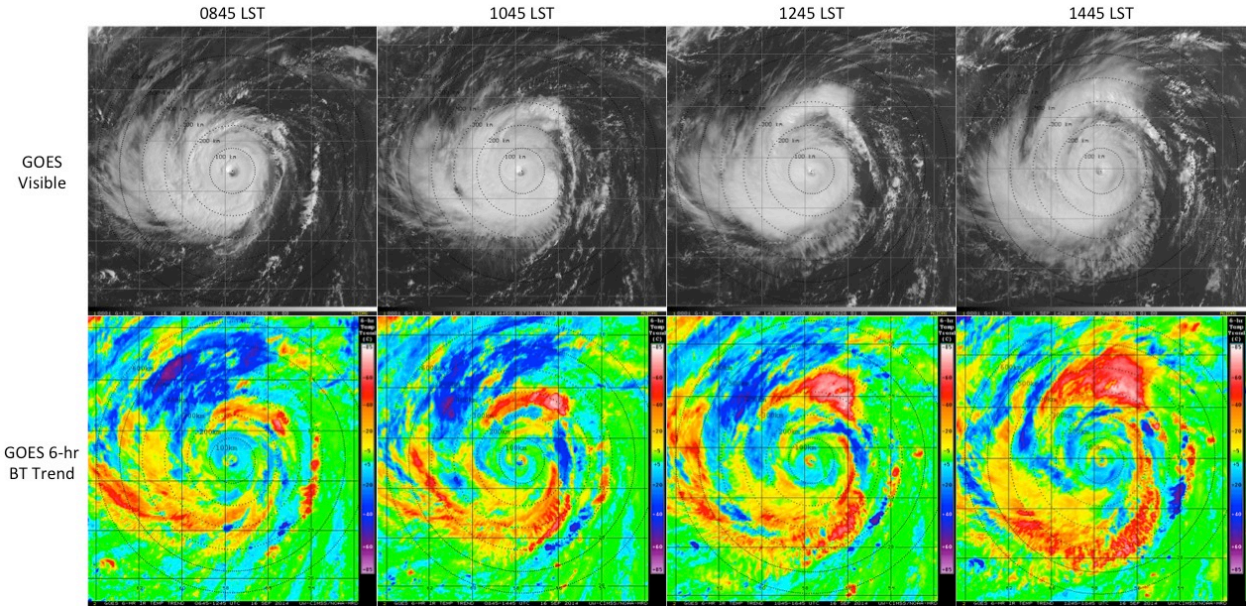

Figure 6.12: (Upper panels) GOES visible imagery showing 2014 Hurricane Edouard on 16 Sep valid every 2-hours from 0945-1445 LST. The corresponding 6-hr GOES IR brightness temperature trend images for these times are shown in the lower panels. The yellow to pink shading (-10 to -85^{o}C IR cooling tendencies) indicates a diurnal pulse propagating away from the storm during this period. 100-600 km range rings (black dashed curves) from the TC center are overlaid on each of the satellite images. Lines of latitude and longitude are marked at 2 degree intervals.

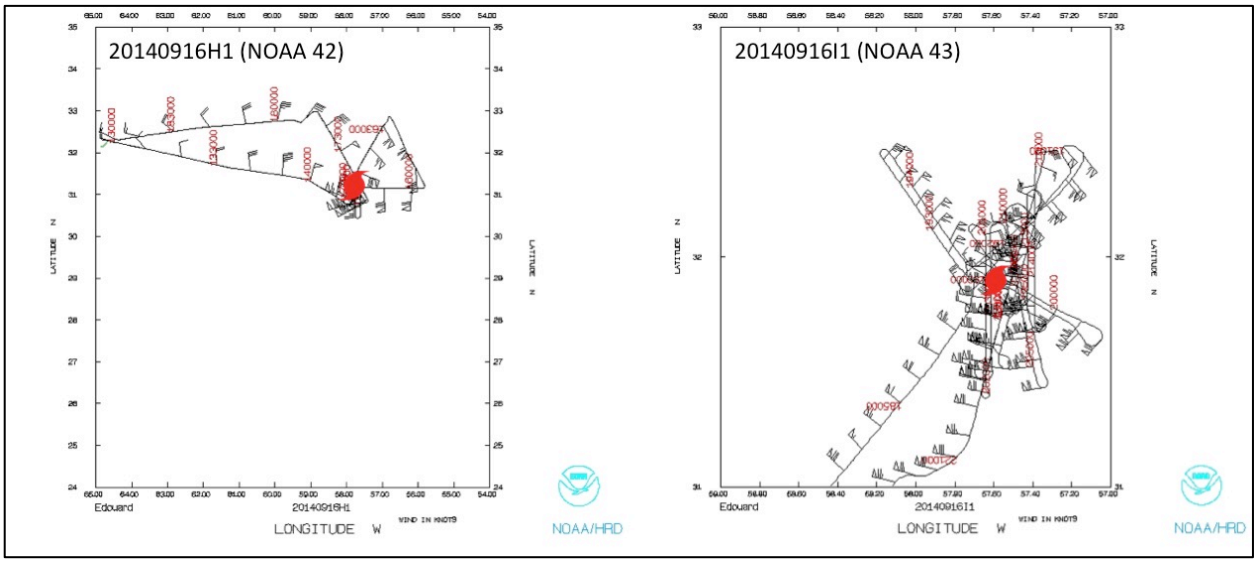

Figure 6.13: Flight tracks for (left) NOAA IFEX WP-3D missions 20140916H1 (NOAA 42) tasked by the NOAA Hurricane Research Division (HRD) and (right) 20140916I1 (NOAA 43) tasked by NOAA NESDIS into Hurricane Edouard on 16 Sep 2014. The hurricane symbols denote the center of Edouard approximately half way through each the WP-3D missions.

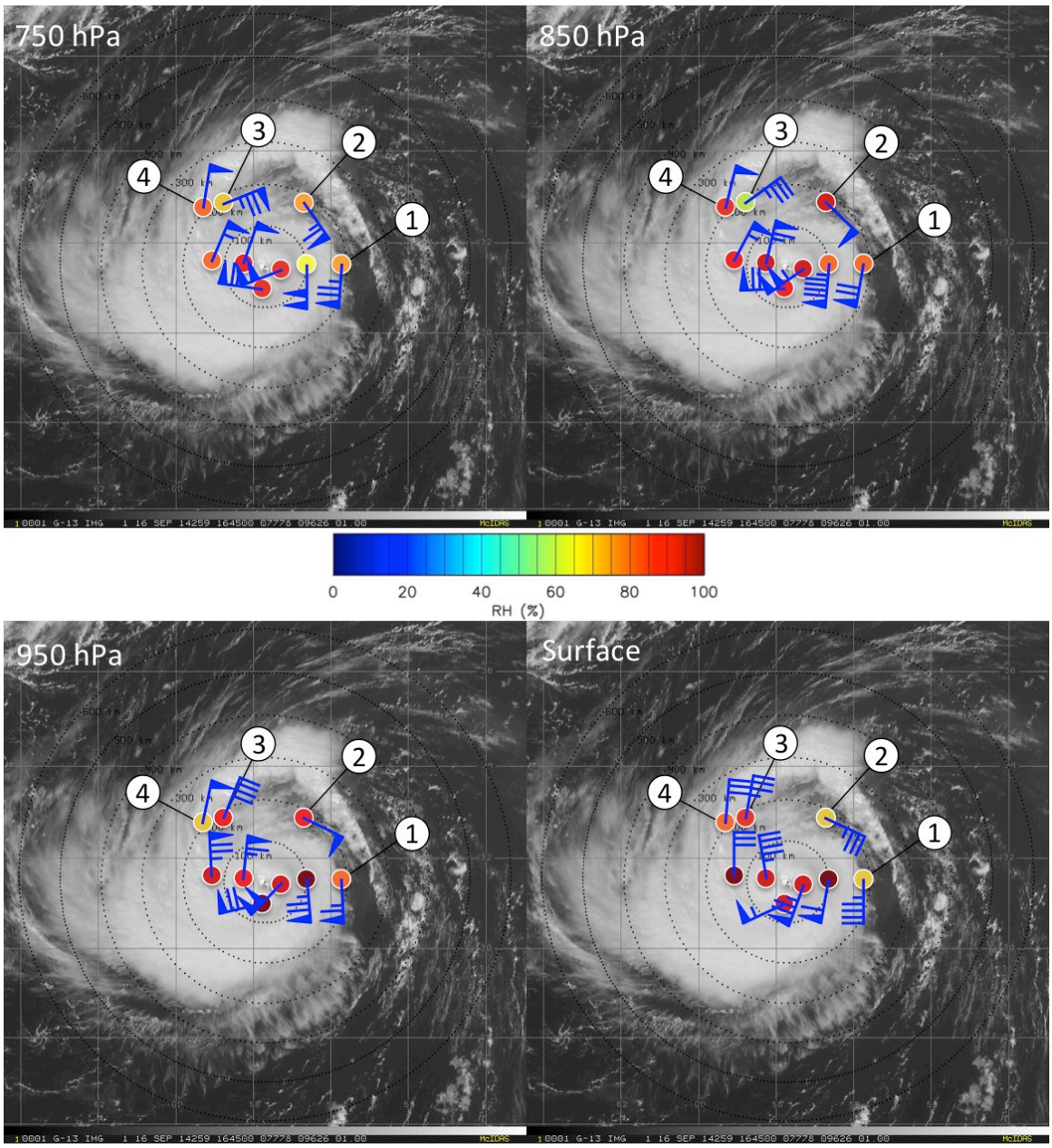

Figure 6.14: GOES visible imagery showing 2014 Hurricane Edouard on 16 Aug at 1645 UTC (1245 LST). Relative humidity (%) and wind speed (kt) for several GPS dropsondes launched during NOAA WP-3D (NOAA 42) mission 20140916H1 are shown at 750 hPa, 850 hPa, 950 hPa, and the surface. Dropsondes 1-4 refer to the dropsonde profiles shown in Fig. 6.15 and are within 70 min of the GOES image. 100-600 km range rings (black dashed curves) from the TC center are overlaid on each of the satellite images and lines of latitude and longitude are marked at 2 degree intervals.

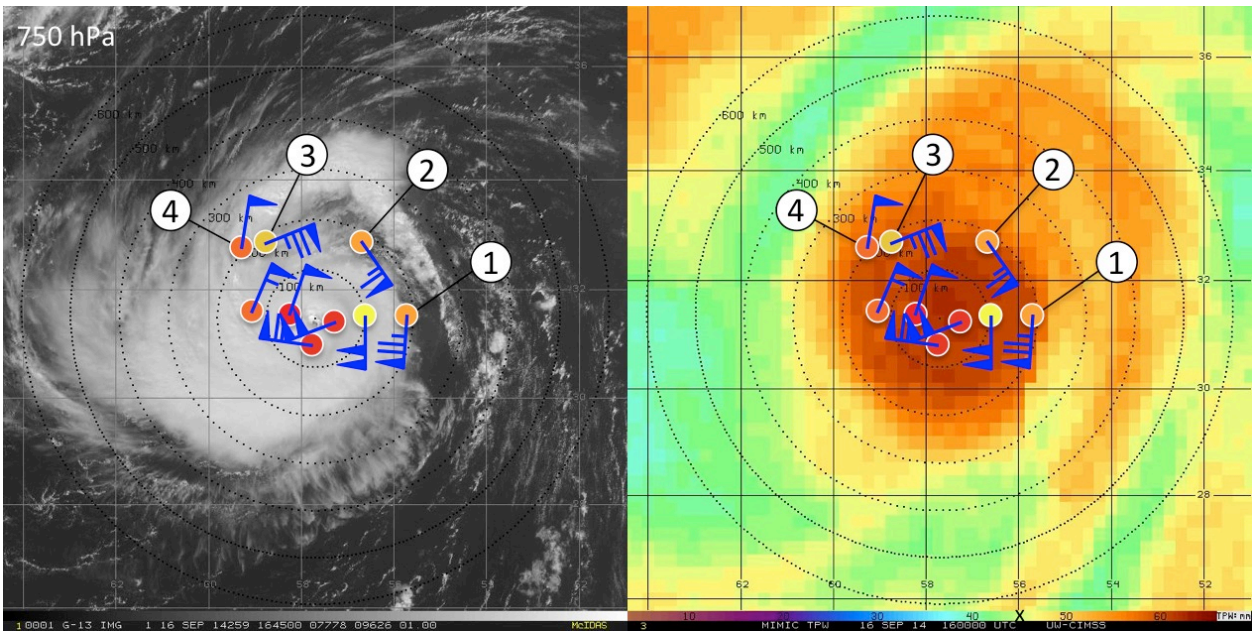

Figure 6.15: GOES visible imagery (left) and TPW imagery (right) showing 2014 Hurricane Edouard on 16 Aug at 1645 UTC (1245 LST) and 1600 UTC (1200 LST) respectively. The 750 hPa NOAA WP-3D (NOAA 42) GPS dropsonde data shown in Fig. 6.14 are overlaid on both images for reference. 100-600 km range rings (black dashed curves) from the TC center are overlaid on each of the satellite images and lines of latitude and longitude are marked at 2 degree intervals. The black "x" in the TPW color bar scale denotes the value of 45 mm TPW.

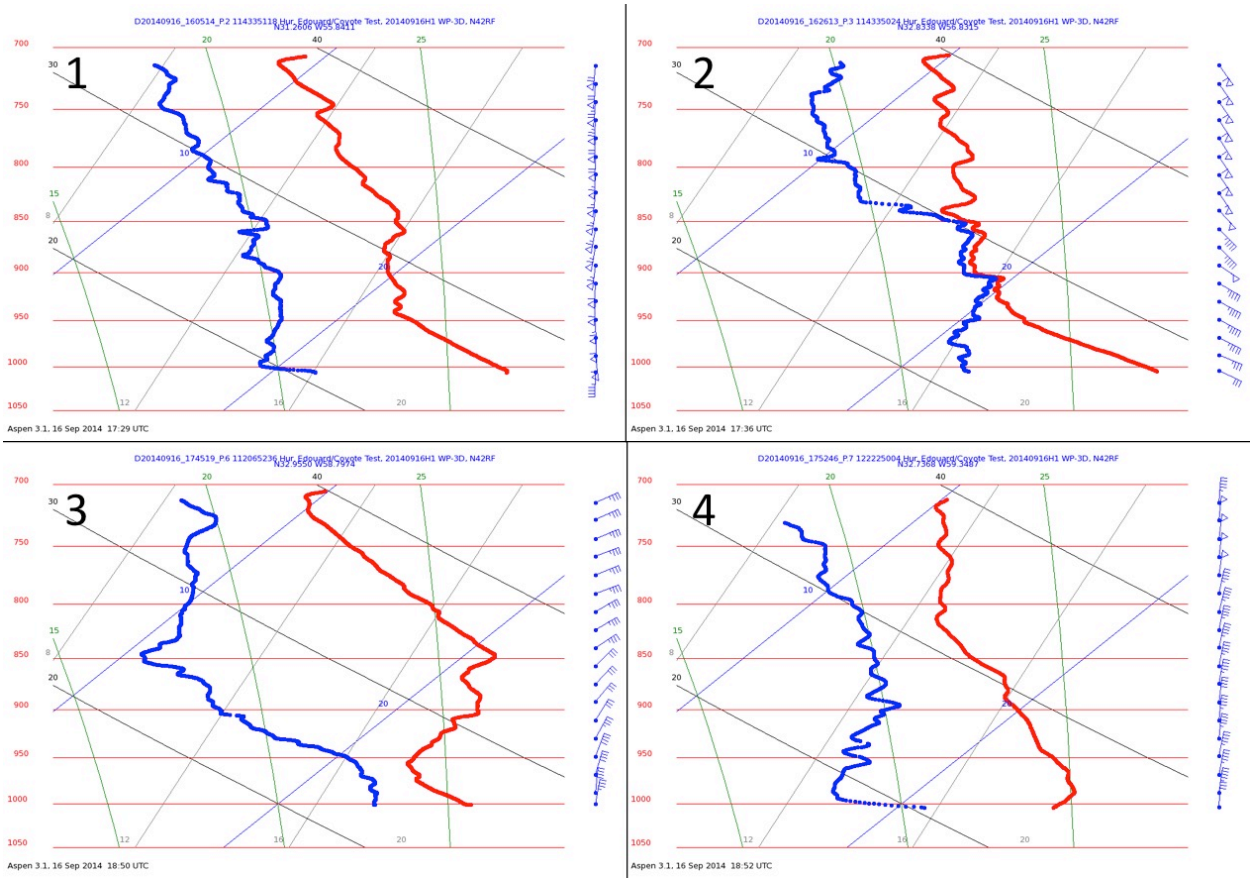

Figure 6.16: NOAA WP-3D (NOAA 42) GPS dropsonde skew-t profiles from Model Evaluation-COYOTE mission 20140916H1. The four GPS dropsondes that are depicted correspond to drop points 1 (1605 UTC/1205 LST), 2 (1626 UTC/1226 LST), 3 (1745 UTC/1345 LST) and 4 (1752 UTC/1352 LST) shown in Fig. 6.14.

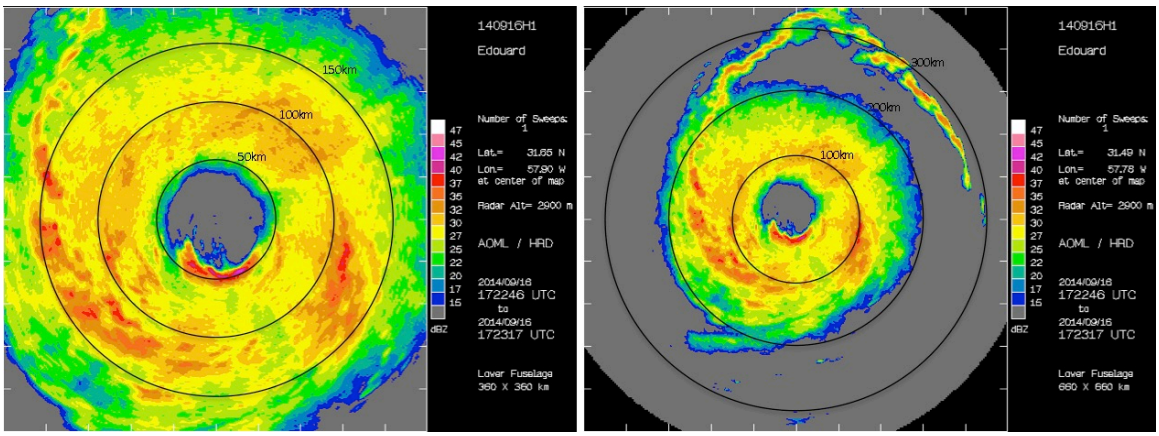

Figure 6.17: NOAA WP-3D (NOAA 42) storm-centered LF radar images (16 Sep 1323 LST/1723 UTC) from Model Evaluation-COYOTE mission 20140916H1. The images show the normal NOAA HRD LF radar domain of 360 x 360 km (left) and an expanded LF radar domain of 660 x 660 km (right). (Left) 50-150 km and (right) 100-300 km range rings (black curves) from the TC center are overlaid on the radar images. A TC diurnal pulse can be seen in the 660 x 660 km LF radar image as a semi-circular arc of high reflectivity (~20-40 dBZ) that is steadily propagating away from the storm at radii of ~175-350 km. The gray circle of near-zero reflectivity at the center of each image represents the position of the WP-3D and is caused by beam interference from the aircraft fuselage.

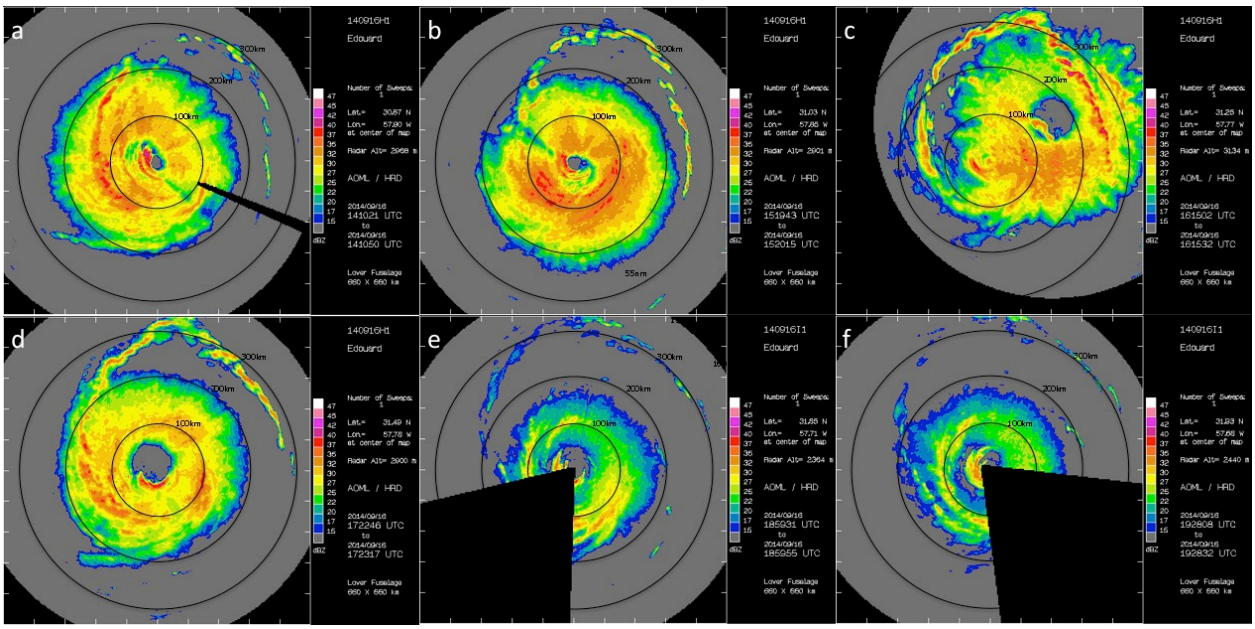

Figure 6.18: NOAA WP-3D (NOAA 42 and 43) storm-centered LF radar images from Model Evaluation-COYOTE mission 20140916H1 and NOAA NESDIS Ocean Winds mission 20140916I1. The images are from 1010 LST/1410 UTC (a), 1120 LST/1520 UTC (b), 1215 LST/1615 UTC (c), 1323 LST/1723 UTC (d), 1459 LST/1859 UTC (e), and 1528 LST/1928 UTC (f). 100-300 km range rings (black curves) from the TC center are overlaid on each of the radar images. A TC diurnal pulse can be seen in the images as a semi-circular arc of high reflectivity (~20-40 dBZ) that is steadily propagating away from the storm at radii of ~150-350 km. The gray circle of near-zero reflectivity in each image represents the position of the WP-3D and is caused by beam interference from the aircraft fuselage.

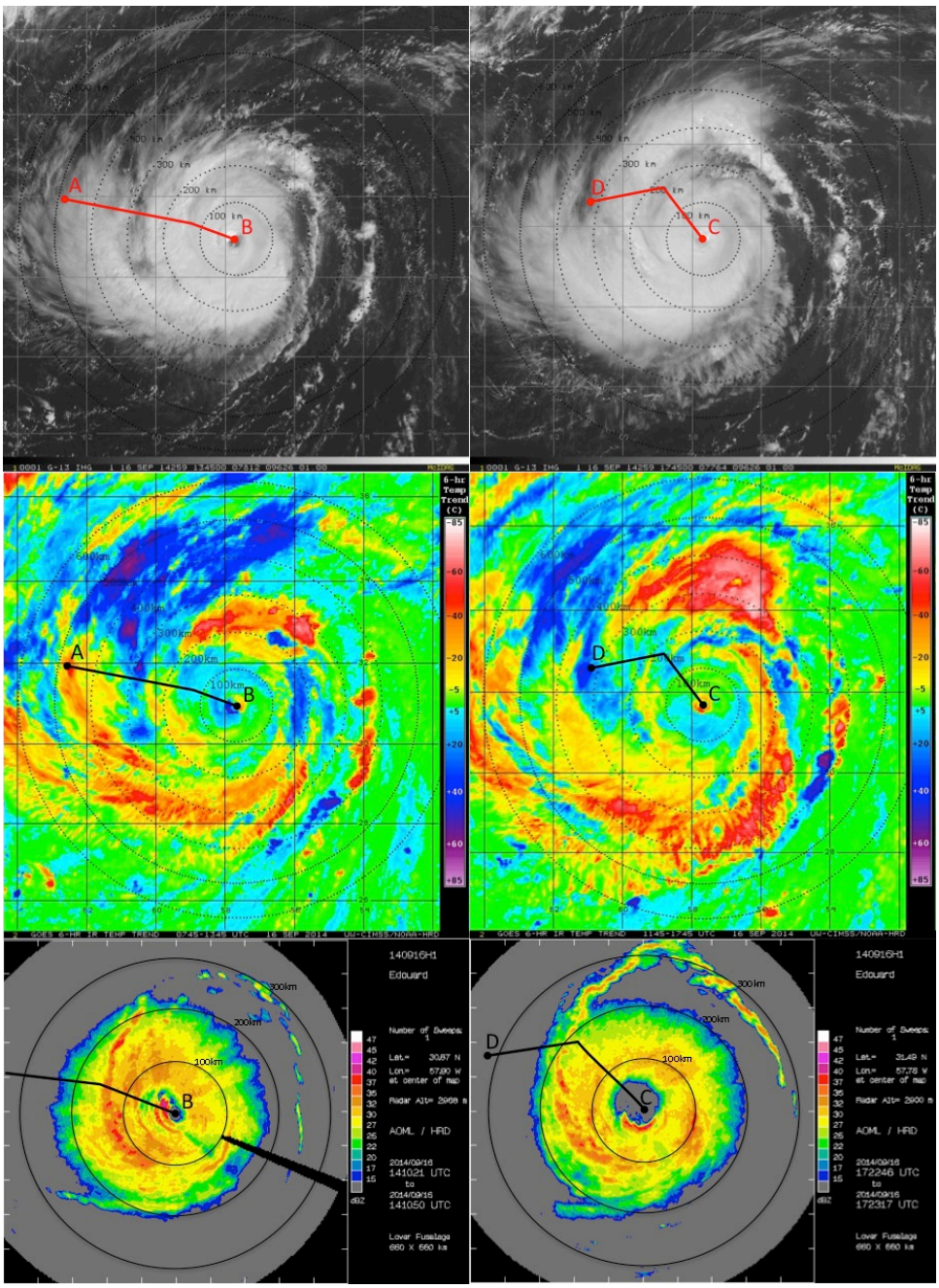

Figure 6.19: (top row) GOES visible, and (middle row) 6-hr GOES IR brightness temperature trend images, and (bottom row) storm-centered LF radar images for 2014 Hurricane Edouard on 16 Sep at (left column) 1045 LST/1345 UTC and (right column) 1345 LST/1745 UTC. The left column images show the WP-3D (NOAA 42) inbound leg used to create the TDR cross sections in Fig. 6.20, while the right column images show the WP-3D (NOAA 42) outbound leg used to create the TDR cross sections in Fig. 6.21. 100-600 km range rings (black dashed curves) from the TC center are overlaid on each of the satellite images. Lines of latitude and longitude in the GOES images are marked at 2 degree intervals.

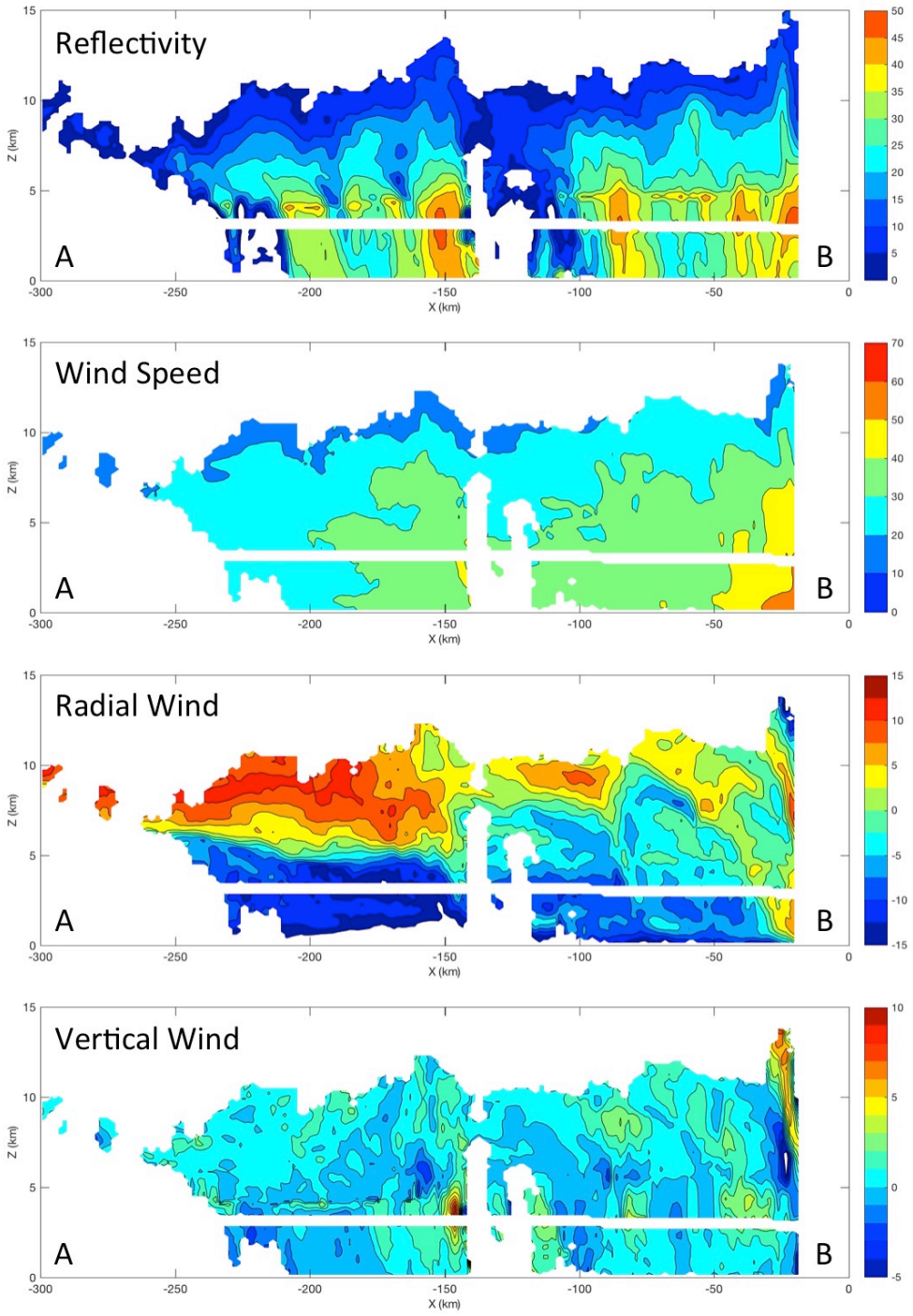

Figure 6.20: Tail Doppler radar-derived cross sections of radar reflectivity (dBZ), wind speed (m s^{-1}), radial wind speed (m s^{-1}), and vertical wind speed (m s^{-1}) from the WP-3D (NOAA 42) inbound leg on 16 Sep 2014 from 1120 LST/1320 UTC (A) to 1416 UTC (B). The flight path for this outbound WP-3D leg (A-B) is shown in Fig. 6.19.

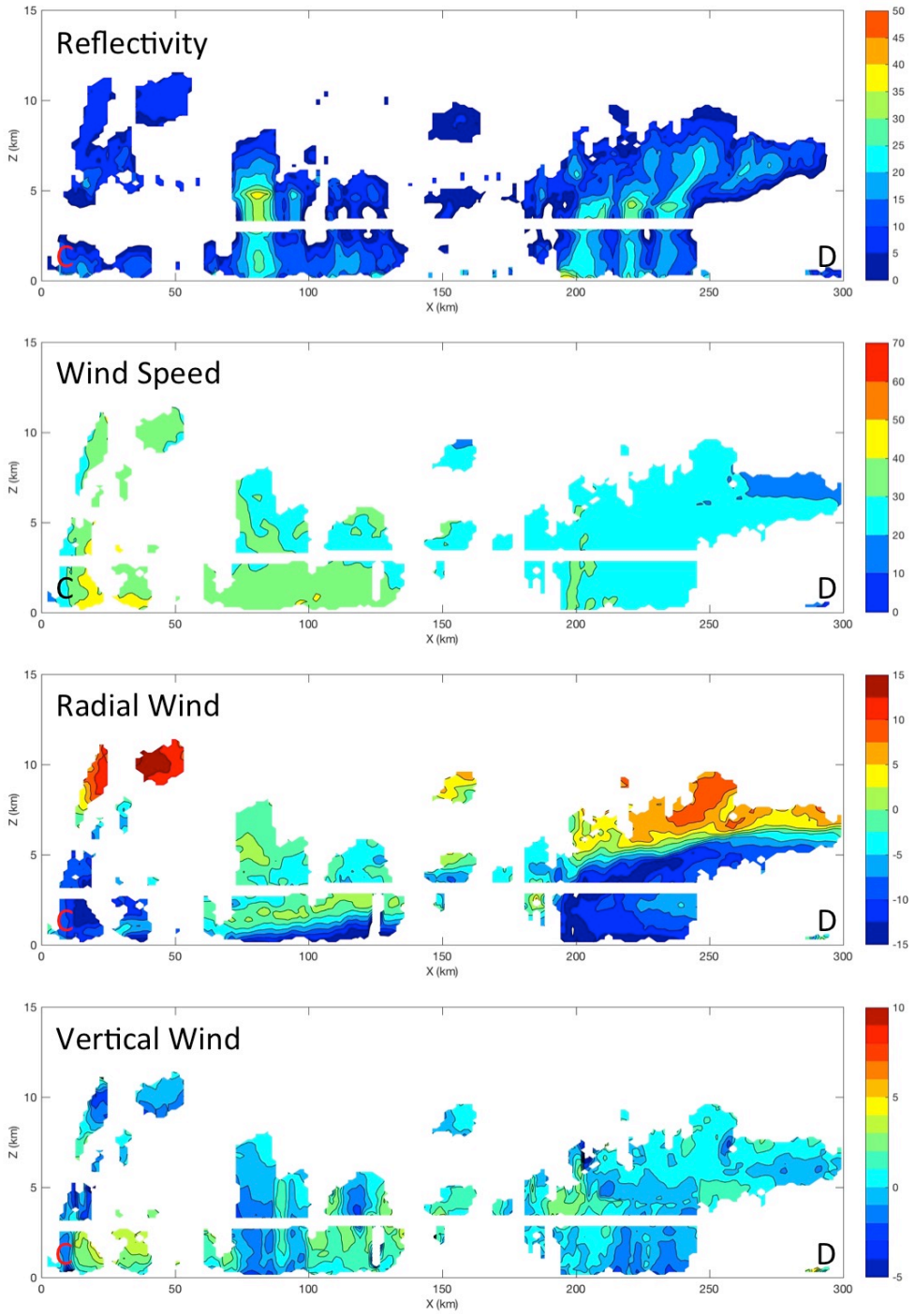

Figure 6.21: Tail Doppler radar-derived cross sections of radar reflectivity (dBZ), wind speed (m s^{-1}), radial wind speed (m s^{-1}), and vertical wind speed (m s^{-1}) from the WP-3D (NOAA 42) outbound leg on 16 Sep 2014 from 1320 LST/1720 UTC (C) to 1812 UTC (D). The flight path for this outbound WP-3D leg (C-D) is shown in Fig. 6.19.

7. Conclusions

7.1 Discussion and Results

This thesis has presented research related to understanding various aspects of the TCDC and accompanying TC diurnal pulses. The main objectives of this research have been to explore satellite, numerical modeling, and observational perspectives of this phenomenon and describe techniques for monitoring it in real-time, its evolution in both time and space, its relevance to TC structure and intensity, and its manifestation in numerical simulations of TCs. Although previous research has recognized the importance of diurnal signals in convection and precipitation as well as the areal extent and temperature of the TC cirrus canopy, no previous studies have identified the coherent, radially propagating nature of the TCDC in TCs and their surrounding environments. This research attempts to first identify the evolving characteristics of the TCDC, how its attributes are presented in satellite imagery, if it can be effectively identified and predicted, and what physical mechanisms may be responsible for its formation. Subsequent research built from these results to explore the implications of the TCDC on satellite-based estimates of TC intensity, operational analyses of significant wind radii around the storm, and numerical model simulations of TCs. The final research effort utilized the findings from these various efforts to guide the identification of TCDC signals and TC diurnal pulses from aircraft observations taken in both the TC inner core and surrounding environment of two major North Atlantic hurricanes. Several scientific questions related to the TCDC were presented in Chapter 1 and were later explored in Chapters 3-6 and discussed below:

1. What are the spatial and temporal characteristics of the TCDC?
2. What remote sensing techniques can be developed/utilized to track the TCDC in time and space?
3. What are the physical mechanisms responsible for the onset and evolution of the TCDC?
4. What is the influence of the diurnal cycle on TC structure (e.g. spiral bands/convective arms outside the inner core), outflow at the level of the cirrus canopy, and upper level divergence)?
5. To what extent are diurnal variations important for TC intensity and structure?
6. What are the implications of the TCDC on the structure and intensity of TCs, African easterly waves, and tropical convection in general?

Research described in Chapter 3 led to the development of a satellite image differencing technique that uses storm centered geostationary satellite IR channels to monitor the TCDC and track TC diurnal pulses emanating from mature TCs. The IR differencing imagery revealed a distinct diurnal pulse in the investigated storms that begins each evening near the time of local sunset and appears as a radially expanding, quasi-symmetric ring of cooling brightness temperatures with marked warming on its inside edge. These TC diurnal pulses appear to steadily move/propagate outward, reaching peripheral radii of the storm by early afternoon local time the following day. In fact, the remarkably consistent diurnal timing of these propagating features inspired the development of a 24-hr conceptual clock that is able to predict their temporal and spatial evolution each day. Potential links between the TCDC and TC structure and intensity was also supported by analyses of operationally estimated 50 kt wind radii from the

Extended Best Track archive and objective satellite intensity estimates from the Advanced Dvorak Technique, where statistically significant diurnal signals in these parameters were found.

The satellite-based analyses in Chapter 3 provided insights related to recognizing and predicting the TCDC in mature hurricanes and its impacts on storm structure and intensity. However, the exact causes of this phenomenon were not obvious from the satellite analyses alone. Therefore, five hypothesized triggering mechanisms were proposed in this chapter that could explain how the TCDC forms and evolves each day. Four of these mechanisms relate to preferential longwave cooling (relative to surrounding clear air) of the cirrus outflow layer near and after sunset each day that rapidly cools and destabilizes the upper portion of this layer. The resulting cooling and destabilization could promote 1) *convectively-driven atmospheric gravity waves*: gravity waves that are generated by deep convection and normally propagate upward into the stratosphere become ducted beneath the relatively cooler, more stable cirrus outflow layer. This gravity wave ducting would be further enhanced if the outflow layer was also associated with vertical wind shear. These radially propagating gravity waves could become more readily detectable as they pass through the TC outflow layer; 2) *radiatively reduced outflow resistance*: destabilization of the outflow layer reduces the vertical gradient of potential temperature in this region of the storm, thereby reducing potential vorticity and increasing IAKE. This would lead to a release in upper-level outflow and could enhance convection below that was previously limited by outflow resistance; 3) *Cloud-cloud-free differential heating mechanism*: the cirrus outflow layer cools more at night and less during the day than surrounding cloud-free regions. The resulting pressure surfaces created by these temperature contrasts would promote inhibited upper level outflow at night and enhanced outflow during the day; 4) *Direct radiation-convection interactions*: shortwave warming during the day that is preferentially occurring in the

region of the outflow layer (relative to surrounding clear air) promotes increased static stability in the middle to upper troposphere. Conversely, at night, preferential cooling at the level of the cirrus canopy relative to the lower troposphere decreases the static stability. These diurnal patterns would enhance convection during the nighttime and early morning hours and could also promote upper-level divergence. The environment just outside the TC inner core, where persistent deep convection may not be occurring, could especially benefit from the reduced middle to upper level static stability that direct radiation-convection interaction processes would promote.

The 5th proposed mechanism discussed in Chapter 3 is the *seeder-feeder* mechanism and does not necessarily describe a trigger for the TCDC and TC diurnal pulses, but rather a mechanism that would support these processes after they were initiated by another mechanism. For example, the seeder-feeder mechanism could be coupled with TCDC mechanism number 1 discussed above, where mesoscale lift associated with a radially propagating gravity wave of sufficient depth could promote the "feeder" mechanism. It also could be linked with mechanism numbers 2-4 discussed above, where radial advection of the cirrus canopy is implied. Ice crystals associated with a radially expanding cirrus canopy in a TC environment (initiated by one of these three processes could help stimulate convection in peripheral rainbands via the "seeder" mechanism.

Although the specific mechanisms that drive the TCDC and associated diurnal pulses could not be verified or refuted by Chapter 3's satellite-based analyses, more than one of the above-hypothesized mechanisms (or another mechanism not considered here) could be acting together in the TC environment to drive TCDC processes each day. Addressing these

hypotheses was an objective of the model-based analyses described in the chapter that followed (Chapter 4).

Examination of a hurricane nature run simulation described in Chapter 4 was aimed at looking for signals of the TCDC in the model, characterizing these signals in time and space, and identifying possible mechanisms associated with its evolution. Detailed 3-dimensiinal analyses of TCDC signals were found in fields of radiation, temperature, moisture, stability, winds, and precipitation. However, these TCDC signals were significantly more robust when the TCDC analysis criteria described in Chapters 2 were satisfied: 1) the TC is at least category 2 intensity ($\geq$43 m s^{-1}); 2) the TC is embedded in a low vertical wind shear environment ($\leq$7.5 m s^{-1}); and 3) the TC is sufficiently removed from land ($\geq$300 km). The NRH1 simulation supports the satellite-based conclusion that these 3 criteria appear to be key factors for conditioning the TC environment to produce robust TCDC signals. When only that portion of the NRH1 simulation is examined when all 3 TCDC analyses criteria were met (03-08 Aug; days 5-10), marked diurnal signals in the aforementioned model parameters emerged. There are definitive fluctuations of radiation, temperature, moisture, stability, winds, and precipitation that appear to reach peak maximum or minimum values in the evening to early morning hours or the mid-morning to afternoon and represent significant changes in the TC and its surrounding environment. These analyses also show that TC diurnal pulses have several thermodynamic, wind, and precipitation traits that are similar to squall lines.

The NRH1 analyses in Chapter 4 suggest that aspects of each of the 5 proposed TCDC mechanisms discussed earlier are present in the TC simulation and also suggests that TC diurnal pulses have thermodynamic wind, and precipitation traits that are similar to squall lines. Although the specific mechanism(s) that act to trigger and sustain the TCDC and TC diurnal

pulses was not clear, analyses of radiation, ice mixing ratio (a proxy for the TC outflow layer), static stability, and winds suggest that nighttime longwave cooling and daytime shortwave warming that are particularly favored in the TC outflow layer (relative to surrounding cloud-free air) are key factors influencing the evolution of the TCDC. The following daily sequence of events is proposed to describe the TCDC life-cycle, including its initiation, radial propagation, and eventual decay each day: first, enhanced nighttime longwave cooling may act to prime (i.e. pre-condition) the TC environment for the initiation of the TCDC by rapidly destabilizing the top of the TC outflow layer in the inner core region. This cooling/destabilization could support several of the TC diurnal pulse triggering mechanisms described above, including trapping of gravity waves, reduction of upper-level potential vorticity, increased IAKE (that would favor a release of outflow), lower pressure in the upper levels (i.e. reduced divergence), and enhanced inner core convection. Second, the nighttime longwave cooling would also rapidly destabilize the region just outside the TC inner core (e.g. R~15-350 km), thereby elevating the level of the LNB and hence, increasing CAPE in this region of the storm where deep convection doesn't always occur and TC diurnal pulses appear to initiate. TC diurnal pulses with hypothesized squall line-like characteristics would encounter convectively favorable conditions as they propagate through this region of the storm in the early to late morning.

Beginning around the time of local sunrise, after the TC diurnal pulse has already been generated and is located at R~200 km, daytime shortwave warming that is also favored in regions of the cirrus outflow layer would begin to dominate the nighttime longwave cooling processes and could lead to the culmination of the TCDC each day. This shortwave warming could act to first to rapidly stabilize the top of the TC outflow layer in the inner core region. This would establish conditions that could support gravity waves that more easily propagate

upward (rather than radially outward) into the stratosphere, a reduction of upper-level potential vorticity, reduced IAKE that would favor more restricted outflow as the day progresses, higher pressure in the upper levels (hence increased divergence), and reduced inner core convection. Second, this shortwave warming would rapidly stabilize the region just outside the TC inner core (i.e. R~150-350 km), thereby lowering the level of the LNB and hence, reducing CAPE in this region of the storm in the early-morning to afternoon hours. During this time, the already-initiated TC diurnal pulse is propagating through the 200-400 km radius range and its vertical extent may become increasingly reduced as the LNB rapidly lowers. If this TC diurnal pulse with squall line-like traits encounters a region of lower to middle level (i.e. ~600-800 hPa) dry air (i.e. TPW values ≤45 mm) as it propagates away from the storm, convectively driven downdrafts could produce gust fronts (i.e. large arc cloud features) that race out ahead of it. Assuming that the 3 TCDC analysis conditions of minimum storm intensity, low vertical wind shear, and minimum distance from land continue to be satisfied, these daytime processes would begin to wane in the late afternoon and around the time of sunset, nighttime longwave dominated processes would once again dominate, commencing the process of priming the TC environment to initiate another TCDC.

Chapter 5 uses a combination of idealized hurricane simulations with varying diurnal cycles to further investigated the TCDC. The simulations used a control run with a normal solar cycle, a daytime only run, and a nighttime-only run. The control run exhibited TCDC signals in thermodynamics and winds that were similar to, though not as robust as the NRH1 simulation and like the NRH1, extended though a deep layer of the atmosphere (~150-925 hPa) and showed a radially propagating TC diurnal pulse in fields of vertical wind that reached a radius of ~300 km. The nighttime-only simulation produced the strongest and most persistent inner core

convection of any run and its TCDC signals (initiated during the first 40 hr of the simulation) in thermodynamics and winds lasted longer than the daytime-only run, suggesting that radiational cooling of the TC environment plays a key role in forcing inner core deep convection and the TCDC. This run also exhibited a radially propagating TC diurnal pulse that, like the control run, reached R~300 km. It is hypothesized that constant longwave cooling preferentially cooled the TC cirrus canopy, thereby cooling the environmental profile, which likely results in an elevated LNB and enhanced CAPE in the region of R~150-350 km. This priming of the peripheral TC environment may have supported TCDC processes and TC diurnal pulses in this simulation. The daytime-only simulation had the weakest, shortest lasting TCDC signals (initiated during the first 40 hr of the simulation) and was the only idealized simulation that did not exhibit a radially propagating TC diurnal pulse. Although some spiral bands were noted in that simulation, they were constrained to R~100-150 km. It is hypothesized that constant shortwave warming preferentially warmed the TC cirrus canopy, thereby warming the environmental profile, which likely resulting in an lower LNB and reduced CAPE in the region of R~150-350 km. This lack of priming of the peripheral TC environment may have suppressed TCDC processes, TC diurnal pulses, and convection in general in this simulation. Times of diurnal minima in lower level radial inflow in the idealized hurricane simulation control run and the periods after these TCDC signals wane in the daytime-only and nighttime-only runs (~72-84 hr into the simulations) could represent intervals when the TC is most protected or insulated from the potentially negative influences of a hostile surrounding environment (e.g. intrusions of low entropy air) when radial entrainment would be reduced.

Chapter 6 built off the satellite and modeling analyses presented in Chapters 3, 4, and 5 by examining the TCDC from an observational perspective that include analyses of 2010

Hurricane Earl and 2014 Hurricane Edouard using GOES water vapor AMVs, GPS dropsondes deployed from the NOAA G-IV jet and WP-3Ds, and LF radar and TDR data from the WP-3Ds. GOES water vapor AMVs in Hurricane Earl suggested that radially propagating diurnal pulses promote enhanced upper-level outflow and divergence that rapidly increase each morning and peak in the afternoon as the TC diurnal pulse propagates away from the storm. It was also shown that afternoon may be a diurnally favorable time of day for the enhancement of TC outflow. GPS dropsondes deployed in the environment of Hurricane Earl indicated that the region radially inward of a TC diurnal pulse exhibits atmospheric profiles that resemble the "onion" soundings that are often seen in the downdraft trailing stratiform region of squall lines, suggesting that the observed TC diurnal pulse may have squall line-like characteristics, that include gust fronts (i.e. arc clouds). These GPS dropsonde soundings show a nearly saturated and approximately moist-adiabatic layer above the melting level (top of the "onion") overlying a sub-saturated and nearly mixed layer below the melting level that is nearly saturated at its base (root of the "onion").

WP-3D GPS dropsonde observations taken in the environment of Hurricane Edouard indicate that the thermodynamic environment just outside the storm's inner core and behind its radially propagating TC diurnal pulse/large arc cloud feature was impacted by convectively driven downdrafts that brought significantly dry air into boundary layer. These observations suggest that large arc cloud events that are associated with TC diurnal pulses can act to stabilize the atmosphere by bringing cool, dry air into the low-levels and boundary layer that can affect the peripheral TC environment for several hours and could be important for TC intensity change. LF radar and TDR data from the same WP-3D mission were used to examine the 3-dimensional convective and wind structure of Hurricane Edouard and showed that this storm's TC diurnal

pulse appears as a ~20 km wide semicircular ring in radar reflectivity that extends from ~0.5-6 km in the vertical and steadily propagates away from the storm. These radar features are associated with enhanced winds/vertical winds and shifting radial flow where the strength and depth of the lower level inflow and middle to upper-level outflow layers increase outside (radially) the radar-indicated TC diurnal pulse location.

Results presented in this thesis highlight TCDC and use a combination of satellite, numerical modeling, and observational analyses to investigate how it can be monitored, its evolution in time and space, its relevance to TC structure and intensity, how it manifests in numerical simulations of TCs, and the mechanisms that both trigger the TCDC and those that prime the environment to support TCDC evolution. New 6-h GOES and Meteosat IR brightness temperature differencing imagery that was developed under this project allowed for detailed analyses of the TCDC that set the stage for the numerical model and observational studies that followed.

The two schematics presented in Chapter 4 (Figs. 4.32 and 4.33) summarize many of the main findings in this work. The first schematic describes the basic state of the TC environment as the TCDC evolves during its early and later stages each day, while the second describes the TCDC-centric daytime evolution of a TC diurnal pulse, associated squall lines and gust fronts, and radial and vertical winds in the lower and upper levels of the storm. It is hypothesized that enhanced nighttime radiational cooling that is particularly favored in the TC outflow layer (relative to surrounding cloud-free air) may act to prime (i.e. pre-condition) the TC environment in a way that favors triggering of the TCDC via convectively-driven gravity waves, radiatively reduced outflow resistance, cloud-cloud-free differential heating, seeder-feeder mechanism, or some combination of these mechanisms. During the daytime, the stabilizing effects of shortwave

warming suppress TCDC process in the storm environment, which leads to the culmination of TCDC each day. Future work will continue to integrate satellite data, numerical model simulations, and observations of the TCDC with a goal of continued advancement of our understanding of this possibly fundamental TC process.

7.2 Future Work

7.2.1 Characteristics of the TCDC and TC Diurnal Pulses

Chapters 4 and 6 presented evidence that TC diurnal pulses have squall line-like characteristics that promote outflow boundaries (i.e. arc clouds) that are hundreds of kilometers in length that can dramatically alter the TC environment. Questions remain as to why these arc cloud features, as well as upper level transverse bands (indicators of upper tropospheric turbulence) seem to both form preferentially near TC diurnal pulses. These analyses could help identify the nature and depth of the TCDC and TC diurnal pulses. Given the apparent radial expansion of the TC cloud field that appears to occur in well-developed storms through a deep layer of the troposphere during the TC diurnal cycle, investigation of the possible relationship between TC diurnal pulses and eyewall replacement cycles is also warranted. In order to assess this possible linkage, a combination of analyses satellite data (e.g. IR brightness temperature differencing imagery, 37 and 85 GHz microwave satellite imagery), high resolution numerical models (e.g. 1 km) and analyses aircraft observations collected in a TC undergoing a secondary eyewall formation should be made.

7.2.2 TCDC Triggering and Environmental Priming Mechanisms

Although findings from this study identified numerous environmental priming (i.e. pre-conditioning) mechanisms that can pre-condition the TC environment to support TCDC processes and TC diurnal pulses, more research is needed to investigate these mechanisms, especially in varying conditions of storm intensity, storm size, and vertical wind shear. To effectively assess the processes that prime the TC environment under these varying conditions, idealized numerical simulations should be carried out. This work also found evidence supporting several of the proposed TCDC forcing mechanisms described in Chapter 3. However, it yet to be determined which mechanism or combination of mechanisms are key to triggering TCDC formation that could later be supported by mechanisms that prime the TC environment.

7.2.3 Convective Diurnal Signals in Non-TCs and Non-Oceanic Regimes

Ongoing research efforts (not shown) suggest that the TCDC may occur in TCs globally and might not be exclusive to mature TCs. There is some indication that a convective diurnal cycle also occurs with other types of organized convection in both the tropics and mid-latitudes (e.g. African easterly waves and mesoscale convective systems). Also, this current research specifically describes the development and evolution of the TCDC over oceanic regions. Since the characteristics of the tropical oceanic diurnal cycle and the convective diurnal cycle over land are quite unique, further investigation is needed to describe how these differing cycles relate to deep convection. Specifically, it is unclear how they might impact convective features that are transitioning from either over land to oceanic regimes (e.g. African easterly waves) or from oceanic to overland regimes (e.g. landfalling TCs).

BILIOGRAPHY

Aberson, S.D., 2010: 10 years of hurricane synoptic surveillance (1997–2006), *Mon. Wea. Rev.,* **138**, 1536-1549.

Aksoy, A., 2013: Storm-relative observations in tropical cyclone data assimilation with an Ensemble Kalman Filter, *Mon. Wea. Rev.,* **141**, 506-522.

Browner, S. P., W. L. Woodley, and C. G. Griffith, 1977: Diurnal oscillation of cloudiness associated with tropical storms. *Mon. Wea. Rev*., **105**, 856–864.

Bergeron, T., 1935: On the physics of cloud and precipitation. *Proc. 5th Assembly U.G.G.I. Lisbon*, **Vol. 2**, p. 156.

Bryan, G. H., and M.D. Parker, 2010: Observations of a squall line and its near environment using high-frequency rawinsonde launches during VORTEX2. *Mon. Wea. Rev.,* **138**, 4076-4097.

Chen, S., and W.R. Cotton, 1988: The sensitivity of a simulated extratropical mesoscale convective system to longwave radiation and ice-phase microphysics. *J. Atm. Sci*., **45**, 3897-3910.

Cotton, W.R, G. Bryan, and S.C. Van Den Heever, 2010: Storm and Cloud Dynamics. Academic Press 809 pp.

Crook, N.A., 1988: Trapping of internal low-level internal gravity waves. *J. Atmos. Sci*., **45**, 1533-1541.

DeMaria, M., M. Mainelli, L.K. Shay, J.A. Knaff, and J. Kaplan, 2005: Further improvement to the Statistical Hurricane Intensity Prediction Scheme (SHIPS). *Wea. Forecasting*, **20:4**, 531-543.

Demuth, J., M. DeMaria, and J. A. Knaff, 2006: Improvement of advanced microwave sounder unit tropical cyclone intensity and size estimation algorithms. *J. Appl. Meteor. Climatol.*, **45**, 1573–1581.

Dunion, J.P., C.D. Thorncroft, and C.S. Velden, 2014: The tropical cyclone diurnal cycle of mature hurricanes. *Mon. Wea. Rev*., **142**, 3900-3919.

Dunion, J. P., 2011: Rewriting the climatology of the tropical North Atlantic and Caribbean Sea atmosphere. *J. Climate*, **24**, 893-908.

Gallina, G.M., and C.S. Velden, 2000: A quantitative look at the relationship between environmental vertical wind shear and tropical cyclone intensity change utilizing enhanced satellite derived wind information. Preprints, *24th Conf. on Hurricanes and Tropical Meteorology*, Ft. Lauderdale, FL, Amer. Meteor. Soc., 7A.4. [Available online at https://ams.confex.com/ams/ last2000/webprogram/24HURRICANES.html.]

Gray, W. M., and R. W. Jacobson, 1977: Diurnal variation of deep cumulus convection. *Mon. Wea. Rev*., **105**, 1171–1188.

Hawkins, J. D., and C. Velden, 2011: Supporting meteorological field experiment missions and post-mission analysis with satellite digital data and products. *Bull. Amer. Meteor. Soc*., **92**, 1009–1022.

Hawkins, J. D., T.F. Lee, K. Richardson, C. Sampson, F. J. Turk, and J. E. Kent, 2001: Satellite multisensor tropical cyclone structure monitoring. *Bull. Amer. Meteor. Soc*., **82**, 567–578.

Hayden, C. M., and R. Purser, 1995: Recursive Filter Objective Analysis of Meteorological Fields: Applications to NESDIS Operational Processing. J. *Appl. Meteor*., **34**, 3-15.

Hock, T.F., and J.F. Franklin, 1999: The NCAR GPS dropwindsonde. *Bull. Amer. Meteor. Soc*., **80**, 407-420.

Holmlund, K., C. Velden, and M. Rohn, 2001: Enhanced Automated Quality Control Applied to High-Density Satellite-Derived Winds. *Mon. Wea. Rev*., **129**, 517-529.

Hong, S.-Y., Y. Noh, and J. Dudhia, 2006: A new vertical diffusion package with an explicit treatment of entrainment processes, *Mon. Wea. Rev*., **134**, 2318–2341.

Houze, R.A., S.A. Rutledge, T.J. Matejka, and P. V. Hobbs, 1981: The mesoscale and microscale structure and organization of clouds and precipitation in midlatitude cyclones. III: air motions and precipitation growth in a warm-frontal rainband. *J. Atm. Sci*., **38**, 639-649.

Iacono, M. J., J. S. Delamere, E. J. Mlawer, M. W. Shephard, S. A. Clough, and W. D. Collins, 2008: Radiative forcing by long-lived greenhouse gases: Calculations with the AER radiative transfer models, *J. Geophys. Res*., **113**, D13103.

Jarvinen, B. R., C. J. Neumann, and M. A. S. Davis, 1984: A tropical cyclone data tape for the North Atlantic basin, 1886-1983: Contents, limitations, and uses. NOAA Tech. Memo. NWS NHC 22, 21 pp.

Kain, J. S., and J. M. Fritsch, 1990: A one-dimensional entraining/detraining plume model and its application in convective parameterization, *J. Atmos. Sci*., **47**, 2418–2436.

Knaff, J. A., S. P. Longmore, D. A. Molenar, 2014: An objective satellite-based tropical cyclone size climatology. *J. Climate*, **27**, 455–476.

Knaff, J.A., and J. F. Weaver, 2000: A mesoscale low-level thunderstorm outflow boundary associated with Hurricane Luis. *Mon. Wea. Rev*., **128**, 3352–3355.

Kossin, J.P., J.A. Knaff, H.I. Berger, D.C. Herndon, T.A. Cram, C.S. Velden, R.J. Murnane, and J.D. Hawkins, 2007: Estimating hurricane wind structure in the absence of aircraft reconnaissance. *Wea. Forecasting*, **22**:1, 89–101.

Kossin, J. P., 2002: Daily hurricane variability inferred from GOES infrared imagery. *Mon. Wea. Rev*., **130**, 2260–2270.

Kraus, E.B., 1963: The diurnal precipitation change over the sea. *J. Atm. Sci*., **20**, 546-551.

Lazzara, M. A., and Coauthors, 1999: The Man computer Interactive Data Access System: 25 Years of Interactive Processing. *Bull. Amer. Meteor. Soc*., **80**, 271–284.

Lee, C. S., K. K. W. Cheung, W.-T. Fang, and R. L. Elsberry, 2010: Initial maintenance of tropical cyclone size in the western North Pacific. *Mon. Wea. Rev*., **138**, 3207-3223.

Lee, T. F., F. J. Turk, J. D. Hawkins, and K. A. Richardson, 2002: Interpretation of TRMM TMI images of tropical cyclones, *Earth Interact.*, **6**, 3.

Lim, K.-S. S., and S.-Y. Hong, 2010: Development of an effective double-moment cloud microphysics scheme with prognostic cloud- condensation nuclei (CCN) for weather and climate models, *Mon. Weather Rev.*, **138**, 1587–1612.

Liu, C., and M. W. Moncrieff, 1998: A numerical study of the diurnal cycle of tropical oceanic convection. *J. Atmos. Sci.*, **55**, 2329–2344.

Mapes, B. E., and R.A. Houze Jr., 1993: Cloud clusters and super- clusters over the oceanic warm pool. *Mon. Wea. Rev.*, **121**, 1398–1415.

Marks, F.D., 1985: Evolution and structure of precipitation in Hurricane Allen (1980). *Mon. Wea. Rev*. **113**, 909-930.

Mecikalski, J.R., and G.J. Tripoli, 1998: Inertial Available Kinetic Energy and the dynamics of tropical plume formation. *Mon. Wea. Rev.*, **126**, 2200–2216.

Metcalf, J., 1975: Gravity waves in a low-level inversion. *J. Atmos. Sci.*, **32**, 351-361.

Mueller, K.J., M. DeMaria, J.A. Knaff, J.P. Kossin, T.H. Vonder Haar:, 2006: Objective estimation of tropical cyclone wind structure from infrared satellite data. *Wea. Forecasting*, **21**:6, 990–1005.

Martin, D.W., 1975: Characteristics of West Africa and Atlantic cloud clusters. GATE Rep. No. **14**, Preliminary Scientific Results, Vol. **1**, 182-190.

Nappo, C.J., 2013: *An Introduction to Atmospheric Gravity Waves*. Academic Press, 359 pp.

Navarro, E.L., and G.J. Hakim, 2016: Idealized numerical modeling of the diurnal cycle of tropical cyclones. *J. Atmos. Sci*., **73**, 4189-4201.

Noh, Y., W. G. Cheon, S. Y. Hong, and S. Raasch, 2003: Improvement of the K-profile model for the planetary boundary layer based on large eddy simulation data, *Boundary Layer Meteorol*., **107**, 421–427.

Nolan, D. S., R. M. Atlas, K. T. Bhatia, and L. R. Bucci, 2013: Development and validation of a hurricane nature run using the joint OSSE nature run and WRF model. *J. Adv. Model. Earth Syst*., **5**, 382–405.

Olander, T. L., and C. S. Velden, 2007: The Advanced Dvorak Technique: Continued development of an objective scheme to estimate tropical cyclone intensity using geostationary infrared satellite imagery. *Wea. Forecasting*, **22**, 287–298.

Pfister, L., K.R. Chan, T.P. Bui, S. Bowen, M. Legg, B. Gary, K. Kelly, M. Proffitt, and W Starr, 1993: Gravity waves generated by a tropical cyclone during the STEP tropical field program. *J. Geophys. Res*., **98**, 273-8638.

Randall, D.A., Harshvardhan, and D.A. Dazlich, 1991: Diurnal variability of the hydrologic cycle in a general circulation model. *J. Atmos. Sci*., **48**, 40-62.

Rogers, R. F., S. Lorsolo, P. Reasor, J. Gamache, and F. Marks, 2012: Multiscale analysis of tropical cyclone kinematic structure from airborne Doppler radar composites. *Mon. Wea. Rev*., **140**, 77–99.

Tang, B., and K. Emanuel, 2012: A ventilation index for tropical cyclones. *Bull. Amer. Meteor. Soc*., **93**, 1901-1912.

Tang, X, and F. Zhang, 2016: Impacts of the diurnal radiation cycle on the formation, intensity, and structure of Hurricane Edouard (2014). *J. Atmos. Sci*., **73**, 2871-2892.

Tripoli, G. J., and W.R. Cotton, 1989: Numerical study of an observed orogenic mesoscale convective system. Part 1: Simulated genesis and comparison with observations. *Mon. Wea. Rev*., **117**, 273-304.

Velden, C.S., B. Harper, F. Wells, J.L. Beven II, R. Zehr, T. Olander, M. Mayfield, C. Guard, M. Lander, R. Edson, L. Avila, A. Burton, M. Turk, A. Kikuchi, A. Christian, P. Caroff, P. McCrone, 2006: The Dvorak tropical cyclone intensity estimation technique: A satellite-based method that has endured for over 30 years. *Bull. Amer. Meteor. Soc*., **87**, 1195-1210.

Velden, C. S., C. Hayden, S. Nieman, W. Menzel, S. Wanzong, and J. Goerss, 1997: Upper-Tropospheric Winds Derived from Geostationary Satellite Water Vapor Observations. *Bull. Amer. Meteor. Soc*., **78**, 173-195.

Weickmann, H. K., A. B. Long, and L. R. Hoxit, 1977: Some examples of rapidly growing oceanic cumulonimbus clouds. *Mon. Wea. Rev*., **105**, 469–476.

Willoughby, H.E., J.A. Clos, and M.G. Shoreibah, 1982: Concentric eye walls, secondary wind maxima, and the evolution of the hurricane vortex. *J. Atmos. Sci*., **39**, 395-411.

Yang, G., and J. Slingo, 2001: The diurnal cycle in the tropics. *Mon. Wea. Rev*., **129**, 784–801.

Zipser, E. J., 1977: Mesoscale and convective–scale downdrafts as distinct components of squall line structure. *Mon. Wea. Rev*., **105**, 1568–1589.